## Colloidal design

*Building, bending and breaking*

Stuij, S.G.

**Publication date**
2020

**Document Version**
Final published version

**License**
Other

# Colloidal Design

## Building, Bending and Breaking

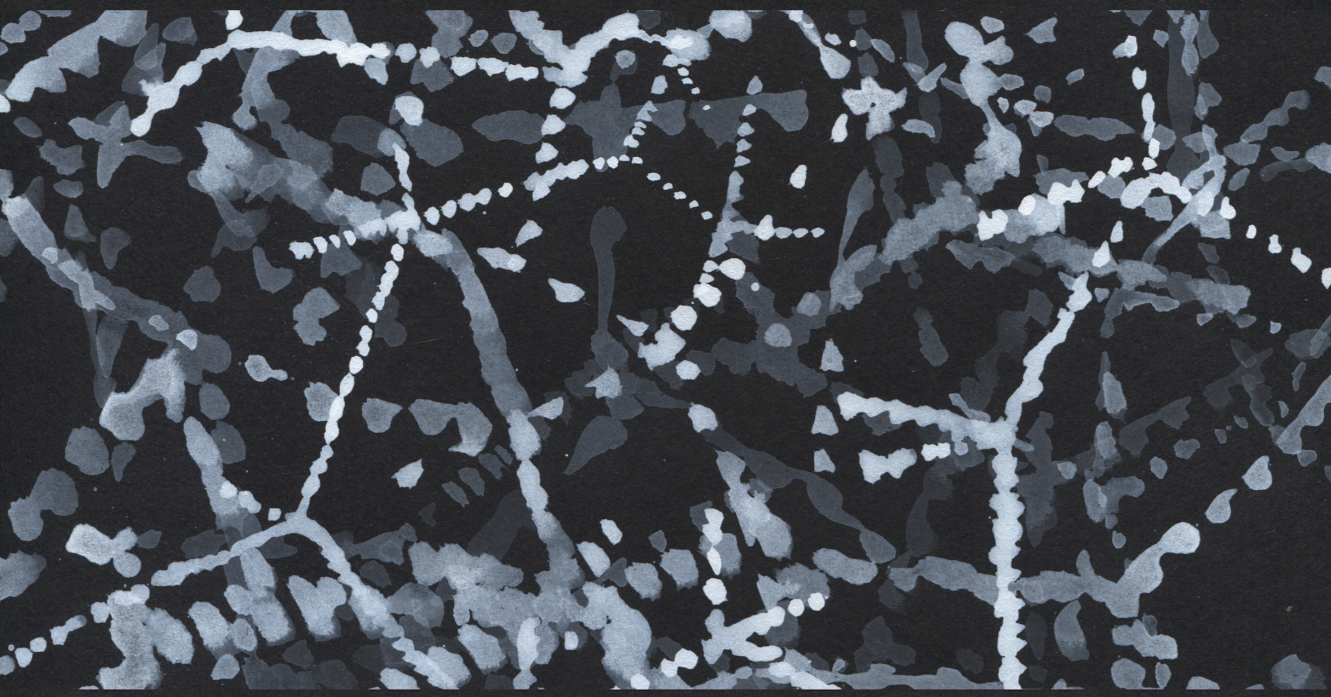

Simon Stuij

# Colloidal Design: Building, Bending and Breaking

Simon G. Stuij

# Colloidal Design: Building, Bending and Breaking

ACADEMISCH PROEFSCHRIFT

ter verkrijging van de graad van doctor
aan de Universiteit van Amsterdam
op gezag van de Rector Magnificus
prof. dr. ir. K.I.J. Maex
ten overstaan van een door het College voor Promoties ingestelde commissie,
in het openbaar te verdedigen in de Agnietenkapel
op woensdag 29 januari 2020 om 12:00

door

Simon Govert Stuij

geboren te Aberdeen.

**Promotiecommissie:**

| | | |
|---|---|---|
| Promotor: | Prof. dr. P. Schall | Universiteit van Amsterdam |
| Copromotor: | Dr. T.E. Kodger | Universiteit van Amsterdam |
| Overige leden: | Dr. S. Sacanna | New York University |
| | Prof. dr. ir. J.H.B. Sprakel | Wageningen University & Research |
| | Prof. dr. S. Woutersen | Universiteit van Amsterdam |
| | Dr. C.J.M. Coulais | Universiteit van Amsterdam |
| | Prof. dr. P.G. Bolhuis | Universiteit van Amsterdam |
| | Prof. dr. ir. E.J.G. Peterman | Vrije Universiteit Amsterdam |

Faculteit der Natuurwetenschappen, Wiskunde en Informatica

UNIVERSITEIT VAN AMSTERDAM


The work described in this thesis was performed in the group prof. dr. Peter Schall at the Institute of Physics, Universety of Amsterdam, Science Park 904 1098 XH Amsterdam. It is financed by the Netherland Organization for Scientific Research (NWO) through a VICI personal grant awarded to prof. dr. Peter Schall.

**ISBN: 9789464020427**
Cover design by Leon Friederichs (*www.farfromready.com*)


The author can be reached at: simonstuij@gmail.com

# Contents

The atoms, as their own weight bears them down
Plumb through the void, at scarce determined times,
In scarce determined places, from their course
Decline a little- call it, so to speak,
Mere changed trend. For were it not their wont
Thuswise to swerve, down would they fall, each one,
Like drops of rain, through the unbottomed void;
And then collisions ne'er could be nor blows
Among the primal elements; and thus
Nature would never have created aught.

–*Lucretius, De Rerum Natura* $\sim 60BC$
(Trans. W. E. Leonard)

CHAPTER 1

# Introduction

## 1.1 Self-assembly in nature

In the summer before starting my physics degree, I read in a home-printed copy of Feynman's physics lectures:

> If, in some cataclysm, all of scientific knowledge were to be destroyed, and only one sentence passed on to the next generations of creatures, what statement would contain the most information in the fewest words? I believe it is the atomic hypothesis (or the atomic fact, or whatever you wish to call it) that all things are made of atoms, little particles that move around in perpetual motion attracting each other when they are a little distance apart, but repelling upon being squeezed into one another. In that one sentence, you will see, there is an enormous amount of information about the world, if just a little imagination and thinking are applied." – *The Feynman Lectures on Physics*

Feynman need not worry, because the notion that all things are made of atoms is firmly engraved in our culture. However, this hardly starts to explain anything about the world and will most likely not impress the next generation creatures too much. It is, after all, rather easy to see how we can go one way: Dissecting things to find everything is made from simple building blocks. But how on earth does nature go the other way? How does the enormous amount of atoms conspire together to make something as sophisticated and delicately ordered like all the living creatures that you see around you? How do things build themselves?

An early suggestion comes from Lucretius (99 BC - c. 55 BC), who was already an atomist 2000 years ago. He proposes the 'clinamen', which denotes the random swerving and swirling of atoms that cause atoms to collide with each other, thus bringing into being our diverse world. Though poetic, this idea is not quite precise enough for modern science. Yet, when interpreting his notion of collisions more generally as (local) interactions, he does seem to foreshadow the modern notion of self-assembly, which can be defined as:

> *Self-assembly*: A process by which disordered building blocks form an ordered structure through only local interactions.[1]

Here, interactions should be understood as the sum of all attractions and repulsions present between the building blocks. In self-assembly, when building blocks are in close proximity, it is these interactions that can cause them to click together in an orderly fashion like Lego blocks. The adjective *local* is essential in this definition. It conveys that building blocks only have local information, and have no awareness of what bigger structure they are forming. For self-assembly to work, one needs at least three ingredients: (i) Building blocks, (ii) interactions that cause the 'clicking' of blocks, (iii) a source of movement, which can be completely random (clinamen-like) but is required to bring the building blocks within close enough proximity in order to interact.

Self-assembly processes do not only happen in living nature or always start with atoms, but can be seen everywhere and at all length scales [7], see Figure 1. When walking over a bridge in a park during fall, you might see leaves arranged in regular patterns. More spectacular might be the rings of Saturn. Initially, Saturn was surrounded by a swirling sea of ice and rock fragments (how this came about is still debated). Collisions and the law of conservation of angular momentum caused these fragments to be confined in narrow beautiful disks. Biology is especially full of self-assembly. Army ants that live in rain forests self-assemble in a multitude of structures, a famous one being 'living bridges' by means of which fellow colony members can efficiently traverse gaps [5]. Diving deeper down in size, one can find fibrin networks that can quickly solidify a drop of blood by spanning a net that connects red blood cells together. Their self-assembly is triggered when a vein is cut, to stop the bleeding as soon as possible. Interestingly, the building blocks of these fibrin networks, fibrinogen proteins, are themselves examples of what could be called the masters of self-assembly: Proteins. Fibrinogen is, like all proteins, a specifically arranged sequence of amino-acids that spontaneously assembles to form the exact right 3d structure. The importance and sophistication of this particular self-assembly process has earned itself a specific name: Protein-folding.

It is a fun exercise to identify the three self-assembly ingredients in all of these cases. Building blocks are quite simple to determine. What is striking is that the building blocks vary widely in complexity. Compare, for instance, the relative simplicity of the dead leaf and the amino acid, with the complexity of the ant or the fibrinogen protein. Interactions and the source of movement are sometimes more difficult to identify. The different length scales and media involved determine the physical principles that govern the interactions and movement, and set the opportunities and challenges for self-assembly there. Rocks around Saturn interact through elastic collisions, and in the vacuum of space they move simply due to inertia. Leaves move as they are pushed by currents and waves in the water, and likely interact by a combination of surface tension and capillary forces. Ants can locomote and grab

[1] This definition was inspired by Skylar Tibbits [1], and should be considered a working definition. An exact definition is difficult to give mainly due to the difficulty of what is meant by order. For a sophisticated attempt to exactly define the closely related term self-organization see Ref. [2]

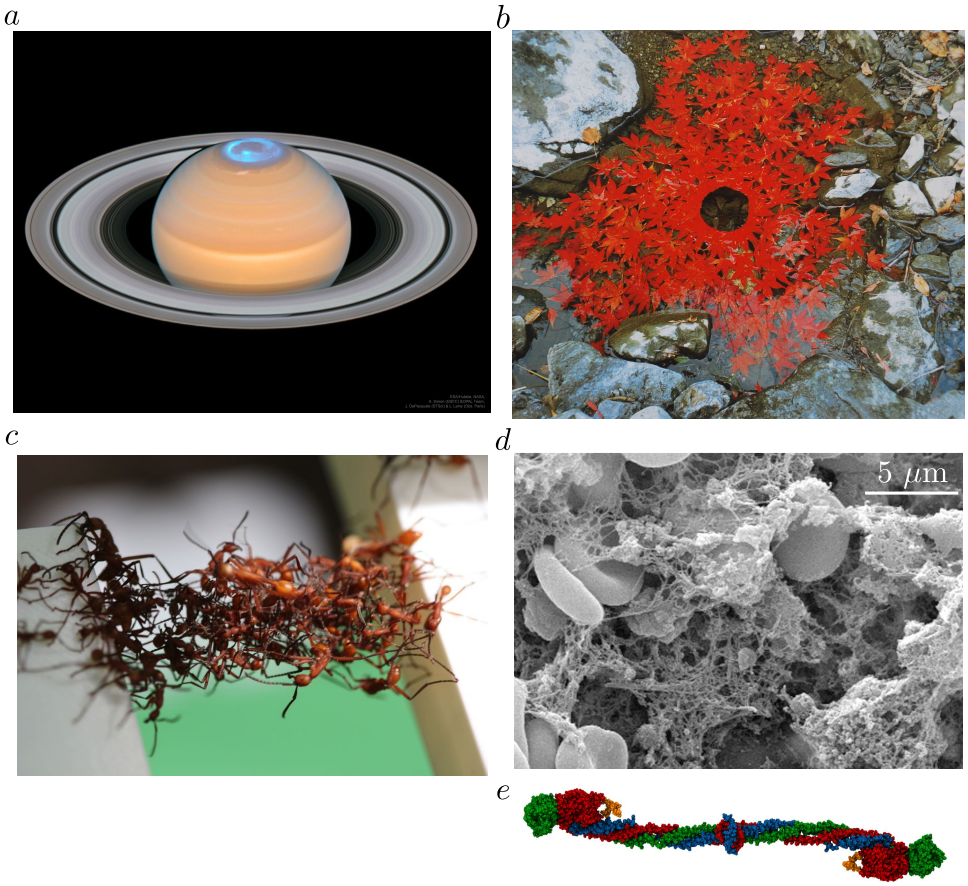


Figure 1.1: Self-assembly processes in nature occur at all length-scales (a) Hubble telescope image of Saturn. Saturn's rings consist of ice and rock particles, dynamically self-assembled in a narrow ring. Shown is also saturn's ultraviolet aurora. (credit: ESA/Hubble, NASA, A. Simon, J. DePasquale., L. Lamy Source: APOD 03−09−2018 [3]) (b) *leaves stitched together to make a floating chain (not shown) the next day it became a hole supported underneath by a woven briar ring* (credit: Andy Goldsworthy [4]) (c) Army ants form a living bridge (credit: Chris Reid and Matthew Lutz [5]) (d) Electron micrograph of fibrin network connecting red blood cells in a blood cloth, (PHIL public domain, credit: Janice Haney Carr) (e) Molecular drawing of an inactive Fibrinogen protein in it's folded state (adopted from [6])

each other with their legs. The realm of microbiology is aquatic. A diverse number of forces exist at this length scale in water, to name a few: Electrostatics, hydrophobic/hydrophilic interactions, dispersion forces. These are all gratefully used by proteins and their complexes, such as fibrin. This rich palette is further supported by a surprising fact. Movement comes for free. That's because water molecules are

constantly jiggling due to thermal energy. All microscopic things that are immersed in water start to experience the individual kicks of the water molecules. This results in an erratic movement called *Brownian motion*. The diverse interactions and the presence of Brownian motion make water at the nano- to microscopic length scale a particularly rich realm for self-assembly, which is an important reason why life originated there, and why the human body consists of roughly 60% water.

There are a lot of surprises in self-assembly, because what you put in does not equal what you get out. In other words, self-assembly of building blocks can lead to emergent unexpected properties; a superstructure can have properties completely absent from those of its building block. This aspect fascinates philosophers [8] and scientists [9–11] as new theories and patterns might be lurking in these emergent behaviors. This is especially true when assembled superstructures sequentially further self-assemble in a hierarchical manner. This happens widely in biology and results in new behavior at each step: Fibrin withstands stress - dispersed fibrinogen doesn't. Cells can reproduce - atoms and proteins can't. Birds can fly - atoms, proteins and cells can't. Obviously, to say birds self-assemble from cells is stretching terminology. Somewhere along the ladder of hierarchical assembly, structures are formed that consume energy and start to sense and process information, at which point self-assembly turns into self-organization. Even higher up, living things emerge that grow and divide. Self-assembly sits at the basis of this ladder. But the exact transitions between levels are grey zones. The goal of self-assembly research is partly to clear these grey zones, and partly to push self-assembling systems to the limits of what is possible, trying to answer questions such as: What are the minimal ingredients to obtain a self-reproducing system? What building blocks and self-assembly driveway is needed to obtain structures with similar mechanical functionality as molecular biomachines?

## 1.2 Self-assembly with colloidal building blocks

Researchers are developing a variety of ways to mimic self-assembly in nature, partly to study fundamental questions. In addition, much of this research is driven by technological promises. At the macroscopic scale there are swarm robots [18], and robots that assemble themselves through folding [19]. Molecular self-assembly acts at the other end of the scale [20, 21], a mature field, that resulted for instance in self-healing polymers [22], with applications in flexible electronics and artificial skin [23]. The current forerunner in the controlled assembly of micro structures should technically be called a hybrid natural/man-made system: DNA origami is able to program self-assembly through a designed sequence of base pairs [24]. Also, the self-assembly of inorganic materials is being pursued, for instance semiconducting nanoparticles, whose controlled assembly has important applications in photovoltaics [25].

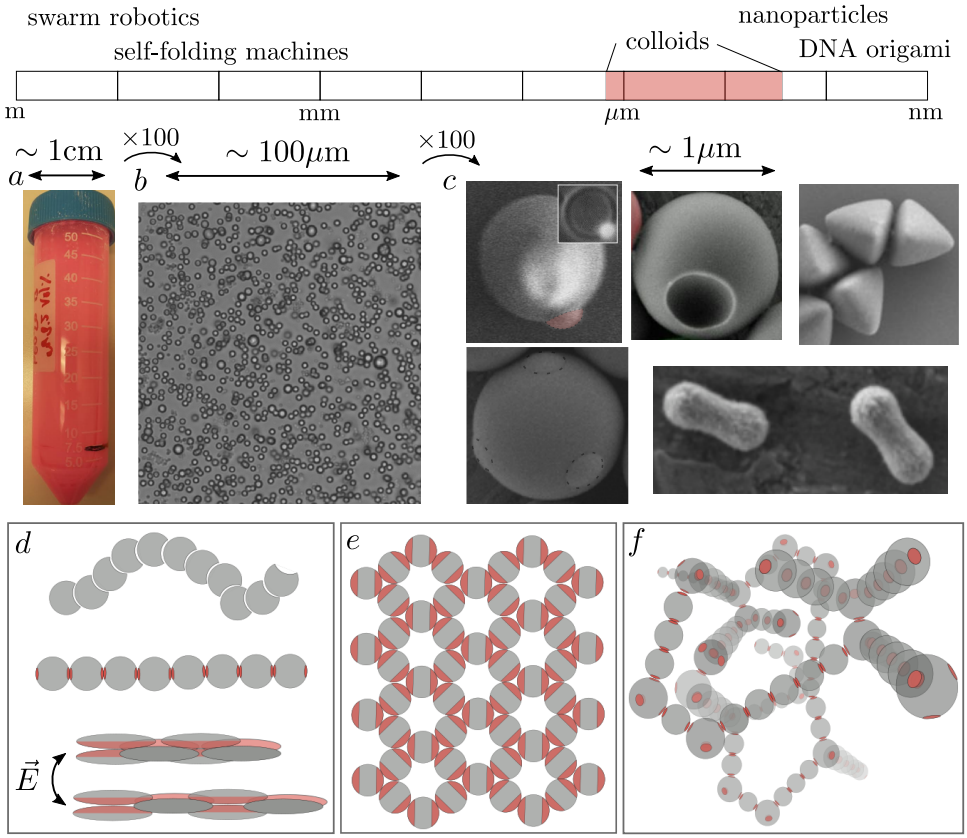


Figure 1.2: Colloids are model building blocks for self-assembly. Top: logarithmic length scale showing the colloidal domain with respect to other artificial self-assembly systems. (a) A typical milky colloidal dispersion, the pinkish color comes from using fluorescently dyed particles. (b) Zooming-in using optical microscopy reveals the sample consists of microscopic floating spheres. (c) Electron micrographs that show colloidal particles have advanced from isotropic spheres to designer shapes. (top left) The authors own attempts at making a snowman particle, inset shows fluorescently label 'head'. (continuing clockwise) Expertly made dimpled particles, tetrahedrons, peanut shaped particles and tetrapatch particles (credit: S. Sacanna, Z. Gong, M. Youssef [12]). (d,e,f) Graphic representations of self-assembled structures. (d) Experimentally realized one dimensional assemblies: Flexible lock-and-key chains [13], more rigid colloidal 'polymers' from dipatch particles [14], extendible colloidal fibers from Janus ellipsoids actuated by an electric field [15]. (e) Experimentally realized two-dimensional Kagomé lattice from triblock colloids [16]. (f) Three-dimensional equilibrium gel network from tetrapatch and dipatch particles, predicted by simulations [17] but so far only indirectly observed for nanoparticles.

### 1.2.1 Colloids, collectivist beings

Colloids appear, at first sight, somewhat inconspicuous amongst these ambitious self-assembling systems. Colloids consist of small particles of a few 100nm in size that are floating in a liquid, suspended by Brownian motion [26, 27], see Fig. 1.2. Such systems, as for instance milk or paint, occur naturally. Usually, they can be recognized by an unspectacular turbid appearance, that results from light scattering. The features of an individual colloidal particle are often close to a sphere.

However, their ordinary appearance is deceiving. To cite a recent review: "A colloid is a dispersion of microscopic particles that are individually unremarkable but collectively interesting" [28]. Colloids stand out as self-assembling building blocks precisely because of their individual simplicity. By making minor changes on the building block level, such as varying particle shape or interaction directionality, the effect on the resulting assembled structure can be investigated conveniently: A colloidal particle is typically big enough to be imaged using light microscopy. This way, the assembly process can be followed directly and dynamically, something that is much more difficult to achieve for smaller building blocks such as nanoparticles and DNA. At the same time, their size is small enough to exhibit Brownian motion as a natural source of movement, in contrast to bigger building blocks, which require active driving mechanism. For these reasons colloids are ideal as a test-bed to study fundamental questions, leading to a close relation between theoretical and experimental work.

Up until recently, colloidal particles were mostly restricted to a completely spherical geometry. Interestingly, already these simplest of building blocks lead to a plethora of interesting collective assemblies [29], from equilibrium hard sphere crystals [30] and attractive ionic crystals [31], to out-of-equilibrium fractal gels [32] and glasses [33]. The similarity of these assemblies to atomic states of matter earned colloids the name of model atoms, and their direct visualization offered insight into fundamental processes that are difficult to study on the atomic scale, such as crystal nucleation [34], defect dynamics [35] and structural rearrangements in glasses [36].

### 1.2.2 Colloids, model building blocks

Continuous advances in synthesis have transformed colloidal particles from isotropic spheres to designer parts with precise control over shape, composition and interaction. For instance, the colloidal particles shown in Fig. 1.2(c) are the result of recent synthesis protocols, yielding snowman particles [37], dimpled particles [13], regular polyhedra like tetrahedra or cubes [38, 39], and peanut shaped particles [40]. Especially optimized for self-assembly are so-called *patchy particles*, that achieve limited valency and directional bonding through a minimal adjustment, a heterogenous surface with well-defined patches of tunable size [38]. The control of colloidal interactions has likewise been subject to continued advances. By grafting complementary DNA strands on particle surfaces, specific interactions that can be programmed such that particles have a 'color' and only bond to specific complementary particles [41],

chiral interactions [42], and flexible bonds with valency [43], have been achieved. In addition, externally controllable interactions using critical Casimir forces [44], thermally sensitive depletants [45], or external electric/magnetic fields [46] allow for the on and off switching of interactions and the tuning of interaction strength, directing the assembly. Finally, colloidal particles can be rendered active through rotating electric fields, the consumption of chemical fuels or local thermal gradients [47]. The non-Brownian dynamics of active colloids can push a system far from equilibrium, resulting in new avenues for dynamic structure formation inspired by biology [48].

These developments at the single particle level take colloidal particles from model atoms to designated building blocks that self-assemble into various designer structures, such as micelles, tubes, chiral helices and shells [49–53], freely jointed mechanisms and chains [13, 43, 54], patchy colloidal 'molecules' and 'polymers' [14], chiral architectures [42], shape-changing and activated filaments [15, 55], or self-spinning microgears [56], see Fig. 1.2(d) for graphic representations of some of these structures. In addition, surprising new lattice equilibrium states have been found, such as the Kagomé lattice assembled from triblock Janus particles [16], see Fig. 1.2(e). Finally, using a hierarchical assembly technique and specific, DNA-programmed interactions, three-dimensional crystals with diamond and pyrochlore sublattices have been assembled [57]. Such crystal structures had long been sought after, because they are predicted to have a large photonic bandgap, which is interesting both for fundamental reasons and for potential optical applications.

These experimental achievements are guided by equally active theoretical efforts [58]. At the basis lie two fundamental and difficult problems that often require numerical simulations. (i) The first is the forward problem of self-assembly: Given a system of building blocks and interactions, to predict the resulting assembled structure. This problem has been extensively explored for patchy particles. Numerical simulations predict these will assemble into new equilibrium states that have no atomic equivalent, such as zero-temperature stable liquids and equilibrium gel networks [17, 59], see Fig. 1.2(f). Together with analytical studies this lead to the identification of the importance of rotational entropy in explaining the stability of open space-spanning structures [60]. In addition, the effect of shape anisotropy has been simulated. By varying facets of hard polyhedra, a variety of crystal, plastic crystal and liquid crystal phases are predicted to form [61], which can be understood through emergent directional entropic forces [62]. (ii) The second fundamental problem is the inverse problem of self-assembly: Given a desired structure, to identify constituents that will assemble into that form. One analytical study proposes a scheme using both directional bonding, and specific colored interactions, and obtains a criterium for the minimum amount of colors needed for the kinetically robust assembly of a desired periodic structure [63]. Beyond periodic structures, ambitious schemes try to emulate self-replication and metabolism in colloidal systems [64]. They show using simulations, that close packed clusters can self-replicate and catalytic cycles can emerge, if interactions are carefully designed using not only specific and valent interactions but also time-dependent interactions [65, 66].

Some of this theoretical work has been translated to experiments or, such as

the Kagomé lattice, was inspired by initial experimental results. Some proposals, such as 'life-like' colloidal systems, seem still to require a lot of innovation. And some predictions appear particularly close to experimental realization, with all the building blocks in place, such as an equilibrium gel made from patchy particles.

### 1.2.3 Colloidal mechanics

The above exposition has focused on individual building blocks and the structures in which they self-assemble, but in order to evaluate and design the functionality of such assemblies, mechanical considerations are of paramount importance. Traditionally, such consideration would start by studying the averaged bulk properties of materials. In contrast to strong materials, for which strength, hardness and toughness are some of the key parameters, colloidal matter is a typical *soft matter*, characterized by a complex rheology involving both flow and rigidity. Indeed, the rheology of colloids features viscoelastic and viscoplastic effects such as shear thinning (yoghurt), shear thickening (corn starch), shear banding and yield stresses [67]. These different rheological responses are intimately connected to the underlying colloidal structure and the hydrodynamics of the suspending liquid. Relating structure to rheology is challenging, involving complex questions concerning network rigidity, the role of entropy and contact mechanics. The improved structural control of novel self-assembly systems could help to answer some of these questions. At the same time, structures with new bulk rheology, so far not seen for colloidal systems, could be designed. For instance, gel networks from patchy particles, as shown in Fig. 1.2(f), have limited connectivity, similar to biopolymer hydrogels such as fibrin. Their rheology might therefore be similar, which is interesting because semiflexible biopolymer networks are known for their particularly rich mechanical behavior [68].

However, with the advent of self-assembled colloidal designer architectures, the traditional focus on bulk rheology is shifting to micromechanical considerations. This is not only done in order to better understand the link between local and bulk behavior, but primarily because some of these architectures are designed to show interesting local mechanical behavior. For instance, the lock-and-key mechanisms [13], actuated shape-shifting Janus ellipsoids [15] and chains showing mechanical instabilities [69] have mechanical functionality that remind of macroscopic meta-mechanical systems [70], see Fig. 1.2(d). Furthermore, spinning microgears demonstrate the potential of coupling activity with small scale rigid structures [56]. Such trends take inspiration from biological protein machines such as the ribosome, or the workings of the cytoskeleton, which more than macroscopic machines make use of delicate mechanical functionality, enabled by shape, mechanisms and self-assembly, to do useful work in a Brownian environment [71].

## 1.3 Thesis outlook

This thesis deals with the assembly of patchy colloidal particles, and the mechanical properties of assembled structures. The colloidal building blocks used, copolymer spheres grafted with polymer brushes [72] and patchy particles made by colloidal fusion [38], are engineered particles optimized by design for self-assembly. An externally controllable interaction is used, called the critical Casimir interaction. This is a temperature-controlled interaction that arises between colloids suspended in a near-critical binary mixtures. With this system we self-assemble various colloidal structures and study their micromechanics.

Chapter 2 introduces the experimental systems and techniques used. This chapter starts out on a conceptual level, with a general discussion on how to make colloidal particles. This is followed by the particle synthesis method, a short introduction to the critical Casimir interaction as a tool for self-assembly, and its application to patchy particle assembly. Finally, the main experimental techniques are summarized, and short literature surveys are provided outlining their previous uses in colloidal science.

In Chapter 3, the critical Casimir interaction is directly measured between two isotropic particles and compared with theoretical models over a wide range of binary solvent concentration. This extends previous studies at the critical concentration to experimental conditions optimal for self-assembly. We thus validate the agreement of theoretical predictions with experimental measurements in a wider solvent concentration range, relevant for assembly. Precise knowledge of the interaction potential is essential to rationally design self-assembly pathways and to interpret the behavior of assembled structures.

This is built upon in Chapter 4, where critical Casimir forces are used to assemble a chain of isotropic particles. Using laser tweezers to perform micromechanical experiments on this chain, we explore the buckling instability of filaments in the presence of thermal fluctuations and plasticity. We identify a novel form of stochastic buckling instability, for which fluctuations become amplified and diverge in the vicinity of the critical buckling transition.

Chapter 5 presents the critical Casimir assembly of patchy particles, showing single bond per patch interactions that are reversible and tunable with temperature. We demonstrate the assembly of various well-defined structures: Small assemblies of dipatch and tetrapatch particles form colloidal 'molecules', such as colloidal pentane. Larger assemblies of dipatch particles form colloidal 'polymers'. By including tetrapatch particles, these polymers cross-link, forming branched clusters that approach a gel network with a mesh size tunable by the ratio of tetrapatch/dipatch particles. Finally, we achieve a true patchy percolated gel network by decreasing the size of the particles to speed up formation kinetics. This structure has a good chance of being an equilibrium gel.

With the realization of a well-controlled and patchy aggregating system, a stage is reached to ask detailed questions about the mechanics of such assemblies. Chapters 6 and 7 explore in detail the mechanics of one of the self-assembled patchy

structures achieved: Straight colloidal dipatch chains. This particularly well-defined and reproducible structure shows rich semiflexible mechanics, and forms an excellent model system for micrometer-size filaments, a common motif in many soft and biological materials. Chapter 6 uses the thermal bending fluctuations of a quiescent chain to show that, like the interparticle radial interaction strength, the bending rigidity increases as temperature is increased closer to the critical point.

The final chapter 7 uses optical tweezers to probe the mechanics of dipatch chains under extreme deformations, inducing buckling and fracture. These tests reveal a mechanical response that resembles the richness of biological filaments, involving buckling, viscoelastic effects and ultimately fracture upon a critical bending. These results provide insight into the mechanics of assembled colloidal structures, essential to the design of functional colloidal architectures.

CHAPTER 2

# Concepts and methods

## 2.1 Colloidal building blocks for self-assembly

### 2.1.1 Colloidal synthesis

This thesis focuses on the assembly and mechanical properties of patchy particle structures. It addresses questions like, how to tune effective interactions, what are the self-assembly pathways and what mechanical properties do the resulting structures have? It is only possible to explore such questions experimentally due to the fine control over the shape and surface functionality of colloids afforded by the recent progress in colloidal chemistry. Indeed, the two types of colloidal particles mainly used in this thesis, copolymer spheres grafted with polymer brushes [72] and patchy particles made by colloidal fusion [38], are sophisticated engineered particles. Their features have been optimized by design for research and include o.a. material control over refractive index and density, surface modification to control charge, fluorescent dyes for optimal microscopic visibility, and well-defined heterogenous surfaces for directional, patchy interactions. Before describing in more detail the synthesis of the patchy particles, I would like to sketch the basic ingredient, which itself is an interesting example of self-assembly.

The essential synthesis technique that lies at the basis of both types of colloidal particles used, is dispersion polymerization [73]. This method is particularly suitable to create particles in the 1 $\mu$m size range, ideal for optical imaging. In dispersion polymerization, monomers are first dissolved in a solvent. In addition, initiator and a steric stabilizer are added. The necessary condition for dispersion polymerization is that the reaction medium is a good solvent for the monomer and the initiator, but does not dissolve the polymer. Therefor, once the polymerization is initiated, the polymer precipitates out of solution. These precipitates form small droplets that initially coalesce and grow by absorbing remaining monomer, until they reach a maximum size at which they become sterically stabilized. By using the right steric stabilizer(s) and the right reaction conditions such as temperature and stirring speed exquisitely monodisperse particles ($< 5\%$) can be created [74].

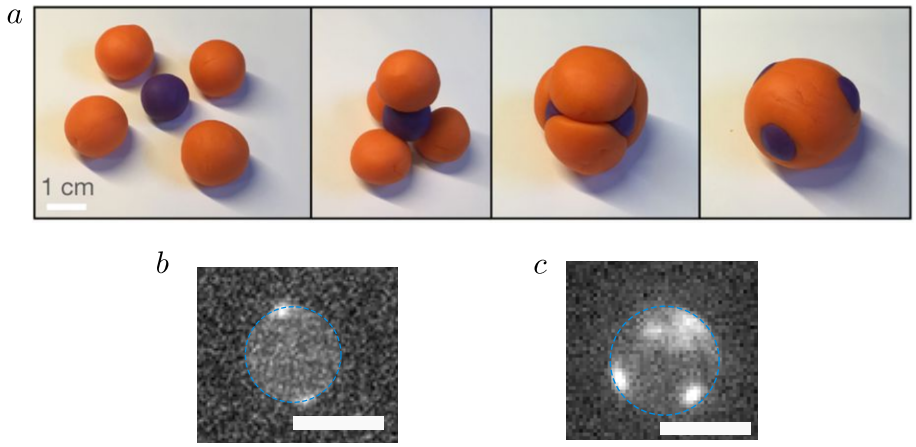


Figure 2.1: Colloidal fusion (a) Play-dough macroscopic model of a colloidal fusion synthesis of a tetrapatch particle, orange spheres represent PS and purple sphere represents TPM, reprinted with permission from ref. [38] (b) epifluorescent image of a dipatch particle obtained through colloidal fusion (DP-B) (c) Tetrapatch particle (TP-A). Scalebars are 3 $\mu$m.

It is interesting to note that dispersion polymerization can in some sense itself be viewed as a self-assembly process. The final size of the particle is spontaneously determined and reproduced with great fidelity by the balance between physico-chemical forces such as capillary interactions and steric repulsion. This is a clear example where a precise structure is acheived without bottom-up fabrication. The widespread applications, and the typical low cost of dispersion polymerization and other similar bulk colloidal synthesis techniques, are in that sense themselves a testament to the promises of self-assembly.

### 2.1.2 Patchy particle synthesis and characterization

Dipatch and tetrapatch patchy particles were synthesized by our collaborator at NYU, following a recently published protocol with minor adjustments, described in ref. [38]. This synthesis, called colloidal fusion, combines polystyrene (PS) and 3-(trimethoxysilyl)propyl methacrylate (TPM) spheres to create composite patchy particles with PS as bulk material and fluorescently labeled surface patches consisting of TPM, see Fig. 2.1. A macroscopic model that gives a visual explanation of the synthesis is shown Fig. 2.1(a). A particular strength of this method is its tunability: By changing only a single parameter, the size ratio $\alpha$ between the PS spheres and TPM sphere before fusion, patchy particles with different number of patches and different patch-sizes are achieved.

Exploiting this tunability, they made tetrapatch particles with smaller and bigger patch sizes referred to as TP-A and TP-B, and dipatch particles, DP-A and

DP-B, with bigger and smaller patch sizes. In accordance with the protocol, the synthesis was done following four main steps. (i) First, they synthesized monodisperse, negatively charged, solid spheres of PS with a diameter of approximately 2.2 $\mu$m. The spheres are prepared by dispersion polymerization with Potassium persulfate (KPS) as radical initiator and Polyvinylpyrrolidone (PVP), following the procedure in ref. [75]. After synthesis they were measured to be negatively charged in water with a zeta potential $V_{zeta} = -55(5)$ mV at 12.5mM NaCl. By using these spheres they deviate slightly from the published protocol which uses purely sterically PVP stabilized PS, and positively charged PS spheres. They deviated because the sterically stabilized PS was less charged ($V_{zeta} = -7(3)$ mV, at 12.5mM NaCl), and therefore less convenient for critical Casimir assembly which requires a hydrophilic PS matrix. Furthermore, the positively charged PS particles turned out to be unstable in the binary mixture. In addition, they synthesized four batches of monodisperse TPM oil droplets with sizes of 1.1, 1, 0.65 and 0.6 $\mu$m that were used for TP-A, TP-B, DP-A and DP-B respectively. The TPM oil was fluorescently dyed with rhodamine (ii) Next, liquid colloidal clusters were created by mixing the solid sphere and oil droplets. In the case of the tetrapatch particles four spheres assembled around a single liquid core. Because of the chosen size ratio between PS spheres and TPM droplets of $\alpha \approx 2$, this resulted in close-packed tetrahedrons with a liquid TPM core. In the case of the dipatch particles ($\alpha \approx 3$), that three solid spheres assemble around a liquid core (iii) Next, 5%wt. dodecyltrimethylammonium bromide (DTAB) is added to the cluster suspension to reach a final conc. of 0.8%wt, followed by the addition of a PS plasticizer (tetrahydrofluran) which caused the $PS$ spheres to deform and effectively fuse, while extruding the liquid TPM core through the interstices of the cluster. The addition of DTAB is necessary because it changes the interfacial tension of PS/TPM making the extrusion more favorable.

After synthesis, the morphology of the patchy particles was carefully characterized. The tetrapatch particles have an average diameter of $d = 3.7(2)$ $\mu$m, and $d = 3.7(1)$ $\mu$m for TP-A and TP-B respectively, where the uncertainty is the polydispersity. The dipatch particles have a diameter $d = 3.2(1)$ $\mu$m, and 3.1(1) $\mu$m for DP-A and DP-B respectively. These sizes were determined in the same solution in which later experiments were performed to take possible swelling effects into account. To measure their sizes, we assembled the particles patch to patch and measured the center-to-center distance between touching particles using optical microscopy. As a consistency check we note that the ratio of dipatch to tetrapatch size is 1.15($\pm$0.05). This is close to the expected ratio $(4/3)^{1/3} \approx 1.1$, which is derived from the fact that dipatch particles are made from three PS spheres and tetrapatch particles from four PS spheres.

In addition, we determined the average patch size of each particle type using a setup that combines optical and atomic force microscopy (AFM). Samples were dried on glass slides such that monolayers form at the drying front. After locating a patch in the right orientation a surface scan was performed, which revealed spherical patches, see Fig. 2.2. The edge of the patch is clearly recognized by a narrow trench and a change in curvature marking the transition form PS bulk to TPM

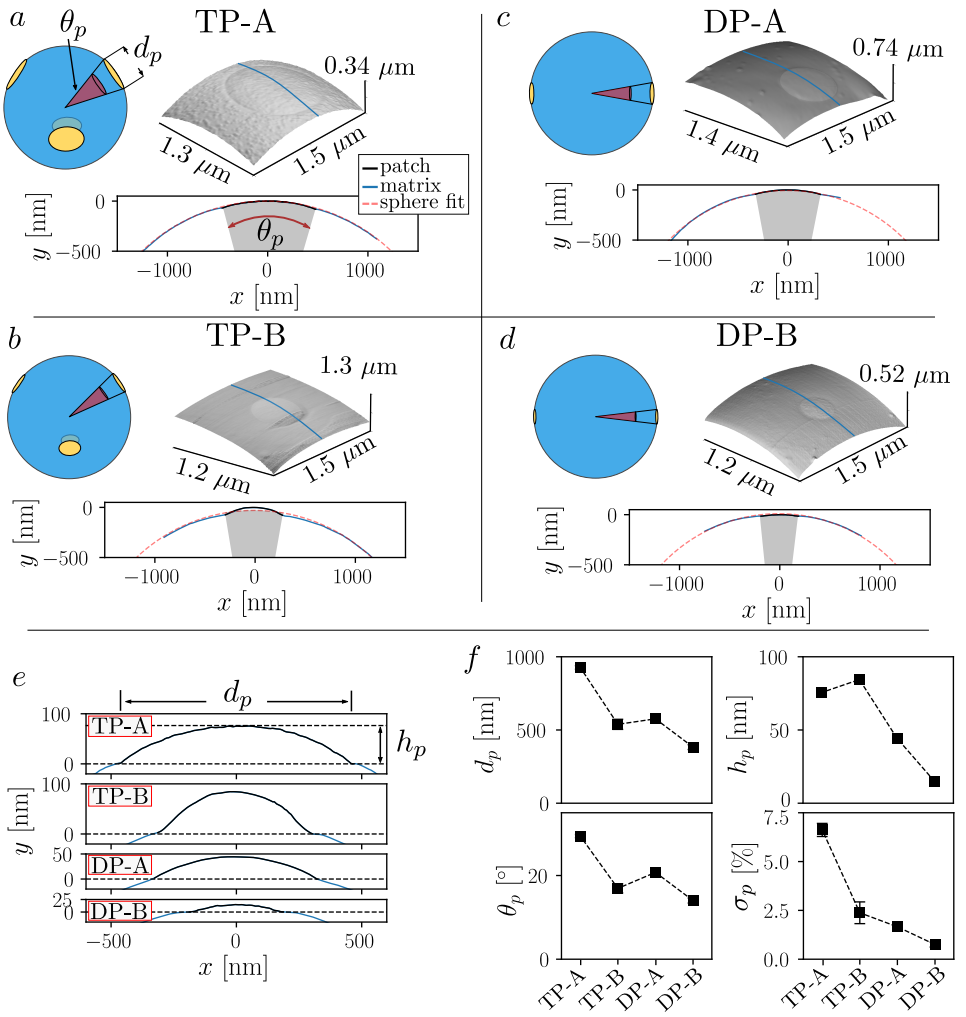


Figure 2.2: AFM measurements of patch sizes of the different patchy particles used (a) TP-A: schematic indicating definition of projected patch diameter $d_p$ and patch arc angle $\theta_p$, surface height measured using AFM (zoom on patch) and height profile along the blue line indicated in the surface plot. (b,c,d) TP-B, DP-A and DP-B (e) Height profile zoomed in on patch, aspect ratio was set to 2. (f) Mean projected patch diameter $d_p$, patch arc angle $\theta_p$, patch height $h_p$, and patch surface fraction $\sigma_p$ averaged over 2,2,4 and 7 AFM measurements of the respective particles

patch material. This trench is caused by the wetting difference between PS and TPM, and reveals the nonzero contact angle between PS and TPM at the material transition point. We determined the size of the patch by measuring the projected patch diameter $d_p$ as defined in Fig. 2.2(a,e). This was done by drawing linear profiles

| Particle name | $d$ [$\mu$m] | $d_p$ [$\mu$m] | $\theta_p$ [°] | $h_p$ [nm] | $R_p$ [$\mu$m] | $\sigma_p$[%] |
|---|---|---|---|---|---|---|
| TP-A | 3.7(2) | 0.93(5) | 30(2) | 75(5) | 1.5(2) | 6.6(5) |
| TP-B | 3.7(1) | 0.54(5) | 17(2) | 84(5) | 0.5(1) | 2.4(5) |
| DP-A | 3.2(1) | 0.58(5) | 21(2) | 45(5) | 1.0(2) | 1.6(2) |
| DP-B | 3.1(1) | 0.38(5) | 14(2) | 15(5) | 1.2(2) | 0.7(2) |

Table 2.1: Patchy particle patch morphology parameters measured using AFM, from left to right: Particle diameter $d$, projected patch diameter $d_p$, patch arc-angle $\theta_p$, patch height $h_p$, patch radius of curvature $R_p$, total particle surface fraction covered by patches $\sigma_p$

crossing the center of the patch and measuring the distance between the patch-bulk transition points. These linear profiles in addition showed a good fit with a sphere with diameter $d = 3.5 \pm 0.1$ $\mu$m for the tetrapatch particles and $d = 3.3 \pm 0.1$ $\mu$m in the case of dipatch particles, Fig. 2.2(red dotted lines). This value is in agreement with the previously determined particle radii validating the AFM measurements.

We quantified the patch size in terms of the patch arc angle $\theta_p$, which is a particle size independent measurement of the patch size, see schematic Fig. 2.2(a,f). The patch arc angle was determined from the projected patch diameter $d_p$ and particle diameter $d$ using the relation $\theta_p = 2\sin^{-1}(d_p/d)$, see table 2.1(third column). Here, the uncertainty is the standard deviation of the measured patches and gives the patch size polydispersity. We note that the polydispersity is a rough estimation limited by the low measurement statistics.

Apart from patch sizes, the AFM measurements also provide information on the height $h_p$ of patches. Interestingly, not all patches stick out equally, as shown by the profiles that are zoomed-in on the patch Fig. 2.2(e,f). Particularly TP-B sticks out significantly from the PS bulk sphere, more than would be expected from simply following the curvature of the PS matrix. This results in a different curvature at the patch than for the rest of the particle. Modelling the patches as spherical caps, we can extract the radius of curvature $R$ of each patch via $R = \left((d_p/2)^2 + h_p^2\right)/2h_p$, see table 2.1. Next to patch size, the patch curvature will influence the inter-patch interaction, as a higher curvature results in less contact when patches are close together and is therefore expected to decrease the interaction strength. In addition we determined the area of each patch using the relation for spherical caps $A = \pi\left((d_p/2)^2 + h_p^2\right)$. The total fraction of the particle surface that is covered with patch material $\sigma_p$ is than $\sigma_p = 4A/(\pi d^2)$ for tetrapatch particles and $\sigma_p = 2A/(\pi d^2)$ for dipatch particles, see table 2.1. This likewise is an important quantity that will determine the interaction strength.

As a final note, we mention that it is possible to create smaller patchy particles using the same method. By using smaller PS and TPM precursor spheres, but keeping their size ratio's similar as discussed above, our collaborators were able to make particles with diameters of approximately 1.5 $\mu$m. In this thesis, we initially focus on the larger particles, whose big size allows for easier characterization. However,

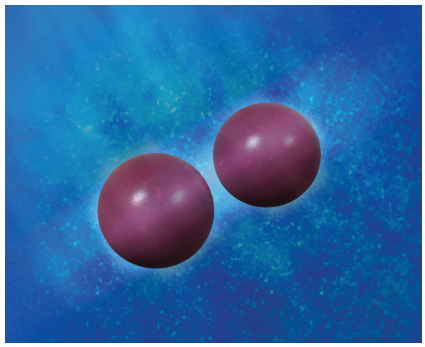

Figure 2.3: Artist impression of two colloids interaction through the critical Casimir interaction in a close to critical medium.

for assembly experiments it is also interesting to employ the smaller particles, which we will demonstrate in the final section of chapter 5. Their faster diffusion dynamics speed up the kinetics of structure formation and made the particles more easily escape trapped states. In addition, their increased gravitational height enables us to study 3d structure formation.

## 2.2 Self-assembly using the Critical Casimir interaction as a driving force

The critical Casimir interaction arises between surfaces (such as two colloids) that are immersed in a medium that is close to a critical phase transition. The behavior of such a critical medium is dominated by critical fluctuations, correlated regions that fluctuate due to thermal energy, which grow in size according to power laws as one approaches the critical point [76, 77]. The size of these correlated regions is quantified by the correlation length $\xi$. When two surfaces, immersed in a critical medium, are close to each other, they confine the critical fluctuations in the gap between them, more specific: The surface impose boundary conditions that reduce the fluctuation spectrum between these surfaces compared to the region surrounding them. These boundary conditions cause a change in the system's free energy, which result in effective interactions. When colloids are immersed in the critical solvent, their surfaces act as boundaries confining fluctuations between them, thus resulting in an effective force between the particles. An artistic impression of a medium with critical fluctuations and two immersed colloids is shown in Fig. 2.3.

Critical Casimir interactions are thus part of the very general class of fluctuation-induced interactions [78]. To this category belong also the ubiquitous van der Waals interaction [21] and the quantum-mechanical Casimir interaction [79], in analogy of which the critical Casimir interaction got its name [80]. Apart from the conceptual

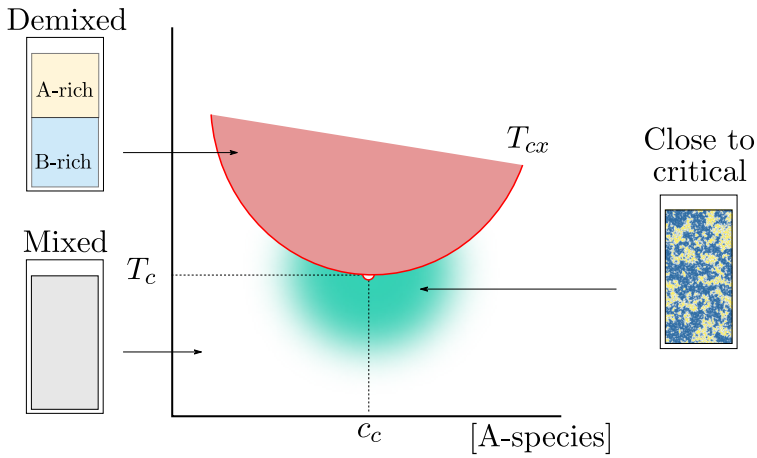


Figure 2.4: Schematic of the phase diagram of a binary liquid mixture of molecular species $A$ and $B$ that phase separates above temperatures $T_{cx}$ (red region) into an $A$-rich and a $B$-rich component. At the critical concentration $c_c$ and critical temeprature $T_c$ the phase transition is critical. In the region surrounding the critical point (turquoise shading) emerge critical fluctuations.

analogy with these other fluctuation-induced interactions, details concerning the strength and form of the critical Casimir interaction depend on the particularities of confining critical fluctuations. The rich physics that arises in such critical systems has yielded a broad literature around the subject [44, 81, 82]. One specific particularity of the critical Casimir interaction is the fact that surfaces often have an adsorption preference for one of the two phases involved in the phase transition. This creates an adsorption layer that extends on the order of the correlation length, shown in the artistic impression by the light blue highlight around the particles. If surfaces have the same adsorption preference, there is an inclination towards overlapping these adsorption layers, resulting in an attractive force that is an important contribution to the effective interaction. On the other hand, when surfaces have opposite adsorption preferences the adsorption layers tend to repel. These effects appear, on first sight, to be of energetic nature, however it also has an entropic contribution as the adsorption layer is never static but fluctuating around a mean. This has led to some controversy over the analogy with fluctuation-induced forces and the rightfulness of the name "Casimir", which are normally thought of as purely entropic effects [82]. However, given that such adsorption effects are taken into account in the modern critical Casimir literature, this thesis will follow the convention of using the name "Casimir".

### 2.2.1 Critical Casimir forces in binary mixtures

From an experimental point of view not every critical system is equally practical as a colloidal medium. The most well known critical phase transitions and historically the first to be discovered concerned the liquid-gas critical point, such as that of water or carbon dioxide [83]. However, the fact that these transitions happen at elevated pressures makes these systems not practical as colloidal mediums. Fortuitously, the universality of critical phenomena causes similar effects to be present in a wealth of other system. In particular, binary liquid mixtures, consisting of molecular species $A$ and $B$, show a phase transition at the coexistent temperature $T_{cx}$ from a mixed phase to a demixed $A$-rich and $B$-rich phase, see Fig. 2.4. At a specific critical concentration $c_c$ of $A$ molecules and temperature $T_c$, this coexistence ends at the critical point. The associated critical fluctuations are in this case correlated regions of elevated concentrations of $A$ or $B$ species with respect to the average concentration. Binary mixtures are interesting as suspending mediums because instead of the pressure, the concentration ratio $c$ of the two liquids is the control parameter for criticality, while operating at convenient (atmospheric) pressures. Especially convenient are binary mixtures that demix upon heating, at temperatures slightly above room temperature. Commonly used are the mixtures 3-methylpyridine and heavy water, exhibiting a critical temperature of $T_c \approx 38°\mathrm{C}$, and 2,6-lutidine and water, with $T_c \approx 33°\mathrm{C}$. These are the systems that will be used in this thesis also, though a range of other binary mixtures are also possible candidates and have been shown to exhibit similar effects. [84–87]

Although colloids in a near-critical binary mixtures allow convenient tuning of interactions, their description is complex. This is at least because of three distinct reasons: (i) First of all, the confinement of critical fluctuations is intimately linked to finite-size effects in critical system [88]. Though these have been extensively studied, they remain technical subjects, which require subtle theoretical analysis. Especially difficult are quantitative predictions in experimentally realistic situations such as curved surfaces, off-critical concentrations, and surfaces that have partial adsorption preferences. Here, analytical solutions are not available and to calculate effective interaction potentials, numerical minimizations and in some cases Monte Carlo simulations have to be used. Chapter 3 contains a detailed comparison of exactly such a calculation with experimental results. (ii) A second source of complexity are other effects that occur close to a demixing phase transition. At concentrations further away from the critical concentration, wetting layers dominant in one of the two binary species can form around the colloid. These have a well-defined surface tension and can bridge with wetting layers around other colloids causing strong interaction [89]. Such strong wetting induced interactions are, however, avoided in this thesis. (iii) Lastly, and importantly, in a conventional colloidal system, charge and ions are paramount to determine its behavior and stability. Most often, charge stabilized colloids have been used in combination with critical Casimir interaction. However predicting what would happen when including free ions and charged colloids in the above picture is not straightforward. Assumptions of DLVO theory break

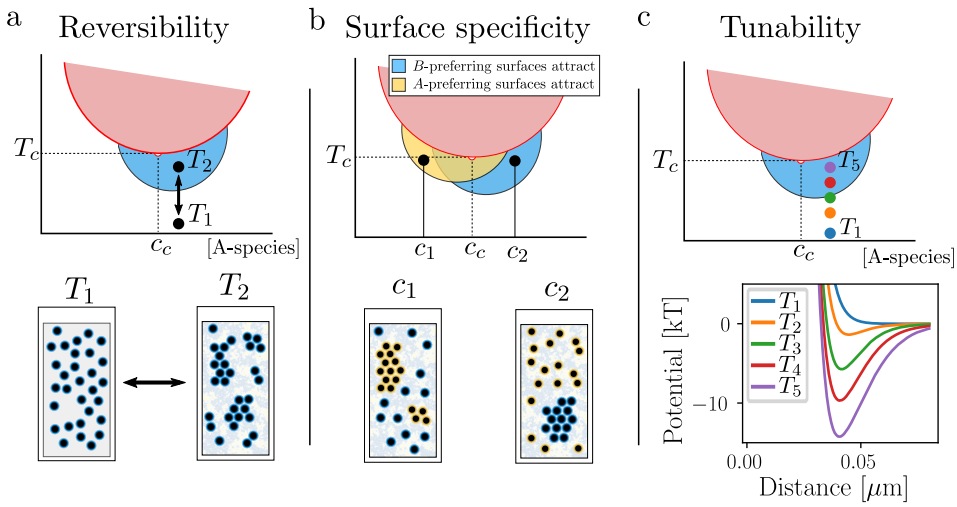


Figure 2.5: Three useful traits of critical Casimir interactions for controlled self-assembly by controling temperature and binary mixture composition. (a) Reversible aggregation of colloidal particles that have an adsorption preference for $B$ molecules (b) Due to the surface specificity of the critical Casimir interaction, $A$ and $B$ preferring colloidal particles attract predominantly on opposite concentrations of $c_c$. (c) The interaction strength is continuously tunable with temperature

down, which assume a homogeneous liquid with equal solvability and permittivity throughout. However the critical compositional fluctuations and the adsorption layer around a colloid break these assumptions dramatically. In addition, ions can alter the interactions between the species A and B of the liquid mixture, and influence the thermodynamics of the mixture itself. It is therefore not too surprising that strong effects upon addition of ions, especially ones that have strong solvation preference for one of two binary species, have been reported. These can switch the adsorption preference of a particle from lutidine to water [90], and can even switch the sign of the interaction from attractive to repulsive [91].

### 2.2.2 A reversible, surface-specific and tunable interaction

The critical Casimir interaction can act as a sophisticated tool: a controlled interaction that allows to study and guide self-assembly. There are three main reasons for this: Reversibility, surface-specificity and tunability, graphically summarized in Fig. 2.5.

*Reversibility.* The interaction strength is set by the distance to the critical point, which can be conveniently changed by increasing and lowering the temperature. If a sample, with colloidal particles that are stable at room temperature, is brought

close to the critical point of the solvent, the induced critical Casimir interaction can overcome the stabilizing forces and cause the particles to aggregate, see Fig 2.5(a). Here, the blue region indicates the temperatures and concentration range where the sample will aggregate. The aggregation can be reversed by decreasing the temperature below the blue region, where the critical Casimir interaction becomes so weak that the particle clusters fall apart. Such reversible assembly is useful for creating a switchable material. In addition, it can act as an analytical tool: Assembly experiments can be repeated at will, allowing to study dynamics and reproducibility of structure formation.

*Surface specificity.* The blue aggregation curve is drawn asymmetrically around the critical concentration $c_c$ in Fig 2.5(a). This aggregation curve refers to a colloidal particle that has an adsorption preference for the $B$ molecular species. The general rule is that particles attract stronger on that side of $c_c$ that is poor in concentration of the molecular species for which the particle has an adsorption preference. In the phase diagram of Fig 2.5 the horizontal axes measures concentration of $A$-species, so the $B$ preferring particle attracts stronger for $c > c_c$. This response can be qualitatively understood in terms of the adsorption layer. If a particle has an adsorption layer of species $B$ this is further from equilibrium for compositions where there are less $B$ molecules, so for $c > c_c$. The increased distance from equilibrium causes a stronger tendency to minimize the size of the adsorption layer, this increases the tendency to overlap adsorption layers, effectively increasing the attraction. The opposite behavior is seen for particles that prefer species $A$, which will attract stronger for concentrations $c < c_c$. In this way the critical Casimir attraction strength becomes surface specific. This has the interesting consequence that a mixture of $A$ and $B$-preferring particle will show aggregation of only $A$-preferring particles for concentrations far enough below $c_c$, and oppositely for concentrations far enough above $c_c$, see Fig 2.5(b). The surface specificity greatly extends possible self-assembly scenarios. For instance, particles that have patches with an opposite adsorption preference as the rest of the particle, are expected to form directional bonds, if the right composition of binary mixture is used.

*Tunability.* More than just being reversible, the critical Casimir interaction is tunable in a continuous manner using temperature. This is illustrated by the effective interaction potential between two particles, shown in Fig 2.5(c). This set of potential curves has been calculated using realistic experimental parameters, as described in chapter 3. It is the sum of a stabilizing electrostatic repulsion and a critical Casimir interaction continuously increasing with temperature. The sum of these two interactions create a well, that will cause particle bonding if deep enough. Interestingly, already before permanent bonding, significant attraction can be present, leading to the observation of liquid as well as crystalline phases [92, 93]. Furthermore, even after bonding occurs, the depth of the well can be increased by increasing temperature further. This affects the mechanical behavior of assembled structures as demonstrated in chapter 6.

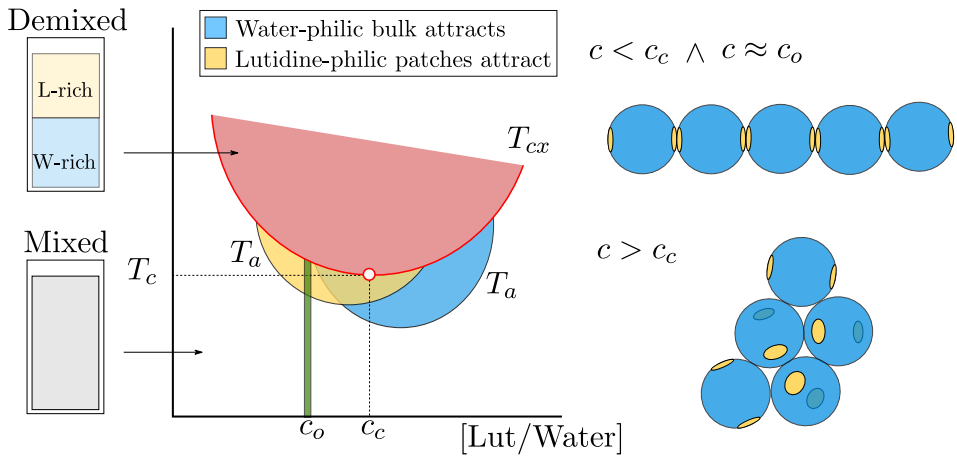


Figure 2.6: Schematic of patchy critical Casimir interaction. The lutidine-water phase diagram shows an inverted demixing phase transition above temperatures $T_{cx}$ (red region), depicted are aggregation lines $T_a$, for lutidine-philic (yellow) and water-philic (blue) surfaces. For patchy particles with lutidine-philic patches and concentrations $c_L < c_c$ patch-to-patch bonding is expected, whereas for $c_L > c_c$ bulk bonding is expected, as demonstrated for the case of dipatch particles.

### 2.2.3 Optimizing binary solvent for patchy interactions

To induce critical Casimir interactions between patches we used a binary mixtures of 2,6-Lutidine ($\geq 99\%$, Sigma-Aldrich) and distilled water. According to literature $c_c = 0.30(\pm 0.005)\%vol$ lutidine and the critical temperature $T_c = 33.9°(\pm 0.3°)$ C, where the error is the variation between literature sources [94]. At lutidine concentrations $c_L$ above critical, $c_L > c_c$, water-philic surfaces that prefer water adsorption over lutidine, show a stronger attraction, see Fig. 2.6. In contrast, at concentration $c_L < c_c$ lutidine-philic surfaces that prefer lutidine adsorption over water, show a stronger attraction. In addition, aggregation regions can also differ in absolute size, in the schematic this is represented by a bigger overall blue than yellow aggregation region. Taking this into account, patchy particles with lutidine-philic patches and a water-philic bulk are expected to show selective patch-to-patch bonding for $c_L < c_c$ above an aggregation temperature $T_a$, see Fig.2.6. Furthermore, there is an optimal lutidine concentration, $c_o$, at which the temperature window between aggregation and phase separation, $\Delta T = T_{cx} - T_a$ of pure patch-to-patch attraction is largest, Fig.2.6 (green bar). We use the terminology water-philic and lutidine-philic instead of hydrophilic and hydrophobic because it is not necessary that a surface is hydrophobic for left side attraction, the only condition is that it prefers lutidine over water. Likewise, it is not necessary that a surface is hydrophilic for right side

attraction, the only condition is that it prefers water over lutidine.

Despite these conceptual ideas, the patchy particles, in their pristine state after synthesis, did not show a strong enough adsorption contrast between patch and bulk to induce patch-to-patch bonding. In order to increase adsorption contrast, two strategies were explored: First we tried silane treatments to increase the hydrophobicity of the TPM patches. This however did not give satisfactory results and furthermore added an extra tedious synthesis step. One problem could be that the silanes (trimethylmethoxysilane and dimethyldimethoxysilane) and salinization method explored, actually did not couple the silane to the patch. This is suggested by the TPM particles having the same zeta potential ($\sim$ 45mV in 15mM NaCl) as untreated particles. Therefore, we instead explored the possibility of adding salts as tertiary elements to the binary mixture. Though only partially understood, especially hydrophilic ions have been shown to effectively shift the adsorption preference of particles in binary mixtures, thereby strongly changing their critical Casimir interaction [90, 91, 95]. Such adsorption change due to salt will depend sensitively on the surface properties of a particle and might thus be different for the TPM patch and PS bulk. As salts we used potassium chloride KCl, magnesium sulfate $MgSO_4$ and calcium chloride $CaCl_2$.

To more efficiently scan the large parameter space of salt and lutidine concentration in a controlled fashion, we first investigated the assembly behavior of the single particles composing the patchy particle. As matrix material we used the PS spheres that are the precursors of the colloidal fusion synthesis. In order to obtain particles representing the patch material, we polymerized TPM droplets under the same conditions as was used to polymerize the patches, using AIBN as radical initiator and in the presence of F108. This resulted in solid particles of diameter $d \approx 1$ $\mu$m. These particles have similar surface properties as the final composite patch particle allowing us to test the aggregation behavior and critical Casimir interaction of the patch and bulk material separately. In order to find optimal parameters we prepared binary mixtures of lutidine and water at various lutidine concentration ranging form $c_L = 23\%$vol to $c_L = 32\%$vol, to the left and right of the critical concentration. Next we added various concentrations of KCl, $MgSO_4$ or $CaCl_2$. We dispersed the isotropic TPM particles in the binary mixtures with salt and washed multiple times using centrifugation.

In order to check for aggregation in the entire parameter space, we performed macroscopic flocculation experiments. This allowed us to test multiple experimental conditions in parallel. Sealed capillaries were immersed in a temperature-controlled water bath. Then, the temperature was slowly increased in a continuous fashion from 32C° to 35C° over 15 hours to ensure thermodynamic equilibrium while recording images at a frame rate of 1 frame per minute. We determined the aggregation temperature by noting the time and corresponding temperature at which visible flocculation occurred, identified by a rapid coarsening of the sample and a strongly increased sedimentation rate. We found that $MgSO_4$ and $CaCl_2$ both shifted TPM's adsorption preference to lutidine-philic with $MgSO_4$ showing a stronger effect, whereas KCl left TPM water-philic. Therefore we continued to work with $MgSO_4$ as it provided the

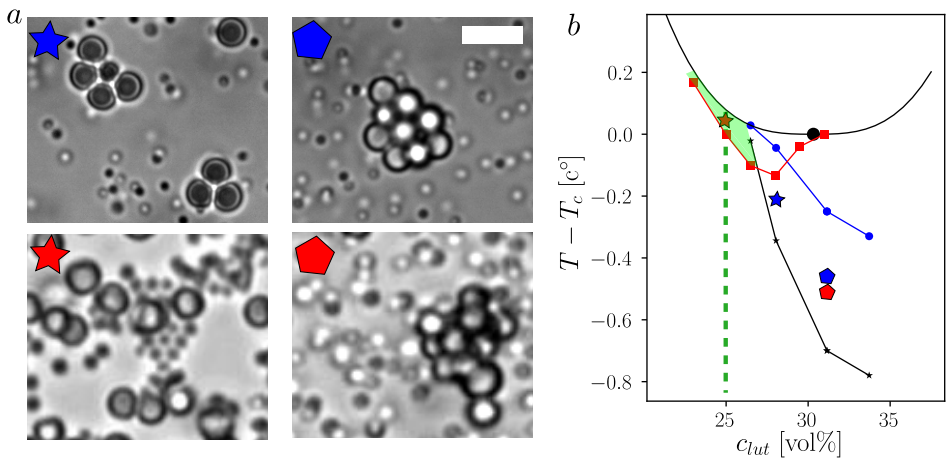


Figure 2.7: Adding magnesium sulfate creates a sweet spot of pure patch material attraction (a) Bright field images showing aggregation contrast of singlet particles consisting of bulk (PS, big particles) and patch material (TPM, small particle). Clockwise, starting top left, conditions are: $c_L = 28\%\text{vol}$ [$MgSO_4$] $= 0$, $c_L = 32\%\text{vol}$ [$MgSO_4$] $= 0$, $c_L = 25\%\text{vol}$ [$MgSO_4$] $= 0.5\text{mM}$, $c_L = 32\%\text{vol}$ [$MgSO_4$] $= 0.5\text{mM}$. Scalebar is $3\mu$m (b) Aggregation diagram showing the shifted aggregation lines $T^*_{cx} - \Delta T_a$ of TPM without salt (blue circles), with [$MgSO_4$] $= 0.5\text{mM}$ (red squares), PS without salt (black stars), black continuous line shows theoretical coexistence temperature of the binary mixture close to critical $T^*_{cx} = T_c(1 + (|c_c - c_L|/B)^{1/\beta})$. Colored stars and pentagons indicate corresponding measurement condition of (a). Green dotted line indicates the optimal lutidine volume fraction for patchy assembly $c_0 = 0.25$.

best contrast.

To check if $MgSO_4$ did not also influence the behavior of the PS surface, mixtures of TPM and PS particles were likewise dispersed in various binary mixtures for microscopic characterization. This time, microscopic experiments were done as the bigger size of the PS prevented macroscopic characterization due to too rapid sedimentation. Furthermore by mixing in TPM particles we could also investigate the PS-TPM interaction. Samples were imaged while the temperature was slowly increased using a temperature-controlled stage connected to a water bath, as described later in this chapter. An oil-immersion objective with 63x magnification was used for imaging. While temperature was increased we used video recordings to identify the aggregation temperature as the temperature at which clear cluster formation occurred, as shown in Fig. 2.7.

Without added salt the PS particles providing the particle matrix exhibit stronger interaction than TPM particles that are of the material that will constitute the particle patch. This happens both for solvent compositions on the right and left side of the critical composition, see Fig. 2.7. This can be seen in the microscope snapshots which show aggregated clusters of PS particles, while the TPM particles still diffuse freely Fig. 2.7(a). Indeed, the aggregation temperature curve of the PS

particles is lower than the TPM aggregation curve for all concentrations of lutidine, Fig. 2.7(b). These aggregation lines are obtained from the measured aggregation temperature $T_a$ at which cluster formation starts, and the measured coexistence temperature $T_{cx}$, identified by bubble formation. The difference $\Delta T_a = T_{cx} - T_c$ is insensitive to calibration uncertainties. We then use the fact that for close to critical lutidine concentrations $T^*_{cx}$ follows the universal equation of state $T^*_{cx} = T_c(1 + (|c_c - c_L|/B)^{1/\beta})$, with $c_c = 0.3$, $T_c = 304$K, $B = 0.6$ and $\beta = 0.3265$ [96]. The aggregation lines are then drawn as $T^*_{cx} - \Delta T_a$. The aggregation lines show that without salt, PS particles (black line) and TPM particles (blue line) aggregate stronger for lutidine concentrations above critical, meaning that they both show the same water-philic affinity and are not suitable to obtain a patch-to-patch attraction. Adding monovalent salt KCl did not change this behavior: The PS particles still showed a stronger attraction and it didn't effect TPM's affinity.

However, by adding only a small amount, 0.5mM, of Magnesium Sulfate the aggregation behavior of TPM particles changes completely: Aggregation disappears for concentrations above critical and instead a stronger critical Casimir attraction is observed to the left of $c_c$, Fig. 2.7(b, red line). This indicates that the adsorption preference of TPM switches to lutidine-philic when adding $MgSO_4$. The aggregation temperature of PS particles is however little affected and remains water-philic as can be seen from the snapshots that show cluster formation of PS still happens at the right side of $c_c$, Fig. 2.7(a, bottom right). While we did not measure aggregation curves as extensively PS particles, we could pinpoint a sweet spot where only TPM particles are expected to attract Fig. 2.7(b, green region). Furthermore, we extract an optimal lutidine concentration $c_o = 0.25$ that shows the largest range of TPM-TPM attraction with PS being not attractive. Indeed, when checking the microscopy images we find that for this concentration, only TPM particles attract, which crystalize due to a low polydispersity while the PS particles freely diffuse Fig. 2.7(a, bottom left).

The change of the TPM aggregation temperature can be understood by a shift in adsorption preference of TPM due to $MgSO_4$. This change of the adsorption preference of TPM is further confirmed by heating the system above the phase separation temperature, see Fig. 2.8. Without salt, TPM particles prefer to go to the bottom, water-rich phase after phase separation, confirming they are water-philic. In stark contrast, with $MgSO_4$ salt, the TPM particles instead prefer the lutidine-rich phase (top) after phase separation, confirming the change to a lutidine-philic affinity. This is confirmed by the iridescent colors due to Bragg scattering at the crystallized TPM particles.

Interestingly, $CaCl_2$ showed a similar change of the adsorption affinity, see appendix. The mechanism behind this affinity shift is not clear to us. A potential explanation could follow similar lines of argument as the previously observed switching of attractive to repulsive critical Casimir forces between substrate and particle upon addition of the hydrophilic salt KBr [91, 95]. However, the fact that we focus on off-critical compositions might add a complication factor. It might also be compared to early experiments which observed an affinity change of silica particles with

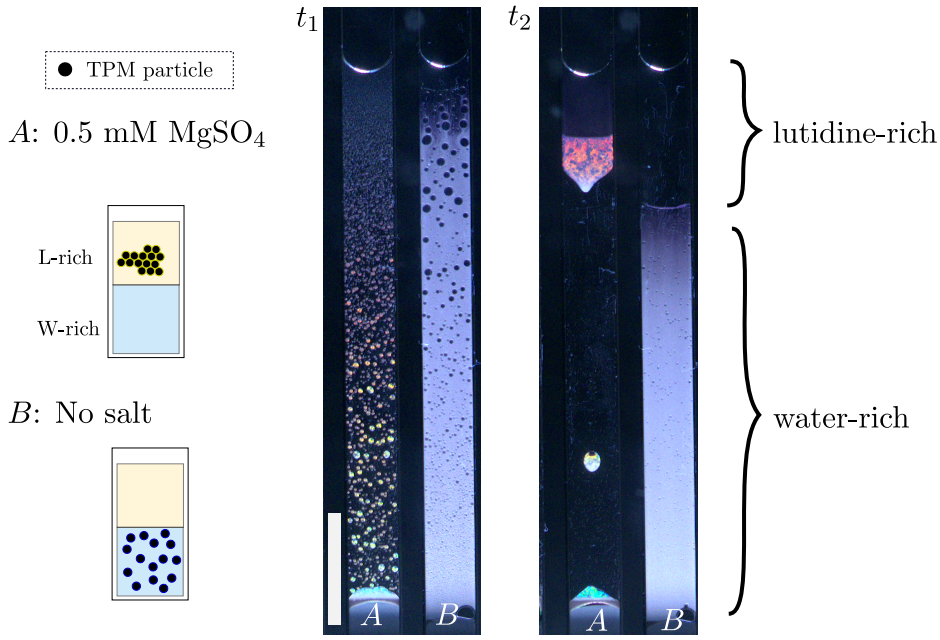


Figure 2.8: Macroscopic observation of water-philic to lutidine-philic phase separation for TPM singlet particles made from patch material. Time $t_1$ is right after phase separation where bubbles are lutidine rich, time $t_2$ is later when the bubbles have coalesced in a top lutidine-rich layer. Sample $A$ contains 0.5mM $MgSO_4$ and sample $B$ contains no salt. Temperature was $T = 38C^\circ$ and lutidine concentration $c_L = 25\%$vol. Scalebar is 1cm. (Video: *https://youtu.be/gllpr4V7rSk*)

the addition of $Mg(NO_3)_2$ [90]. Intriguingly, in that case salt caused particles to switch from lutidine-philic without salt to water-philic with, which is the opposite affinity shift as we observe.

In spite of this lack of complete understanding, we thus establish a reliable protocol that yields patchy critical Casimir interactions using the affinity contrast between patch and bulk upon addition of $MgSO_4$. In conclusion the optimal binary solvent, that showed the largest temperature window for patchy interactions was obtained using $MgSO_4$ at a lutidine volume fraction $c_L = 0.25$. We note that, for salt concentrations $\gtrsim$ 0.5mM $MgSO_4$, the PS particle bulk was observed to aggregate irreversibly in some occasions at room temperature. In order to stay sufficiently away from this point we will use in the remainder of this thesis a concentration of 0.375mM $MgSO_4$.

## 2.3 Experimental techniques

The experimental imaging and characterization techniques used in this thesis are, in approximate order of appearance: Dynamic light scattering, confocal microscopy, optical tweezers, bright-field microscopy, epifluorescent microscopy and atomic force microscopy. Apart from atomic force microscopy, which was used purely to characterize particle morphology after synthesis, all these techniques required temperature controlled setups in order to control/tune the critical Casimir interaction. In this section I briefly describe the two most prevalent techniques used: Optical microscopy and optical tweezers. In addition, I elaborate on how temperature control was achieved in the different setups used. Finally, subpixel accurate locating is discussed.

### 2.3.1 Optical Microscopy

Traditionally, scattering techniques with visible, neutron and x-ray sources, have been the prime tool to investigate colloidal solutions [97]. Their advantage is provided by an efficient access to global, sample averaged properties. These techniques have, for instance, allowed the structural characterization of the diverse phases of isotropic monodisperse colloidal particles, from crystals [30] to fractal gels [32] and glasses [33]. A growing interest in local behavior pushed the application of optical microscopy techniques in colloid science. Complementary to scattering techniques, real-space microscope images can resolve structure and dynamics at the individual particle level [98]. Especially confocal microscopy, which is able to record three dimensional images deep in the sample bulk, has gained popularity [99]. Quantitative analysis of such data was made possible by the increased computational and storage capabilities of computer hardware, and the creation of automatic particle localization algorithms [100, 101]. Microscopy techniques truly exploited the uses of colloids as a model atomic system, allowing a direct visualization of fundamental processes that are difficult to study on the atomic scale, such as crystal nucleation [34], defect dynamics [35] and structural rearrangements in glasses [36].

The current interest in taking colloids from model atoms to designated building blocks that self-assemble in designer architectures with diverse functionality [28], follows largely from these microscopy techniques. This has been the technique of choice, especially since most work in this area has so far focused on small assemblies and local mechanisms. Important achievements have been revealed using 3d confocal microscopy such as shape-changing filaments and chiral architectures [15, 42]. In addition, conventional bright-field microscopy is a useful tool for systems that have two-dimensional structure, and has for instance been used to study active flocking and activated chains [55, 102].

Optical microscopy of colloids is complicated by the fact that colloidal particles are in size often close to the optical resolution limit. Resolution is defined as the minimum distance two objects have to be apart to be able to distinguish them. There are fundamental limits to resolution which are due to the wave nature of light. Even

ideal point sources transform to extended patterns, called point spread functions, when traveling through an optical system due to finite range of scattering angles captures by the lens. The overlapping of point spread functions sets the maximum resolution achievable with a given lens. An often used maximum resolution is given by the Abbe diffraction limit [103],

$$R = \frac{\lambda}{2NA}, \tag{2.1}$$

where $\lambda$ is the wavelength of light used and $NA$ the numerical aperture of the objective used for imaging. A system using white light with a wavelength maximum at 550 nm, and an oil-immersion objective with $NA = 1.4$, will have a maximum resolution of $R = 280$ nm. This is close to, but significantly smaller than the size of colloidal particles used in this thesis, which vary in diameter between $2 - 4$ $\mu$m.

It is important to note that the diffraction limit gives an idealized resolution for point sources. In practice, the actual resolution is further limited by the contrast between signal and background. Bright-field microscopy, which uses transmitted white light, can suffer from out-of-focus light, scattered from particles above or below the focal plane. This limits its use mainly to dilute samples or samples that consist of a single 2d layer of particles. Epifluorescent microscopy uses monochromatic light to excite fluorescent markers. A filter transmits only the fluoresced light, which is used to create the image. This increases contrast between particle and background. In addition, by using multiple fluorescent markers, it allows to distinguish different parts of a particle (such as patch and bulk). However, epifluorescent microscopy is still limited to dilute or 2d samples. Laser scanning confocal microscopy (here simply referred to as confocal microscopy) overcomes this limitation. Using a focused laser, points in the sample is illuminated one-by-one exciting fluorescently labeled particles. The fluorescent light from the sample travels back through the objective and is used to form an image. In addition, a pinhole is placed in the conjugate focal plane to reject out-of-focus light. By scanning the laser focus point by point using rotating mirrors an image is created. In this way the image is essentially build up as a series of point sources. The advantage is that only light from a narrow focal plane is recorded, and by shifting the focus height sequentially, an accurate 3d image can be constructed.

This thesis relies on optical microscopy. Confocal microscopy is used to measure the critical Casimir interaction potential in chapter 3. In that case, confocal microscopy was used to be able to image in the sample bulk and avoid wall effects. Later chapters on the other hand rely on bright-field microscopy as we studied structures that sedimented to the sample floor forming 2d layers.

### 2.3.2 Optical tweezers

Optical tweezers use a strongly focused beam of light to trap small objects, ranging from micron sized beads to atomic vapors [104]. The resulting nanometric confinement and control has revolutionized fields ranging from ultracold atomic physics

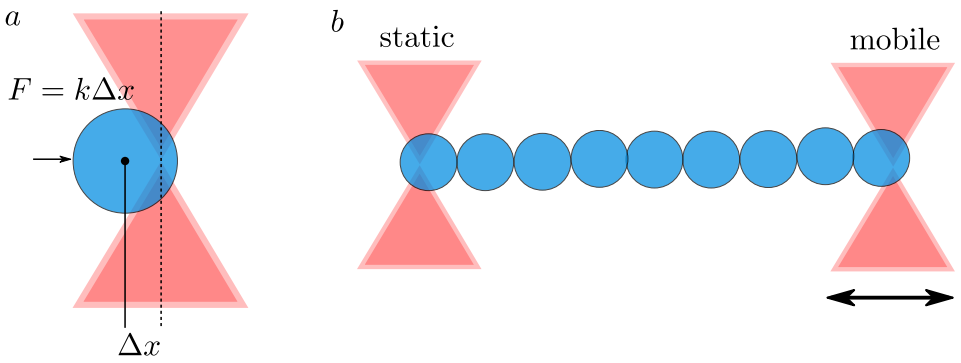


Figure 2.9: Optical tweezers can be used to probe the mechanics of colloidal structures (a) Sketch of a colloidal particle in a focused laser beam that acts as Hookean spring (b) Two tweezer setup that is used to exert tensile and compressive forces on a colloidal structure, in this case a colloidal chain.

[105] to biophysics [106]. A recent testament of their importance has been the 2018 Nobel prize in physics, which was awarded to Arthur Ashkin for his invention of optical tweezers [107, 108]. A microscopic particle is trapped by a single laser beam through a balance of radiation pressure that tends to push the particle upwards and gradient forces that push the particle to the laser focus [109]. For tightly enough focused beams, as can be achieved using high aperture immersion objectives, particles are stably trapped in three dimension, and assuming a harmonic potential, the tweezer acts as a Hookean spring, see Fig. 2.9(a).

In colloidal science, early applications of optical tweezers included controlled diffusion experiments and measurements of the interaction potential between two spheres [110]. This line of research is continued, recent results of particular interest to the work in this thesis are the measurement of the non-additivity of critical Casimir forces using optical tweezers [111], and the creation of a micro engine by active rotation of a trapped particle immersed in a binary mixture [112].

Beyond investigating properties of individual colloids, optical tweezers can also be used to study the mechanics of assembled colloidal structures. A single bead in an optical tweezer can act as a probe to perform micro rheology measurements [113, 114]. By using two optical tweezers, two-point tests can be performed [69, 115]. For instance, by grabbing a structure at opposite ends, compressive and tensile stresses can be exerted by changing the distance between the two tweezers, see Fig. 2.9(b). This mode of operation is similarly used to study the mechanical properties of biomolecules and filaments such as DNA and actin. A difference is that in those cases anchor particles need to be tethered to the materials of inquiry, which itself can typically not be trapped in a controlled fashion. This is often not necessary for colloidal structures, as the constituting colloids can act as natural anchor. By using more than two tweezers, more diverse mechanical tests can be performed, such as three point tests and shear experiments [116].

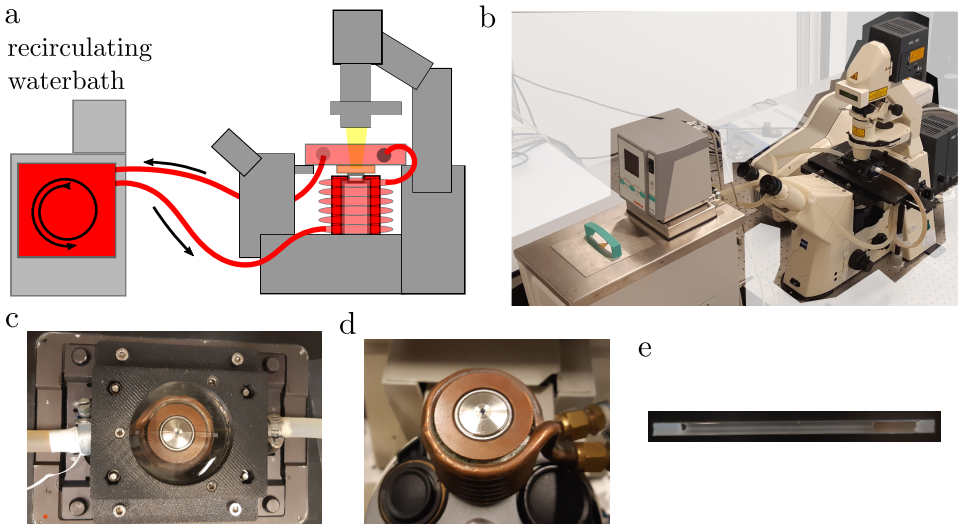


Figure 2.10: Inexpensive way to achieve precise (±0.02K) temperature control on a bright field and confocal microscopy setup with immersion objectives (a) Schematic of water circulator and microscope, elements through which temperature controlled water flows are indicated in red, sample is in orange (b) Photograph of setup (c) Zoom-in on glass flow cell and objective heater, in between which the capillary sample is visible (d) Objective inside objective heater (e) Capillary with colloidal sample.

Using optical tweezers as micromechanical probes, complements the global rheology provided by a rheometer with local information. Furthermore, it provides a way to study the mechanical behavior of self-assembled colloidal architectures designed with local microscopic mechanisms, that so far have mainly been studied on a structural level using microscopy.

### 2.3.3 Temperature control

> "It appears, therefore, that the expression, *animal life*, is nearly synonymous with the expression, *animal heat*. ... The grand necessity, then, for our bodies, is to keep warm, to keep the vital heat in us."
>
> — Henry David Thoreau, Walden

To take full advantage of the critical Casimir interaction, fine temperature control is essential. Furthermore, this temperature control needs to be integrated with the microscope and tweezer setups in order to study in-situ the effect of changing temperature and interaction. This was achieved by different types of setup partly fabricated in-house.

The first type uses a circulating temperature-controlled water bath (Julabo F25 ME) as shown in Fig. 2.10. Temperature can be manually set through the thermostat

interface or through a connected computer using serial communication. The water is continuously pumped through two elements, an objective heater and flow cell, that were designed and fabricated in the in-house workshop, see Fig. 2.10(c,d). The objective heater is made from a brass hollow block that fits tightly around the objective, which is wound by cupper tubes through which the hot water flows. The flow cell is made from glass in order to allow for transmitted light for bright-field microscopy. It is constructed by fusing a glass petri dish with a glass plate to create a hollow cell. Additionally, two glass hose barbs are fused at opposite ends of the flow cell. All connections are fused as gluing is prone to leakage due to the pressurized flow and temperature variations. A 3d-printed container tightly holds the glass flow cell and rests on the sample stage. Hoses are used to connect the objective heater and flow cell in series with the pump. For experiments we use glass capillaries (Vitrocom) Fig. 2.10(e). The samples are attached to the flow cell on top and are in contact through the immersion oil with the heated objective below. In this way the sample is heated from both sides and a temperature control with a precision of 0.02K was achieved. An additional advantage of using this circulating heating setup is that it also provides active cooling. This setup was used in chapters 4,5 and 6.

Two other similar setups were developed. One electrical heating stage relied on resistive heating elements instead of water circulation. In this design, a similar brass hollow collar is placed around the objective. Inside the collar, a resistive heating element and a thermocouple are placed, which are connected to a digital temperature controller (Omron E5CN). In addition, a brass block with resistive heating element and thermocouple replaces the flow cell and heats the sample from above. Because this brass block is not transparent, this particular setup can only be used with microscopy techniques that illuminate through the objective, such as epifluorescence or confocal microscopy. The benefit of the electrical heating is that it heats very fast and that there is no risk of water leakage. The achieved temperature precision was approximately identical to the precision of the water circulator setup 0.02K. The electrical heating setup was used for the confocal experiments of chapter 3.

A third setup was developed for the tweezer setup in chapter 7, based on circulation. This tweezer setup involved imaging with an immersion condenser lens. To heat this condenser lens and the sample attached to it, another collar, wound with cupper hoses, as used for the objective, was fabricated to fit around the condenser lens. Because the sample contact is less direct in this case, precisions of only approximately 0.05K were achieved.

### 2.3.4 Particle locating with subpixel accuracy

Many of the results in this thesis depend on the ability to precisely locate the center of a particle based on microscopy video recordings. Although the *resolution* of a conventional microscope is fundamentally limited by the wavelength of light, as shown by Eq. 2.1, the locating *accuracy* of a single particle, when sufficiently separated from nearby particles, can be much higher than this. In fact, accuracy can even be

higher than the pixel size. In an image with pixel size $s_{px}$, a particle can be located with an uncertainty $e = s_{px}/spa$, where $spa$ is the subpixel accuracy, which using conventional locating algorithms is on the order of 10 [100]. Given a pixel size of $s_{px} = 100$ nm, typical for a 63x objective, this leads to an accuracy $e = 10$ nm, much higher than the Abbe limit $R = 280$.

The possibility of subpixel accurate locating stems from the fact that the image of a particle is not a single bright pixel but a profile that extends over multiple pixels. By interpolating between the intensity profile of the image, a subpixel accuracy is reached that in principle is given by $spa \propto \sqrt{N_{px}}$, with $N_{px}$ the number of pixels constituting the intensity profile [99]. This is analogous to super-resolution microscopy techniques. In that case, instead of multiple pixels, multiple photons are used to extract information on length scales smaller than the photon itself, such that the diffraction limit can be broken, and has to be replaced by $R_{SR} \propto R/\sqrt{N_{fot}}$, with $N_{fot}$ the number of photons used to take an image [117]. In reality, the locating accuracy is not only determined by image size, but additionally by the static imaging noise inherent in any imaging system, and dynamic errors that arise from the movement of particles during image acquisition [118].

The exact way to interpolate the center of the particle from the particle image can differ. The method of choice needs to balance optimal accuracy and optimal speed, which depends on the number of particles and the length of the video recording. An intuitive approach is to use non-linear fitting of a model to the intensity profile, such as a gaussian profile [119]. The advantage of model fitting is that also more complicated image models can be used, such as point spread functions [117], particle scattering holograms [120], or non-spherically symmetric models for anisotropic particles [121]. Though such fitting approaches are least sensitive to noise, they require significant computational cost. In contrast, a more efficient algorithm commonly known as the "Crocker and Grier" algorithm (CG), in reference to its pioneering developers [100], makes iterative improvements on an initial best particle center estimate. It determines the center coordinate $\vec{c_i}$ by calculating the center-of-mass (as weighed by the intensity) of a masked area around the previous center estimate $\vec{c_i}$ [100, 121]:

$$c_i = \frac{\sum_{dist(\vec{x},\vec{c_{i-1}})\leq R} I(\vec{x})\vec{x}}{\sum_{dist(\vec{x},\vec{c_{i-1}})\leq R} I(\vec{x})}, \tag{2.2}$$

where $I(\vec{x})$ is the intensity at pixel $\vec{x}$ and $R$ the radius of the circular mask. The CG algorithm has found widespread use in the soft matter community and a number of different language implementations exist. A particularly well documented and actively maintained version is the open-source python implementation Trackpy [122], which has been used throughout this thesis.

# 2.4 Appendix

## 2.4.1 Other multivalent salt

The effect of salt on the aggregation and associated surface affinity of TPM particles was not only investigated for $MgSO_4$ but also for monovalent KCl and $CaCl_2$. As seen in Fig. 2.11, KCl does not induce a boundary condition change of TPM: The strongest aggregation remains for lutidine concentrations $c > c_c$. Interestingly adding both KCl and $MgSO_4$ seems to render the effect of KCl null. However, $CaCl_2$ has a similar effect as $MgSO_4$.

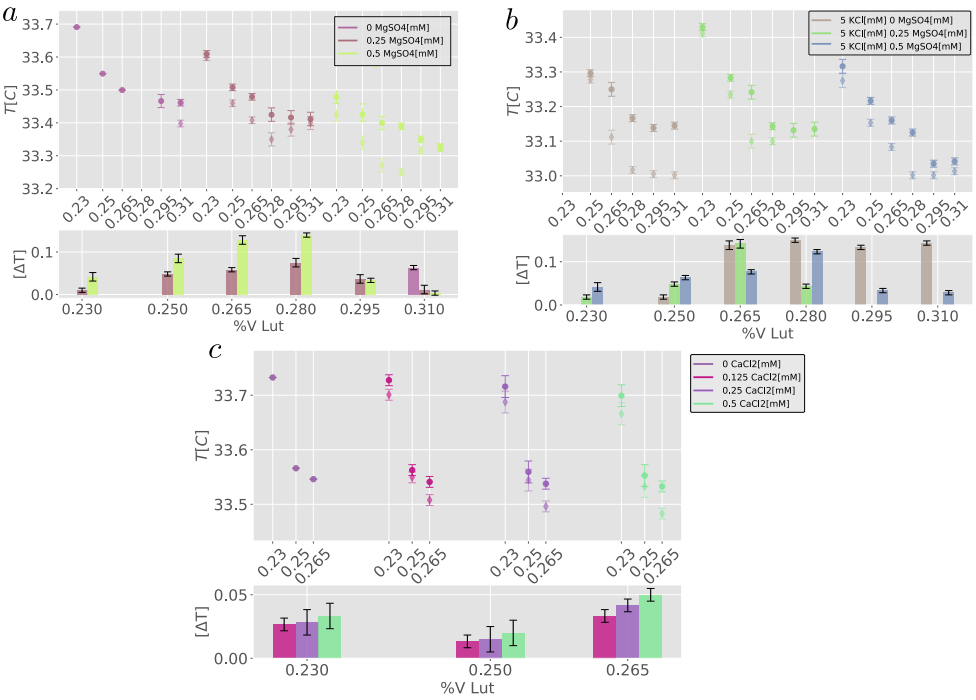


Figure 2.11: Effect of salt on aggregation temperature $T_a$ (rhombuses) and coexistence temperature $T_{cx}$ (spheres). (a) Three concentrations of $MgSO_4$, top panel $T_a$ and $T_{cx}$ as a function of lutidine concentration, bottom panel $\Delta T = T_{cx} - T_a$ between coexistence temperature and lowest aggregation temperature. (b) similar for KCl and mixtures with $MgSO_4$. (c) similar for $CaCl_2$

CHAPTER 3

# Critical Casimir interactions between colloids around the critical point of binary solvents

*Critical Casimir interactions between colloidal particles arise from the confinement of fluctuations of a near-critical solvent in the liquid gap between closely-spaced particles. So far, the comparison of theoretical predictions and experimental measurements of critical Casimir forces (CCFs) has focused on the critical solvent composition, while it has been lacking for off-critical compositions. We address this issue by investigating CCFs between spherical colloidal particles around the critical point of a binary solvent through a combination of experiments, previous Ising Monte Carlo simulation results and field-theoretical methods. By measuring the correlation length of the near-critical solvent and the pair potentials of the particles in terms of radial distribution functions and by determining the second virial coefficient, we test in detail theoretical predictions. Our results indicate that the critical Casimir theory gives quantitative correct predictions for the interaction potential between particles in a near critical binary mixture if weak preferential adsorption of the particle surface is taken into account.*

## 3.1 Introduction

Precise knowledge of the interaction potential is essential to rationally design self-assembly pathways and to interpret the behavior of assembled structures. Advances in the statistical mechanical theory and computer simulations of critical Casimir forces (CCFs) allow prediction of the range and strength of CCFs. Likewise, recent experimental techniques have provided direct measurement of the effective potential, allowing verification of the theoretical predictions. (Recent developments are reviewed in Ref. [44] with a focus on experiments, and in [82] with a focus on the theory.) By using total internal reflection microscopy, the critical Casimir potential (CCP) between a colloidal particle and a planar wall suspended in a near-critical binary mixture has been measured [89, 123, 124]. Furthermore, the effective potential between colloidal particles has been measured using confocal microscopy [93, 125, 126]. For a sufficiently dilute suspension of solute, the potential of mean force $V_{mf}(r) = -k_b T \ln g(r)$ can be identified with the effective pair potential $V(r)$, while the pair correlation function $g(r)$ can be determined directly from confocal microscopy images.

In Chapter 2, the potential for patchy assembly using critical Casimir forces was demonstrated. We showed that in order to obtain a aggregation contrast between patch and particle bulk material, off-critical concentrations are required. However, particularly at off-critical compositions, the origin of the critical Casimir force remains debated. Early experiments [127–129] already reported that the temperature - composition region $(T, c)$, in which colloidal aggregation occurs, is not symmetric and strong aggregation occurs on the side of the critical composition $c_c$ poor in the component preferred by the particles. This preference gives rise to an effective surface field $H_s$ conjugate to the solvent order parameter at the surface, causing an adsorption layer rich in the preferred component. The critical Casimir potential is therefore expected to depend strongly on the composition of the solvent, as well as on the strength of the surface field. Both dependencies have been recently worked out in theoretical predictions of the CCF between two spherical particles as a function of thermodynamic fields $(T, c)$ [96] and surface field [130]. Experiments [93, 125] on dilute suspensions of poly-$n$-isopropyl acrylamide microgel (PNIPAM) particles clearly showed the effect of solvent composition on the effective pair potential for two representative off-critical compositions. The theoretical modeling however remained limited to the asymptotic exponential form of the CCP, valid only for large ratios $r/\xi$, and the extracted length scale of the CCP differed from the bulk correlation length. In a subsequent paper [125], the fitting procedure was extended to include the standard scaling law for the bulk correlation length, $\xi_t = \xi_t^{(0)}|t|^{-\nu}$, with the nonuniversal amplitude $\xi_t^{(0)}$ as the only fit parameter. Yet, the reduced deviation $(T_{cx} - T)/T_{cx}$ from the actual coexistence temperature $T_{cx}(c)$ was used instead of $t$, neglecting the explicit solvent-composition dependence of $\xi$ and hence of the CCP. In an attempt to further improve the theoretical prediction of the experimental $g(r)$ close to the critical composition, Mohry et al. [96] explicitly accounted

for the solvent-composition dependence of the CCP. But as the amplitude $\xi_t^{(0)}$ was inferred from the experimental data presented in Ref. [131], and the critical mass fraction $\omega_{3\mathrm{MP,c}}$ of the liquid mixture has significant uncertainty, the fitting procedure was again not optimal. A reliable comparison of experimental measurements and theoretical predictions needs an accurate solvent phase diagram and simultaneous measurement of the solvent correlation length for internal calibration. Such dedicated measurements of critical Casimir interactions remain elusive. As a result, there is active debate about the nature of the attractive force in particular for off-critical compositions. Most notably it remains unclear whether a critical Casimir force alone can explain the observed colloidal attraction. One of the difficulties is the inevitable simultaneous presence of various contributions to the effective pair potential. Hence, well-calibrated theoretical and experimental results are required to improve the interpretations.

Here we combine measurements, theory and results of previous Monte Carlo simulations to investigate the effective interactions of spherical colloidal particles in a binary solvent based on consistent, well calibrated data. To internally calibrate our measurements and link to theoretical predictions, we complement measurements of the pair correlation function with dynamic light scattering measurements of the solvent phase diagram and correlation length. We perform measurements for various solvent compositions, varying temperature for each of them to approach the solvent two-phase coexistence curve from the homogeneous mixed phase. To most reliably compare measurements of particle interactions with theoretical predictions, we directly compare virial coefficients that are unaffected by particle locating inaccuracy and polydispersity. This allows us to demonstrate for the first time a fully consistent quantitative description of the critical Casimir interaction from the internally calibrated solvent phase diagram and correlation length based on only one remaining fit parameter, the effective surface field of the particles. We obtain very good agreement between measurements and predictions of the CCP in the entire near-critical composition range. These results indicate that the observed attraction is indeed dominated by a critical Casimir force, identified by its characteristic temperature and composition dependence.

This chapter proceeds as follows: In Sec. 3.2.1 we present the theoretical background, defining the CCP and its universal scaling function. We show how the solvent composition is related to the scaling variable describing thermodynamic states at off-critical composition. We present methods to calculate the scaling function of the CCP for these states. In Sec. 3.2.2 we discuss the scaling behavior of the CCP for colloids exhibiting a weak adsorption preference for one of solvent components. In Sec. 3.2.3 we introduce the model for an effective pair potential between colloidal particles. The discussion in Sec. 3.2 forms the basis for the interpretation of the experimental results. Section 3.3 describes experimental measurements and data analysis, and in Sec. 3.4 we present in detail the experimental results for the bulk phase diagram and the bulk correlation length of the pure solvent, the pair potential between colloids and the second virial coefficient, comparing them with the theoretical predictions. Conclusions and a discussion of perspectives are provided in

Sec. 3.5. Details of the numerical procedures are provided in the appendices.

## 3.2 Theoretical background

### 3.2.1 Critical Casimir interactions

The solvent-mediated force, $f_s$, between two spherical particles with radius $R$, a surface-to-surface distance $D$ apart, is defined as

$$f_s = -\frac{\partial \mathcal{F}^{ex}}{\partial D} = -\frac{\partial(\mathcal{F} - V f_b)}{\partial D}, \tag{3.1}$$

where $f_b$ is the bulk free energy density of the solvent and $\mathcal{F}$ is the free energy of the solvent in the macroscopically large volume $V$ excluding the volume of two suspended colloids. The critical Casimir force (CCF) $f_C$ is the universal contribution to $f_s$, which emerges upon approaching the bulk critical point of the solvent. The associated critical Casimir potential (CCP) is

$$V_C(D) \equiv \int_D^\infty \mathrm{d}z\, f_C(z). \tag{3.2}$$

In order to analyze experimental data for the pair potential of colloidal particles immersed in a near-critical mixture, detailed knowledge of the critical Casimir potential in the whole neighborhood of the critical point of the binary solvent, i.e. as a function of both temperature and solvent composition close to $(T_c, c_c)$, is necessary. The relevant scaling fields of the near-critical solvent are $t = (T_c - T)/T_c$ (for the solvent with lower-critical point considered here) and the bulk ordering field, $h_b$, conjugate to the order parameter. The bulk field $h_b$ is proportional to the deviation of the chemical potential difference $\Delta\mu = \mu_a - \mu_b$ of the two species $a$ and $b$ from its critical value, i.e. $h_b \sim \Delta\mu - \Delta\mu_c$. Each point in the solvent phase space is uniquely defined by a value of $t$ and $h_b$. (We note that the form of the fluid scaling fields differ from those of the Ising model due to the lack of symmetry between coexisting phases of fluids; the actual scaling fields are linear combinations of $T$ and $h_b$, which we neglect here). For the demixing phase transition of a binary liquid mixture, the order parameter (OP) $\phi$ conjugate to the field $h_b$ is proportional to the deviation of the composition $c_a$ of species $a$ from its value $c_{a,c}$ at the critical point, i.e. $\phi = c_a - c_{a,c}$. The composition $c_a = \varrho_a/(\varrho_a + \varrho_b)$ is defined by the number densities $\varrho_\alpha$, $\alpha \in \{a, b\}$ of the molecules of species $a$ and $b$, respectively. We generally leave out the explicit $a$ dependence as this choice is arbitrary and write $\phi = c - c_c$. The OP can be controlled experimentally by changing the mass or the volume fraction of one of the components of the mixture.

According to finite-size scaling theory [88, 132], the critical Casimir potential exhibits scaling described by a universal scaling function $\hat{\Theta}$ determined solely by the universality class of the solvent and the surface universality classes of the surfaces of

the colloids in contact with the binary liquid mixtures near their segregation transition [81, 133–136]. The relevant bulk universality class for colloidal suspensions is the Ising universality class in spatial dimension $d = 3$. Surfaces of colloidal particles generically exhibit preferential adsorption of one of the two components of the mixture. This preference results in the enhancement of the order parameter $\phi$ close to the particle surfaces, characterized by an effective surface field $H_s$ acting on $\phi$. Such surfaces belong to the universality class of the so-called normal transition [133]. One usually refers to the boundary conditions (BCs), imposed on the fluctuations of the order parameter, as (+) or (−) depending on whether the surface favors $\phi > 0$ or $\phi < 0$, respectively. If we assume strong adsorption $H_s = \pm\infty$, the CCP for spherical surfaces depends on three scaling variables, and we can write

$$V_C(D)/(k_BT) = \frac{R}{D}\hat{\Theta}\left(\mathcal{Y} = sgn(t)\frac{D}{\xi_t}, \Delta = \frac{D}{R}, \Lambda = sgn(h_b)\frac{D}{\xi_h}\right), \quad D = r - 2R > 0, \tag{3.3}$$

where $\xi_t(t \gtrless 0) = \xi_{t,\pm}^{(0)}|t|^{-\nu}$ and $\xi_h = \xi_h^{(0)}|h_b|^{-\nu/(\beta\delta)}$ are the solvent correlation lengths governing the exponential decay of the solvent bulk two-point order parameter (OP) correlation function along the specific paths $t \to 0^{\pm}$ for $h_b = 0$, and $h_b \to 0$ for $t = 0$, respectively, and $\pm$ refers to the sign of $t$. The amplitudes $\xi_{t,\pm}^{(0)}$ are non-universal but their ratio $\xi_{t,+}^{(0)}/\xi_{t,-}^{(0)}$ is universal. The amplitude $\xi_h^{(0)}$ is also non-universal; $\nu$, $\beta$, and $\delta$ are standard bulk critical exponents [137].

The bulk correlation length $\xi$ depends on both scaling fields $t$ and $h_b$, and close to the bulk critical point, can be written in the scaling form

$$\xi(t, h_b) = \xi_t\, \Xi\left(|\Sigma| = \frac{\xi_t}{\xi_h}\right), \tag{3.4}$$

where the universal bulk scaling function $\Xi$ satisfies $\Xi(|\Sigma| \to \infty) = 1$ and $\Xi(|\Sigma| \to 0) = |\Sigma|^{-1}$ (The functional form of $\Xi(|\Sigma|)$ depends on the sign $\pm$ of $t$, but not on the sign of the bulk scaling variable $\Sigma$). The thermodynamic paths of fixed solvent composition are particularly experimentally relevant, and we thus take the convention to write the scaling function of the critical Casimir potential $\hat{\Theta}$ as a function of the scaling variables $\mathcal{Y}, \Delta, \Sigma$ rather than $\mathcal{Y}, \Delta, \Lambda$. We further relate the scaling variable $\Sigma$ that depends on the only indirectly known field $h_b$ to the solvent OP $\phi$, which is the direct experimental control parameter. For this purpose, we use the equation of state, which close to the critical point takes the scaling form [137]

$$h_b = \mathcal{D}\, sgn(\phi)\, |\phi|^{\delta}\, \mathrm{F}_{\pm}\left(sgn(t)\, |t\mathcal{B}/\phi|^{1/\beta}\right), \tag{3.5}$$

where $\mathrm{F}_{\pm}(|X| = |t\mathcal{B}/\phi|^{1/\beta})$ is a universal scaling function and $\pm$ refers to the sign of $t$. $\mathcal{D}$ and $\mathcal{B}$ are non-universal amplitudes that depend on the definition of $\phi$. $\mathcal{B}$ is defined via the near-critical behavior of the bulk OP on the coexistence curve:

$$\phi_b(t \to 0^-, h_b = 0) = \mathcal{B}\, |t|^{\beta}. \tag{3.6}$$

Note that experimentally, the phase coexistence curve may be determined in terms of weight fraction, mole fraction or number density of one component, all of which yield different amplitudes $\mathcal{B}$ that are directly related to each other. The transformation of the OP is given in Appendix 3.6.1. $\mathcal{D}$, $\mathcal{B}$, and the correlation length amplitudes $\xi_{t,\pm}^{(0)}$ and $\xi_h^{(0)}$ are related to each other by universal amplitude ratios such that only two of them are independent [137, 138]. To linear order in $X$, the universal scaling function $\mathrm{F}_\pm(|X|)$ has the form $\mathrm{F}_\pm(|X|) = 1 \pm |X|$, capturing the crossover between the critical behavior at $t = 0$ and $h_b = 0$ [137]. In terms of the scaling variables $\Sigma$ and $X$, the equation of state takes the scaling form

$$\begin{aligned} sgn(\Sigma)\,|\Sigma|^{\beta\delta/\nu} = \\ (R_\chi \delta/Q_2)^{\delta/(\delta-1)} (Q_\xi^+/Q_\xi^c)^{\beta\delta/\nu} \\ \times\, sgn(X)\,|X|^{-\beta\delta}\, F_\pm(|X|), \end{aligned} \tag{3.7}$$

where $R_\chi$, $Q_2$, $Q_\xi^+$, and $Q_\xi^c$ are universal amplitude ratios [137].

For all parameters which are needed for comparison with the experiment, in principle, it is possible to determine the CCP in the bona fide sphere-sphere geometry by using mean-field approximation. Numerically, however, this task is too demanding. The other possibility is to express the scaling function of the CCP between two spheres in terms of the scaling function $\vartheta_{||}^{(d=3)}$ of the CCFs between two parallel plates by using the Derjaguin approximation [139]. The CCFs between two parallel plates (film geometry) can be determined by using mean field theory within the framework of Landau-Ginzburg theory [140]. Some results beyond mean-field theory are also available, e.g., from MC simulations [141–146] or within the extended de Gennes-Fisher local functional method [96, 147, 148]. We should remark that the validity of the Derjaguin approximation is limited to temperatures corresponding to $\xi \lesssim R$, for which the CCF acts at colloidal surface-to-surface distances $D$ small compared to $R$. Encouraged by observations that in many cases the Derjaguin approximation works surprisingly well even for $D \lesssim R$ [149, 150], we will use this approximation to describe experimental data. Specifically, we calculate the scaling function of the CCP in terms of the scaling variable $\Sigma$ using [89, 139, 151]

$$\Theta^{(d=3,Derj)}(\mathcal{Y}, \Delta \to 0, \Sigma) = \pi \int_1^\infty \mathrm{d}x (x^{-2} - x^{-3}) \vartheta_{||}^{(d=3)}(x\mathcal{Y}, \Sigma). \tag{3.8}$$

The scaling function $\vartheta_{||}^{(d=3)}$ is calculated using two approaches: the local functional approach, described in detail in Ref. [96, 147], and the "dimensional" approximation introduced in Ref. [152, 153]. Within the "dimensional" approximation, the scaling function $\vartheta_{||}^{(d=3)}(\mathcal{Y}, \Sigma)$ is constructed such that for $h_b \to 0$ it reduces exactly to $\vartheta_{||}^{(d=3)}(\mathcal{Y}, \Sigma = 0)$ and for fixed values of $\mathcal{Y}$ its functional form is the one obtained from mean-field theory ($d = 4$):

$$\vartheta_{||}^{(d=3)}(\mathcal{Y}, \Sigma) = \frac{\vartheta_{||}^{(d=4)}(\mathcal{Y}, \Sigma)}{\vartheta_{||}^{(d=4)}(\mathcal{Y}, \Sigma = 0)} \vartheta_{||}^{(d=3)}(\mathcal{Y}, \Sigma = 0). \tag{3.9}$$

We take $\vartheta_{||}^{(d=3)}(\mathcal{Y}, \Sigma = 0)$ from MC simulation data [142, 143] and assume that within the mean-field expressions $\vartheta_{||}^{(d=4)}(\mathcal{Y}, \Sigma)$, the scaling variables involve the critical bulk exponents in spatial dimension $d = 3$. Thus the approximation concerns only the shape of the scaling function itself, which typically depends on the spatial dimension only mildly. The function $\vartheta_{||}^{(d=4)}(\mathcal{Y}, \Sigma)$ is calculated within Landau-Ginzburg theory via the so called stress tensor [96, 154].

### 3.2.2 Critical Casimir potential for weak adsorption preference

While the scaling form of the critical Casimir potential in Eq. (3.3) is valid for strongly adsorbing particles in the limit $H_s = \pm\infty$, for weakly adsorbing particles, the CCP depends also on the surface field $H_s$ via a scaling variable $h_s = \tilde{H}_s|t|^{-\Delta_1}$. Here, $\tilde{H}_s = H_s/(k_B T)$ and $\Delta_1$ is the surface counterpart of the bulk gap exponent [133]. Theoretical and MC simulation results for the film geometry indicate [130, 155–157] that while the amplitude of CCFs decreases, the shape of the scaling function $\vartheta_{||}$ does not vary significantly with $h_s$. Hence, within mean field theory and in $d = 4$ the dependence on $h_s$ at the critical concentration ($\Sigma = 0$) can be reduced to a re-mapping [130]

$$\tilde{\vartheta}_{||}^{(d=4)}(\mathcal{Y}, \Sigma; h_s) = s^d \, \vartheta_{||}^{(d=4)}(s^{-1}\mathcal{Y}, \Sigma) \tag{3.10}$$

with a rescaling parameter $s = s(h_s)$. To the best of our knowledge, it has not been studied yet whether such a rescaling holds in $d = 3$ and for off-critical concentrations, though we expect a similar result but with a parameter $s(h_s, h_b)$ that depends also on the bulk ordering field $h_b$, at least if $h_s$ and $h_b$ have an opposite sign.

We show the scaling function $\tilde{\Theta}^{(d=3,Derj)}$ for the scaling parameter $s = 0.84$ and $(+,+)$ BCs in Fig. 3.1(a) (solid lines). The experimentally accessible range of the scaling function is usually limited to its exponential tail [93, 123, 158]. In this range, we found that one may mimic the rescaling using an effective temperature offset $t_{\text{off}}$ that shifts the relative temperature according to

$$t' = \frac{T_c - T_{\text{exp}} + \Delta T_{\text{off}}}{T_c} = t + t_{\text{off}}, \tag{3.11}$$

combining effects of a weak surface field (Sec. 3.2.3) and any small remaining temperature uncertainties: While the rescaling (solid lines) and the temperature offset (dashed lines) have different functional form close the critical point $\mathcal{Y} = 0$, they give the same exponential decay for $\mathcal{Y} \gg 1$. We show the resulting pair potentials in Fig. 3.1(b), where we have added the electrostatic repulsion present in the charge-stabilized colloidal system, see next section. Within the range of $\mathcal{Y}$ explored in the experiment, the two approaches are indiscernible. We will employ $t_{\text{off}}$ as a fitting parameter; any finite value of $t_{\text{off}}$ should be understood as indicating the presence of weak surface fields that corresponds to a rescaling of the scaling function of the

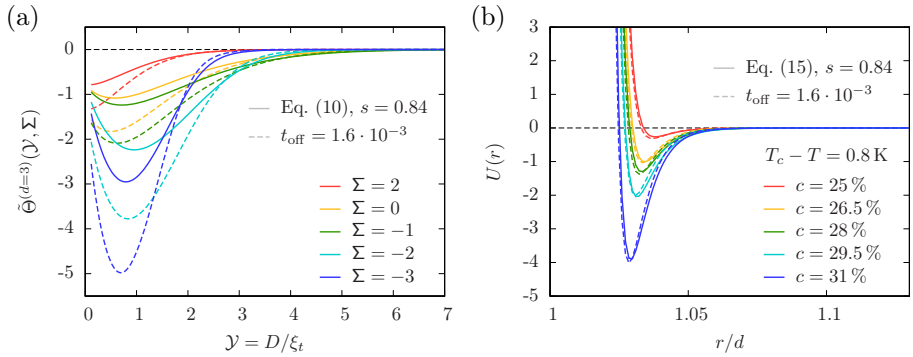


Figure 3.1: (a) Scaling function $\tilde{\Theta}^{(d=3)}$ of the CCP obtained from $\Theta^{(d=3)}$ for $(+,+)$ BCs by rescaling according to Eq. (3.10) with $s = 0.84$ (solid lines) for several values of $\Sigma$. Rescaling mimics the case of particles with weak surface fields (note that it is exact only for $\Sigma = 0$ in $d = 4$). The same effect can be achieved by using the temperature offset $t_{\rm off} = 0.14$ (dashed lines) - at least for the exponentially decaying tails of the scaling function. (b) The two rescaling methods with the same values, but shown for the pair potential Eq. (3.15). The scaling variable $\Sigma$ has been replaced by the composition $c$ (see main text).

CCP. This rescaling is expected to depend on the bulk field $h_b$, and therefore on the composition of the solvent.

### 3.2.3 Effective potential

Besides the critical Casimir forces, there are other interactions between the colloidal particles, including van-der-Waals attraction, and hard-core and screened electrostatic repulsion of the charge-stabilized particles. Because of the large length-scale ratio between the colloidal particles and the solvent molecules, one can ignore the discrete nature of the solvent and use a simplified pair potential model as a background interaction potential. This background potential adds onto the CCP, but is present also outside the critical solvent regime, capturing the essential features of the stable suspension on the relevant mesoscopic length scale. For the repulsive component, we employ the widely used Yukawa potential of particles charge-stabilized against flocculation [26, 159, 160]:

$$V_{rep}(D)/(k_BT) = U_{rep}(D) = (U_0/(\kappa D))\exp(-\kappa D), \qquad D = r - 2R > 0. \quad (3.12)$$

where the Debye screening length $\kappa^{-1} = \sqrt{\epsilon k_B T/(e^2 \sum_i \rho_i)}$ (see, e.g. Ref. [161]), with $e$ the elementary charge, $\epsilon$ the permittivity of the solvent relative to vacuum, and $\rho_i$ the number density of ions, sets the range of the repulsion. A simplified, purely exponential form of the repulsive pair potential,

$$V_{rep}(D)/(k_BT) = U_{rep}(D) = A\exp(-\kappa D), \quad (3.13)$$

is often used for suspensions in which $\kappa^{-1} \ll R$ for distances $2R > D > R + \kappa^{-1}$, for which all curvature effects associated with the spherical geometry of the colloidal particles effectively drop out [21, 162]. The corresponding condition $\kappa^{-1} \ll R$ is practically satisfied for the experimentally relevant systems for which the Debye length is of the order of 10 nm and the colloidal size of the order of 1 $\mu$m. The amplitude $A$ is given by [26]

$$A = U_0/(2\kappa R) = 2\pi(\epsilon\epsilon_0)^{-1}\Upsilon^2\kappa^{-2}R/(k_BT), \tag{3.14}$$

where $\epsilon_0$ is the permittivity of the vacuum, and $\Upsilon$ is the surface charge density of the colloidal particles.

The amplitude of the Van der Waals dispersion forces, the Hamaker constant, depends on the dielectric properties of the materials involved in the experiment under consideration [161]. In our nearly index-matched colloidal suspensions, this amplitude is strongly reduced, and we estimate these dispersion forces to be negligible at the particle separations relevant in our studies.

Our pair potential model for colloidal particles interacting in near-critical solvents due to screened electrostatic and critical Casimir forces hence corresponds to the sum of Eqs. (3.12) and (3.3):

$$U(r) = \begin{cases} \infty, & D < 0 \\ U_{rep} + U_C^{(d=3)} = (U_0/(\kappa D))\exp(-\kappa D) + (1/\Delta)\Theta^{(d=3,Derj)}(\mathcal{Y}, \Sigma), & D > 0. \end{cases} \tag{3.15}$$

Using this effective pair potential, we can calculate the second virial coefficient $B_2$, which for dilute suspensions is a useful measure of the strength of the attraction and may be a useful measure for predicting of the onset of colloid aggregation. For radially symmetric spherical particles [163], $B_2$ is calculated from the pair potential using

$$B_2 = 2\pi \int_0^\infty \mathrm{d}r\, r^2 \left[1 - \exp(-U(r))\right]. \tag{3.16}$$

$B_2$ occurs in the expansion of pressure $p$ in terms of the number density $\rho$ of the colloid $p(\rho)/(k_BT\rho) = 1 + B_2\rho + \ldots$ as a leading correction to the ideal gas pressure. It has been shown that an extended law of corresponding states can be applied to colloidal suspensions with short-ranged interactions [164, 165], meaning that different systems exhibit approximately the same thermodynamic behavior if they have the same value for the reduced second virial coefficient $B_2^* = B_2/B_2^{(hs)}$, independent from details of the pair interaction. Here, $B_2^{(hs)} = 2\pi d^3/3$ is the second virial coefficient of a *h*ard-*s*phere reference system with diameter $d$. For systems with a soft-core repulsion and an attractive contribution, as is the case here, the reference system is commonly chosen to be a hard-core interaction with an effective diameter $d_{\text{eff}} > 2R$ in order to incorporate effectively the soft-core repulsion. The separation of the pair potential into a repulsive and attractive part is not unique. We follow the Weeks,

Chandler, and Andersen [166] (WCA) separation into an attraction

$$U_a(r) = \begin{cases} U_{min}, & r \leq r_{min} \\ U(r), & r > r_{min}, \end{cases} \tag{3.17}$$

where $U_{min} = U(r_{min})$ is the minimum of the pair potential, and a repulsion

$$U_r(r) = \begin{cases} U(r) - U_{min}, & r \leq r_{min} \\ 0, & r > r_{min}. \end{cases} \tag{3.18}$$

The effective diameter is given by the repulsive contribution via

$$d_{\text{eff}} = \int_0^\infty \mathrm{d}r \, \left[1 - \exp(-U_r(r))\right]. \tag{3.19}$$

Only a few attractive model interactions allow to calculate $B_2$ analytically. For the sticky hard-sphere model [167] of vanishing interaction range and strength given by the inverse stickiness parameter $\tau$, one finds $B_2^* = 1 - 1/(4\tau)$. A gas-liquid phase transition is found for values of $\tau$ smaller than a critical value, leading to $B_2^* < B_{2,c}^* = -1.212$ [168, 169]. Though critical Casimir interactions are long-ranged (algebraically decaying with distance) right at the critical point, in the experimentally studied regime near the critical point, the interaction is short-ranged (exponentially decaying with distance). We can thus evaluate the "stickiness" of the particles by comparison of the experimental results for $B_2^*$ with the sticky hard-sphere model in the form of $B_{2,c}^*$.

## 3.3 Experimental measurements

### 3.3.1 Correlation length

As suspending solvent we use a binary mixture of 3-methylpyridine (3MP) and heavy water prepared from distilled 3MP (purity $\geqq 99.5\%$) and heavy water ($D_2O$, purity $> 99\%$). Solvents are prepared with 3MP weight fractions $c$ ranging from 23.5 to 33%, around the critical 3MP weight fraction $c_c \sim 28.0\%$ [170]. To introduce a well-defined ion concentration, we add 1mM KCl salt; this concentration is of the same order as used in previous studies, and is well below concentrations where anomalous effects due to ion-solvent coupling start to occur [91, 171–175].

We use dynamic light scattering to determine both the phase-coexistence temperatures $T_{cx}$ of the solvents as well as the solvent correlation lengths; for these measurements, we load 400 $\mu$l of the binary solvent into a NMR tube which we flame seal, while keeping the solvent in the tube cold to minimize compositional changes due to solvent evaporation. The scattered intensity is monitored at an angle of 90° to the incident beam, corresponding to a diffraction vector $q = 4\pi n/\lambda \sin(\theta/2)$ of length 19 $\mu\text{m}^{-1}$, where we use the refractive index $n = 1.39$ for the binary solvent

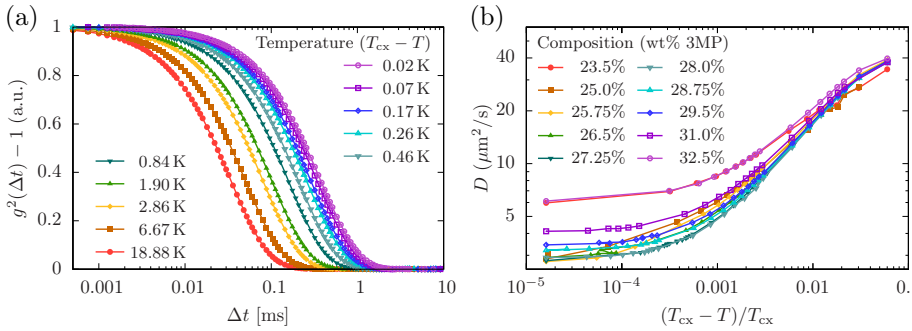


Figure 3.2: (a) Normalized second-order autocorrelation functions acquired through dynamic light scattering of solvent fluctuations. Dots are data points from a sample of $c = 29.5\%$ of which for clarity only a selection of the total temperatures measured is depicted. Solid lines are fits based on the single exponential decay of the first-order autocorrelation function. (b) Extracted effective diffusion coefficients for all the temperatures and compositions in the dataset as a function of the normalised temperature distance from the phase-coexistence temperature $T_{cx}$.

that depends slightly on temperature [131], and the wavelength of the incident He-Ne laser light $\lambda = 633$ nm. For each composition, we perform measurements at around 20 temperatures with a temperature stability of $\sim 0.01\,^{\circ}\mathrm{C}$, ranging from room temperature to slightly above the solvent phase separation temperature, $T_{\mathrm{cx}}$. After every temperature change, we let the sample chamber equilibrate for 20 minutes, and then record the scattered intensity for 5 minutes to determine its autocorrelation function. Phase-separation temperatures, determined from the sudden disappearance of the solvent scattering, are used to map the phase diagram of the binary solvent around its consolute point. These measurements yield the critical temperature $T_{\mathrm{c}} = 37.30\,^{\circ}\mathrm{C}$ from phase separation of the solvent with critical composition. Below $T_c$, the solvent correlation lengths are determined from the temperature-dependent autocorrelation function of the scattered intensity. These autocorrelation functions are well-described by single-exponential decays with a characteristic time constant $\tau$, as shown for solvent composition $c = 29.5\%$ close to the critical composition in Fig. 3.2(a). Here, the autocorrelation functions have been normalized by dividing by the proportionality factor obtained from the single exponential fit. We use the fitted decay time to compute the effective diffusion coefficient $D = (q^2\tau)^{-1}$, which we show as a function of temperature for various solvent compositions in Fig. 3.2(b).

This effective diffusion coefficient is related to the size of the correlated regions $\xi$ via a relation analogous to Stokes-Einstein relation for Brownian particles, but depending intricately on additional microscopic details. Notably, close to the critical point, the diffusion coefficient decomposes into a critical and a background contribution [131],

$$D = D_{\mathrm{c}} + D_{\mathrm{bg}}, \tag{3.20}$$

similar to the viscosity that likewise separates into a critical and background part,

$$\eta = \eta_{\mathrm{bg}} + \eta_{\mathrm{c}}. \tag{3.21}$$

Bhattacharjee et. al. [176] have worked out a crossover function $H$ that relates $\eta$ to $\eta_{\mathrm{bg}}$,

$$\frac{\eta}{\eta_{\mathrm{bg}}} = \exp(z\, H(Q_0\, \xi, q_D/q_c)), \tag{3.22}$$

where $z = 0.065$ is a critical exponent (prediction from mode-coupling theory in good agreement with experiments), $Q_0$ a system-dependent wave number and $q_D/q_c$ is the ratio of two wave numbers; $q_D/q_c \to \infty$ corresponds to the case of a dominant background contribution whereas $q_D/q_c \to 0$ to the case of vanishing background. For a full expression of $H$ we refer to Appendix 3.6.2. We assume that around the critical point the crossover function $H$ depends on the thermodynamic state only via $\xi$ in the first variable, i.e. the ratio $q_D/q_c = \text{const.}$ is independent of $\phi$ and $T$. For $q_D/q_c \ll 1$, which holds for the present experimental system, the crossover function $H$ depends only weakly on $q_D/q_c$.

Using Eqs. (3.21) and (3.22) we can derive the expressions for the diffusion coefficient. The critical part is given by [131, 177, 178]

$$D_{\mathrm{c}} = \frac{\mathcal{R}\, k_B T}{6\pi\, \eta\, \xi}\, K(q\,\xi)\left(1 + b^2 (q\,\xi)^2\right)^{z/2}, \tag{3.23}$$

where $\eta$ is the full viscosity, and $\mathcal{R} \approx 1.05$ is a universal dynamic amplitude ratio [178, 179], $K(x) = 3/(4x^2)[1 + x^2 + (x^3 - x^{-1}) \arctan x]$ is the Kawasaki function [180], and we adopt the value $b = 0.55$ from Ref. [178] for the correction to scaling. The background contribution to the diffusion coefficient is given by [131, 177, 178]

$$D_{\mathrm{bg}} = \frac{k_B T}{16\, \eta_{\mathrm{bg}}\, \xi}\, \frac{1 + (q\,\xi)^2}{q_c\, \xi}. \tag{3.24}$$

From this it is possible to rewrite the complete expression for the diffusion coefficient as a function of $\xi$, $\phi$ and $T$ depending on the known constants $\mathcal{R}$ and $z$ and the a priori not known $\eta_{\mathrm{bg}}$ and constants $Q_0$ and the ratio $q_D/q_c$, see Appendix Eq. (3.38). We determine $\eta_{\mathrm{bg}}$ as function of $T$ and $\phi$ by extrapolating off-critical measurements to the critical region; here we use the polynomial approximation and viscosity data from Ref. [181]. We are thus left with a relation with three unknowns: $\xi$, $Q_0$ and $q_D/q_c$, which we solve via numerical root finding, by determining iteratively the correlation length $\xi$ that yields the same diffusion coefficient as experimentally determined. For the details, see Appendix 3.6.2. Best agreement is obtained for $Q_0 = 0.17\,\mathrm{nm}^{-1}$, $\xi_{t,+}^{(0)} = 0.44\,\mathrm{nm}$ and $q_D/q_c = 0.235$, which is used in the following section for all experimental samples, at critical and off-critical weight fractions. Based on these fitting values, the prediction for the critical viscosity has been checked against data from Ref. [181] with good agreement, see Appendix 3.6.2.

### 3.3.2 Colloidal suspension

To study particle interactions, we synthesize copolymer particles [72] whose polymer ratio is tuned (FEMA:tBMA, 10.5:89.5 %vol) to match the density of the binary solvent at the critical composition [125]. The density match allows observation of the particles without much disturbance by gravity. Additionally, during the synthesis we add 2 vol% ethylene glycol dimethacrylate (EGDMA), a crosslinker that minimizes the swelling of the particles in the binary mixture. Compared to previously used microgel particles [93], these polymer particles are rigid, allowing more straightforward comparison with theory predictions for hard electrostatically stabilized particles. The particles are dyed with a cross-linkable fluorescent probe (Cy3) during synthesis. These particles are hydrophilic, preferring the aqueous component of the binary mixture, as confirmed by their assembly in the water-rich phase after phase separation. The particle diameter in water is $d_0 = 2.0\,\mu$m with a polydispersity of $< 5\%$ as measured by dynamic light scattering and using a second order cumulants fit. We estimate the polydispersity to be 3% based on previous, more accurate measurements of particles made using the same synthesis technique which is known to be very reproducible [72]. In the binary mixture, the particles swell slightly. We determined a diameter of $d = 2.12\,\mu$m by confocal microscopy and assume the same polydispersity as in water. The particles have a negative surface charge with a measured zeta-potential of -166 meV, as measured by electrophoresis on particles in a binary mixture with composition $c = 31\%$ at 25°C (Malvern Instruments Zetasizer Nano Series). At higher temperatures, composition fluctuations interfere with the measurement, and the results become less accurate. We use the semi-empirical equation of Loeb, Overbeek, and Wiersema [182] to relate the zeta potential to the surface charge density according to

$$\Upsilon(\zeta) = \epsilon\epsilon_0 \frac{k_B T}{z\,e}\,\kappa\,\left[2\sinh\left(\frac{z\,e\,\zeta}{2\,k_B T}\right) + \frac{4}{\kappa R}\,\tanh\left(\frac{z\,e\,\zeta}{4\,k_B T}\right)\right]. \tag{3.25}$$

The resulting surface charge density is $\Upsilon = -0.17\,e/\mathrm{nm}^2$.

Colloidal suspensions with solvent composition $c = 25$, 26.5, 28, 29.5 and 31% are prepared by washing the particles four times in the binary solvent with the highest 3MP weight fraction $c = 31\%$ with 1 mM KCl and then diluting with 1 mM KCl-$D_2O$ solution to the final solvent composition. The resultant colloid volume fraction is $\phi \sim 0.5\%$. For microscopy, the samples are filled into rectangular glass capillaries with dimensions 40 mm by 4 mm by 0.2 mm (Vitrocom,borosilicate glass). Due to their small volume, the capillaries are not flame sealed, as this would lead to irreproducible aggregation temperatures [183], but instead closed using 3MP-resistant Teflon grease, and subsequently sealed using epoxy glue.

### 3.3.3 Pair potential

Confocal microscopy is used to image the particles and study the temperature and composition-dependent particle pair correlation function $g(r)$ that indicates the probability of finding a particle at a distance $r$ from a reference particle relative to the ideal gas distribution. We use a laser-scanning confocal microscope (Zeiss LSM5 Pascal) with a 63X, 1.4 NA oil immersion objective. The sample and objective lens are heated using a home-made heating stage and a resistive heating element around the objective resulting in a temperature stability of $\sim 0.02\,^{\circ}\mathrm{C}$. To ensure good temperature calibration consistent with light scattering, we use the phase-separation temperature of each sample as a reference. We first determine the aggregation temperature $T_a$ by increasing the temperature in steps of $0.1\,^{\circ}\mathrm{C}$, noting when aggregation occurs and then taking the average of the last two temperatures for $T_a$. We then measure temperature-dependent pair correlations below $T_a$ by heating the colloidal suspension to the desired temperature, equilibrating for 15 min, and recording 2000 images of particle configurations $\sim 30\,\mu$m above the bottom glass slide to avoid any influence of the boundaries. The particles diffuse during image acquisition; the scanning time for our field of view of $140 \times 140\,\mu$m with a resolution of $1024 \times 1024$ pixels is 1.58 s. This time is sufficiently large compared to the diffusion time in the potential well or alternatively the width of the $g(r)$ peak of $\sim 0.4\mu$m for the frames to be uncorrelated on the length scales that are relevant for the pair interaction. On the other hand, this time would significantly distort the diffusing particles during three-dimensional acquisition of image stacks; we therefore restrict our analysis to two dimensions. It was shown in [184] that if care is taken to discriminate out-of-plane features, 2D data is able to reproduce the actual $g(r)$ as accurately as 3D data.

Particle centers are then located in the horizontal plane using a Python adaptation of a standard particle tracking algorithm [100, 122]. We minimize the known effect of an attractive bias for features at close distance by choosing a small long-wavelength cutoff when applying the bandpass filter to the images. Furthermore, to eliminate dim spurious features and particles out of the focal plane, we applied a minimum brightness threshold of 50% of the brightness of the in-plane features. The horizontal locating uncertainty of a diffusing particle is estimated to be 75 nm from the uncertainty due to noise, limits of the algorithm itself and the root mean square displacement (RMSD) of a particle during the time it takes to scan an individual particle. To be explicit, the RMSD during the scanning time (23 ms) of an individual particle is $\sim 80$ nm; assuming that the locating determines the average position of the diffusing particle, this gives an uncertainty of 40 nm, half the RMSD. The locating uncertainty due to noise and algorithmic limitations was determined from repeated imaging of stationary particles to be $\sim 35$ nm. The vertical resolution, i.e. vertical range around the focal plane in which particles are located, is determined to be $3.2\,\mu$m from the brightness of stationary particles as a function their out-of-plane displacement, from which we estimate a half-width at half-maximum of $1.6\,\mu$m or a full width of $3.2\,\mu$m. We expect this to be the upper limit for the vertical range.

This way, we identified typically around 40 features per frame, corrresponding to an average volume fraction of 0.27%, indicating that we indeed are in the low-volume fraction regime and can neglect many-body effects.

To study particle pair potentials, we link experimental and predicted pair correlation functions, focusing first on data taken at 3 K below the critical temperature, where critical Casimir interactions are vanishingly small and the pair potential is dominated by the electrostatic repulsion. The inverse Debye screening length $\kappa$ estimated from the added 1mM salt and the dissociated particle surface charges is $\kappa^{-1} \sim 6\,\mathrm{nm}$ (varying slightly with temperature and composition, which we take into account), which should yield a sharp increase in the $g(r)$ as shown in Fig. 3.3(a) (green curve). In contrast, the experimental $g(r)$ determined from particle tracking is much softer. This softness arises from the locating uncertainty, the polydispersity of the particles, and the effective slice thickness. To incorporate these effects we compare the experimental pair correlation function with the *projected* theoretical function $g_{\mathrm{proj}}(r' = \{x', y', z'\})$

$$g_{\mathrm{proj}}(r') = \int_{-\infty}^{\infty} \mathrm{d}z \int_{-\infty}^{\infty} \mathrm{d}y \int_{-\infty}^{\infty} \mathrm{d}x\, f_{\{0,\sigma_z\}}(z) f_{\{y',\sigma\}}(y) f_{\{x',\sigma\}}(x) g(\sqrt{x^2+y^2+z^2}), \tag{3.26}$$

in which the probability distributions $f_{\{x',\sigma\}}(x)$, $f_{\{y',\sigma\}}(y)$ and $f_{\{0,\sigma_z\}}(z)$ account for the uncertainty in the two horizontal directions and the vertical direction, respectively, with the in-plane spreads $\sigma = \sigma_x = \sigma_y$ being equal. To incorporate the different sources of uncertainty, we model them using the normal distributions

$$f_{\{\mu,\sigma\}}(x) = \frac{1}{\sqrt{2\pi}\sigma} e^{-\frac{(x-\mu)^2}{2\sigma^2}} \tag{3.27}$$

with mean $\mu$ and width $\sigma$. Note that we enforce $g(r < d) = 0$, so that no configurations with physically overlapping pairs contribute to the integral, though the *projected* result may appear to have particle overlap. The three-dimensional integral in Eq. (3.26) can be straightforwardly evaluated numerically, yet, the kernel of three normal distributions lends itself to apply a Monte-Carlo integration, where each set of random numbers can be interpreted as one realization in the experiment.

As seen in Fig. 3.3(a), this uncertainty indeed makes the $g(r)$ look much softer. We determine the values of the broadening parameters by fixing $\sigma_z = 6\sigma$ based on the optical spreads and varying $\sigma$ till a good agreement is obtained for Fig. 3.3(a). For a vanishing critical Casimir interaction this seems to be $\sigma/d = 0.067$. This number is very reasonable given the horizontal locating uncertainty of 75 nm and the particle size variation due to polydispersity of $\sim 60\,\mathrm{nm}$, giving a total variance of $\sim$ 135nm corresponding to $\sigma/d \sim 0.064$. Also $\sigma_z = 6\sigma \sim 0.8\,\mu\mathrm{m}$ is smaller than the limit for the half-width of the effective slice thickness of $1.6\mu$m, but comparable to the particle radius. More accurate fitting of the tracking uncertainties is hardly justified given the limited statistics and noise affecting the pair correlation function $g(r)$.

The broadening of the $g(r)$ holds also when critical Casimir forces act between the particles. As an example, we show pair correlations at temperatures close to

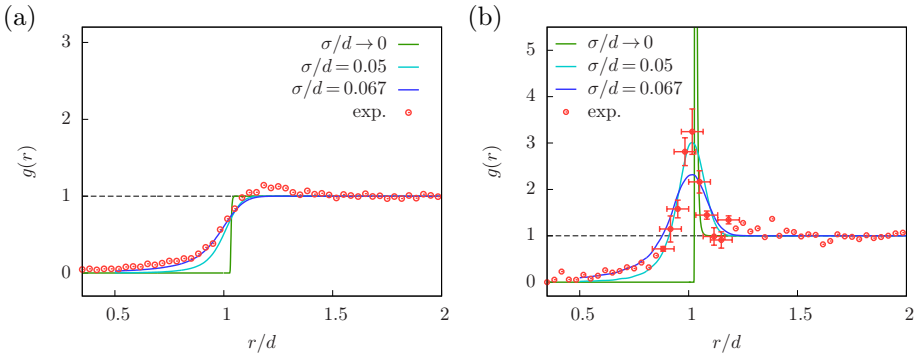


Figure 3.3: Influence of the positional uncertainty in particle tracking on the pair correlation function $g(r)$. The experimental tracking results (red points) are for $c = 28\,\%$. (a) $\Delta T = 3$ K, for which the interaction is dominated by the electrostatic repulsion. The green curve $\sigma/d \to 0$ represents the electrostatic repulsion as modeled by Eq. (3.15), with the inverse Debye length $\kappa$ being $\sim 6$ nm. The theory predicts a much sharper step than indicated by the experimental results. However, incorporating positional uncertainties due to polydispersity, optical shifts and the limited resolution of the digitized images, using Eq. (3.26) with an uncertainty $\sigma = \sigma_x = \sigma_y$ in the image plane and $\sigma_z = 6\sigma$ for the vertical resolution, results in a good agreement for $\sigma/d = 0.05$ (cyan curve) and $\sigma/d = 0.067$ ($\widehat{=}1$ px; blue curve). (b) Close to the critical point (red points: $\Delta T = 0.4$ K), the strong critical Casimir attraction results in a peak of the pair correlation function $g(r)$ at $r/d \simeq 1$. The theoretical model Eq. (3.15) ($\sigma/d \to 0$; green curve) shows only some agreement for $r/d > 1$. When incorporating the positional uncertainties with $\sigma/d = 0.05$ and $\sigma/d = 0.067$ (cyan and blue curve), the shape of the peak changes and resembles more closely the experimental results. Around the peak, we indicate the estimated error. The lateral error in the plot represents $\Delta r = 1$ px and the error $\Delta g$ is given by the standard deviation of the $g(r)$ values between sets calculated using different cutoffs for the brightness in the algorithm.

$T_c$ in Fig. 3.3(b) (red points), where we compare the experimental data with pair correlations computed from the full pair potential of Eq. (3.15). Due to the critical Casimir attraction, the pair correlation function develops a strong peak close to $r/d = 1$ (green curve). When incorporating the tracking uncertainty with $\sigma/d = 0.05$ (light blue), and $\sigma/d = 0.067$ (dark blue), the correlation peak broadens, yielding good agreement with the experimental data. The figure suggests that the smaller uncertainty $\sigma \lesssim 0.05d = 106$ nm leads to better fit, while Fig. 3.3(a) suggested that far below $T_c$, when the repulsion is dominant, the larger uncertainty of $\sigma = 0.067d = 141$ nm describes the data best. Since our interest lies in capturing the critical Casimir attraction, in the following, we generally adopt a value of $\sigma/d = 0.05$ for comparison with the experimental results.

We note that a measure insensitive to these experimental inaccuracies is given by the virial coefficient that is unaffected by the experimental broadening: In the

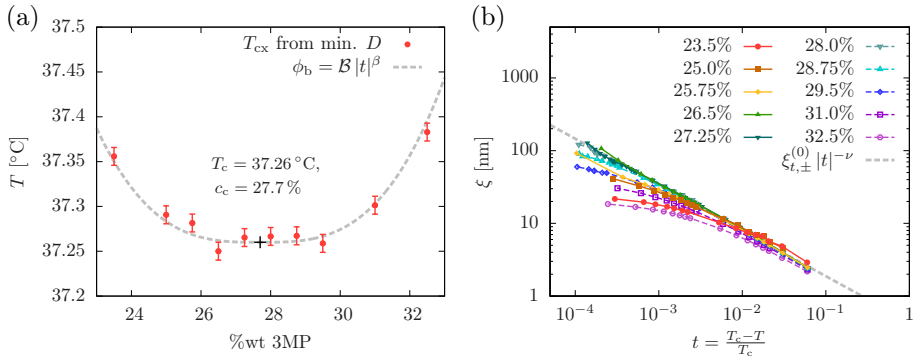


Figure 3.4: Coexistence curve and correlation length of the binary solvent determined by dynamic light scattering. (a) Phase separation temperature as defined from the minimum of the diffusion coefficient. The coexistence curve is theoretically expected to follow $\phi_b = \mathcal{B}\,|t|^\beta$ from Eq. (3.6), where $\mathcal{B}$ is a non-universal amplitude specific to the solvent. The error bars indicate the limited temperature resolution given by $\Delta T$. We find good agreement for $\mathcal{B} = 0.6$ and for the critical point at $T_c = 37.26\,°C$, $c = 27.7\,\%$ (cross symbol). (b) Correlation length $\xi$ as a function of $t = (T_c - T)/T_c$ for various compositions. For compositions around $c_c \approx 28\%$, the correlation length clearly follows the power law $\xi^{(0)}_{t,\pm}\,|t|^{-\nu}$, with $\xi^{(0)}_{t,+} = 0.44\,\text{nm}$ found from the numerical minimization. Curves for off-critical compositions bend downwards, as expected.

low-density limit where $g(r) \approx e^{-U(r)}$, the second virial coefficient is related to the radial distribution function via $B_2 = \int_V \mathrm{d}\vec{r}\,[1 - g(\vec{r})]$. One can verify that for any normalized and symmetric distribution function for $f_{\{\mu,\sigma\}}$ in Eq. (3.26), the virial coefficient of the broadened distribution $g_{\text{proj}}$, $B_{2,\text{proj}} = \int_V \mathrm{d}\vec{r}\,[1 - g_{\text{proj}}(\vec{r})]$, is identical to $B_2$. Hence, despite the choice and disparity between $g(r)$ and $g_{\text{proj}}(r)$ as input, there is only one unique thermodynamically relevant $B_2$. We have also confirmed this numerically.

# 3.4 Results

## 3.4.1 Solvent phase diagram and correlation length

The solvent phase diagram extracted from dynamic light scattering is shown in Fig. 3.4(a). The phase separation temperatures can indeed be fitted with the bulk coexistence relation $\phi_b = c - c_c = \mathcal{B}\,|t|^\beta$ from Eq. (3.6). For the fit, we have fixed the critical exponent $\beta = 0.3265$ to its theoretical value [137], and left the amplitude $\mathcal{B}$ and the coordinates of the critical point $(c_c, T_c)$ as adjustable parameters. Note that the values presented here are not based solely on fitting of the experimental coexistence data, but from a combination with further analysis below. We find $\mathcal{B} = 0.6$, close to the amplitude $\mathcal{B} \simeq 0.5$ [96] derived from the phase diagram

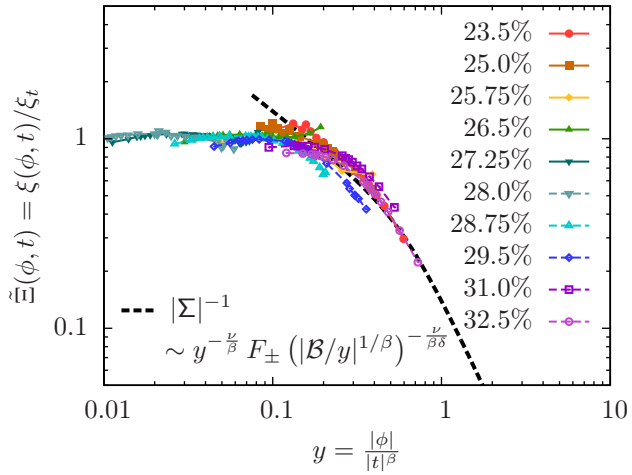


Figure 3.5: The ratio $\tilde{\Xi}(\phi,t) = \xi(\phi,t)/\xi_t$, i.e. the correlation length $\xi(\phi,t)$ normalized by the scaling law $\xi_t = \xi_{t,\pm}^{(0)} |t|^{-\nu}$. This is analogous to the scaling function $\Xi(|\Sigma|)$ in Eq. (3.4), except plotted for $y = |\phi|/|t|^{\beta}$ instead of the scaling variable $\Sigma$. There are two limiting cases, $\tilde{\Xi}(y \to 0) = 1$ and $\tilde{\Xi}(y \to \infty) = |\Sigma|^{-1}$. For the latter, $y \to \infty$, the experimental results of $\tilde{\Xi}$ are in good agreement with the linear approximation of the EOS for $\Sigma$ in Eq. (3.28) (black dashed curve), even for intermediate values of $y$.

of the pure 3MP-$D_2O$ binary mixture [170]. The coordinates of the critical point $c_c = 0.277$, $T_c = 37.26\,^{\circ}\mathrm{C}$ are slightly shifted from the literature values of $c_c = 0.28$ and $T_c \approx 38.5\,^{\circ}\mathrm{C}$ [131, 170, 181] due to the presence of salt [185, 186], which is known to lower the phase separation temperature [187].

We show the scaling of the correlation length upon approaching the critical temperature in Fig. 3.4(b). At the critical composition $c_c$, the correlation length follows the Ising power-law scaling, while for $c \neq c_c$ it deviates increasingly from this divergence, as expected. Although the divergence at the critical composition was achieved by construction (as explained in Section 3.3.1 and Appendix 3.6.2), nevertheless the success of the method is still compelling since the hereby calculated correlation length $\xi(\phi(h_b,t),t)$ reproduces the full scaling behavior with respect to solvent composition.

To show this, we consider the correlation length $\xi(\phi,t)$ normalized by that at the critical composition, $\tilde{\Xi}(\phi,t) = \xi(\phi,t)/\xi_t$; this ratio is analogous to the scaling function $\Xi(|\Sigma|)$ in Eq. (3.4), but with $\phi$ and $t$ as independent variables. Note that the relation $\Sigma(\phi,t)$, such that $\tilde{\Xi}(\phi,t) = \Xi(|\Sigma(\phi,t)|)$, corresponds to knowing the equation of state. In the linear form in Eq. (3.7), $\Sigma$ depends only on $X = t|\mathcal{B}/\phi|^{1/\beta}$. By introducing the variable $y = |\phi|/|t|^{\beta}$ given directly by the experimental state, we recast this as $X = \pm|\mathcal{B}/y|^{1/\beta}$, where the sign depends on $t$. This variable allows us to approach the critical point along the two relevant thermodynamic paths: for $y \to 0$, i.e., $|\phi| \ll |t|^{\beta}$, the critical point is approached along the critical composition ($\phi$=0) by varying the temperature $t \to 0$; in this case one expects $\xi(\phi{=}0,t) = \xi_t$ and

$\tilde{\Xi}(y \to 0) = 1$. For $y \to \infty$, where $|\phi| \gg |t|^\beta$, the critical point is approached along the critical isotherm ($t$=0) through variations of composition $\phi \to 0$. One expects that in this limit (see Eq. (3.7))

$$\tilde{\Xi}(y \to \infty) = |\Sigma|^{-1} = \tilde{B}\, y^{-\frac{\nu}{\beta}}\, F_\pm \left(|\mathcal{B}/y|^{1/\beta}\right)^{-\frac{\nu}{\beta\delta}} \tag{3.28}$$

with the amplitude [153]

$$\tilde{B} = (R_\chi \delta/Q_2)^{-\frac{\nu}{\beta(\delta-1)}} \left(Q_\xi^c/Q_\xi^+\right) \mathcal{B}^{\frac{\nu}{\beta}}$$

that contains a combination of several universal amplitude ratios. We check these predictions by plotting $\tilde{\Xi}$ as a function of $y$ in Fig. 3.5, and find very good agreement in both limits. While we cannot fully follow the limit $y \to \infty$ as this thermodynamic path is not practical in the experiment, we find that already $y > 0.1$ is sufficiently large for $\tilde{\Xi}(y)$ to start approaching the linear approximation of $|\Sigma|^{-1}$. The scaling function $F_\pm(|\mathcal{B}/y|^{1/\beta})$ in this approximation contains the non-universal amplitude $\mathcal{B}$, which we take as $\mathcal{B} = 0.6$ as determined from the coexistence curve, indicating the fundamental correspondence based on the EOS. For the amplitude $\tilde{B}$ we obtain from simple fitting $\tilde{B} = 0.15$, in good agreement with the value $\tilde{B} = 0.145$ obtained with $\mathcal{B} = 0.6$ and the amplitude ratios given in Ref. [137].

### 3.4.2 Pair potential and virial coefficient

Building upon this consistent description of the bulk properties of the liquid mixture, we now turn to the critical Casimir interactions between suspended particles. We first focus on the critical composition. Particle pair correlation functions for various temperatures are shown in Fig. 3.6. For this critical composition, we can fit all pair correlations with a single parameter $\Delta T_{\text{off}}$ that accounts for the finite surface fields, as explained in section 3.2.2. Best agreement with the dimensional approximation model (solid lines) is obtained for $\Delta T_{\text{off}} = 0.55\,\text{K}$ or a rescaling parameter $s = 0.78$, corresponding to a value of $h_s \approx 70$ for the the scaling variable of the surface field based on the short distance approximation described in Ref. [130]. Since this approximation is valid for $h_s \gtrsim 10$ and the universality class of the surface boundary conditions switches from the normal to the special transition for $h_s \to 0$, it appears the observed particles are moderately weak and still adhere to the normal universality class.

We now exploit the full solvent-composition dependence. For 3MP-rich compositions ($c > c_c$), the particles aggregate as far as 1 °C below the critical temperature, indicating strong attraction, while for 3MP poor compositions ($c < c_c$), this temperature interval of aggregation is very small and diminishes until aggregation is no longer observed. This is in agreement with the well-known fact that the attraction is strong in solvents poor in the component preferred by the particles. To compare with theoretical predictions, we take advantage of the internally calibrated correlation length to compute the critical Casimir attraction, and we add the electrostatic

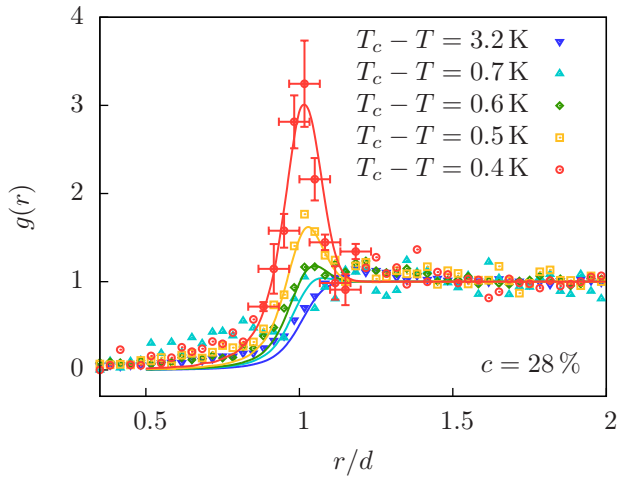


Figure 3.6: Pair correlation function $g(r)$ for solvent composition $c = 28\,\%$, close to the critical composition, for different temperatures. The experimental results (symbols and error bars) are compared to results of the pair potential model Eq. (3.15) using the dimensional approximation for the scaling function $\Theta^{(d=3,Derj)}$, and using Eq. (3.26) to account for the experimental broadening (solid lines). A temperature offset of $\Delta T_{\mathrm{off}} \approx 0.55\,\mathrm{K}$ was used to account for the weak hydrophilic adsorption preference of the particles.

repulsion obtained from pair correlation measurements sufficiently far from $T_c$. In principle, there are no other remaining parameters in the case of strong adsorption. To account for the weak hydrophilic adsorption preferences of our particles, we again use the effective temperature offset $t_{\mathrm{off}}$, which depends on the solvent composition. We find that even for off-critical compositions we can fit all pair correlation functions for the different temperatures using the single parameter $t_{\mathrm{off}}$ varying systematically with composition. We show examples of measured and predicted pair correlation functions for a composition to the left and right of the critical point in Fig. 3.7. In both cases, good agreement is observed for all temperatures. The resulting predicted pair potentials are also shown. Note the difference in horizontal scale between the observed radial distributions and the predicted pair potentials due to the experimental broadening.

The particle aggregation behavior provides an independent check of the validity of the model based on the colloidal state not affected by any quantitative uncertainties of particle tracking. Theoretically, we can predict where aggregation occurs from the second virial coefficient $B_2$ (see Sec. 3.2.3) following the argument in Ref. [153], while experimentally, we can observe the onset of aggregation directly. We compare the theoretical curve for the onset of aggregation, as obtained from the critical value $B_2^* = -1.2$ of the sticky sphere model, with the experimental aggregation points in Fig. 3.8. Very good agreement is observed. In particular, the asymmetry of the

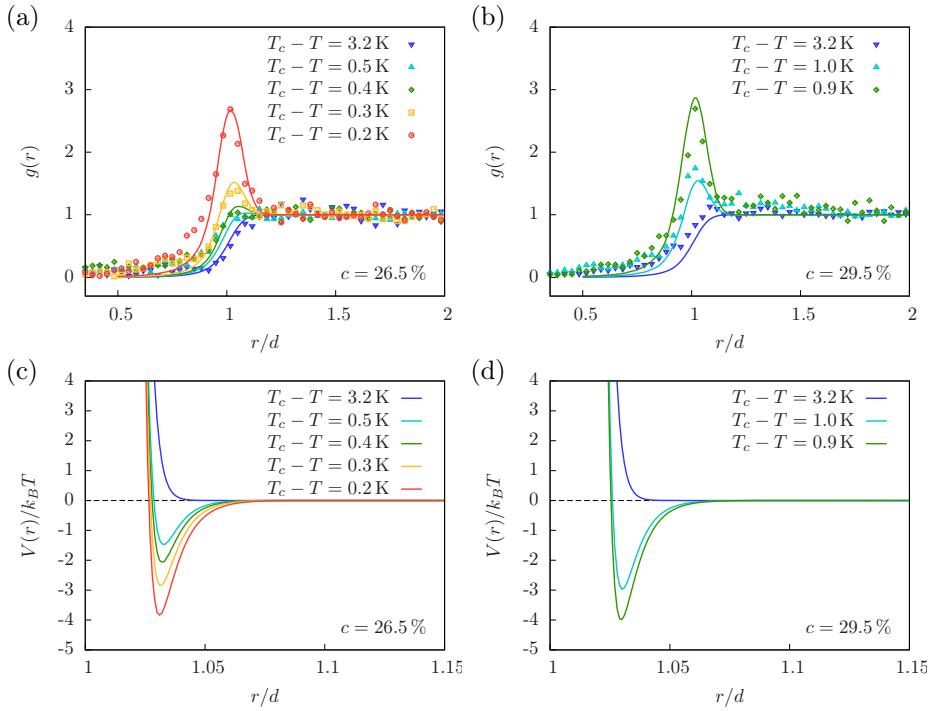


Figure 3.7: (a) and (b): Pair correlation function $g(r)$ for the off-critical compositions $c = 26.5\,\%$ (with $\Delta T_{\mathrm{off}} = 0.7\,\mathrm{K}$) and $c = 29.5\,\%$ (with $\Delta T_{\mathrm{off}} = 0.18\,\mathrm{K}$). The experimental results (points) are compared to the dimensional approximation (solid lines). (c) and (d) Theoretically predicted pair potentials $U(r) = V(r)/k_bT$ for the same composition.

aggregation region is very well reproduced. We also indicate the aggregation region predicted for the case of strong adsorption, i.e. for vanishing $t_{\mathrm{off}}$ (black dashed curve). As expected, it extends further below $T_c$, as strongly adsorbing particles exhibit a stronger attraction. Yet, the shape of the aggregation region, especially its pronounced asymmetry, does not change qualitatively.

We investigated particle pair interactions just below aggregation in more detail. Taking advantage of the fact that the virial coefficient is unaffected by the experimental broadening as it is based on the integrated pair potential, we can compare virial coefficients computed from the raw measured $g(r)$ directly with theoretical predictions without any need to account for experimental inaccuracy and particle polydispersity. In fact, one can show that any distorting influence described by normalized symmetric distribution functions, such as the optical broadening, leaves the second virial coefficient unchanged (see Sec. 3.3.3). We therefore compute experimental $B_2$ values directly by numerically integrating the measured $g(r)$. Specifically, we calculate the reduced second virial coefficient $B_2^* = B_2/B_2^{(hs)}$ (see Sections 3.2.3 and 3.3.3)

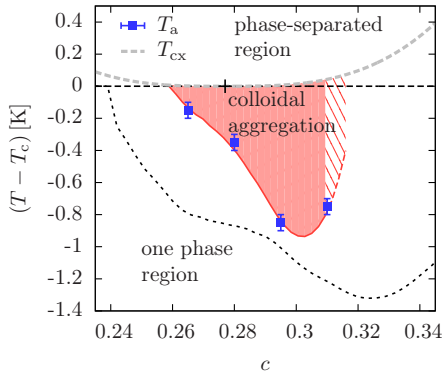


Figure 3.8: Phase diagram showing the coexistence curve $T_{cx}$ and the experimentally observed aggregation points $T_a$, compared to the $B_2$ isoline with the critical value $B_{2,\mathrm{crit}} = -1.2$ of the sticky sphere model. The critical point is marked by a cross symbol. Within the shaded area, colloids aggregate and the pair potential cannot be measured experimentally. In the hatched part, $B_2$ is determined based on a polynomial extrapolation of $t_{\mathrm{off}}$ beyond the experimental range, which may not resemble the actual shape of the colloidal aggregation region. The black dotted curve indicates the aggregation line predicted for strongly adsorbing particles.

in the low-density limit, by numerically integrating $B_2 = 2\pi \int_0^\infty \mathrm{d}r\, r^2\,(1 - g(r))$. In order to treat the limited experimental data range, we assume $g(r < r_0) = 0$ below the smallest distance $r_0$ of the data set, and we apply a smoothing factor to $g(r)$ for large separations.

Experimental and theoretical values of $B_2^*$ in the entire temperature-composition plane are compared in Fig. 3.9(a). The color map indicates the theoretically predicted values, while colored dots along the experimental compositions (dashed lines) indicate the measured values. Good qualitative agreement is observed. For quantitative comparison, we plot $B_2^*$ values as a function of temperature in Fig. 3.9(b). The bottom panel shows $B_2^*$ values superimposed for the different solvent compositions, while the top panel shows the same data shifted vertically for clarity, providing a perspective view of the $B_2^*$ values above the temperature-composition plane. Experimental data (dots) and theoretical predictions (lines) show very good agreement for all compositions. The values $B_2^* = 1$ far below the critical temperature indicate the system is dominated by a short-range repulsion, described by an effective hard-core model. Starting from $T - T_c \sim 1\,\mathrm{K}$ at solvent compositions of around $c \sim 30\,\%$, $B_2^*$ quickly drops to negative values, indicating the rise of an attractive critical Casimir interaction. This is in line with previous studies of the virial coefficient close to the critical point [188, 189]. The comparison based directly on the raw measurements provides good evidence that it is indeed the critical Casimir interactions that underlie the colloidal attraction in the investigated solvent composition range. Hence, this direct comparison suggests that not only at the critical composition, but also at these

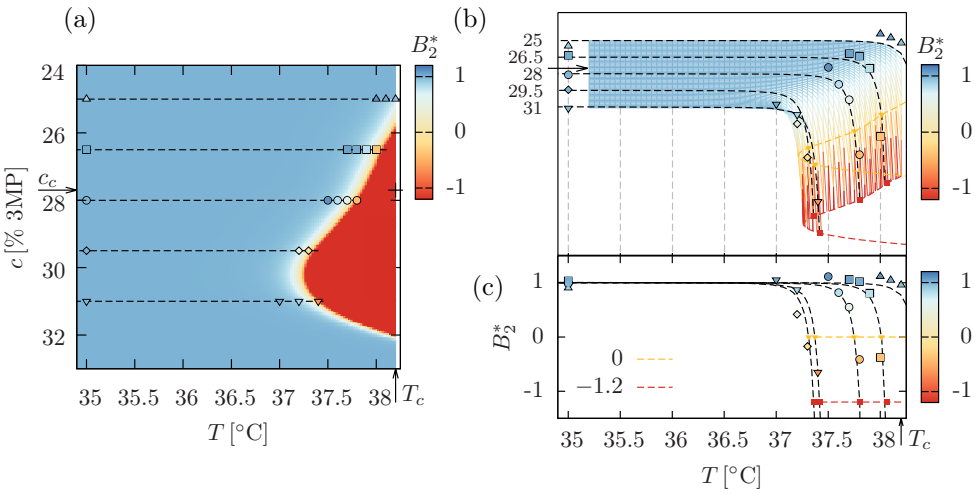


Figure 3.9: Composition and temperature dependence of the reduced second virial coefficient from measured $g(r)$ (symbols) and from theory (lines and colored surface). (a) Color map in the temperature-composition plane indicates theoretically predicted, and colored symbols experimental $B_2^*$ values. Values $B_2^* \sim 1$ depicted in blue indicate a significant repulsion, while values $B_2^* \sim -1$ depicted in red indicate strong attraction. Yellow marks the crossover. Also indicated by arrows are the critical temperature $T_c$ and composition $c_c$, and the critical point (cross symbol). (b, c) $B_2^*$ values as a function of temperature along the experimental solvent compositions (dashed lines in (a)). Values in (c) are shifted vertically, providing a perspective view on the temperature-composition plane in (a). Dashed yellow and red lines indicate isolines of $B_2^* = 0$ and $B_2^* = -1.2$, marking, respectively, the crossover from repulsion to attraction, and the critical value of the sticky spheres model.

off-critical compositions, the attraction is described in terms of a critical Casimir force rather than by wetting effects. Yet, at even higher off-critical compositions, wetting effects are expected to eventually take over and dominate the attraction as clearly observed in Ref. [123].

We finally highlight the composition dependence of particle interactions by showing the theoretically calculated pair potentials for two fixed temperatures in Fig. 3.10. As already observed for the virial coefficients, the strongest attraction occurs for compositions $c = 29.5 - 31\,\%$, well above the critical composition $c_c = 27.7\,\%$. For $\Delta T = 1.0\,\mathrm{K}$ (Fig. 3.10(a)), the interaction is still small at $c = 28\,\% \approx c_c$ and below, whereas at higher composition $c > c_c$, the critical Casimir force leads to a notable attractive potential well. The depth of the potential minimum for $c = 29.5\,\%$ becomes close to $-3\,k_BT$, but no aggregation is yet observed (compare Fig. 3.8). For

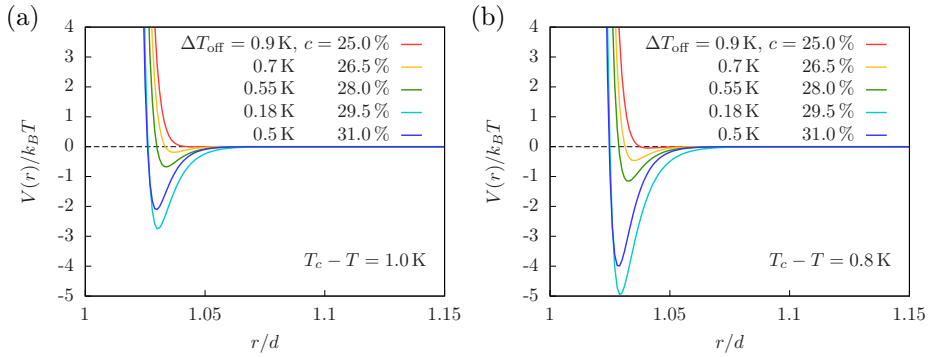


Figure 3.10: Pair potential $U(r) = V(r)/k_bT$ predicted by the dimensional approximation, for different compositions at fixed temperature $T_c - T = 1.0\,\text{K}$ (a) and $T_c - T = 0.8\,\text{K}$ (b).

$\Delta T = 0.8\,\text{K}$ (Fig. 3.10(b)), the depth of the potential minimum has increased considerably, exceeding $-3\,k_BT$ for $c = 29.5\,\%$ and $c = 31.0\,\%$, leading to aggregation in the experiment. For the critical composition $c = 28\,\%$ and below, the attraction is still small. We find that the criteria $B_2^* \lesssim 1.2$ of the sticky sphere model provides a quantitatively good estimate for the onset of aggregation, while the earlier, simple criteria that the depth of the potential minimum exceeds $-3\,k_BT$ [158], is qualitatively in line with our findings, but may not provide a quantitatively reliable estimate.

Furthermore, Fig. 3.10 reports the parameters $\Delta T_{\text{off}}$ for each composition for which we have obtained the best agreement between the experimental $g(r)$ and the theoretical predictions. As discussed in section 3.2.2, $\Delta T_{\text{off}}$ is an effective rescaling in the case of weakly adsorbing particles. Thus, the same systematic trend carries over to the scaling parameter $s(h_s, h_b)$. To our knowledge, the dependence of $s$ on $h_b$ has not been studied yet (see Ref. [130] for $s(h_s) = s(h_s, h_b = 0)$). Our measurements indicate a systematic dependence that itself is asymmetric around the critical composition, i.e., the behavior depends strongly on the signs of $h_s$ and $h_b$. Further studies could focus on the dependence of colloidal aggregation on the strength of the surface adsorption.

## 3.5 Conclusion

We investigated the interactions of colloidal particles in near-critical binary solvents by internally calibrated measurements and theoretical modeling. Across the entire solvent composition range investigated, we find good agreement between particle pair correlation measurements and an effective theoretical model of critical Casimir interactions using an offset temperature $\Delta T_{\text{off}}$ to account for the weak surface adsorption of the particles. It is known that at the critical composition, the influence of

weakly adsorbing surface fields amounts to a rescaling of the scaling function of the potential. We thus expect that the rescaling holds also at off-critical concentrations, albeit with a rescaling value $s$ dependent on the composition of the system. We find that within the experimentally accessible range, $s$ and $\Delta T_{\text{off}}$ provide alternative parameters that fit the experimental data equally well. The benefit of the effective temperature offset $\Delta T_{\text{off}}$ is that it offers an intuitive interpretation of the experimental data. The good agreement between theory and measurements we observe here for all temperatures with a systematically composition-dependent rescaling parameter suggests that it is indeed a critical fluctuation force, i.e. the critical Casimir force, that dominates the particle attraction in the investigated near-critical regime. Our results hence extend the validity of the critical Casimir description from critical to off-critical compositions in the near-critical regime. The adsorption preference dependence of the critical Casimir force highlighted here provides a powerful means to realize attractive patchy particle systems, and binary or ternary particle systems. Because the adsorption preference can be tuned by chemical surface modification or the addition of salt, this allows tuning colloidal interactions A-A, A-B, B-B, etc. between specific particle pairs (A,B) or between particle patch (A) and bulk (B), for realizing and designing complex bonded colloidal materials.

# 3.6 Appendix

## 3.6.1 Choice of order parameter

There is a freedom of choice in the definition of the order parameter. For a binary liquid mixture, several closely related and equally measurable quantities can be considered: mass, volume, molar and number concentration. In the analysis of the experimental results, we employ mass fraction of 3MP, denoted by $c_a^{(wt)}$ within this appendix. From a microscopic point of view, the number fraction $c_a^{(n)}$ may appear to be the more fundamental choice. One can convert between the latter two choices, using the molar masses $M_a$ and $M_b$ of the two components $a$ and $b$, via

$$c_a^{(wt)} = \frac{c_a^{(n)} M_a}{c_a^{(n)} M_a + c_b^{(n)} M_b} = \frac{c_a^{(n)} \Omega}{c_a^{(n)} (\Omega - 1) + 1}, \tag{3.29}$$

with $\Omega = M_a/M_b$. For the specific mixture of 3-methylpyridine and heavy water, one has $M_a = M_{3MP} = 93.13\,\text{g/mol}$ and $M_a = M_{D_2O} = 20.03\,\text{g/mol}$, so that $\Omega = 4.65$. Note that the two choices for the order parameter are not proportional to each other.

For the OP, it is required that $c_a^{(wt)} - c_{a,c}^{(wt)} = \pm \mathcal{B}_{wt} |t|^\beta$ for $t \to 0$. Using this in Eq. (3.29) we find

$$\frac{\Omega (c_a^{(n)} - c_{a,c}^{(n)})}{[(\Omega - 1) c_a^{(n)} + 1][(\Omega - 1) c_{a,c}^{(n)} + 1]} = \pm \mathcal{B}_{wt} |t|^\beta \text{ for } t \to 0. \tag{3.30}$$

Using the fact that $c_a^{(n)} - c_{a,c}^{(n)}$ can also serve as the OP, it follows that $c_a^{(n)} - c_{a,c}^{(n)} = \pm\mathcal{B}_n\,|t|^\beta$ and

$$\frac{\Omega\,\mathcal{B}_n|t|^\beta}{[(\Omega-1)(c_{a,c}^{(n)} \pm \mathcal{B}_n\,|t|^\beta)+1][(\Omega-1)c_{a,c}^{(n)}+1]} = \mathcal{B}_{wt}\,|t|^\beta, \text{ for } t \to 0. \tag{3.31}$$

so that

$$\begin{aligned}\lim_{t\to 0}\mathcal{B}_{wt} &= \lim_{t\to 0}\frac{\Omega\,\mathcal{B}_n}{[(\Omega-1)c_{a,c}^{(n)}+1]^2 \pm \mathcal{B}_n\,|t|^\beta[(\Omega-1)^2 c_{a,c}^{(n)}+\Omega-1]} \\ &= \frac{\Omega}{[(\Omega-1)c_a^{(n)}+1]^2}\,\mathcal{B}_n \\ &= \Omega[1+(\Omega^{-1}-1)c_a^{(wt)}]^2\,\mathcal{B}_n.\end{aligned} \tag{3.32}$$

Thus, close to the critical point, the two non-universal amplitudes $\mathcal{B}_{wt}$ and $\mathcal{B}_n$ can be still considered to be different normalizations of the OP.

We have checked that plotting the phase separation temperatures in terms of the mole fraction and then fitting the coexistence curve (see Fig. 3.4) yields the value for $\mathcal{B}_n$ that is in agreement with Eq. (3.32). Note that for concentrations far off the critical one, the different choices for the OP would be reflected in the equation of state Eq. (3.5). However, we consider it only in the linearized form, which is valid in the vicinity to the critical point.

### 3.6.2 Extended discussion of the methods for determining the correlation length

**Full expressions relating diffusion coefficient to correlation length**

The crossover function $H$ as worked out by Bhattacharjee et. al. [176] is given by

$$\begin{aligned}H(\xi, q_D, q_C) = \frac{1}{12}\sin(3\,\psi_D) - \frac{1}{4\,q_C\,\xi}\sin(2\,\psi_D) + \frac{1}{(q_C\,\xi)^2}\left(1-\frac{5}{4}(q_C\,\xi)^2\right)\sin(\psi_D) \\ - \frac{1}{(q_C\,\xi)^3}\left[\left(1-\frac{3}{2}(q_C\,\xi)^2\right)\psi_D - |(q_C\,\xi)^2-1|^{3/2}L(\omega)\right],\end{aligned} \tag{3.33}$$

with,

$$w = \left|\frac{q_C\,\xi-1}{q_C\,\xi+1}\right|^{1/2}\tan\left(\frac{\psi_D}{2}\right), \quad \text{and,} \quad \psi_D = \arccos\left(\frac{1}{\sqrt{1+q_D^2\,\xi^2}}\right), \tag{3.34}$$

and,

$$L(\omega) = \begin{cases}\ln\left(\frac{1+\omega}{1-\omega}\right), & \text{for } q_C\,\xi > 1 \\ 2\arctan(|\omega|), & \text{for } q_C\,\xi < 1\end{cases} \tag{3.35}$$

The crossover function $H$ can be more conveniently expressed in terms of the ratio $Q_0\,\xi$ of the viscosity wave number in terms of the correlation length and $q_D/q_C$ indicating the strength of the background contribution (see Eq.(3.22)). From the relation $Q_0^{-1} = (1/2)\,e^{4/3}\left(q_c^{-1} + q_D^{-1}\right)$ [176, 178, 179], the substitutions

$$q_D\,\xi \mapsto \frac{1}{2}\,e^{4/3}\,Q_0\,\xi\left(1 + \frac{q_D}{q_C}\right), \tag{3.36}$$

$$q_C\,\xi \mapsto \frac{1}{2}\,e^{4/3}\,Q_0\,\xi\left(1 + \left(\frac{q_D}{q_C}\right)^{-1}\right) \tag{3.37}$$

in terms of $Q_0\,\xi$ and $q_D/q_C$ follow.

Therefore, using Eqs. (3.20, 3.23) and (3.24), the full diffusion coefficient amounts to

$$D(\xi,\phi,T;Q_0,q_D/q_C) = \frac{k_B T}{6\pi\,\eta_{\mathrm{bg}}(\phi,T)\,\xi}\times \left[\mathcal{R}\,\frac{K(q\,\xi)\left(1+b^2(q\,\xi)^2\right)^{z/2}}{\exp(z\,H(Q_0\,\xi,q_D/q_c))} + \frac{1+(q\,\xi)^2}{\frac{8}{6\pi}\,e^{4/3}\,Q_0\,\xi\,(1+(q_D/q_C)^{-1})}\right] \tag{3.38}$$

**Calculation of the correlation length**

The computational task at hand is determining from Eq. (3.38) inversely the correlation length $\xi$ that yields the same diffusion coefficient as experimentally determined. Apart from the known experimental state $(\phi, T)$, the arguments $Q_0$ and $q_D/q_c$ are unknown and need to be determined simultaneously. In order to find optimal values for $Q_0$ and $q_D/q_c$ we implement an iterative approach inspired by Ref. [131]. In our approach we assume $Q_0$ and $q_D/q_c$ to be independent of $\phi$ and $T$. This means that the dependence of viscosity on the closeness to critical point is fully described by the $\xi$. We then determine the optimal $Q_0$ and $q_D/q_c$ values as the ones that give the best agreement of the resulting $\xi$ with the power law $\xi_t = \xi_{t,+}^{(0)}\,|t|^{-\nu}$ for compositions around $c \approx 0.28$. More specifically, we minimize the least-square deviation of the logarithmic values

$$\sum_i \left(\log\xi_i - \log\left(\xi_{t,+}^{(0)}\,\left|\frac{T_c - T_i}{T_c}\right|^{-0.63}\right)\right)^2,$$

for all $\{\xi_i, T_i\}$ data points of the 27.25% and 28% samples. Note that we fix the critical exponent $\nu = 0.63$ but leave $\xi_{t,+}^{(0)}$ to be optimized. Close to the critical point, as the value of the diffusion coefficient drops, the relative experimental error increases significantly; due to the sensitivity of our procedure to these errors, we disregard samples with $t < 10^{-4}$. One interesting observation is that the procedure becomes more resilient against these experimental errors for $\mathcal{R} > 1$, indicating that the critical part of the diffusion coefficient as given in Eq. (3.23) is indeed more

appropriate than a simple Stokes-Einstein relation ($\mathcal{R} = 1$) (see Appendix 3.6.2). As consistency checks, we have tested three variants: first, we have varied only $Q_0$ for $q_D/q_c = 0$, i.e. for vanishing background, with the additional constrain that $Q_0\,\xi_{t,+}^{(0)} = 0.15$. This value was taken from Ref. [181] where it was found by fitting to experimental data of the critical contribution to the viscosity. We find an optimal fit with $Q_0 = 0.36\text{nm}^{-1}$ and $\xi_{t,+}^{(0)} = 0.42\,\text{nm}$. In the second case, we have minimized for both $Q_0$ and $\xi_{t,+}^{(0)}$, still keeping $q_D/q_c = 0$. This yields $Q_0 = 0.22\,\text{nm}^{-1}$ and $\xi_{t,+}^{(0)} = 0.435\,\text{nm}$, so that $Q_0\,\xi_t^{(0)} = 0.096$. Lastly, we have allowed for a finite value of $q_D/q_c$, yielding the best agreement with $Q_0 = 0.17\,\text{nm}^{-1}$, $\xi_{t,+}^{(0)} = 0.44\,\text{nm}$ and $q_D/q_c = 0.235$, so that $Q_0\,\xi_{t,+}^{(0)} = 0.075$. In order to validate our approach we note that the values for $Q_0\,\xi_{t,+}^{(0)}$ that we obtain in the second and third case are not far removed from this in the first case; small changes can be expected because our mixtures contain salt [131, 186].

**Comparisons of viscosity values for three different fitting procedures**

In this work, the primary purpose of the crossover function $H(Q_0\,\xi, q_D/q_C)$ is to determine the correlation length $\xi$ from the diffusion coefficient. However, we want to point out a further application as a means to indirectly measure the viscosity ratio. This serves also as an consistency check for our fitting procedure.

Assuming the power law $\xi_t = \xi_{t,+}^{(0)}\,|t|^{-\nu}$, the viscosity ratio in Eq. (3.22) depends only on the fitting values $Q_0\,\xi_{t,+}^{(0)}$ and $q_D/q_c$.

The resulting viscosities for the present mixture, based on the three fitting variants discussed in Appendix 3.6.2, are shown in Fig. 3.11. Overall our estimates are slightly below the viscosity data of Ref. [181] for the pure binary mixture 3MP-$D_2O$. Still, we find reassurance in the overall agreement, since estimating the viscosity is not the primary focus of this procedure.

**Critical Diffusion coefficient**

Here, we argue why the expression given by Eq. (3.38), which is dominated by the critical part in Eq. (3.23), reproduces the behavior of the measured diffusion coefficient given in Fig. 3.2(b). In literature, Eq. (3.23) is often called a (pseudo-)Stokes-Einstein relation, especially when setting $\mathcal{R} = 1$ [179]. However, this is more of an analogue than a rigorous statement, as the self-diffusion of the OP is not governed by the same relation as the Brownian motion. If we naïvely assume the Stokes-Einstein relation in which the radius of the Brownian particles is replaced with the size of the correlated scattering features, i.e., the correlation length $\xi$, so that

$$D = \frac{k_B T}{6\pi\eta\xi}, \tag{3.39}$$

we obtain inconsistent results: as we know that $\xi$ is a power law of $t$ close to $T_c$, we would then expect that $D$ also follows a power law, i.e., a straight line in Fig. 3.2.

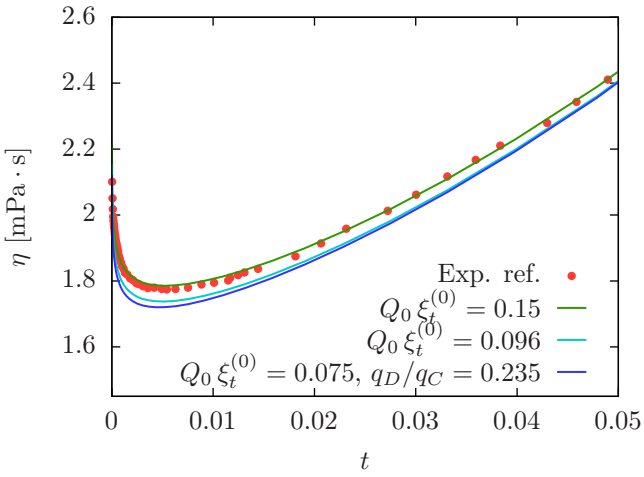


Figure 3.11: Estimated viscosity of the present mixture 3MP / heavy water with 1mM KCl at the critical weight fraction $c \approx 0.28$, based on values from the fitting procedure of the diffusion coefficient (see appendix). The experimental values of Ref. [181] are for the pure binary mixture without salt.

However, we find that instead $D$ flattens out and approaches a constant value upon decreasing $t$. In contrast, saturation of $D$ is captured correctly by Eq. (3.23). In the critical limit $x = q\,\xi \gg 1$ one has $K(x) \propto x$ [190] and $H(Q_0\,\xi \to \infty, q_D/q_c) = \ln(Q_0\,\xi)$ [176], so that

$$\lim_{\xi\to\infty} D_\mathrm{c} = \frac{\mathcal{R}\,k_B T}{6\pi\,\eta_\mathrm{bg}\,Q_0^z\,\xi^{1+z}}\,b^z (q\,\xi)^{1+z} = \text{const.}, \tag{3.40}$$

leading to a saturation of the diffusion coefficient at $T = T_c$, as observed in the experiments. Note that it is sufficient to look at $D_\mathrm{c}$ to explain this saturation since the background $D_\mathrm{bg}$ given by Eq. (3.24) becomes negligible for large $\xi$. $D_\mathrm{bg}$ contributes to the deviation from a power law that is observed for large $t$, due to effects of the viscosity on a different, non-critical temperature scale.

For our fitting procedure, we have used newer estimates that give as the value of the universal amplitude $\mathcal{R} = 1.05$ [178, 179]. This slight deviation from 1 is of significant importance. Since $\lim_{\xi\to\infty} D_c = \text{const.}$, the diffusion coefficient becomes insensitive to the actual value of the correlation length, but is still proportional to the universal amplitude $\mathcal{R}$. Conversely, in our procedure we find for $\mathcal{R} = 1$ widely varying results for the correlation length $\xi$, amplifying small experimental errors of the diffusion coefficient. These issues are significantly reduced for $\mathcal{R} = 1.05$, supporting the finding that the universal amplitude $\mathcal{R} > 1$. In consequence, there is no particular limit in which the Stokes-Einstein relation in Eq. (3.39) can be obtained from Eq. (3.23).

CHAPTER 4

# Stochastic buckling of a chain of isotropic colloids

*The vast majority of soft and biological materials, gels and tissues, are made from micrometer-size, slender structures such as bio filaments, colloidal and molecular chains, which are believed to crucially control their mechanics. These constituents show intriguing extreme mechanics, mechanical instabilities and plasticity, which besides attracting significant theoretical attention, have not been studied experimentally, and as such remain poorly understood. Here, we investigate, by experiments, simulations and theory, the mechanical instabilities of a slender, self-assembled colloidal structure, observing a novel form of stochastic buckling, where thermal fluctuations and associated entropic force effects are amplified by the vicinity of a buckling instability. We fully characterize how the persistence length and plasticity controls the stochastic buckling transition, leading to intriguing higher-order buckling modes. These results elucidate the interplay of geometrical, thermal and plastic interactions in the nonlinear mechanics of thermal, self-assembled structures, crucial to the mechanical response and function of fiber-based soft and biological materials, as well as the rational design of novel micro- and nanoscale architectures.*

# 4.1 Introduction

Due to recent advances in colloidal synthesis and interaction control, colloidal self-assembly has become a promising platform for designer materials with controlled internal architecture and tunable physical properties [28, 38, 191], such as unprecedented photonic [192], shape-changing [15, 55] and mechanical properties [193]. Self-assembled colloidal structures also form excellent model systems to describe complex and biological materials like gels [194, 195], biological cell membranes [196] and filaments [197, 198], or flocking behavior [102]. To date, there has been an extensive focus on the dynamical and structural aspects of self-assembly [65, 199], while the mechanical instabilities of self-assembled objects have been experimentally much less explored; yet, they play a crucial role in the response of soft materials [200–202] from biological networks [68] to mechanical metamaterials [70]. Semi-flexible biofilaments, polymers and biological shells have been shown to undergo signatures of mechanical instabilities [203, 204], on which thermal excitations can have an important effect [205–209]. However, experimental insight into these instabilities in synthetic architectures such as colloidal assemblies is lacking. In particular, potentially crucial factors such as the effective elastic interactions, the role of geometric non-linearities, stochastic noise and plasticity are virtually unexplored.

Here, we focus on the simplest and most widespread form of a mechanical instability on the simplest form of a self-assembled structure: the buckling of an initially straight colloidal chain upon compression. Combining optical tweezer and microscopy experiments, molecular dynamics simulations and theory, we observe that such thermal chain undergoes an elastic buckling instability upon compression, accompanied by divergence of thermal bending fluctuations. Molecular dynamics simulations and continuum modelling allow identifying the critical exponents, and exploring entropic effects in the full range of persistence length, from stiff to the freely jointed chain. Finally, we show that plastic rearrangements lead to localized deformation at higher compression that can lead to buckling into higher-order modes. These results, uncovering the nature of mechanical instabilities in self-assembled structures, provide a crucial step towards understanding the complex mechanics of soft architectures, central to the mechanical function of biological materials and the design of functional colloidal materials.

# 4.2 Methods

## 4.2.1 Experiments

Our system consists of copolymer particles [72] that we assemble into chains using temperature-dependent critical Casimir attractions [82]. The attractive force arises from the confinement of fluctuations of a binary solvent between the surfaces of the colloidal particles. The particles have a radius of $r = 1.25\mu$m and are suspended in a binary solvent of lutidine and water with lutidine weight fraction $c_L = 0.32$ and

with 5mM potassium chloride, in which they sediment into a quasi two-dimensional layer. Salt (5mM potassium chloride) is added to screen the electrostatic repulsion. By setting the temperature to $\Delta T = 5.5°\text{C}$ below the critical temperature $T_c = 33.6°\text{C}$, we induce an attraction with potential depth $E \sim 10k_BT$ and range $\sim 0.01r$ that causes assembly of the particles. We use optical tweezers to grab the ends of assembled colloidal chains.

For the optical tweezers, laser light of 1064nm was used at a power of $20 \pm 5$mW. The trap constants were determined by tracking the Brownian movement of a single colloidal particle in the trap and fitting its displacements from the trap center with a gaussian distribution to obtain the standard deviation $\sigma_{trap}$. We used a long measurement time such that the out-of-trap displacements become Boltzmann distributed. Assuming a harmonic trap, the trap constant is then determined by $k = kT/\sigma^2_{trap}$. We obtain $k = 0.9 \pm 0.2\text{pN}/\mu\text{m}$, where the error is estimated based on the locating accuracy of $\epsilon_{track} = 0.02\mu$m. The partial absorption of the laser light by the binary solvent causes a local heating of 0.5K at the trap. This was determined by measuring the temperature at which phase separation occurs in the laser focus and subtracting that from the phase separation temperature when the laser is turned off. This temperature increase is expected to cause a slight increase of the critical Casimir attraction close to the trapped bead.

We used two optical tweezers to push on the colloidal chain as follows: Starting from a straight chain, we apply a compressive displacement $u$ by moving one of the optical tweezers at a constant rate of 27nm/s towards the other. We then image the individual particles at a frame rate of $20s^{-1}$, and locate their centers in the image plane with an accuracy of 20nm using particle-tracking software [122]. In addition, we measure the force exerted on the chain from the bead displacement out of the static trap using $F = k(y - y_{trap})$, where $y$ and $y_{trap}$ are the positions of the trapped bead and trap center, respectively. We define $L$ as the end-to-end distance of the chain, and $L_0 = 24.7 \pm 0.1\mu$m as the end-to-end distance for vanishing force $F = 0$.

### 4.2.2 Molecular dynamics simulations

We support our experiments with molecular dynamics simulations of the buckling of a colloidal chain. Colloidal particles with position $\boldsymbol{r_i}$ in an assembled chain satisfy the Langevin equation:

$$m\ddot{\boldsymbol{r}}_i = -\frac{kT}{D}\dot{\boldsymbol{r}} - \nabla_{\mathbf{r}_i} V + \sqrt{2D}\xi \tag{4.1}$$

with $D = kT/\gamma$ the diffusion coefficient, $\gamma$ the viscous drag coefficient, $\xi$ a normalised stochastic force, and

$$V = \frac{k}{2} d_0^2 \sum_{i=1}^{N-1} (\epsilon_i - 1)^2 + \frac{k_\theta}{2} \sum_{i=1}^{N-2} (\theta_i - \theta_{i,0})^2, \tag{4.2}$$

where $d_0$ is the equilibrium bond distance, $\theta_{i,0}$ the equilibrium angle, $\epsilon_i = |\boldsymbol{r}_{i+1} - \boldsymbol{r}_i|/d_0 - 1$ and $\cos(\theta_i) = (\boldsymbol{r}_{i+2} - \boldsymbol{r}_{i+1}) \cdot (\boldsymbol{r}_{i+1} - \boldsymbol{r}_i)/|\boldsymbol{r}_{i+2} - \boldsymbol{r}_{i+1}||\boldsymbol{r}_{i+1} - \boldsymbol{r}_i|$. On

timescales $\Delta t > \frac{mD}{kT}$ the Langevin equation can be considered overdamped and reduces,

$$\dot{\boldsymbol{r}}_i = -\frac{D}{k_B T}\nabla_{\mathbf{r}_i} V + \sqrt{2D}\xi. \tag{4.3}$$

These can be simulated by molecular dynamics simulations following the Ermak-McCammon equation [31]:

$$\boldsymbol{r}_i(t+\Delta t) - \boldsymbol{r}_i(t) = -\frac{D}{kT}\nabla_{\mathbf{r}_i} V \Delta t + \sqrt{2D\Delta t}\xi, \tag{4.4}$$

We simulate an infinitely stiff trap by fixing the positions of the two end particles. Trap movement is then implemented by moving one end particle towards the other.

Time, length and energy were expressed in natural units such that $t_D = d_0^2/D = 1\mathrm{t_D}$, $kT = 1\mathrm{kT}$, $d_0 = 1\mathrm{d_0}$. In all simulations the timestep was set to $\Delta t = 2^{-16}\mathrm{t_D}$ which is small enough to have a stable integration. In order to compare with experiments all quantities where later rescaled using the experimental values $D = 0.138\mu\mathrm{m}^2/\mathrm{s}$, $kT = 4.14 \times 10^{-21}\mathrm{J}$ corresponding to $\sim 0.004\mathrm{pN}\mu\mathrm{m}$, and $d_0 = 2.74\mu\mathrm{m}$.

The experimental values of the bending and stretching stiffness as determined from the experimental force are, respectively, $k_\theta = 1048\mathrm{kT}$, and $k = 14760\mathrm{kT/d_0^2}$. To simulate the compression experiment, we moved the trap in 128 steps of $\Delta u = 0.01\mathrm{d_0}$ starting from $u_i = -0.3\mathrm{d_0}$, with a waiting time of $t_{step} = 32\mathrm{t_D}$ at each step. This gives a similar total displacement as the experiment. The compression speed is much lower than in the experiments in order to obtain better statistics. For the analysis, we disregarded the first $8\mathrm{t_D}$ after each trap displacement to allow for equilibration. In experimental units, this entire ramp translates to a total displacement of $u_{tot} = 3.5\mu\mathrm{m}$ over a time of 62 hours with each step taking 30 min, giving an effective speed of $v_{trap} = 0.9\mathrm{nm/min}$.

We further extended the simulations by incorporating elasto-plastic effects. In these simulations, we allowed an instant plastic relaxation to occur at a threshold angle $\theta_p$, such that the new equilibrium bond angle becomes $\theta_{0,i} = \theta_c$. We used the same $k_\theta$ and $k$ value as for the previous elastic simulations. A continuously increasing trap displacement was simulated for a total time of $t_{tot} = 1.9\mathrm{t_D}$, increasing from $u_i = -0.3\mathrm{d_0}$ to $u_f = 2.5\mathrm{d_0}$. This translates to a trap speed of $v_{trap} = 37\mathrm{nm/s}$, close to the actual experimental value. In order to estimate the critical bending angle, we performed 50 simulation runs at a number of $\theta_c$ ranging from 0.1 to 0.2rad, with steps of $0.01rad$. The best fitting $\theta_c$ was determined by comparing the average plastic compression $u_p$ to the experimental value. This gave $\theta_c = 0.21rad$.

## 4.3 Euler buckling

To investigate its buckling behavior, we subject the initially straight colloidal chain to continuously increasing compression. We observe that the chain undergoes a sharp buckling transition at a well-defined compressive displacement $u_c$, as shown in Fig. 4.1b. In the vicinity of $u_c$, fluctuations significantly increase, in agreement with

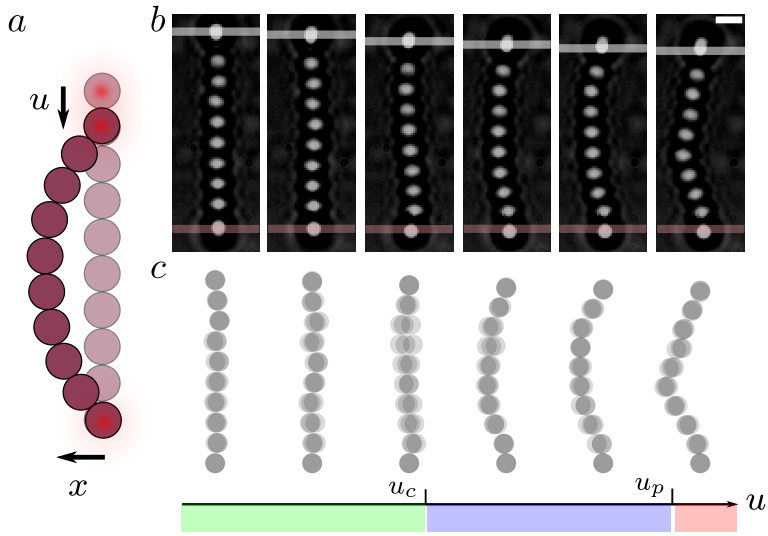


Figure 4.1: Buckling of a colloidal chain. (a) Sketch of the colloidal chain compressed by optical tweezers (red dots). (b) Bright-field microscope images of the chain at $u = -0.45, -0.25, 0.2, 0.6, 0.8, 1.0\mu$m, respectively from left to right, under a compressive displacement. White bars indicate the position of the laser trap that is slowly displaced and red bars the position of the static trap. The scale bar is $3\mu$m. The color code demarcates regions of the straight, elastically and plastically buckled chain, bounded by $u_c$ and $u_p$, respectively. (c) Overlay of three reconstructed chains, one corresponding to the still shown in panel (b), one taken 1.5 seconds earlier (light grey) and one 1.5 seconds later (dark grey). (Video: *https://youtu.be/iRoV5pJP3U4*)

recent predictions [210], as clearly visible in the superposition of three reconstructed images in Fig. 4.1c; their analysis and effect on buckling is the key novelty of our paper. Upon further compression, the fluctuations decrease again, and finally, a kink appears at a well-defined large compressive displacement $u_p$.

To further elucidate this buckling behavior, we measure the force exerted by the trap on the chain as a function of the compressive displacement $u$ Fig. 4.2a. We observe a linear increase up to a critical displacement $u_c$ beyond which the force remains essentially constant. Such force-displacement curve is strongly reminiscent of a classical Euler buckling problem [211–213]. To confirm the validity of this analogy, we map our result onto that of a continuous beam. We use the Euler buckling criterion for the critical force $F_c = \pi^2 B/L_0^2$ and the critical displacement $u_c = F_c/S$, where $B$ is the bending modulus and $S$ the linear stiffness of the beam. Determining the critical force $F_c = 0.19 \pm 0.02$pN and displacement $u_c = 0.21 \pm 0.02\mu$m by interpolation, we find that the bending rigidity of the chain is $B = 11.9 \pm 1$pN$\mu$m$^2$ and the linear stiffness is $S = 0.9 \pm 0.1$pN/$\mu$m, corresponding to a persistence length of $L_p = B/kT = 2900 \pm 240\mu$m, similar to microtubules [68]. Furthermore, this stiffness value is consistent with that obtained from a linear fit to the pre-buckling slope

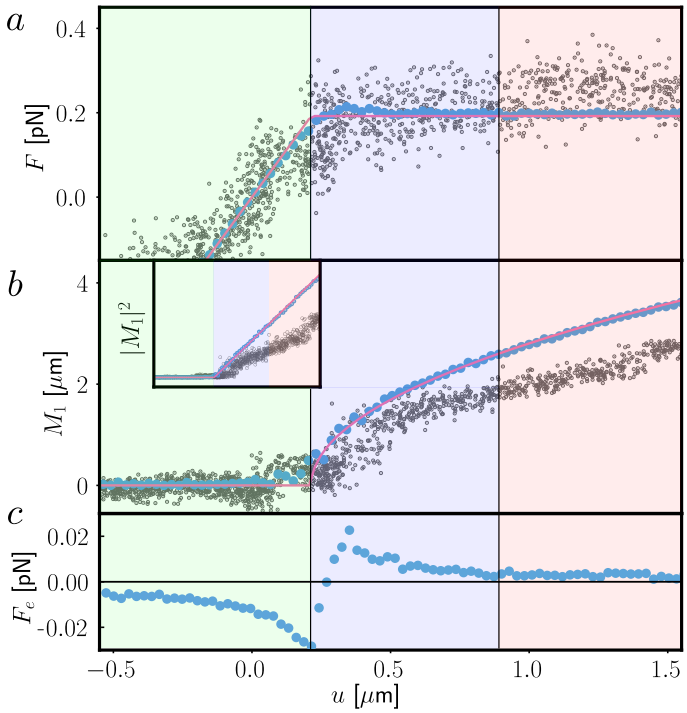


Figure 4.2: Elastic buckling regime: bending force and first Fourier mode, experiments (grey dots), simulations (blue dots) and continuum model (purple line) (a) Compressive force $F$ exerted by the tweezer on the chain versus displacement, $u$. Note that all experimental data points are depicted, while the simulation data has been averaged over fixed $u$. (b) Amplitude of the first Fourier mode $M_1$ of the particle deflections. Only positive mode amplitudes corresponding to positive deflection of the chain are shown. The inset shows the same quantity squared. (c) Entropic force from simulations, see text.

$S = 0.8 \pm 0.1\text{pN}/\mu\text{m}$. Such an excellent agreement between a model for athermal slender structures and our thermally activated colloidal chain is striking.

The validity of this mapping is further confirmed by the shape of the buckled state, which we quantify by the amplitude $M_1$ of the first Fourier mode of the beam deflection (see appendix for details) as a function of the compressive displacement $u$ Fig. 4.2b. While this amplitude is close to zero in the pre-buckling regime, $u < u_c$, it sharply departs from zero and increases as $M_1 \propto (u - u_c)^{1/2}$ beyond the buckling point, see Fig. 2b inset. Again, this result is qualitatively similar to that of a macroscopic Euler buckling problem [211–213]. Note that such deflection-displacement curve provides an independent measure of the critical displacement $u_c = 0.21 \pm 0.02\mu\text{m}$, which is equal to the previous one within experimental errors. These results are consistent with and rationalize previous studies reporting a bending

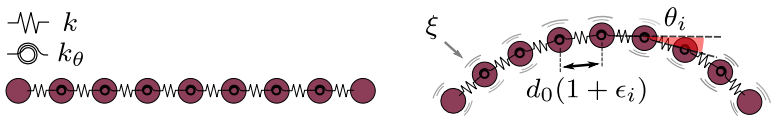


Figure 4.3: Schematic of the model system used for the simulations and the analytical model.

rigidity of linear assembled structures [69, 116, 214].

*Numerical simulations.*— We further rationalize the experimental findings by molecular dynamic simulations of elastically coupled particles in two dimensions subjected to thermal fluctuations, see Fig. 4.3. Specifically, we solve the overdamped Langevin equation [215]:

$$\dot{\boldsymbol{r}}_i = -\frac{D}{k_B T}\nabla_{\mathbf{r}_i} V + \sqrt{2D}\xi, \tag{4.5}$$

where $\xi$ a normalized stochastic thermal force, $D = 0.138 \pm 0.1\mu\text{m}^2/\text{s}$ is the diffusion coefficient measured experimentally by tracking diffusing colloids, and $T$ the temperature equal to the experimental temperature. The potential energy is given by:

$$V = \frac{k}{2} d_0^2 \sum_{i=1}^{N-1} \epsilon_i^2 + \frac{k_\theta}{2} \sum_{i=1}^{N-2} (\theta_i - \theta_{i,0})^2, \tag{4.6}$$

with $\epsilon_i$ the extension of bond $i$, $\theta_i$ the angle between bonds $i$ and $i+1$, and $\theta_{i,0}$ the equilibrium angles which vanish for the initially straight chain. The equilibrium bond distance is determined from experiments as the average particles separation $d_0 = L_0/N - 1$. We also take the bending rigidity and bond stiffness from the experimental measurements $k = S(N-1)$ and $k_\theta = B/d_0$ and assume an infinite trapping potential. We then apply compression by moving the traps stepwise towards each other with a displacement $u_{step} = 0.01 d_0$ and waiting time $t_{step} = 32 d_0^2/D$ between each step, yielding an average compression rate of 0.9nm/min, much slower than the experiments, allowing us to acquire good statistics. Despite the simple assumptions of the numerical model, the results are in good agreement with the experiments, see Fig. 4.2. The force and deflection curves both predict the buckling instability at $u_c$ and correctly describe the force behavior; the quantitative deviations are likely due to (i) plastic effects, and the fact that (ii) the experimental boundary conditions (laser traps) do not allow complete free rotations of the trapped colloids.

## 4.4 Fluctuations and entropic effects

We can use the simulations to extract the entropic contribution $F_e$ to the compressive force associated with the thermal fluctuations of the colloidal chain. We do so by subtracting from the compressive force at room temperature the force at zero

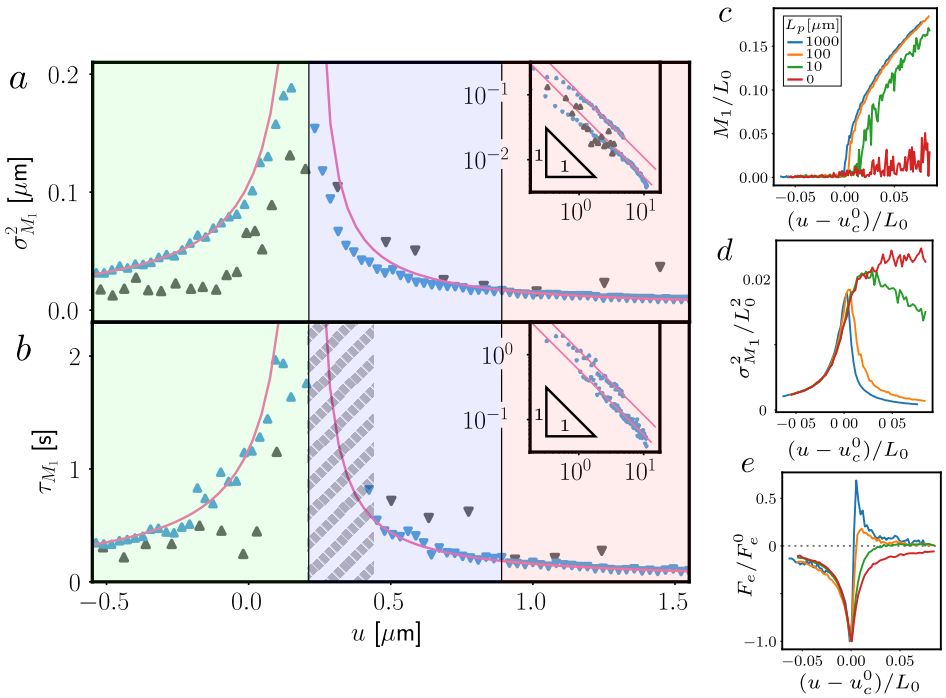


Figure 4.4: Fluctuations close to buckling. (a) Variance $\sigma^2_{M_1}$ of $M_1$ above the mode of its distribution versus the compressive displacement $u$. The inset shows a loglog plot of $\sigma^2$ versus $|u-u_c|/u$. (b) Correlation time $\tau$ of $M_1$. Inset: loglog plot of $\tau$ versus $|u-u_c|/u$. Experimental (numerical, continuum model) data is represented by grey triangles (blue triangles, purple lines). Simulation and continuum model values are divided by a factor of 3 to fit on the same axis. (c-e) MD simulations for decreasing chain persistence length showing normalized first Fourier amplitude $M_1$ (b), variance (c) and entropic force $F_e$ versus normalized $u$ shifted by the zero temperature buckling compression $u_c^0 = \pi^2 B/SL_0^2$. Blue, orange, green, red curves correspond to respectively 1, 1/10, 1/100 and 0 times the experimental bending rigidity. The variance was calculated over a limited time window of 1s.

temperature. $F_e$ shows a characteristic signature of the buckling transition Fig. 4.2c: It diverges and changes sign at the buckling transition (from compressive to repulsive), reflecting the change in the contour length of the chain upon buckling and the associated change in the number of chain configurations. Yet, the magnitude of $F_e$ is just below the experimental resolution, and cannot be resolved experimentally.

Nevertheless, we can measure the fluctuations directly by monitoring the variance of the Fourier amplitudes. We focus on the first mode and compute its variance $\sigma^2_{M_1} = \langle (M_1 - |\bar{M}_1|)^2 \rangle_{M_1 \geq |\bar{M}_1|}$. Upon approaching the buckling point, this variance grows and diverges Fig. 4.4a. The double-logarithmic plot (inset) suggests a divergence $\sigma^2_{M_1} \sim |u-u_c|^{-\nu}$ with exponent $\nu = 1$. We also measure the typical time

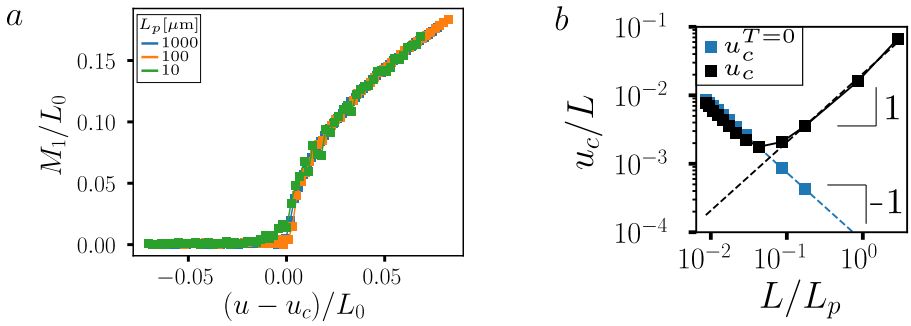


Figure 4.5: Transition to low persistence length. (a) Scaling collapse of the first mode amplitude, $M_1$ versus normalized $(u-u_c)$ with $u_c$ the buckling displacement. (b) Extracted normalized buckling point $u_c$ as a function of flexibility. Two scaling regimes are evident: Exponent -1 associated with the chain compressibility for low flexibility (high bending stiffness), and a regime with exponent +1 associated with the loss of bending rigidity.

scale of fluctuations, $\tau_{M_1}$, from exponential fits to the decay of the autocorrelation function $C(\Delta t) = \langle M_1(t)M_1(t+\Delta t)\rangle$; this fluctuation time shows likewise a significant increase upon approaching $u_c$, see Fig. 4.4b. Yet, the uncertainty and limited number of data points do not allow us to pinpoint the divergence of these growing fluctuations quantitatively.

*Continuum model.*— This stochastic buckling transition is described in a simple— analytically solvable— continuum limit of Eq. (2), known as the extensible elastica [216]. In this limit, the energy can be decomposed into independent contributions from each Fourier mode. To first order in $u$, the energy dependence on the first mode amplitude $M_1$ becomes a double-well, given by

$$V_1 = \frac{S\pi^2}{4L_0}(u_c-u)M_1^2 + \frac{S\pi^4}{32L_0^2}M_1^4 + \mathcal{O}(u^2) + \mathcal{O}(M_1^6), \tag{4.7}$$

where $u_c = B\pi^2/SL_0^2$, $B$ the bending rigidity and $S$ the stretching stiffness. Higher modes exhibit a single harmonic energy dependence and equilibrate to zero (see appendix). Mechanical equilibria of this extensible elastica, prescribed by the condition $\partial V_1/\partial M_1 = 0$, are given by $M_{1,m} = 0$ in the pre-buckling regime ($u < u_c$), and by $M_{1,m} = \pm 2/\pi\sqrt{L_0(u-u_c)}$ in the post-buckling regime ($u > u_c$). The corresponding forces, are $F_m = ku/2$ for $u < u_c$ and $F_m = F_c(1+(u-u_c)/2L_0)$ for $u > u_c$. Furthermore, assuming bending energies obey a Boltzmann distribution in equilibrium, one finds that both $\sigma^2_{M_1}$ and $\tau_{M_1}$ diverge with a power of $-1$, see appendix. These predictions are in perfect agreement with the experiments and simulations as shown in Figs. 4.2 and 4.4 (pink curves). A physically appealing picture emerges from these results: once in presence of stochastic noise, the classical buckling transition remains a supercritical bifurcation, but the vicinity of the bifurcation is associated with fluctuations of diverging magnitude and timescale.

This mean-field buckling behavior diminishes for higher fluctuations. We simulated chains with lower bending rigidities exhibiting stronger fluctuations and find that the buckling transition looses its sharp character and eventually vanishes Fig. 4.4c. Concomitantly, the divergence of buckling fluctuations broadens and eventually disappears Fig. 4.4d. This is associated with a striking change in the entropic force Fig. 4.4e that looses its characteristic change of sign: the positive branch at $|u - u_c^0| > 0$ vanishes, indicating the gradual transition to the freely jointed chain being always attracted to zero end-to-end distance. These results are in qualitative agreement with the analytic results for a filament with decreasing bending rigidity in [208]. Furthermore, other routes towards stronger fluctuations reveal a similar loss of the buckling transition as shown by simulations of longer chains and higher temperatures in the appendix. To fully elucidate the transition from rigid to flexible chains, we collapse the buckling curves in Fig. 4.4c by plotting them versus $u - u_c$, where we subtract the critical buckling displacement, see Fig. 4.5a; the extracted $u_c$ shows two scaling regimes: it first decreases and then increases with increasing chain flexibility, see Fig. 4.5b. The initial decrease with exponent $-1$ is due to the additional compressive component of the chain; the same decrease is observed for vanishing temperature (blue data $u_c^{T=0}$), for which, according to Euler buckling, $u_c$ is given by $u_c^{T=0} = F_c/S \propto L_p^{-1}$, thus the exponent $-1$. Towards higher flexibility, however, $u_c$ grows with exponent $+1$, reflecting the transition from a rigid beam to a freely joint chain, for which $u_c$ becomes infinite. We thus find that the buckling transition increases linearly with increasing flexibility of the chain. Thus, it gradually diminishes as the energetic advantage of buckling in the lowest mode ceases together with the bending rigidity.

## 4.5 Plastic buckling

We also explored plastic effects. At even larger displacements $u > u_p$, the chain undergoes localized bending deformations as shown in Fig. 1b and c (utmost right images), which we find to be irreversible upon releasing the applied compression. To quantify this degree of localization, similar to plastic events in amorphous materials, we calculate the inverse participation ratio (IPR), which varies between $N - 2$ for fully localized deformations and 1 for distributed deformations, as defined by

$$IPR = (N-2)\frac{\sum_{i=1}^{N-2}\hat{\theta}_i^4}{(\sum_{i=1}^{N-2}\hat{\theta}_i^2)^2}. \tag{4.8}$$

Here $\hat{\theta}_i = |\theta_i| - \langle|\theta_i|\rangle_{u<u_c}$, i.e. the local angular deviation from the straight chain. When the chain buckles elastically, the IPR remains small, see grey curve in Fig. 4.6a, while at larger compression $u = u_p = 0.89 \pm 0.02\mu$m, when the chain develops a kink, a clear spike appears. The value of about 6, which is only slightly smaller than the maximum $N - 2 = 8$ indeed suggests very localized deformations. These features can be easily reproduced in the simulations, when we augment our numerical

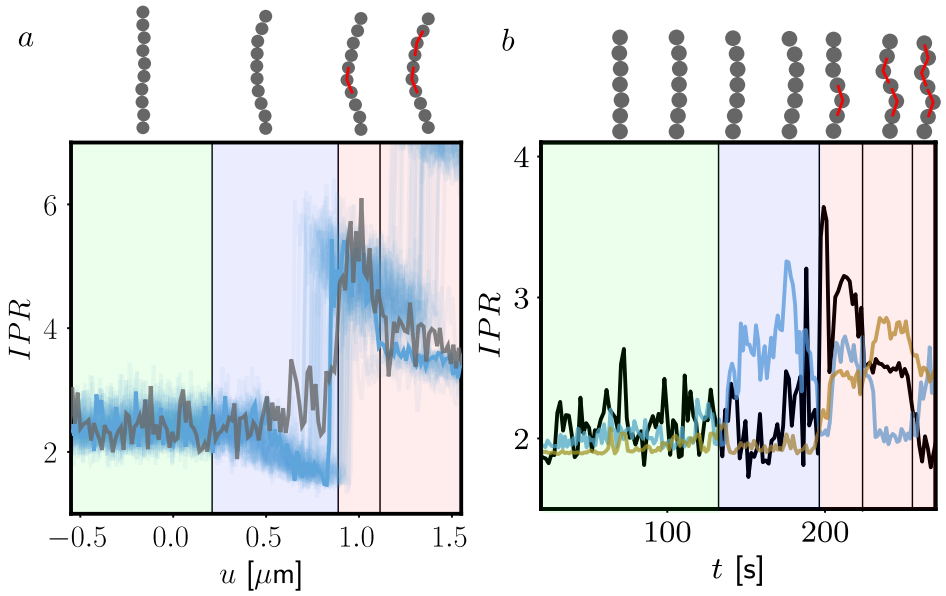


Figure 4.6: Plastic buckling. (a) Inverse participation ratio (IPR) of the experimental chain (grey), and of 50 independent MD simulation runs (blue shading) as a function of continuously increasing compression. The simulations are performed with elastic parameters as in Fig. 4.2 and $\theta_c = 0.21$ rad. Vertical lines and colors distinguish regimes of the straight, elastically and plastically buckled chain, and indicate two plastic slippage events. Reconstructed snapshots show the experimental chain for $u = 0$, 0.5, 1 and 1.5 $\mu$m, with snapped bonds highlighted in red. (b) The IPR (black), $M_1$ (blue) and $M_2$ (yellow) versus time of a different compression experiment. Here, the chain was shorter ($N = 7$), and the trap was moved stepwise, by $\delta u = 0.1\mu$m every 60s. (Video: *https://youtu.be/R9IR5LIa1GU*)

model with a simple elasto-plastic model. Beyond a threshold angle $\theta_p$, an instant plastic relaxation occurs such that the equilibrium bond angle becomes $\theta_{0,i} = \theta_p$. Taking a value $\theta_p = 0.21$rad gives results qualitatively and quantitatively similar to the experiment, see blue shading in Fig. 4.6a. By repeating 50 simulations we obtain an average $u_{p,sim} = 0.84\pm0.09$mum, which indeed corresponds to the value $u_p$ observed in the experiments. Intriguingly, the combination of elasto-plastic dynamics and thermal noise can further lead to higher-order buckling modes when the chain is compressed at higher compression rates Fig 4.5b. We observe a sequence of buckling transitions through mode 1, mode 2 and mode 3, that we interpret as a sequence of plastic events, as clearly shown by the mode 1 and 2 amplitudes (blue and olive) and IPR (black).

## 4.6 Summary and Outlook

We have experimentally demonstrated the rich stochastic buckling dynamics for a colloidal chain under uniaxial compression, and rationalized our experimental results by simulations and analytic modelling. In the elastic regime, bending interactions and stochastic noise lead to diverging bending fluctuations. With decreasing persistence length, as higher-order modes are excited, this divergence smoothens, and the buckling transition eventually vanishes. Important biological filaments have persistence length of e.g. $L_p = 5000\mu$m for microtubules, of similar order as our colloidal chain, while for actin filaments, $L_p = 17\mu$m, putting those already in the large fluctuation regime, where the buckling transition smoothens [217]. These results have important consequences for the mechanics of biological tissue [68] and colloidal gels. Depending on the mesh size relative to the persistence lengths, filament buckling interactions become important, and the observed divergence of fluctuations then translates into an entropic contribution to the stress, which should manifest in the rheology of such networks. Our results open up unique avenues for self-assembled colloidal structures with advanced nonlinear mechanics of relevance for the understanding of the rheology of gels [195], the mechanics of living tissues [68] and of designer colloidal architectures [70].

# 4.7 Appendix

## 4.7.1 Mode definition and effective mode diffusion constant

After locating the particles in the chain, a mode decomposition is performed in the following manner: First, the out-of-line deflection of every non-trapped particle $j$ is calculated as the perpendicular distance $x_j$ from the line connecting the two trapped particles at the ends. Next, a scaled discrete sine transform of type 1 is performed on $x_j$ defined by:

$$M_i = \frac{2}{N-1} \sum_{j=1}^{N-2} x_j \sin(\frac{\pi}{N-1} ji) \quad i = 1, ..., N-2 \tag{4.9}$$

Here the normalization has been chosen such that:

$$x_j = \sum_{i=1}^{N-2} M_i \sin(ij \frac{\pi}{N-1}) \quad j = 0, ..., N-1 \tag{4.10}$$

Based on the overdamped Langevin equation of individual colloids, Eq. 4.2.2 in the main text, we can derive an equivalent dynamical equation in terms of modes, given by:

$$\dot{M}_i = -\frac{D_M}{k_B T} \nabla_{M_i} V + \sqrt{2D_M}\xi. \tag{4.11}$$

Here $D_M$ is an effective diffusion coefficient. This coefficient is equal for all modes and can be derived by inserting Eq. 4.10 in Eq. 4.2.2 of the main text. This gives $D_M = 2D/(N-1)$.

## 4.7.2 Theoretical model

We parameterize the shape of an extensible elastica by $\boldsymbol{r}(s) = (x(s), y(s))$ with $s$ running from 0 to $L_0$, the rest length. The compressive strain is defined as $\gamma(s) = \sqrt{(dx/ds)^2 + (dy/ds)^2}$ and the orientation angle as $\phi(s) = \arctan(dy/dx)$. The energy functional of an elastica including elastic energy and work exerted by a compressive force $F$ is given by [32]

$$V = \frac{B}{2} \int_0^{L_0} \left(\frac{d\phi}{ds}\right)^2 ds + \frac{L_0 S}{2} \int_0^{L_0} (\gamma - 1)^2 ds + F \left( \int_0^{L_0} \gamma \cos(\phi) ds - R \right). \tag{4.12}$$

Here $R = L_0 - u$ is the end-to-end length, $B$ is the bending rigidity and $S$ the stretching stiffness of the elastica. Minimizing $V$ with respect to $\gamma$ and $F$, we find

$$\gamma = 1 - \frac{F}{SL_0} \cos\phi, \quad F = SL_0 \frac{\int_0^{L_0} \cos\phi ds - R}{\int_0^{L_0} (\cos\phi)^2 ds} \tag{4.13}$$

Inserting these back into Eq. 4.12, we obtain an energy $V_\phi$ purely as function of the orientation angle, given by

$$V_\phi = \frac{B}{2}\int_0^{L_0}\left(\frac{d\phi}{ds}\right)^2 ds + \frac{SL_0}{2}\frac{\int_0^{L_0}\cos(\phi)ds - R}{\int_0^{L_0}(\cos\phi)^2 ds}$$

This is the energy we will use to determine the equilibrium angles $\phi(s)$ and also the size of thermal fluctuations in $\phi$. Note that it is indeed correct to use $V_\phi$ to determine the equilibrium. However, using $V_\phi$ to determine the size of fluctuations disregards the effect of thermal fluctuations in $\gamma$ and $F$. These fluctuations are not uncoupled from fluctuations in $\phi$, as can be seen from Eq. 4.12. Yet, we assume that these fluctuations have negligible influence.

After a Fourier transform assuming Neumann boundary conditions

$$\phi = \sum_{n=1}^{\infty}\alpha_n\cos(\frac{n\pi}{L_0}s), \tag{4.14}$$

$V_\phi$ decomposes into $V_\phi = Su^2/2 + \sum V_{\alpha_n}$. It follows that up to a critical compression $u_c$ all modes equilibrate to zero. After $u_c$, the first mode becomes nonzero and the chain buckles, which can be seen from

$$V_{\alpha_1} = \frac{SL_0}{4}\left(u_c^0 + \frac{u^2}{L_0} - u\right)\alpha_1^2 + \frac{S}{32}\left(L_0^2 - \frac{7uL_0}{2} - 2u^2\right)\alpha_1^4 + \mathcal{O}(\alpha_1^6), \tag{4.15}$$

where $u_c^0 = \pi^2 B/SL_0^2$. The buckling compression of the first mode is found by determining the root of the term in front of $\alpha_1^2$, giving $u_c = \frac{L_0}{2}\left(1 - \sqrt{1 - 4u_c^0/L_0}\right)$. In the regime that we probe experimentally, $u_c/L_0$ and $u/L_0$ are small numbers. Therefore, $u_c \approx u_c^0$, and lowest order terms dominate in $V_{\alpha_1}$, which reduces to

$$V_{\alpha_1} = \frac{SL_0}{4}\left(u_c^0 - u\right)\alpha_1^2 + \frac{SL_0^2}{32}\alpha_1^4 + \mathcal{O}(u_c^2) + \mathcal{O}(u^2) + \mathcal{O}(\alpha_1^6) \tag{4.16}$$

Minimizing this energy we see that the equilibrium first mode is given by

$$\alpha_{1,m}^2 = \begin{cases} 0 & u < u_c \\ \frac{4}{L_0}\Delta u + \mathcal{O}(\Delta u^2) & u > u_c, \end{cases} \tag{4.17}$$

with $\Delta u = u - u_c$.

To derive the compressive force up to first order in $\Delta u$, care has to be taken to solve $\alpha_{1,m}^2$ from Eq. 4.15 one order higher in terms of $u_c/L_0$. Doing that and inserting in Eq. 4.13 one obtains

$$F = \begin{cases} Su & u < u_c \\ F_c(1 + \Delta u/2L_0) + \mathcal{O}(\Delta u^2) & u > u_c. \end{cases} \tag{4.18}$$

where $F_c = Su_c$.

As a last step to obtain the double-well potential stated in the main text we have to transform $\alpha_1$ to $M_1$, defined by Eq. 7.1. Using that for small deflection and compressions we have $M_1 = L_0\alpha_1/\pi$, and Eq. 4.16 becomes Eq. 4.7.

Furthermore, we can derive an expression for the variance $\sigma^2_{M_1}$ of the first-mode amplitude. If we assume that in equilibrium, the bending energies given by Eq. (4.15) obey a Boltzmann distribution, then the mode fluctuations around the average become Gaussian distributed with variance

$$\sigma^2_{M_1} = \begin{cases} \frac{2kTL_0}{\pi^2 S}|u_c - u|^{-1} & u < u_c \\ \frac{kTL_0}{\pi^2 S}|u_c - u|^{-1} & u > u_c. \end{cases}, \tag{4.19}$$

Note that this approach breaks down for $u >\sim u_c$, in the post-buckling regime near the buckling point, where the distribution becomes bimodal rather than a single Gaussian as predicted by Eq. 4.19. For the fluctuation time, the overdamped dynamics for a harmonic-well predicts that $\tau_{M_1} = \sigma^2_{M_1}/D_{M_1}$, where $D_{M_1} = 2D/(N-1)$ is the effective mode diffusion.

### 4.7.3 Exploring the strong fluctuation regime

Here, we investigate the large-fluctuation regime in more detail. Specifically, we address the effect of increasing fluctuations achieved by (i) increasing temperature, (ii) decreasing the bending rigidity, and (iii) increasing the number of particles of the colloidal chain in the MD simulations. Each of these routes increases the flexibility $f = L/L_p$ of the chain, where $L_p = B/kT$ is the persistence length, and $L$ the total length of the chain. It has been predicted theoretically that for stiff to semi-flexible compressible rods with persistence length $L_p < L$, thermal fluctuations contribute an additional entropic force $F_e$ (on top of the non-thermal compressive force $F$, Eq. 4.18) of $O(T)$ far away from $u_c$ and $O(\sqrt{T})$ near $u_c$ [210]. Other theoretical work, which assumes an incompressible semi-flexible rod in two dimensions, predicts a critical entropic force increase $F_{e,c} \propto kT$, [207, 208].

The simulation results for increasing temperature, decreasing bending rigidity, and increasing number of particles are shown in Fig. 4.7, columns from left to right, respectively. As a unique feature of the buckling transition, the entropic force (top row) switches sign when crossing $u_c$ from negative (favoring compression) to positive (favoring expansion). The negative (tensile) entropic force upon approaching $u_c$ from the left reflects the driving force towards larger number of configurations with decreasing end-to-end distance. At buckling, the force changes sign as the buckled state (mode 1 fluctuation) again suppresses the number of accessible configurations (higher-order fluctuations). The resulting positive (repulsive) entropic force leads to an extra buckling force barrier increasing the buckling compression, such extra force barrier was predicted by both theoretical groups [208, 210]. Furthermore, we find, as predicted by [210] but contradicting [208], that for $L_p < L$ the amplitude of this positive peak goes as $O(\sqrt{T})$, as can be seen by the collapse of peak height when rescaling by $\sqrt{kT}$ (second inset top left). Further away from $u_c$ the entropic

force scales with $O(T)$, as can be seen by the collapse when rescaling by $kT$ (first inset top left), also inline with [210]. The discrepancy between the two theoretical predictions, and our closer agreement with [210], could be explained by the fact that our simulation assume a compressible chain, more closely agreeing with the theoretical model of [210].

The entropic effects clearly increase with increasing flexibility $f$ of the chain. As fluctuations become more prominent at higher temperature, smaller bending stiffness, and for longer chains, the amplitude of the negative (pre-buckling) entropic force grows. The negative region also extends as $u_c$ drifts to the right. This can be seen in the growing region in between the negative and positive peak of $F_e$. The positive peak on the other hand decreases in amplitude (inset top left, top middle), until it vanishes and $F_e$ shows only attraction towards $u = 0$, reflecting the behavior of a freely joint chain with a continuously increasing entropic tensile force upon decreasing end-to-end distance. These effects are less visible in the data of the increasing chain length (right column), which are limited to lower chain flexibilities due to computational costs of equilibrating long chains.

As a result of this trend, $u_c$ disappears: very flexible chains lose the signatures of the buckling transition. This is most clearly observed in the gradual disappearance of

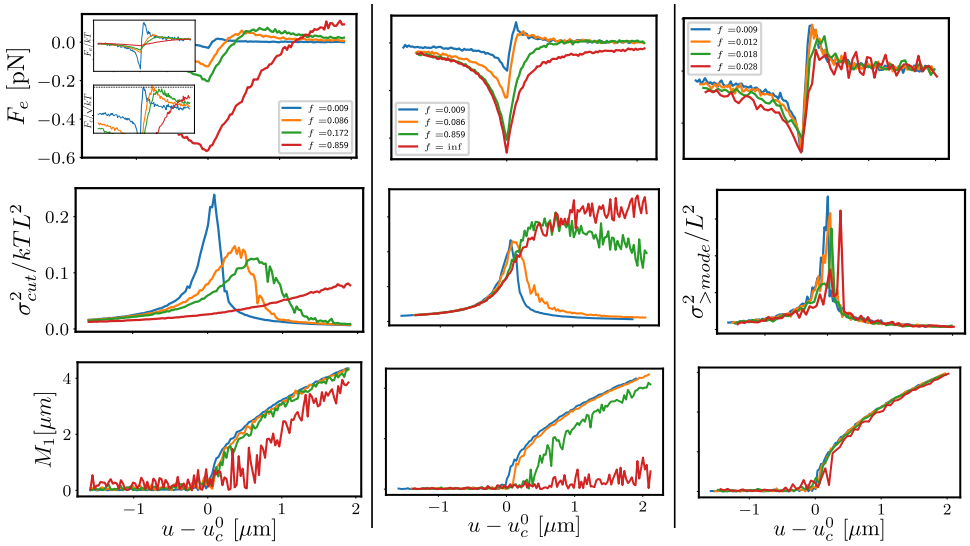


Figure 4.7: MD simulation effect on $F_e$, $\sigma^2$ of three different routes that increase the flexibility of the system: first column increasing $T$, second column $B$, third column $N$. $F_e$ is calculated by subtracting the non-thermal $F$, Eq. 4.18, from the measured $F_{sim}$. $\sigma^2_{cut}$ is the variance of the $M_1$ over a time window of around 1s. $\sigma^2_{>mode}$ is are fluctuations above the mode of the distribution as defined in the main text. All simulations were run using the same protocol as described above for the elastic simulation.

the characteristic kink of the first-mode amplitude, as shown in the bottom row. At the same time, the divergence of fluctuations (middle row) decreases and eventually vanishes. Hence, the thermally activated buckling transition with its characteristic diverging fluctuations as described by mean-field theory is observed only in a limited range of small fluctuations, where the predominantly elastic chain (with flexibility $L/L_p < 1$) has an energetic advantage of buckling into the lowest mode (opposed to the excitation of higher modes).

### 4.7.4 Effective compressibility

The stretching stiffness $S \sim 1\text{pN}/\mu\text{m}$ of the chain that we obtained from the slope of the $F - u$ curve is unexpectedly low. A best guess of the interaction potential of these particles, is shown in Fig. 4.8a. Though this theoretical potential is not expected to be quantitatively accurate due to the binary system being realtively far from critical, we can use it for an order of magnitude estimation of the bond strength. From a harmonic approximation around the minimum of the potential we expect a $k_{expect} \sim 10^4$ pN/$\mu$m and thus a $S_{expect} \sim 10^3$ pN/$\mu$m. This two orders of magnitude difference can be understood when looking at the time development of the individual bond distance, see Fig.4.8b. The figure shows that only the bonds at the end of the chain, close to the trap, appear compressible. In fact the bonds in the middle do not systematically compress and only show a variation on the order of 10 $nm$, equal to the locating accuracy. This is consistent with a lower than locating accuracy maximal compression of $\sim$ 5 nm that's expected from $k_{expect}$ over the experimental force window. From this we conclude that the high compressibility is not due to the interparticle potential but results from the boundary conditions of the chain. One possible cause could be out of plane movement of the particles close to trap. This would result in an apparent compressibility when looking at projected coordinates. Because these effects are difficult to model we have decided to treat the chain as having an effective compressibility. This deviation between experimental and simulation conditions might explain the quantitative disagreement in the fluctuation amplitude, Fig. 4.4. These are lower in the experimental case than predicted by simulation. From Eq. 4.7 we indeed see that a lower $S$ would decrease the fluctuation amplitude.

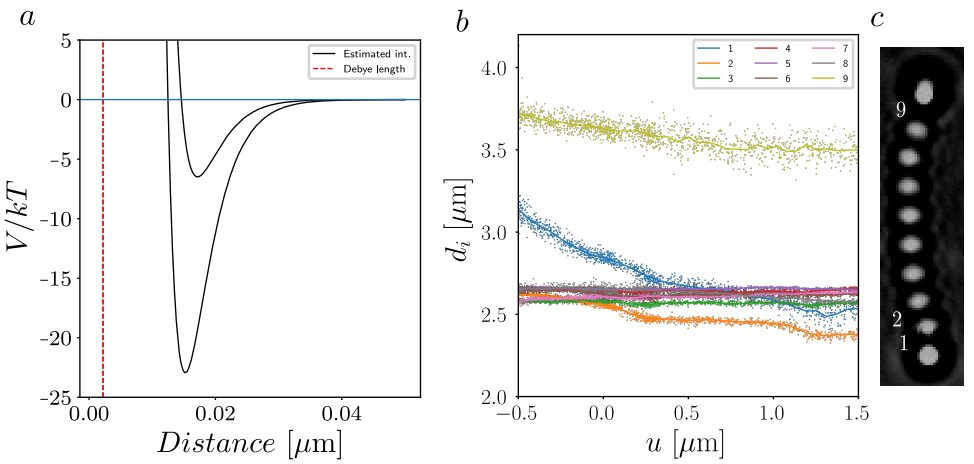


Figure 4.8: (a) Effective interaction potential based on chapter 3, for $\Delta T = 5.5K$ ($6.5k$), top curve (bottom curve). As theoretical model input parameters the experimental parameters of our specific binary mixture were used, the particle surface charged was taken to be $-0.17$ e/nm$^2$ and the $r_{wet} = 1.38$ which was fitted by matching the aggregation temperature of theory and experiment. (b) The individual bond distances $d_i$ as a function of $u$, dots are all data points, lines are averages. The bond number $i$ is defined in (c).

CHAPTER 5

# Critical Casimir self-assembly of patchy colloids

*Patchy particles are an attractive system to assemble via in and out-of-equilibrium pathways in order to create functional designer materials. However, achieving specific single-bonded particle interactions remains challenging. Here we present a versatile system showing single bond per patch interactions that are reversible and tunable using temperature dependent Critical Casimir forces. We assemble different types of "colloidal molecules" using dipatch and tetrapatch particles and mixtures thereof: Small clusters of dipatch particles form short chains, tetrapatch particles introduce tetrahedral bond angles that result among others in zigzag chains and cyclic structures. We categorize these small clusters using an analogy with aliphatic carbon compounds such as butane and pentane. Larger number of dipatch particles form analogues of polymers that can crosslink with the addition of tetrapatch particles and we study their formation kinetics. Finally we show that, by decreasing particle size to speed up growth kinetics, dipatch and tetrapatch mixtures form a percolated gel. These results demonstrate the assembly control that patchy particles in combination with the in-situ controllable critical Casimir interaction offer.*

## 5.1 Introduction

Continuous advances in synthesis have yielded sophisticated colloidal building blocks with control over shape, composition and interaction [38, 41]. These building blocks have been shown to self-assemble into various designer structures such as micelles, tubes and shells [49, 50, 53], freely jointed mechanisms and chains [13, 43, 54], chiral architectures [42] or shape-changing and activated filaments [15, 55]. However, apart from lattice structures, which are global equilibrium states [16], these designer assemblies are so far limited to a small number of particles not integrated in a larger matrix. In order to create functional materials, multiple of these components need to be structured hierarchically. This requires a detailed knowledge and control over in and out of equilibrium self-assembly pathways [41, 63, 218]. A common ingredient in many approaches to program self-assembly pathways are limited valence particles with directional bonds. Patchy particles are an especially attractive system to achieve limited valency and directional bonding as they use only a minimal adjustment, a heterogenous surface with well-defined patches of tunable size, to carry considerable self-assembly information [219, 220]. Though simulations have thoroughly explored these systems [59, 221, 222], experiments so far have only achieved patches that are large and form more than one bond [16, 49, 223], or assemblies that are limited to a small number of particles [14]. However, small patches resulting in a single bond per patch would lead to more deterministic structures and thus carry more direct assembly information.

Here we present a versatile system showing single bond-per-patch interactions that are reversible and tunable using temperature-dependent Critical Casimir forces. Critical Casimir forces exploit the universal temperature dependence of solvent fluctuations in near-critical binary mixtures to induce effective particle interactions that can be finely adjusted via the temperature-dependent solvent correlation length. Furthermore, Critical Casimir forces depend uniquely on the boundary conditions, which are determined by the adsorption preferences of the mixture's components at the confining surface [96, 124, 224]. Selective bonding should result between particle patches when they have the opposite adsorption preference as the particle matrix, as has recently been demonstrated by grafting a hydrophobic polymer on a patch surface of an elsewhere hydrophilic particle [223]. Here, we achieve an adsorption contrast by adding higher valent ions (Magnesium Sulfate) to a binary solution (Water/Lutidine) and using a recently developed patchy particle system with fine control over patch size and a clear material contrast between bulk and patch [38]. We show that upon addition of Magnesium Sulfate, patches become lutidine-philic, meaning they have an adsorption preference for lutidine over water whereas the particle bulk is water-philic. This adsorption contrast enables the patch-to-patch assembly by critical Casimir forces in solvents with lutidine concentrations below the critical concentration.

Using this system, we assemble dipatch and tetrapatch particles and show that for small assemblies, these form colloidal molecules with structures analogous to aliphatic carbon compounds such as butane and hexane. In addition, we show that

larger assemblies of dipatch particles form colloidal polymers, and we find that these colloidal polymers have an exponential size distribution. By including tetrapatch particles, these polymers cross-link, forming branched clusters that instead show a power-law size distribution, and approach a space-spanning network with a mesh size tunable by the ratio of tetrapatch/dipatch particles. We characterize the assembly kinetics and show how the aggregation speed is tuned by both concentration and temperature. We further show two dynamic regimes, an initial linear regime followed by a slower regime dominated by crowding. Finally, we achieve a true patchy percolated network by using smaller particles to speed up the growth kinetics, possibly reflecting a true equilibrium gel.

## 5.2 Observation of patchy particle assembly

### 5.2.1 Methods

To investigate the effect of critical Casimir interaction between patchy particles and to study the formation and structure of patchy clusters, dipatch and tetrapatch particles were dispersed in the binary mixture either in pure form, or at the desired ratio. In order to only have critical Casimir interactions between patches we used the "optimized" binary mixture at a volume faction of 0.25 lutidine water and added 0.375mM $MgSO_4$, see chapter 2. This salt concentration was chosen to be significant enough to turn patches lutidine-philic yet be small enough to not de-stabilize the system.

Various patchy particles were used to explore the system (see chapter 2 for synthesis and characterization). We studied the effect of patch-size by comparing cluster formation of particles TP-A and DP-B, with sizes of $d = 3.7(2)$ $\mu$m and $d = 3.1(1)$ $\mu$m that have respectively the largest and smallest patch size. To study the effect of mixing dipatch with tetrapatch particles, we used dipatch particles DP-A and tetrapatch particles TP-B, with sizes of $d = 3.2(1)$ $\mu$m and $d = 3.7(1)$ $\mu$m, that have approximately the same patch size and only differ in the number of patches, and are expected to have the same interaction strength between patches. Finally, smaller dipatch ($d = 1.6 \pm 0.1$ $\mu$m) and tetrapatch particles ($d = 1.8 \pm 0.1$ $\mu$m) were used to study the effect of decreasing particles size. All the suspensions were filled into capillaries, which were subsequently sealed using chemically resistant Teflon grease. Owing to their size, particles quickly sediment to the bottom of the capillary forming a single monolayer.

*Small-scale structures.* Initially the sample volume fraction $\approx 0.002$ was kept low, forming a monolayer with surface coverage $\phi \approx 0.1$, which was determined by particle counting and using $\phi = N\pi r_{part}^2/A$, with $N$ the number of particle in field of view with area $A$ and $r_{part}$ the particle radius. Such a low coverage prevents the formation of continuous space-spanning structures, ideal for studying the formation and structure of patchy clusters of a limited number of particles $N \lesssim 20$.

To study particle assembly, we used the temperature-controlled microscope setup

as described in chapter 2. Critical Casimir forces were induced by quenching temperature to a small temperature offset, $\Delta T = 0.1$K, below the phase separation temperature $T_{cx}$. In order to demonstrate the reversibility and study the break-up dynamics, temperature was subsequently decreased, and we observed that the structures that had formed split up and the particles redispersed. Such heating and cooling cycles were performed multiple times varying the final low temperature between $\Delta T = 2$K, for a strong decrease of interaction strength, and $\Delta T = 0.2$K for a minor decrease. To image the arrangement of patches we used epifluorescent imaging. In addition, bright field imaging was used to identify the center of the patchy particle.

*Larger-scale structures.* Next, we prepared samples of DP-A particles at two higher volume fractions $\approx 0.005$ and $\approx 0.01$. After sedimentation, this resulted in a monolayer with surface coverage $\phi \approx 0.2\%$ and $\phi \approx 0.4\%$. Depending on the sample concentration approximately $2000 - 4000$ particles were in the field of view. Furthermore, samples with additional amount of tetrapatch particles were prepared by mixing the dipatch samples with tetrapatch particles TP-B, at well-defined fractions of $c_{4p} = 0.1$ and 0.2. Before each experiment, the exact surface fraction was determined to account for sample density inhomogeneities due to a not completely flat capillary.

Particles were left to assemble over a period of approximately 12 hours. During the assembly process, images were recorded at a frame rate of $10^{-1}$fps. To study the effect of interaction strength on the assembly, we performed different assembly runs on the same samples varying $\Delta T$ from 0.18K to 0.05K. Below 0.18K no significant bonding was observed. After each assembly experiment, the temperature was lowered to $\Delta T = 0.5$K in order to redisperse the sample. We then initiating aggregation again through a quench to a different temperature , etc.

Bright-field microscopy was used for imaging and the particle centers were identified using particle tracking software [122]. We then performed a clustering algorithm which connects particles that are bonded for a sufficient amount of time: The algorithm works such that first, tentative particle bonds are identified using a first distance criterium. Next, all bonds are tracked over time and we selected only bonds that persist for sufficient time. This allows us to distinguish between real bonds and temporary collisions between neighboring particles. These "true" bonds are then clustered together with the original located particles. To do this we employ a trick: the bonds are temporarily considered "particles" located in between the two particles they bond. We then perform a second clustering algorithm on this bonds plus particle dataset using a distance criterion approximately half that of the first distance criterion. In this way particles that do not form a true bond will not be considered part of the cluster. This algorithm allows us to successfully identify clusters even at high particle concentrations, where the distinction between truly bonded particles and merely colliding particles is difficult.

*Smaller particles.* Lastly we studied the effect of particle size on the assembled structure by using smaller particles. We prepared a dipatch/tetrapatch mixture with a 10% fraction of tetrapatch particles. The particles were dispersed in the same bi-

nary mixture as before. Conveniently, the effect of volume fraction on the assembled structure could be explored using only a single sample. This was possible, because the capillaries used in our experiment (Vitrocom, $50x2x0.2$mm) are not completely flat rectangles, but are slightly bulged, with a centerline that is approximately $20\mu$m lower than the edges. By letting the particles settle for a sufficient amount of time, this resulted in an equilibrium sedimentation profile with a maximal density in the middle, gradually decaying towards the edges of the capillary.

Next, critical Casmir interactions were induced by quenching temperature to $\Delta T = 0.1$K. After waiting $\sim$ 1 hours to allow for particle aggregation, we used 3d confocal imaging to image the fluorescently dyed particles. We used confocal microscopy because the particles increased gravitational height resulted in structures more properly explored using 3d imaging. In these images the particle centers also fluoresce dimly because some of the patch fluorophore has migrated to the PS matrix during synthesis. Similarly as the bigger particles, when temperature is increased to $\Delta T = 0.1$, the smaller patchy particles form patch to patch bonds.

### 5.2.2 A reversible patchy bond

With $MgSO_4$ salt, patches are more lutidine-philic and thus aggregate in lutidine-poor solvents: The lutidine-philic patches localize lutidine-rich solvent fluctuations in the gap between two patches, leading to attractive critical Casimir interactions between di- and tetrapatch particles as shown in Fig. 5.1. Both tetra- and dipatch particles form directional patch-to-patch bonds at temperatures close to $T_c$ in binary mixtures with lutidine concentration $c_L < c_c$, as shown by the microscopy images in Fig. 5.1. This is evident from the fluorescently dyed patches merging to form a single bond. In addition, the geometry of the assembled structure reveals the specific direction of the interaction: The tetrapatch particles form kinked structures with 2d projected bond angles $\theta \approx 110°$, reflecting the tetrahedral patch positions, Fig. 5.1(a). In this case, the 2d projected bond angles approximately correspond to the actual 3d bond angles as the small gravitational height of the particles ($\sim 0.5$ $\mu$m) causes the formation of a quasi 2d plane. Furthermore, the bonded patches reside in the same plane in contrast to the out-of-focus free patches of the middle three particles.

The figure also shows the aggregation and break-up behavior of the particles as a function of temperature. We find that the critical Casimir induced bonding is fully reversible and tunable with temperature. When lowering the temperature $T$ below the aggregation temperature $T_a$ all bonds eventually break apart. The breakup kinetics depend on how far below $T_a$ the temperature is decreased. In the case of the tetrapatch particles, we lowered the temperature far below $T_a$, resulting in a short breakup time $\sim$ 1s of all bonds at the same time. For the dipatch chain, on the other hand, we lowered the temperature only slightly below $T_a$. In that case, bonds break only slowly over the time span of $\sim$ 10min and sequentially. This shows qualitatively the continuous tunability of the interaction. Just below $T_a$ the interaction is not strong enough to permanently bond but still significant enough to

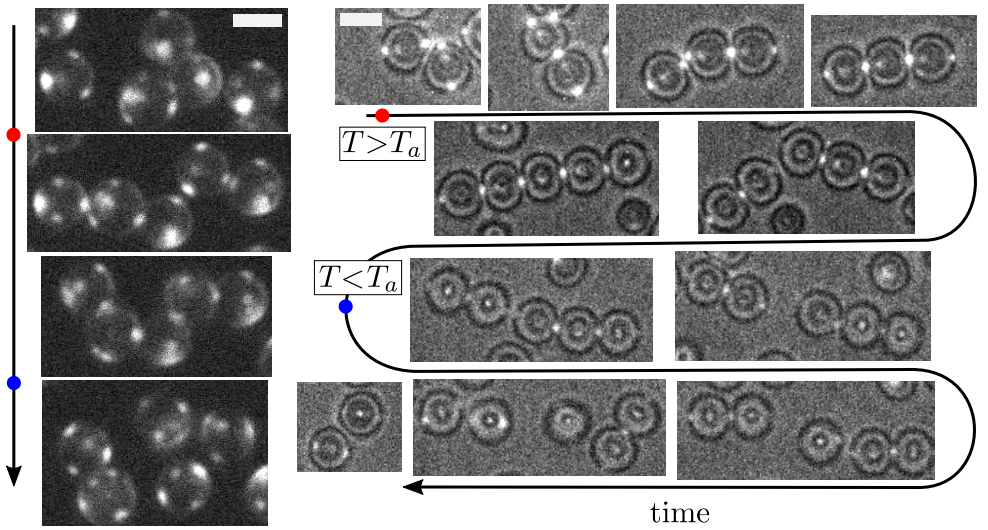


Figure 5.1: Reversible patchy critical Casimir interaction (a) Epifluorescence microscopy stills of tetrapatch particle (TP-A) assembly showing fluorescently dyed patches. Temperature is quenched from $\Delta T = 2\text{C}^\circ$ to $\Delta T = 0.1\text{C}^\circ$ (between red and blue dot), and finally back to $\Delta T = 2\text{C}^\circ$, time difference between first three frames is 2 minutes and between two last frames 10s. (b) Epifluorescence microscopy stills of dipatch particle (DP-B) assembly showing fluorescently dyed bright patches, in addition low intensity bright field lighting shows particle centers. Temperature was quenched similarly as for tetrapatch particles however upon return temperature was lowered to $\Delta T = 0.2\text{C}^\circ$. Time between each frame is approximately 5 minutes. Scale bars are 3 $\mu$m, in both cases $63x$ magnification was used. (Video: *https://youtu.be/atY_CygObJk*)

stay bonded for some time. Further below $T_a$ no significant interaction is present.

Dipatch particles form straight chains, reflecting the position of patches at opposite poles on the particle, Fig. 5.1(b). We also found that the formation kinetics of dipatch particles is much slower and happens more sequentially than for tetrapatch particles. Indeed, the five-particle dipatch chain takes $\sim$ 30min to form, whereas the five-particle tetrapatch chain takes only $\sim$ 20s to form, a factor of $\sim$ 100 slower. This can be understood as a direct consequence of the larger patch surface coverage, $\sigma_p$, of the tetra-patches which are both bigger in diameter and number. The patch-size measurements discussed in chapter 2, yielded a surface coverage of $\sigma_p^{TP} = 6.6\%$ for the tetrapatch particles used here and of $\sigma_p = 0.7^{DP}\%$ for the dipatch particle. For a sticky interaction, the aggregation speed, $v$, is expected to be approximately proportional to the square of the patch coverage, $v \propto \sigma_p^2$, as two patches have to meet each other for bonding. This predicts a factor $(\sigma_p^{TP}/\sigma_p^{DP})^2 \sim 100$ faster aggregation for the tetrapatch particles in agreement with observations. The exact aggregation speed will also be influenced by a possible different interaction strength

and different initial volume fractions between the two samples. However these effects are expected to be minor given the similar $\Delta T$ which determines the critical Casimir strength and the similar volume fractions. This shows that patches not only control the morphology of the formed structures but also strongly influence the formation kinetics.

### 5.2.3 Colloidal molecules: A classification of small patchy structures

By carefully analyzing the zig-zag structures, we find that these assemblies of a small number of patchy particles form structures analogous to hydrocarbons with the patchy particles taking the place of carbon atoms and the open patches the place of hydrogen, see Fig. 5.2. In this mapping, tetrapatch assemblies are analogous to saturated alkanes where each carbon is tetravalently coordinated. Beyond linear assemblies such as a colloidal analog of butane, we observe cyclic compounds, in particular cyclopentane and, rarely, cyclohexane, see Fig. 5.2(b). By including dipatch particles we can extend our range of molecular structures to unsatured hydrocarbons by identifying a dipatch-dipatch bond in between two tetrapatch particles as a triple carbon bond. This way we can observe the different structural isomers of colloidal butyn, see Fig. 5.2(c). The images shown here are all 2d projections, while in reality these structures have 3d conformations, which can for some images be seen by the top and bottom patches being out of focus. The 2d projections provide quite accurate representations of the actual structure because of their quasi-2d nature. However, some of the structures shown here, such as colloidal butane and hexane, likely have significant out-of-plane corrugation which would be better visible using 3d confocal imaging.

The colloidal analogues have their own properties not shared with molecules: For instance, due to sedimentation the particles live in a quasi 2d plane and we observe two non-equivalent forms of colloidal butane, Fig. 5.2(a). In one case subsequent tetrapatch bonds form oppositely oriented bond angles creating a zigzag structure (colloidal butane), in the other case bond angles are oriented in the same direction forming a semi-circular structure (colloidal butane'). Transitions between these two states are possible but involve rotation in the z-direction which costs significant energy. Another difference is that the empty patches, which represent hydrogen atoms, are too far away from each other to interact with each other whereas in molecules they do. This increases the rotational freedom of especially the capping patchy particles who only have a single bond.

Numerous assemblies are observed that don't have a direct molecular analog. For example Fig. 5.2(d), would correspond to the indicated structure, but because the colloid does not form a double, it has on more (or multiple) free patches available (highlighted in red). For instance, when one dipatch particle resides between two tetrapatch particles the straight geometry suggests this should be mapped to two double bonds. However, this results in non-physical carbon compounds with pentavalent carbon atoms that have too many hydrogen atoms. Another source of dis-

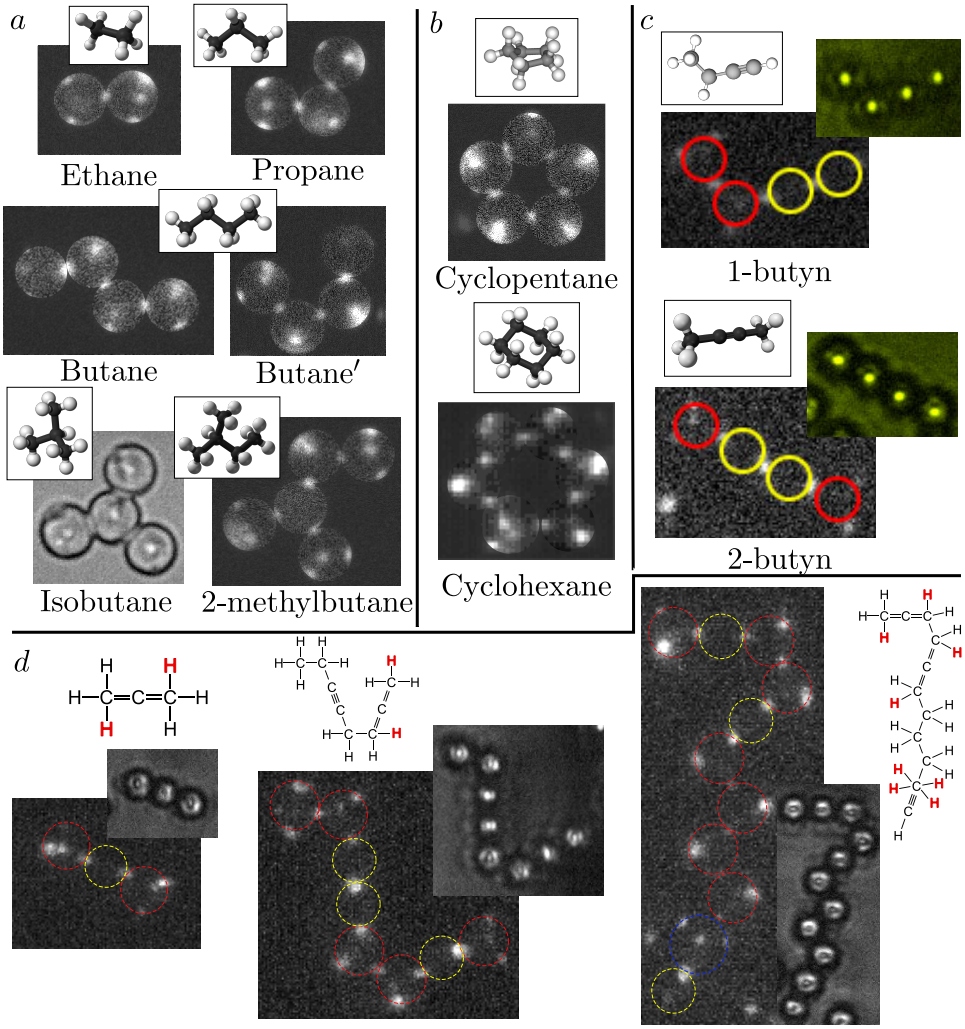


Figure 5.2: Colloidal analogues of hydrocarbon molecules (a) non-cyclic tetrapatch structures and their molecular equivalents (b) cyclic tetrapatch compounds, (c) mixtures of tetrapatch (red) and dipatch particles (yellow) (d) Colloidal molecules that have no molecular analogue, higher order hexapatch particle in blue

crepancy is that during synthesis sometimes higher order patchy particles are formed. When those get incorporated in structures this also produces colloidal molecules with no chemical equivalent.

Yet, in the cases where the mapping exists it respects geometry. Some of the mechanical properties of a molecule might be related to their colloidal analogous, especially those that are determined by morphology rather than interaction details.

These might include vibrational modes or the switching of 3d conformations.

## 5.3 Colloidal polymers

So far, we focused on clusters of a small number of patchy particles. However, in order to create functional self-assembling materials, control over larger structures with more particles is necessary. With size, the number of degrees of freedom grows, and thus the complexity. In order to keep this complexity manageable, we first focus on the assembly of dipatch particles. As shown, their limited valency results in the formation of solely linear structures, chains. In comparison, the possible structures that can be formed by particles bonding with more than two neighbors grows exponentially with cluster size, as shown above by the many molecular analogous formed by the tetrapatch particles, or the multiple compact clusters of isotropic and Janus particles [51, 199]. This strong structural reduction for dipatch particles allows us to investigate detailed questions concerning formation kinetics and many-body steric effects. In a second step, we add a limited number of tetrapatch particles to the dipatch samples that act as branching points of chains, to tune structure formation in a controlled way.

### 5.3.1 Colloidal polymers from dipatch particles

When temperature is increased close to $T_c$, dipatch particles polymerize into chains of various length, see Fig. 5.3(a). Application of the clustering algorithm enables us to identify individual chains, even in regions where these are located close to each other, as can be seen by the coloring. Mostly linear straight chains form, which can bend slightly when they get longer. However, we also see some kinks and branching points, which we associate with the presence of particles of higher valency. To explore the analogy with polymers, we define the concentration of chains of length $x$ as $P_x = N_x/N$, with $N_x$ the number of chains of length $x$ and $N$ the total number of chains. Apart from an excess of singlets, the distribution of chain lengths shows an exponential decay (Fig. 5.3a). Such a distribution can be described as a geometric distribution $P_x = p^{(x-1)}(1-p)$, where $p$ is the probability that a particle is bonded [225]. While polymerization progresses, $p$ increases closer to 1, as can be seen from the slope of the fitted red line, equal to $log(p)$.

To study the growth kinetics in more detail, we characterize the evolution of chain lengths. In analogy to polymer molecules, we define the number-average degree of polymerization $X_n$, weight-average degree of polymerization $X_w$, and polydispersity index PDI, given by [226]

$$X_n = \frac{\sum xN_x}{N}, \quad X_w = \frac{\sum x^2 N_x}{\sum xN_x}, \quad PDI = \frac{X_n}{X_w}. \tag{5.1}$$

The former, $X_n$, indicates the average chain length, while the second quantity, $X_w$, describes the average length weighed by the mass of the chain. This second quantity

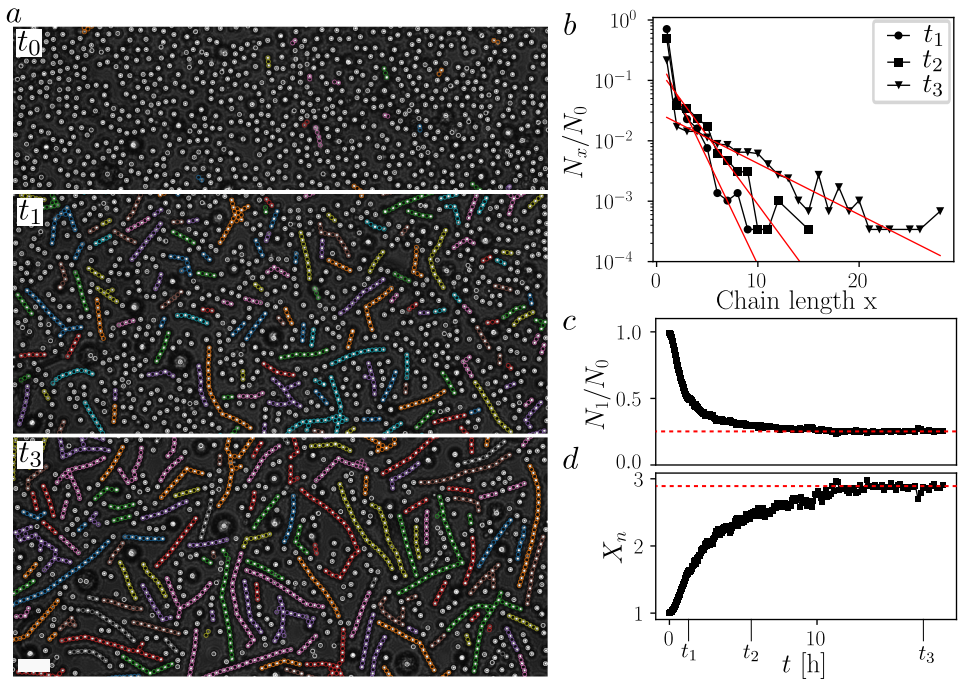


Figure 5.3: (a) Experimental bright field microscopy images of dipatch particles polymerizing in chains. At $t_0$ interaction is turned on by a temperature quench to $\Delta T = 0.08$K, $t_1 = 2$hours $t_3 = 18$hours. Overlain are circles centered at located particle coordinates and identified bonds, circles are colored identical if the particles and bonds belong to the same chain, singlets are in white. Scale bar is 25$\mu$m (b) Chain length distribution at $t_1$, $t_2$ and $t_3$. (c) Decrease of monomer concentration versus time (d) Number average degree of polymerization. Red dotted lines show saturation value. (Video: *https://youtu.be/DmA70xEYrzY*)

is less sensitive to small chains as they carry little mass, such that $X_w > X_n$. The last quantity, $PDI$, is a measure for the polydispersity, the spread in the size distribution. If all chains have the same length, $X_w = X_n$ and $PDI = 1$, while for a geometric distribution $PDI = 1 + p$.

As chains form, the number of monomers $N_1$ decreases over time, see Fig. 5.3(b). Chains do not only grow by monomer addition, oligomer bonding also occurs in which two chains bond to form a single longer one. Such polymerization conditions are similar to "step-growth polymerization" also known as "polyaddition polymerization" [226]. The bonding of dipatch monomers and oligomers into chains is captured by an increasing degree of polymerization $X_n$, see Fig. 5.3(c). Both the rate of decrease of monomers and the rate of increase of polymerization gradually slow down over time until they saturate at a constant value. Though bond dissociation occurs, it is unlikely that an equilibrium steady state is reached given the low dissociation rate

associated with the high average bond lifetime which we estimate to be $\gtrsim$ 10h. This estimation is based on observing that only around 5% of formed bonds dissociate during the assembly experiment. We thus hypothesize that the observed saturation is due to crowding effects.

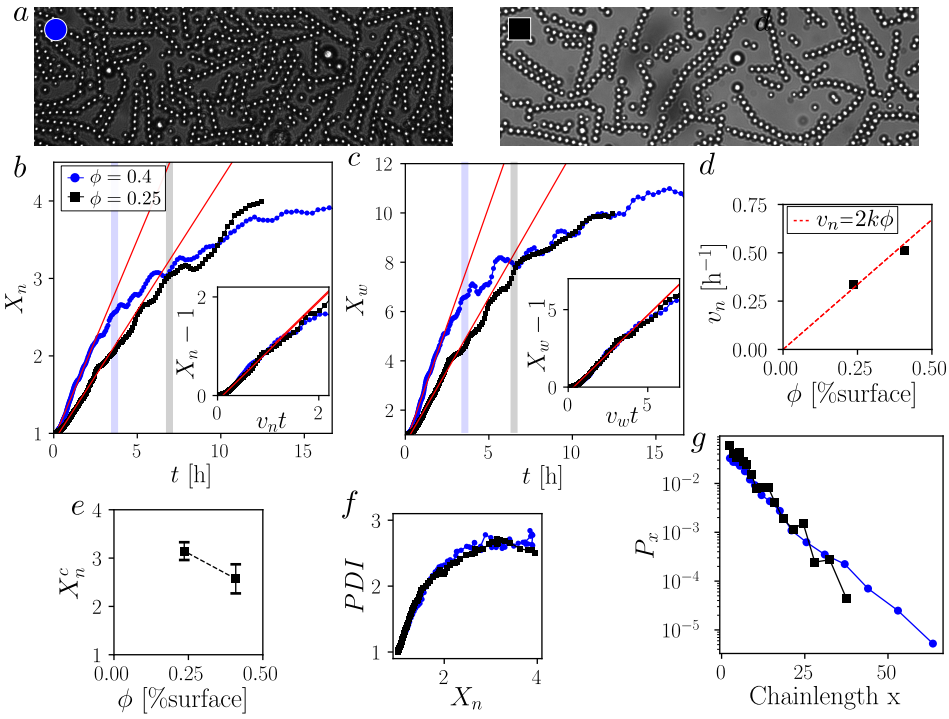


Figure 5.4: Colloidal polymers at two different concentration, in all graphs blue (black) circles (squares) correspond to a surface coverage $\phi = 0.41(3)$%area and $\phi = 0.24(3)$%area. Samples were set to approximately the same interaction strength at $\Delta T = 0.12$ (blue) and $\Delta T = 013$ (black). (a) Microscopy images of the two samples at the end after 10 hours of assembly (b) Number average degree of polymerization, red lines are linear fits of the initial growth rate, vertical bars indicate the time from which growth rate becomes sublinear due to crowding. Inset shows a rescaling using the slope of the linear fit $v_n$ (c) Similar for the weight average degree of polymerization. (d) Initial polymerization growth rate $v_n$ and linear fit $v_n = 2k\phi$ with reaction rate $k = 0.6$ h$^{-1}$%$_{\text{surf}}^{-1}$ (e) Critical polymerization $X_n^c$ at the transition to sublinear growth. (f) Polydispersity index versus degree of polymerization (g) Geometric chain length distributions averaged over final frames

To investigate effects of dynamic frustration due to crowding we varied the surface coverage, $\phi$, while keeping the temperature (interaction potential) constant. Upon decreasing the volume fraction, the polymerization process is initially slower, see Fig. 5.4(b,c). Surprisingly, at later times, the less dense sample overtakes the

denser samples. This is counterintuitive as the growth rate is expected to scale with concentration, and suggests that indeed crowding effects are present. To extract the initial polymerization rate before crowding, we fitted a linear growth model to the data points that satisfy $X_n < 2$ given by:

$$X_n = v_n(t - t_0) + 1, \tag{5.2}$$

where $v_n$ is a growth rate and $t_0 \approx 0$ is a small offset that was kept as a fitting parameter to account for deviations from linearity at short times, for instance due to thermal equilibration of the heating stage. A similar fit was done for $X_w$ to obtain a growth rate $v_w$. The fits, indicated by red lines in Fig. 5.4(b,c), show that a linear growth initially agrees well with the data. This is further shown by the data collapse in the insets.

A linear growth as described by Eq. 5.2 is reminiscent of step-growth polymerization, which predicts a growth rate proportional to the initial monomer concentration $v_n = 2k\phi$, where $k$ is the rate constant [225, 226]. By plotting $v_n$ as a function of the concentration $\phi$ we indeed observe a linear trend, see Fig. 5.4(d). From the fit, we extract a rate constant $k = 0.6\ \mathrm{h}^{-1}\%_{\mathrm{surf}}^{-1}$. We attribute this slow rate to the large diffusion time $\tau_{diff}$ and the small reactive surface portion of the patches. The self diffusion time $\tau_{diff} = d^2/D = 260(5)$s, where we have used the particle diameter $d = 3.2(2)\ \mu$m, and the diffusion constant $D = 0.035(5)\ \mu\mathrm{m}^2/\mathrm{s}$, which was measured by tracking the diffusion of particles before bonding.

After the linear regime another growth regime is entered. The transition occurs at a reasonably well-defined critical time $t_c$ and associated polymerization $X_n^c$ where a strong slope change occurs, most clearly visible in the weight averaged polymerization $X_w$, see vertical bars in Fig. 5.4(b,c). We determined $t_c$ as the moment the relative error is bigger than 10%, $(X_n^{fit} - X_n)/X_n > 0.1$. This criterium is somewhat arbitrary but allows us to compare both experiments systematically, see Fig. 5.4(e). It shows, that the transition for the less dense sample not only occurs at a later time but also reaches a higher critical polymerization $X_n^c$. This means that this delay is not simply a consequence of a lower linear growth rate but that the cause of the transition is reduced for the less dense sample. We therefore interpret this transition as due to dynamic frustration. While chains form, rotational diffusion gets more frustrated making it more difficult for free binding sites to find each other. For lower volume fraction, this frustration occurs later, as chains can grow larger before they start hindering each other.

Nevertheless, the decreased growth rate and delayed crowding transition do not appear to influence the size distributions. This is seen by the polydispersity index that collapses if plotted versus $X_n$, Fig. 5.4(f). This is further confirmed by the final distributions, which appear similar for both experiments, see Fig. 5.4(g). The $PDI$ saturates at a value approximately 2.5. This is higher than expected for a geometric distribution and likely caused by a overabundance of unreactive monomers.

Another interesting dependence concerns the bond strength. The strength of the critical Casimir interaction is directly controlled by temperature. We find that the polymerization kinetics speed-up when approaching $T_c$, see Fig. 5.5(b). Rescaling

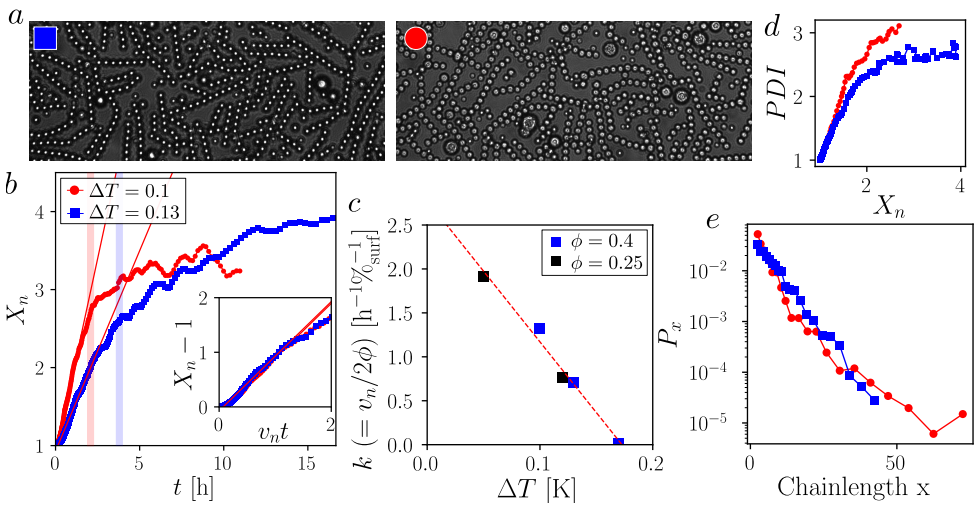


Figure 5.5: Colloidal polymers at different temperatures, red (blue) circles (squares) correspond to a distance to the critical temperature $\Delta T = 0.1$ and $\Delta T = 0.13$ at approximately the same volume fraction $\phi = 0.42$ (red) $\phi = 0.41$ (blue). (a) Microscopy images of the two samples at the end after 10 hours of assembly (b) Number average degree of polymerization, red lines are linear fits of the initial growth rate, vertical bars indicate the time from which growth rate becomes sublinear due to crowding. Inset shows a rescaling using the slope of the linear fit $v_n$ (d) Reaction constant obtained from the initial polymerization growth rate via $k = v_n/2\phi$, shown as a function of temperature with a linear interpolation (red dotted line), black and blue squares refer to measurement with two different particle concentrations (e) Polydispersity index versus degree of polymerization (f) Chain length distributions averaged over final frames

time with the initial growth rate $v_n$ obtained by fitting again collapses the growth of $X_n$ at early times. Using the previously established relation $k = v_n/2\phi$ we can then extract the dependence of $k$ on $\Delta T$. Combining all the experiments we obtain a clear trend where the reaction constant increases with increasing interaction strength, see Fig. 5.5(c). A heuristic fit $k = \alpha\Delta T + \beta$ (red dotted line) predicts no significant assembly beyond $\Delta T \approx 0.18$, which agrees with observations.

Beyond the linear growth regime both temperatures show the breakdown of the initial regime and a transition to a slower kinetics, Fig. 5.5(b). Interestingly, at higher temperature the transition happens for slightly higher $X_n^c$. As these samples have the same particle concentration this suggests that the slower kinetics is not only influenced by crowding but also by interaction strength. An explanation could be that the observed assembly slow down is not only caused by crowding but also by break-up events. These are less frequent for higher interaction strength as the bond life time increases.

### 5.3.2 Crosslinked colloidal polymers from dipatch tetrapatch mixtures

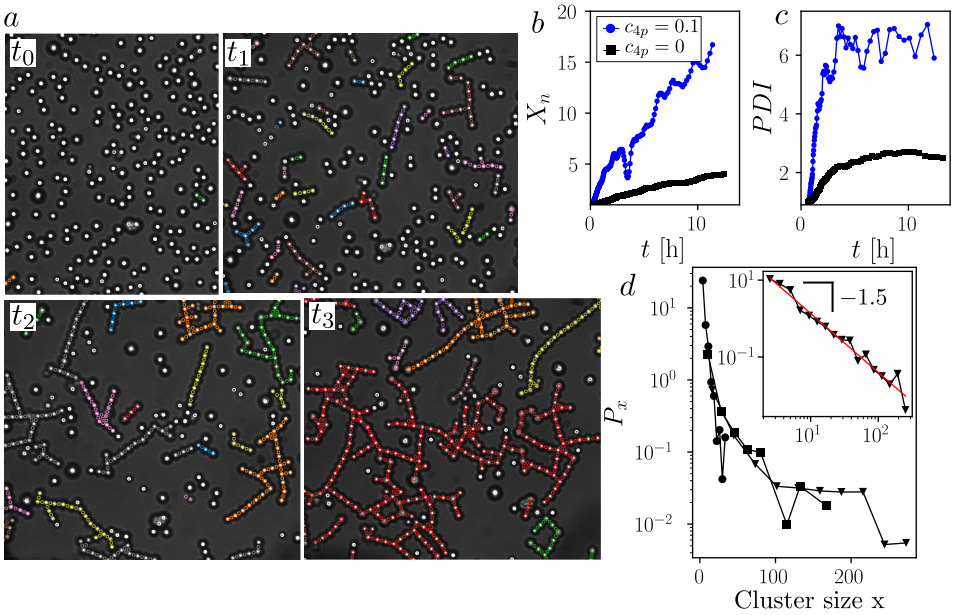


Figure 5.6: Including tetrapatch particles crosslinks colloidal polymers (a) Experimental bright field microscopy images of dipatch particles mixed with a fraction $c_{4p} = 0.1$ of tetrapatch particles polymerizing into branched and crosslinked chains. At $t_0$ interaction is turned on by a temperature quench to $\Delta T = 0.08$K, $t_1 = 10$ minutes $t_2 = 1$ hours, $t_3 = 10$ hours. Overlain are circles centered at located particle coordinates and identified bonds, circles are colored identical if the particles and bonds belong to the same chain, singlets are in white. (b,c) Number average degree of polymerization and polydispersity index , for comparison also the previously studied samples without extra tetrapatch particles $c_{4p} = 0$ are shown. (d) Cluster size distribution on semi log and log-log scale (inset) with a power law fit (red line).

By including a fraction $c_{4p} = 0.1$ of tetrapatch particles with respect to dipatch particles, kinked and highly branched chains assemble that form a crosslinked polymer analog, see Fig. 5.6(a). In this growing network, tetrapatch particles act as crosslinkers connecting linear strands made from dipatch particles. The singlet concentration $N_1/N_0$ and mean cluster size, $X_n$, show an initial linear growth regime followed by a second slower regime, similarly as for dipatch assembly, Fig. 5.6(b). However, as expected from the increased number of binding sites, the growth of the structure happens significantly faster. Furthermore, the cross-linked polymer reaches a much larger mean cluster size. In addition, a much higher polydispersity is reached as shown in Fig. 5.6(c). This can be understood from the full cluster size distribu-

tion, which starts off exponential but quickly develops a pronounced tail resulting in a large $PDI$, see Fig. 5.6(d). This is markedly different from the purely linear polymers that remained exponential throughout. The final distribution approaches a power law $P_x \propto x^w$, with a power $w = 1.5(1)$, see inset of Fig. 5.6(d).

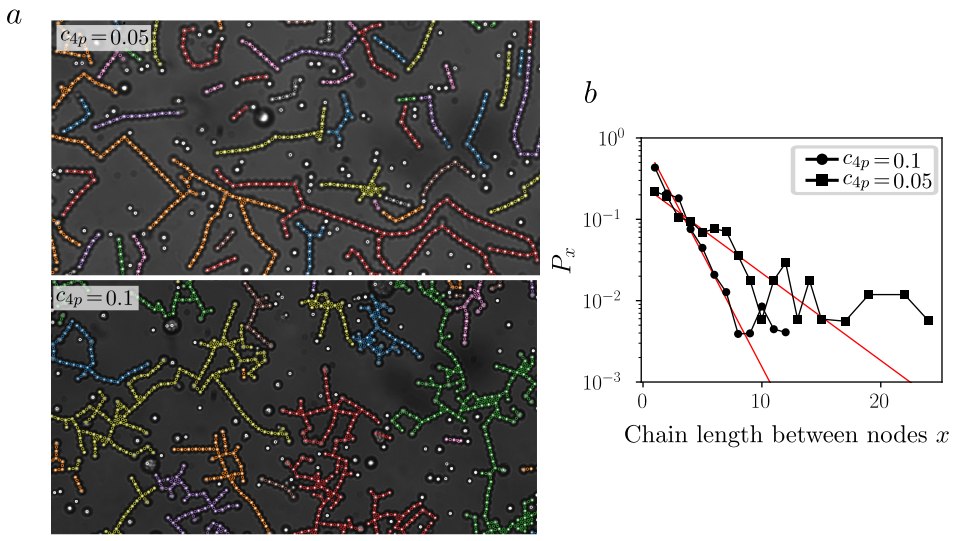


Figure 5.7: Tuning crosslinked polymer morphology by amount of tetrapatch particles (a) Images of two different tetrapatch to dipatch fractions (b) Distribution of strand length in between particles that are bonded with three or more particles.

Reducing the fraction of tetrapatch particles decreases the number of crosslinks and results in longer chains of dipatch particles between branch points that act as nodes in the network, see Fig.5.7. We can quantify this by first identifying the node particles that have more than two neighbors, and running the clustering algorithm without these particles, identifying only dipatch chains. The resulting distribution of strand lengths connecting branching points shows an exponential decay, with a characteristic length scale that is higher when less tetrapatch particles are present, see Fig.5.7. We can thus tune the network morphology by the amount of tetrapatch particles: Including more tetrapatch particles decreases the average mesh size.

## 5.4 Patchy colloidal gels

The previous results suggest that with increased aggregation time and at high enough volume fraction, the branched dipatch-tetrapatch clusters can percolate to form a space spanning network and reach a gel state. However, such long aggregation times make these experiments tedious. To speed up the formation kinetics we used smaller particles. These smaller particles, with sizes of $d = 1.6 \pm 0.1$ $\mu$m (dipatch) and

$d = 1.8 \pm 0.1$ $\mu$m (tetrapatch) do not only diffuse faster, but they also have a larger gravitational height $z_g \approx 3$ $\mu$m. Because in this case $z_g > d$ settled particles can diffuse vertically over each other, avoiding being trapped.

The resulting network structures are shown in Fig. 5.8. The images suggest the formation of a three-dimensional network. We observe that for low volume fraction branched polymer structures form (a). When volume fraction increases, these structures grow larger (b), after reaching a high enough volume fraction, a percolated network forms (c,d): Higher valent tetrapatch particles connect dipatch strands into an interconnected network. The dipatch strands vary in length, and some have grown quite long, reaching maximally $\sim 15$ particles. When strands meet, they do so predominantly at preferred angles $\sim 110°$, a consequence of tetrahedral symmetry of the tetrapatch particles. This is indicated using yellow wedges with a fixed inner angle, overlaid for some example nodes. Some nodes deviate from this angle which can be explained partially by a minor fraction of non-tetrahedral symmetric patchy particles. Additionally, these deviations are explained by optical artifacts. The images show only a single optical slice of a structure that extends slightly in z. A more exact investigation would require 3d localization to determine the bond angles.

Due to the fact that the increased gravitational height ($z_g = 3\mu$m) is higher than the particle diameter, these particles are not as much confined to a 2d sediment as the previously used bigger particles. Instead, they form a layer that is around three particle diameters thick. This has the interesting consequence that strands can overlap, as can be seen by the side views (confocal z-slices), in Fig 5.8(e,f,g). These images show dipatch strands, on the bottom of the capillary, being crossed by other dipatch strands.

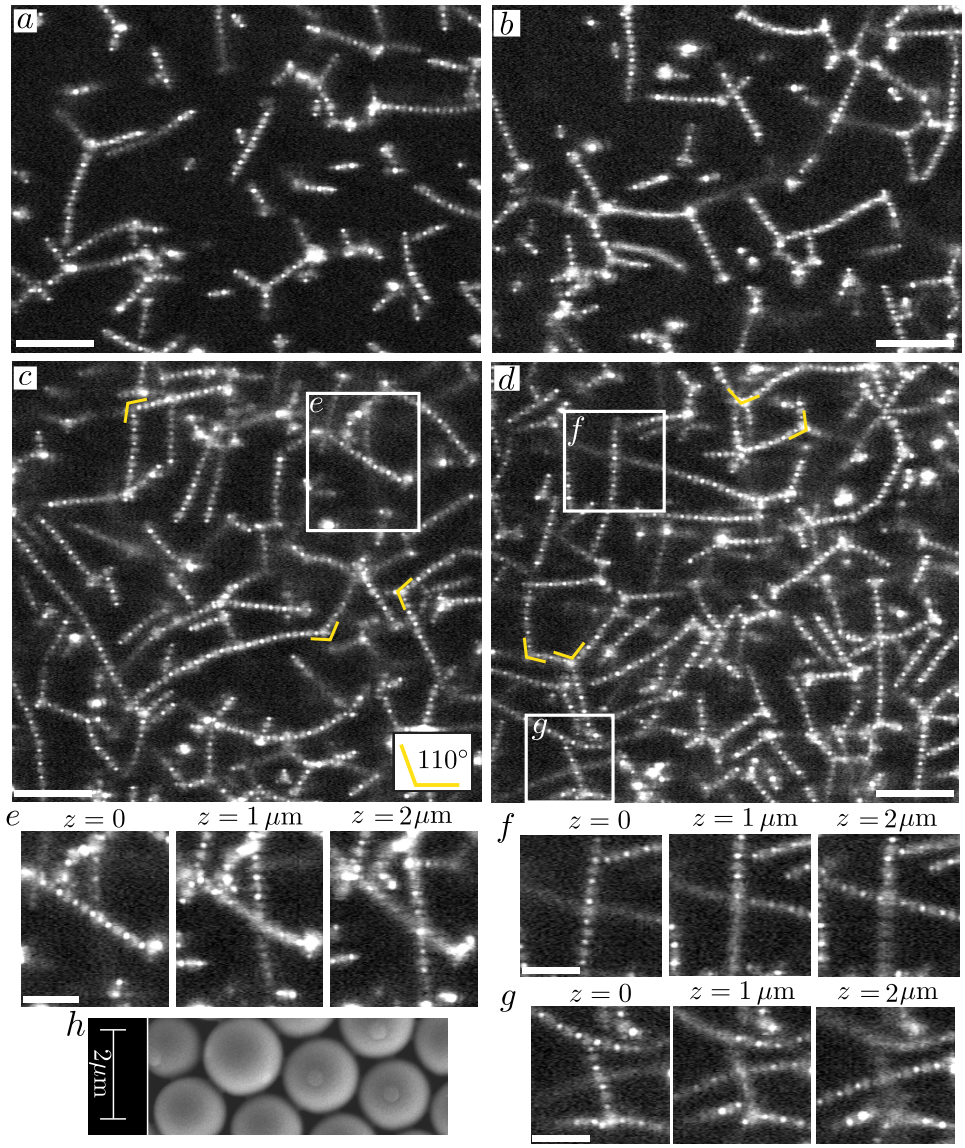


Figure 5.8: Patchy colloidal gels made from smaller dipatch particles mixed with a fraction of tetrapatch particles (10%), after 1 hour assembly at $\Delta T = 0.1$ (a,b,c,d) Confocal microscope slices of structures for increasing particle densities, (c,d) have a high enough density to feature a percolated network. The z-focus is chosen close to the capillary floor, at the height where most patches are in focus. The scalebar is 10 $\mu$m. Yellow wedges in (c,d) measure 110°. (e,f,g) Zoomed-in 3d stacks of area's marked by white rectangle in (c,d) that feature overlapping gel strands, each series shows 3 slices with 1 $\mu$m in between. (h) Electron micrograph the small patchy particles. (Video: *https://youtu.be/zWmYgxifbU8*)

It is interesting to compare these patchy particle colloidal gels to a conventional colloidal gel that arises through arrested phase separation. Though they are both percolated disordered networks, the features of the patchy colloidal gel are markedly different. First of all, conventional gel strands do not have a fixed width, but typically are multiple particles wide and vary strongly in thickness throughout the network. Here, the width cannot grow beyond single particle as the particles' binding sites fully occupied. This is clearly demonstrated by the overlaying gel strands that do not bond, even though they are touching. Such behavior will be impossible in a conventional gel where overlapping strands will connect to form a node. Another interesting difference lies in the nodes: A conventional gel has nodes consisting of dense closely packed particle regions, with a random number of strands meeting, at random intersection angles. In the patchy gel, however, nodes consist of single higher valent particles instead of close packed clumps. These higher valent particles are tetrapatch particles, restricting the number of possible connecting branches to a maximum of four and fixing the angle at which strands connect to tetrahedral angles $\sim 110°$.

Such structural differences will likely be accompanied by rheological differences between conventional and patchy gels. For instance, the fact that all particle strands are of unit width and nodes are single particles, will cause the mechanical stability of the gel to be much more sensitive to the bending rigidity of the individual bonds. Put in another way, due to the limited valence, $f$, of the dipatch ($f = 2$) and tetrapatch ($f = 4$) particles, the connectivity of the patchy gel network is on average $f = 2.2$. This is well below the Maxwell criterium, which states that an isostatic structures needs a least 6 bonds per particle in order to obtain overall rigidity. However, this criterium neglects the contribution of bending rigidity between bonds. Effects of shear resistance and resulting bending rigidity of dipatch particle chains will be explored further in the following chapters 6 and 7. If indeed such bonds possess significant bending rigidity these gels are accurate analogues of semiflexible networks found in biological gels such actin, collagen and fibrin network, with intriguing properties owing to the competition between bending energetics and entropic elasticity [68].

Finally, it is interesting to think about the thermodynamic difference between patchy particle and conventional gels. For patchy particle gels, gelation is simply due to the energetic advantage of maximizing the amount of bonded patches, whereas for conventional gels, a kinetic arrest needs to take place. The deeper consequence of this difference, which has been shown by simulations, is that patchy gels are thermodynamic equilibrium states and will not show aging [194, 221]. Such a fundamental contrast has prompted researchers to exclaim that these equilibrium patchy gels can be considered as a new disordered state of matter [59, 227]. In order to verify if the patchy gel that was formed in our system is indeed an equilibrium gel, more extensive characterization is required, involving a more quantitative structural determination through particle locating and dynamic studies to study formation kinetics and aging.

## 5.5 Discussion and conclusion

We demonstrated a new method based on the critical Casimir effect, to obtain reversible patch bonding between dipatch and tetrapatch particles using higher valent salt to induce boundary condition contrast. This method eliminates the necessity of often difficult secondary surface treatments during synthesis, potentially applicable to other particles as well. We showed that we can mimic different types of molecules using these patchy particles. Small clusters form analogues of carbon molecules. Larger number of dipatch particles form analogues of polymers that can crosslink with the addition of tetrapatch particles. In addition, we showed that smaller dipatch and tetrapatch mixtures form percolated gel networks.

We observed exponential chain length distributions for the linear polymer system in agreement with literature/theory on molecular polymers. Exponential distributions are expected for a variety of systems. For instance, reaction-limited step-growth polymerization shows an exponential distribution [225, 226]. This kind of polymerization is a non-equilibrium process. However, also in simulations of equilibrium polymerization of two-patch particles, exponential distribution are observed [228]. Therefore, one cannot conclude on the mechanism of growth from the length distribution alone.

It is interesting to compare the observed growth kinetics with colloidal polymerization for much smaller nanoparticles, in which $X_n$ was likewise found to increase linearly with time [225]. There, a description in terms of a reaction limited step-growth process was found to apply which assumes a bond formation kinetics independent of chain length [226]. This suggest the early regime in our case also can be understood as step-growth polymerization. However, upon later times the linear growth breaks down and a transition to slower growth is observed, leading to a non-equilibrium steady state. We identified the main cause of this slow down as frustration by crowding. By decreasing the particle concentration the degree of frustration is lowered and the transition is delayed. In addition bond breakage is observed. This also slows down the growth kinetics and could in principle lead to an equilibrium steady state if crowding could be avoided by using low concentration samples. However, due to the slow kinetics and associated long measurement times, we are unable to conclude whether for lower concentration an equilibrium steady state can be reached.

The results presented here establish the critical Casimir self-assembly of patchy colloids, and open many new opportunities of colloidal assembly. The small-scale colloidal molecules are designer colloidal structures on their own right, and it will be interesting to explore their mechanical properties in a similar way as was done for the simple chains in chapter 4. Furthermore, here we have not considered the out-of-plane 3d conformation of some of these structures. For specifically the cyclic compounds, colloidal pentane and hexane, these might show similar stable 3d conformations as known from their molecular analogues, e.g. chair and boat conformations. In that case, they would be examples of microscopic self-assembled structures with mechanical multistability, which is a desirable property for the design of metamate-

rials [70].

Going beyond small-scale structures, simulations have shown that patchy particles can show equilibrium gelation, forming disordered networks that are thermodynamically stable [194, 221]. The cross-linked clusters that we assembled using mixture of dipatch and tetrapatch particles likely form space-spanning networks with increased number of particles and aggregation time. In addition, using smaller particles, the faster formation kinetics allows the formation of gels on easily accessible timescales. The increased gravitational height of these smaller particles makes it feasible to density match particles and solvent. These are good potential candidates for equilibrium 2d and 3d gels, of which experimental realizations exist, but only using nanoscopic particles [229, 230]. The direct imaging available for equilibrium gels of micron sized particles would provide an improved way to study not only their structure, but also their mechanical properties. The mechanical properties of such equilibrium gels have been recently shown to sensitively depend on the interplay between valence and network structure [231]. The control over these parameters using patchy particles provides opportunities for tuning material elasticity.

CHAPTER 6

# Mechanics of fluctuating dipatch chains: tuneable bending rigidity and internal friction

*Bending rigidity determines the stability and functionality of slender structures ubiquitous in soft and biological materials such as colloidal gels and biopolymer networks. We use critical Casimir bonded dipatch particles to create colloidal chains that act as well-controlled analogues of such slender microscopic structures. By studying the dynamics of thermally induced bending fluctuations we characterize the mechanics of these chains. We show that they are well modeled as semiflexible filaments, with a persistence length that is set by patch size and the strength of the critical Casimir bond. We furthermore reveal visco-elastic effects on longer timescales that we attribute to internal friction. Our results show that the critical Casimir force can not only be used to in-situ rationally control the radial interaction strength between particles but, by using patchy particles, also the shear rigidity between bonded colloids. This further extends to uses of this well controlled model system and paves the way for using patchy particle assemblies as building blocks of colloidal architecture with bending rigidity as a rational control parameter.*

# 6.1 Introduction

With the realization of a well controlled and patchy aggregating system, we reach a stage were we can ask detailed questions about the physics of such assemblies. The directed interaction causes the formation of geometrically reproduceable structures such as straight chains or networks with specific bond angles, some of which have molecular or biological analogues. Because patchy assemblies are more open, these geometrically defined structures have interesting, distinct rheological properties, determined by the local bonds and small scale structures that they form.

Aggregated colloids often form rigid bonds that can resist shear and develop bending rigidity, [116, 214]. Bending rigidity is an important considerations for controlled self-assembly of a desired colloidal architecture as it influences the formation process and effects the final structural stability [232]. Bending rigidity can also have interesting dynamic effects, for instance when coupled with activity flexible chains diffuse markedly faster compared to their stiff counterparts [233]. As described in chapter 4, also Critical Casimir aggregated colloids form rigid bonds, with the advantage that we can tune the attractive strength by changing the temperature w.r.t. the critical point. The radial interaction strength increases as predicted from theory and observed in experiment [123], further confirmed for off-critical compositions in chapter 3. However it is so far not studied what the effect of temperature on bending rigidity will be.

In this chapter, we explore in detail the mechanics of a chain of dipatch particles bonded with the critical Casimir interaction. We look at the thermally induced fluctuations of a quiescent chain as a function of the distance to the critical point. In analogy to biological filaments such as actin filaments and microtubules, we show that the chain can be modeled as an semiflexible filament with well-defined bending rigidity. We find that, like the interparticle radial interaction strength, the bending rigidity increases as temperature is increased closer to the critical point. We furthermore perform an extensive dynamic analysis that reveals a rich visco-elastic behavior. Fluctuation relax in a two-step dissipative processes, which we associate with external drag friction and internal friction most likely due to slow conformational changes. This strengthens the analogy with biological filaments, which also show significant visco-elastic behavior [234]. These result pave the way for using patchy particle assemblies as building blocks of colloidal architectures with bending rigidity as a rational control parameter. Especially for low coordinated self-assembled structures, such as the patchy colloidal gel described in the previous chapter, bending rigidity is paramount in determining rheological behavior. Programmatic control over bending rigidity could dramatically shift a materials response from rigid to floppy or from bending dominated to stretching dominated [235, 236].

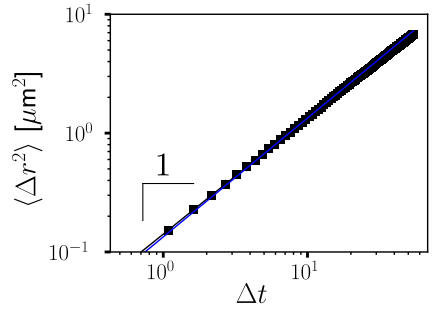


Figure 6.1: Diffusion dynamics of dipatch particles (a) average mean square displacement of 300 particles of batch A. Blue line is a fit to two d diffusion $\langle \Delta r^2 \rangle = 4D\Delta t$.

## 6.2 Methods

We used spherical dipatch colloidal particles with two different patch sizes, see chapter 2 for synthesis and characterization. The larger patch particles, referred to as DP-A particles, have an average radius of $r = 1.6 \pm 0.05$ $\mu$m, where the uncertainty is the polydispersity, see table 2.1 in chapter 2. The smaller patch particles, referred to as DP-B particles, have an average radius of $1.55 \pm 0.05$ $\mu$m. Their patch sizes can be quantified in terms of the patch arc angle $\theta_p = 2\sin^{-1}(d_p/(d))$, with $d_p$ the patch diameter, finding for DP-A particles $\theta_p = 21°(\pm 2)$. Here the uncertainty is the standard deviation of the measured patches and gives the patch size polydispersity. Whereas DP-B particles had a patch size of $\theta_p = 14°(\pm 2)$.

In order to induce Critical Casimir interactions, particles were dispersed in a binary mixture of water and lutidine with a lutidine volume fraction of $c_{lut} = 25\%$. Salt (0.375 mM Magnesium sulfate) is added to induce an adsorption preference contrast between patch and particle bulk, such that lutidine preferentially adsorbs to the patches whereas water to the particle bulk, as described in chapter 5. The particular binary mixture and salt concentration was chosen to obtain optimal critical Casimir conditions with a largest temperature window of patch-to-patch attraction, as described in chapter 2. In addition the added salt screens the electrostatic repulsion leading to a Debye length of $\lambda_D = 4.5$ nm. The phase separation temperature was measured to be $T_{cx} = 33.75°$C. From now on, rather than mentioning the absolute temperature of the system $T$, we refer to temperature mainly relative to this coexisting temperature by defining $\Delta T = T_{cx} - T$. The density of the binary mixture is $\rho_s = 0.981$ g/ml, and the density of the colloids is $\rho_{part} \approx \rho_{PS} \approx 1.05$ g/ml. Due to their size and higher density the particles readily sediment into a quasi two-dimensional layer. This can be explained by their gravitational height $z_g = kT/(\Delta mg)$, where $\Delta m = \frac{4\pi}{3} r^3(\rho_{part} - \rho_s)$ is the buoyant mass. For DP-A particles $z_g = 0.4$ $\mu$m and for DP-B particles $z_g = 0.35$ $\mu$m. These heights are significantly smaller than the particles radii causing the particles to form an effective monolayer once settled.

Because these particles are so close to a wall their dynamics is significantly slowed down due to hydrodynamics effects [237]. Before assembling the particles into chains we did a careful characterization of single particle dynamics in the binary mixture at $\Delta T = 2$, where critical Casimir forces are absent. This has been done to later compare single particle dynamics with the dynamics of chain bending fluctuations. The average mean square displacement of sedimented DP-A particles is shown in Fig. 6.1a. Fitting to a diffusive power law we obtain $D = 0.035 \pm 0.005$ $\mu$m$^2$/s, and an effective drag coefficient $\gamma = kT/D = (120 \pm 20)$ mPas$\mu$m. The diffusion coefficient is two times as low as expected from $D_{einstein} = kT/6\pi r\eta = 0.074\mu$m$^2$/s. Here we used that at $T = 30$ C° the viscosity $\eta = 1.9$mPas for the binary mixture [238]. The difference between the measured $D$ and $D_{einstein}$ is not surprising given the gravitational height of the colloids $z_g \approx 0.4\mu$m. For $z_g < r$ diffusion is expected to slow down significantly due to hydrodynamic particle wall interactions, according to [237]

$$D = D_{einstein}\left(1 - \frac{8}{15}\ln(1-\beta) + 0.029\beta + 0.04973\beta^2 - 0.1249\beta^3\right)^{-1}, \qquad (6.1)$$

where $\beta = r/h$ and $h$ the height of the particle center. Fitting this equation we find $h - r = 0.2$ $\mu$m, of the same order of magnitude as $z_g$ and a better estimation of the actual height.

### 6.2.1 Experimental protocol and imaging

After the particle samples were prepared they were placed on a temperature controlled microscope and let to sediment forming a homogeneous quasi 2d dispersion. Next, dipatch chains were formed by heating the sedimented patchy colloids to a $\Delta T = 0.10$ K below $T_{cx} = 33.75$°C. At this temperature patches become attractive whereas the particle bulk remains repulsive, as shown in chapter 5. Fine temperature control is achieved using an objective collar and sample heater coupled to a single water bath with a setting accuracy of 0.01 K and thermal stability estimated at 0.02 K.

To evaluate thermally induced fluctuations, we used conventional light microscopy to image chains conformations at a frame rate of 2 fps at various temperatures over a time of 30 minutes at each temperature. We used bright field microscopy instead of fluorescent microscopy in order to avoid artefacts due to bleaching during the long measurement time. The particle density was chosen such that chains of significant lengths could assembly yet be low enough to minimize steric interactions due to crowding. In the field of view chains of different length $N$ were present, with $N$ ranging from an effectively single dipolar bond $N = 3$ to a longest chain $N = 15$. This big field of view allowed us to compare bending fluctuations of differently sized chains using only a single recording. Most analysis was performed on the $N = 15$ chain, but in order to investigate the effect of length we also looked at shorter chains. Temperature was increased stepwise to a maximum $\Delta T = 0.05$ K, with steps of 0.02 K,

waiting at least 10 minutes before measuring to ensure thermal and mechanical equilibration at each step. By doing so we gradually increased the critical Casimir force as we get closer the phase separation temperature. Next, temperature was similarly decreased to $\Delta T = 0.2$ K. When a temperature $\Delta T = 0.17$ K was reached some bonds of the chains broke. When decreasing temperature to $\Delta T = 0.2$ K all bonds disintegrated due to the reversibility of the critical Casimir interaction. Particle centers are located in the recorded image plane with pixel size 103 nm with a subpixel accuracy of $\epsilon = 20$ nm using particle-tracking software [122].

The above described procedure was used for the larger-patch DP-A particles. To investigate the effect of patch size we performed similar fluctuation experiment with the small-patch DP-B particles. These experiment were done at only a single temperature. Chains were assembled at a fixed $\Delta T = 0.10 \pm 0.05$K. Fluctuating chains were recorded at a frame rate of 20 fps. The slightly higher uncertainty in temperature, and the higher recording frame rate with respect to the previous measurements are because a different setup was used.

## 6.3 Results and discussion

### 6.3.1 Static analysis: elastic moduli tunable by temperature

Images of the assembled chains are shown in Fig. 6.2. Fig. 6.2a shows a zoomed out bright field image giving an overview of the assembled chains that were studied. Fig. 6.2b shows an epifluorescent close up of a single chain, proving that only the labeled fluorescent patches form bonds. The chains, though on average straight, fluctuate due to thermal noise. With decreasing temperature (decreasing critical Casimir interaction strength) the amplitude of these fluctuations increases. This can be seen by comparing the amplitude of undulation between a chain at $\Delta T = 0.5$ and $\Delta T = 0.15$, see Fig. 6.2c. The amplitude of thermal fluctuations is expected to scale inversely with chain stiffness. Therefor, these qualitative observations are the first indications that show the tunability of bending rigidity with temperature. Decreasing temperature further to $\Delta T = 0.17$, causes chain breakup as the critical Casimir interaction becomes to weak for the chain to remain fully bonded.

We define the tangent angle $\phi_i = \arctan\left(y_{i+1} - y_i\right)/(x_{i+1} - x_i)$ of each bond and the bending angle $\theta_i = \phi_{i+1} - \phi_i$ as depicted in Fig. 6.3(a,b). We measure the variation in bending angles at a fixed temperature over a time period of 30 minutes, Fig. 6.3(c,d). Over time these bending angles fluctuate around zero, as can be seen by the density profiles of individual angles which are centered at zero, shown for 3 representative cases in Fig. 6.3(e). This confirms the chain is straight on average. We fit the density profiles to a gaussian distribution (black lines), to obtain standard deviations $\sigma(\theta_i)$, a measure for the amplitude of fluctuation. Not each angle shows the same deviation. To obtain a fluctuation measure for the whole chain we average all angles and plot the density profile. Repeating the measurement at

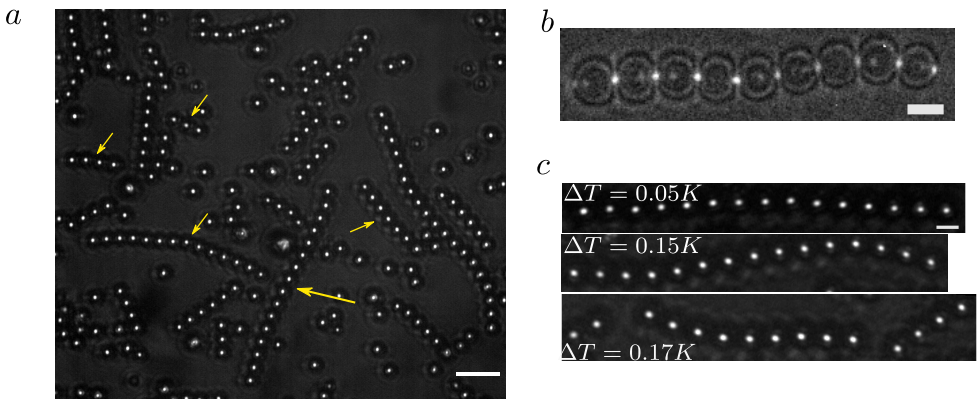


Figure 6.2: Chain assembly of dipatch particles and temperature dependent fluctuations (a) Aggregated chains at $\Delta T = 0.1 \pm 0.01$K, scale bar 10 $\mu$m. Bigger blobs are non-patchy remnants of the particle synthesis, that do not bind and only show steric interaction. Big yellow arrow indicates the chain used for most analysis, smaller arrows indicate some of the smaller chains that were analyzed to study the effect of size (b) Epifluorescence overlay on a bright field microscopy image showing that only the labeled fluorescent patches form bonds, scalebar 3 $\mu m$ (c) Bright field image of particle centers showing that a chain has higher amplitude fluctuations at lower temperatures and breaks at $\Delta T = 0.17$. In order to increase locating accuracy the image focus was set slightly below conventional bright field focusing, this way a high contrast bright center is obtained.

different temperatures, shows a clear systematic narrowing of this density profile with increasing temperature, see Fig. 6.3(f). The density profile is well fitted by a gaussian distribution (black) with standard deviation $\langle\sigma(\theta_i)\rangle$. We obtain a clear decrease of fluctuations with increasing temperature, as shown in Fig. 6.3(g). The exact amount is reversible when we decrease the temperature again. We thus conclude that, within accuracy, between going up and down in temperature: there is no aging of the bonds. Note that these measured deviations are well above deviations that could be attributed to the locating uncertainty $\epsilon = 20$nm, which results in a bond angle uncertainty $\epsilon_\theta = 3\epsilon/d \approx 0.025$rad. Thus, they represent true movement of the particles.

As noted, at a single temperature not all bending angles of a single chain show the identical amount of fluctuation, see Fig. 6.3(h). Interestingly, this variation in flexibility is conserved over the different temperatures; bonds that are most flexible at one temperature are also most flexible at another. This suggests that this variation is a characteristic of this particular chain and not measurement noise. For a significant part such variation can probably be attributed to a polydispersity in the exact patch size. Based on the AFM measurements (chapter 2) we estimated the patch arc angle polydispersity to be on the order of 10%, giving a patch area polydispersity of 20%. Given that interaction strength scales with patch area this could

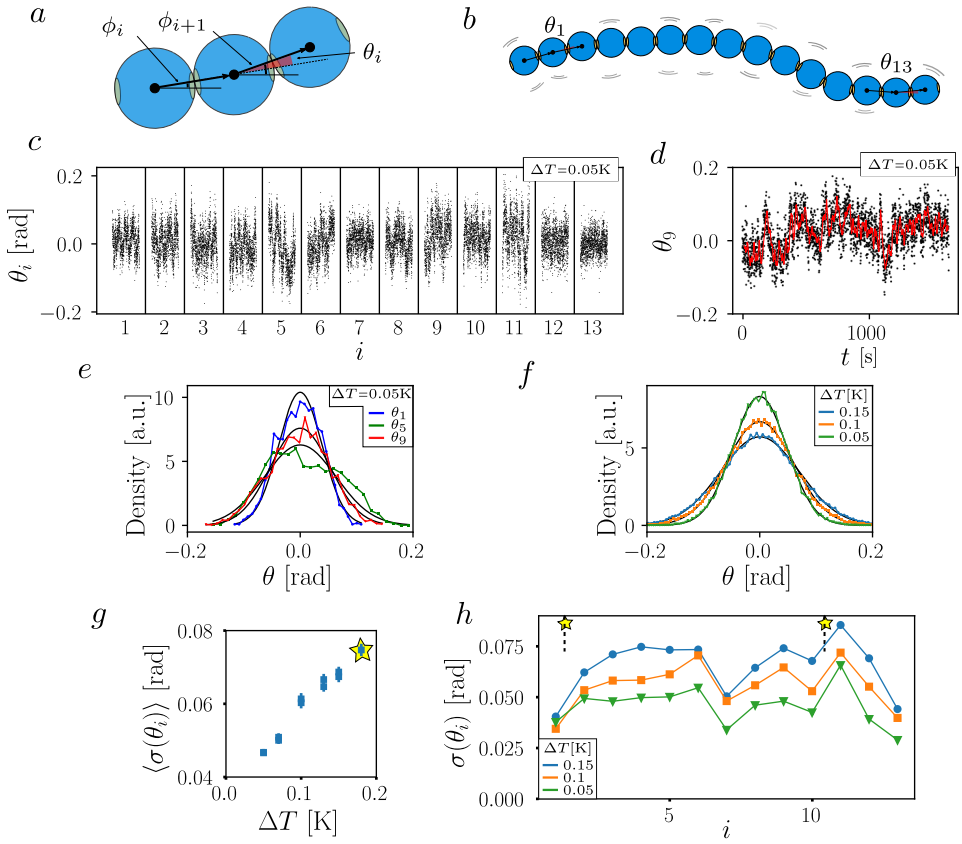


Figure 6.3: Fluctuating bending angles and their temperature dependence (a,b) definition of the tangent angle $\phi_i$ and bending angle $\theta_i$ (c) Time traces of each bending angle at $\Delta T = 0.05$ measured at 2 fps over 30 min (d) Zoom-in of one representative bending angle $\theta_9$, red line is a rolling mean 10s (e) Density plot of three bending angles at a single temperature $\Delta T = 0.05$. Black lines are Gaussian fits. (f) Density plot of the averaged bending angles along the chain for three different temperatures and Gaussian fits (black lines) (g) The average standard deviation $\langle\sigma(\theta_i)\rangle$ obtained by fitting the Gaussian fit if the averaged bending angle density as a function of $\Delta T$. Each point corresponds to a 30 minute measurement, error bars give the variation in $\sigma$ along the chain. The star indicates the breaking temperature and amount of fluctuations right before the breaking event. (h) Standard deviation $\sigma(\theta_i)$ along the chain at three different temperature of the same chain. Stars indicate the position of the snapped bonds. All data corresponds to the same $N = 15$ chain depicted in Fig. 6.2c

explain the flexibility variation, if flexible bonds are ones made from particles with small patches. Another source of variation can be attributed to possible mechanical coupling between bonds. In a strongly coupled chain, particles will not fluctuate

independently from each other, but instead fluctuate along with global vibrational modes. Such vibrational modes are not symmetric along the chain. For instance, the expected lowest energy mode would be similar to a half sine wave which has maximum bending at the middle of the chain and no bending at the ends of the chain. This might explain the fact that particularly the bending towards the end of the chain are measured to have a lower amplitude of fluctuation. In addition, we point out that one of the two bonds that breaks first is associated with the bending angle that shows highest fluctuations. This suggests that by identifying bonds with highest bending fluctuations we can identify structural weak spots, which will break first upon decreasing the attraction strength.

To explore mechanical coupling between the particles and to obtain effective bending rigidities we analyzing the shape fluctuations using a Fourier decomposition technique developed in previous studies of biofilaments and applied to colloidal chains before [197, 234]. We express the tangent angles as a sum of cosines:

$$\phi_i = \sqrt{\frac{2}{L_0}} \sum_{n=0}^{N-2} \alpha_q \cos\left(q_n s_i\right), \quad i \in 1, ..., N-1 \tag{6.2}$$

Here $n$ is the mode number, $\alpha_q$ is the mode amplitude of the $n$-th mode with wave vector $q_n$, where $q_n$ is defined as $q_n = n\pi/L_0$, $L_0$ is the contour length of the chain and $s_i = (i - 1/2)d$ the discrete arclength along the chain, with $d = L_0/(N-1)$ the average particle diameter. The number of particles is $N$, such that there are $N-1$ bond tangent angles along the chain. The zeroth-mode is merely a global chain orientation, and will not be considered hence forth. Eq. 6.2 is similar to the expression for continuous filament, with the only difference that we use a discrete Fourier transform. The mode inaccuracy as a consequence of the locating error $\epsilon$ follows the relation [217]

$$\sigma^2_{noise}(\alpha_q) = \frac{4}{L_0}\epsilon^2 \left[1 + (N-2)\sin^2\left(n\pi/2(N-1)\right).\right]. \tag{6.3}$$

Fig. 6.4a shows time traces of the mode amplitudes of a chain at a fixed temperature. The amplitude of all modes are centered around the $y = 0$ axis, confirming the low intrinsic curvature of the chain. The amplitude of the mode fluctuations contains information about the bending rigidity. To determine it quantitively, we consider the worm-like chain Hamiltonian given by

$$U = \frac{B}{2}\int_0^{L_0} \frac{\partial\phi}{\partial s}^2 ds, \tag{6.4}$$

where $B = kT\ L_p$ is the bending rigidity, proportional to $L_p$ the persistence length. If we assume that every mode is excited on average with the same thermal energy $kT$ (equipartition theorem), then the variance of the mode amplitudes, corresponding to wave number q, is given by

$$\sigma^2(\alpha_q) = \frac{kT}{Bq^2} \tag{6.5}$$

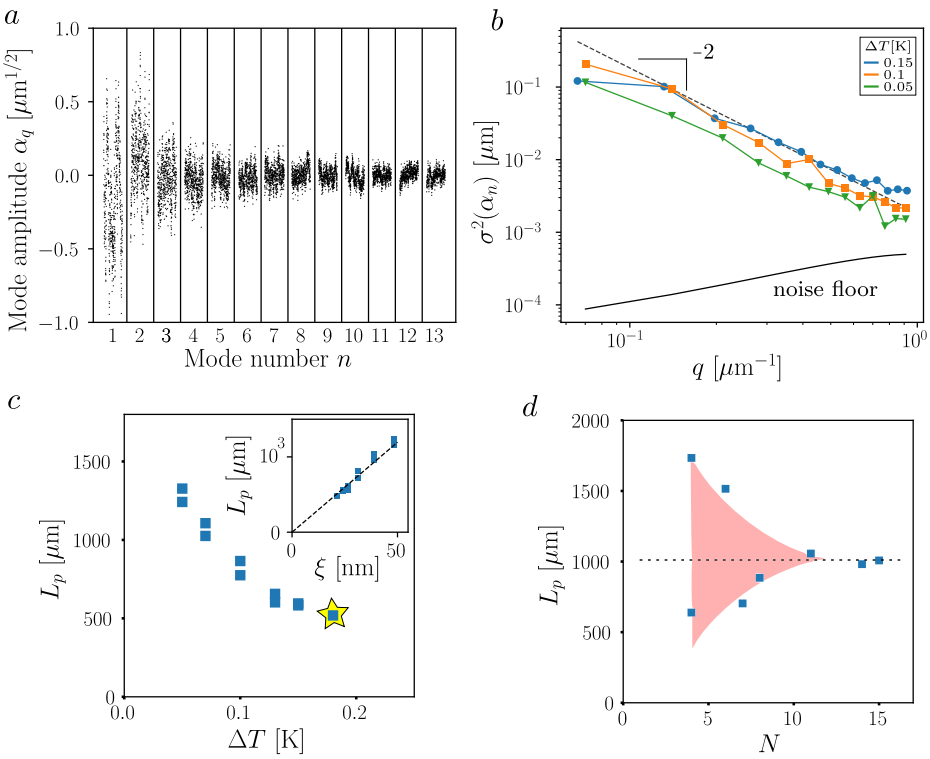


Figure 6.4: (a) Time traces of mode amplitudes at $\Delta T = 0.05$ K (b) Variance of mode amplitude as a function of $q$ for three different temperatures. Striped line is a $q^-2$ fit for midrange $q \in [0.1, 0.6]$ at $\Delta T = 0.15$. Noise floor is based on a tracking accuracy of 20nm. (c) Fitted persistence length versus $\Delta T$, star indicates the breaking temperature. Inset shows $L_p$ versus $\xi = \xi_0(\Delta T/T_c)^{-0.63}$, with $\xi_0 = 0.19$ nm. Black line is a fit of $L_p/\xi$. (d) $L_p$ versus $N$ for different chains at $\Delta T = 0.1$, red area and dotted lines are guides to the eye. All data in (a,b,c) corresponds to the same $N = 15$ chain.

Fig. 6.4b shows the measured variance of the modes as a function of $q$ at three different temperatures. Indeed we observe a power-law decay with slope $-2$ over a $q$-range of 0.1 $\mu$m$^{-1}$ to 0.7 $\mu$m$^{-1}$, which validates the mapping of the chain as an elastic filament. Short wavelengths deviate upwards, which can be explained by the discreteness of the chain. Short wavelengths are also more susceptible to noise, however for a conservative estimate of $\epsilon = 20$ nm, the noise floor remains well below the measured variance. Deviations from the expected power law are also observed for the longest wavelength, which we associate with a long relaxation time of these long wavelength modes, which is of the order of the measurement time.

The temperature dependency shows that mode fluctuations increase when de-

creasing temperature, like the fluctuations in bending angles. We can extract the persistence length at each temperature by fitting to Eq. 6.5 for midrange wavelengths. The resulting values (Fig. 6.4c) show a clear decrease from $L_p \sim 1500\mu$m to $L_p \sim 500\mu$m. Which, normalized by particle diameter, translates to $L_p/d \sim 470$ and $L_p/d \sim 160$, showing that these chains are in the semi-flexible regime, with a finite persistence length that's significantly longer than the particle diameter. However a linear relation is recovered if we plot $L_p$ against the correlation length $\xi = \xi_0 \Delta T/T_c^{-0.63}$, see Fig. 6.4c(inset). Here we approximated $\xi$ by the correlation length at the critical composition. Our composition deviates from the critical one by 5% vol causing the real $\xi$ to be slightly smaller. Making this assumption we can fit a phenomenological slope $L_P/\xi = 24 \pm 0.3$.

We also investigated the size dependence of $L_p$ by measuring chains of different length at the same temperature. Fig. 6.4d shows that down to $N = 10$ $L_p$ remains constant with respect to the longest chain length we measured. For shorter chains however, $L_p$ starts deviating and becomes highly variable. This can be understood both from the inappropriateness of a continuum description and the bigger sensitivity to patch size polydispersity. The reproducibility of $L_p$ for $N \geq 10$ reassures that the bending rigidity is not sensitive to a particular chain but a system property tunable by temperature.

### 6.3.2 Dynamic analysis: two relaxation timescales

So far we have considered purely static properties by averaging quantities over total measurement time. However, already the deviation at low q (long wavelength) suggested that dynamic effects may play a role. Here, we investigate the dynamic effects of the fluctuating chain by monitoring the mean-square mode amplitude as a function of lag time. A fluctuating elastic filament with energy given by Eq. 6.4 is expected to satisfy the Langevin dynamics [234]

$$B\frac{\partial^4 u}{\partial s^4} + \gamma \frac{\partial u}{\partial t} = f(s,t), \tag{6.6}$$

here $u(s,t)$ is the transverse position related to the tangent angle $\phi = \partial u/\partial s$, $f$ a random thermal noise and $\gamma$ is the drag coefficient per unit length of the filament. It has been shown that to a good approximation the Fourier modes of Eq. 6.2 act as normal modes [234]. In that case, the Langevin dynamics are solved in terms of the mean-square mode amplitude that relaxes to the final static variance of Eq. 6.5 according to a single-exponential [234]:

$$\frac{1}{2}\langle(\alpha_q(t+\Delta t) - \alpha_q(t))^2\rangle_t = (1 - e^{-\Delta t/\tau})\frac{kT}{Bq^2} \tag{6.7}$$

where $\Delta t$ is the lag time between images, and $\tau$ the relaxation time of the mode. The relaxation times $\tau$ are given by [234]

$$\tau \simeq \frac{\gamma}{Bq_*^4}, \tag{6.8}$$

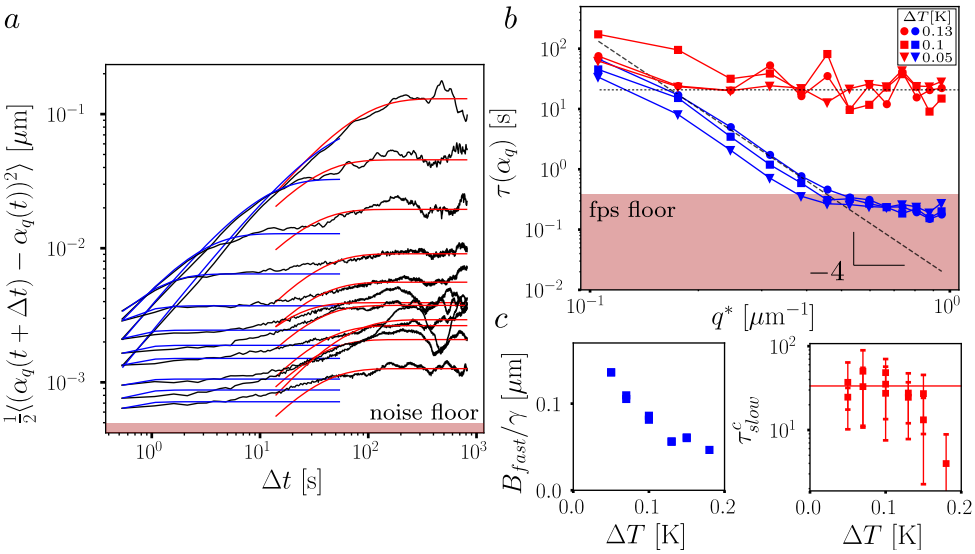


Figure 6.5: (a) Mean-squared amplitude versus lag time for modes $n \in [1, 8]$ at $\Delta T = 0.05$K. Blue (red) lines are exponential relaxation fits to the fast (slow) relaxation processes. (b) Fitted relaxation times $\tau_{fast}$ (blue) and $\tau_{slow}$ versus $q_*$ (red) for three different temperatures. Dotted slope corresponds to $q_*^{-4}$ fit of $\tau_{fast}$ at $\Delta T = 0.13$K. Red lower shading indicates to the minimum experimentally accessible $\Delta t = 0.5$s between frames. (c, left): Temperature dependence of fast bending rigidity and drag coefficient from power law fit. (c, right): Saturation values of $\tau_{slow}$ determined from averaging $\tau_{slow}$ for $q_* > 0.2\mu\text{m}^{-1}$, error bars are the standard deviation of those values.

where $q_* \approx (n + 1/2)\pi/L_0$.

Fig. 6.5(a) shows the mean-square amplitude of the different modes as a function of lag time for a single measurement. Interestingly, except for the first two modes, our data is not properly described by a single-exponential relaxation. This becomes clear when looking at the higher order modes $n > 3$. The mean-square amplitude relaxes in two steps. An initial exponential relaxation followed by a short plateau and a second relaxation. The initial exponential relaxation indicates an elastic process. We have separated it from the second, by performing a least-square fit with a linear weighing favoring small $\Delta t$, see Fig. 6.5(a, blue lines).

Fig. 6.5(b) shows that this initial fast relaxation time follows a clear $q_*^{-4}$ dependence, as expected from Eq. 6.8, from the second mode up to the minimal lag time set by the experimental acquisition rate. This gives confidence in our fitting approach and confirms that this first relaxation is an elastic process. The deviation of this dependence (see e.g. the first mode) is due to the fact that the second relaxations has a similar relaxation time, thus mixing both processes. Fig. 6.5(b) also shows that by increasing temperature the correlation times decrease. The extracted bending rigidity divided by the drag coefficient, $B_{fast}/\gamma$ is shown in Fig. 6.5(c,left panel).

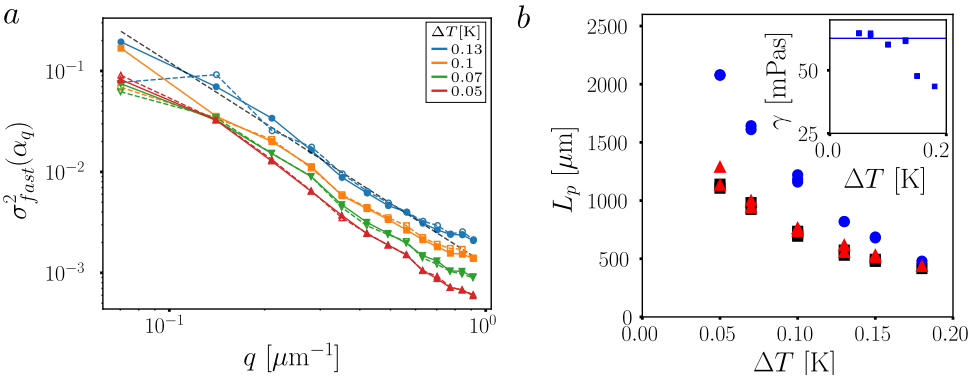


Figure 6.6: (a) Amplitude $\sigma^2_{fast}$ of the fast exponential relaxation fit versus $q$ for four different temperature. Open/closed markers or dashed/solid lines corresponde to two independent measurement (b) (Blue,red,black) $L_p$ from fitting a $q^{-2}$ dependence to ($\sigma^2_{fast}$,$\sigma^2_{slow}$,$\sigma^2_{static}$). Inset: the transverse drage coefficient per unit length, $\gamma$, determined by dividing $B_{fast}$ with data from Fig. 6.5(c), line corresponds to mean $\gamma$ of $\Delta T \leq 0.13$

This consistent behavior further validates the analysis and forms an independent demonstration of the elastic tunability of the system.

The second relaxation does not appear to be well-captured by an exponential which indicates a non-elastic process. We have still performed a similar exponential fit but with an opposite weighing (red lines). Strikingly, this second slow relaxation time does not decay with $q$ but tends to a constant $\tau^c_{slow}$. Fig. 6.5(c,right panel) shows $\tau^c_{slow}$ as a function of $\Delta T$. The large error bars don't allow for a resolvable trend with $\Delta T$. Averaging over all points we obtain a $\langle \tau^c_{slow} \rangle = 30 \pm 10s$. The highest two temperatures seem to fall below this line, however for these temperatures the timescales of the two regimes mix and the fitting procedure becomes inaccurate.

After having addressed the dynamics, we can get back to the amplitudes that we obtain from the two exponential fits. We call them $\sigma^2_{fast}(\alpha_q)$ and $\sigma^2_{slow}(\alpha_q)$, as they correspond respectively to mode variance after the first and second relaxation times. The final slow amplitude $\sigma^2_{slow}$ follows closely the static variance (not shown). Fig. 6.6(a) shows $\sigma^2_{fast}$ as a function of $q$ and for multiple $\Delta T$'s. A remarkably clean signal is recovered for the higher $q$ values. The dependence on temperature becomes very sharp. Indeed, disregarding the two longest modes, variances decrease for every single $q$ value upon decreasing $\Delta T$. Maybe even more impressive is how well two independent measurements at the same temperature overlap. It is interesting to compare this with Fig. 6.4(a). There, higher $q$ appeared noisy. Given the low locating noise floor this was actually surprising. Now we can understand that this apparent noise was due to the slow second relaxation. The effective persistence length associated with the two relaxation processes by fitting with Eq. 6.5 is shown in Fig. 6.6(b). The fast elastic response shows an approximately factor two higher rigidity as the slow and static response. We can use this extracted $B_{fast}$ to calculate

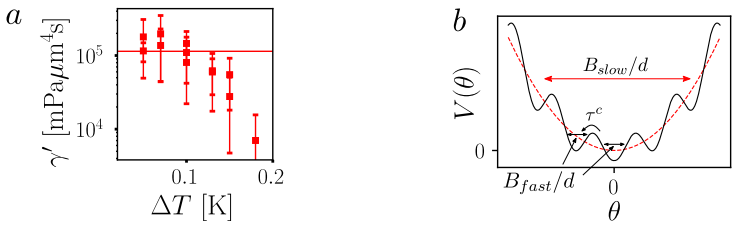


Figure 6.7: Internal friction coefficient $\gamma'$ as a function of $\Delta T$, determined by multiplying $\tau^c_{slow}$ with $B_{static}$

$\gamma$ from their previously determined ratio. The inset shows that this drag coefficient remains constant at least for the reliable lower $\Delta T$'s. Taking an average we obtain $\gamma = 63 \pm 2$ mPas. This value can be compared with a direct measurement of the transverse drag coefficient of the center of mass of the chain, $\gamma^T_{COM} = 31 \pm 3$ mPas, see appendix Fig. 6.9 and accompanying discussion. Though these values are reasonably close to each other given the completely independent and indirect determination, their is a significant discrepency. The transverse drag as determined from bending is higher by a factor of 2. One potential source of this extra bending drag could come from the rotational drag of the colloidal particles. When an excited bending mode relaxes particles not only have to translate laterally, but also have to rotate, which is not taken into account when equating the drag coefficient of Eq. 6.6 with $\gamma^T_{COM}$. Given this and the reasonable agreement between $\gamma$ and $\gamma^T_{COM}$, we find it most likely that the source of the initial damping is indeed drag due to hydrodynamic interactions between particles and solvent.

The secondary relaxation process on the other hand happens at a timescale too long to be explained by drag, and furthermore doesn't show the expected $q_*^{-4}$ dependence. Constant relaxation times similar to what we observed in the second relaxation process have been observed before in microtubules [234, 239, 240]. These effects are attributed to extra energy losses from internal friction distinguished from the external friction of drag. In microtubules these energy losses are attributed from fluid flow through narrow pores, which are absent in our case. However, we can use the same analysis strategies as used in these reference, which are generally valid in the presence of internal friction [239]. In this case the Langevin dynamics of a filament is modified with an additional dissipatory term:

$$B\frac{\partial^4 u}{\partial s^4} + \gamma\frac{\partial u}{\partial t} + \gamma'\frac{\partial}{\partial t}\left(\frac{\partial^4 u}{\partial s^4}\right) = f(s,t). \tag{6.9}$$

The third term represents internal friction. In this case, mode relaxations become modified with respect to Eq. 6.8 such that

$$\tau = \frac{\gamma + \gamma' q_*^4}{B q_*^4}, \tag{6.10}$$

where $\eta' = \gamma'/a^4$, with $a$ the filament diameter, can be considered an effective inter-

nal viscosity. This equation implies that at wavevectors larger than $q^c \sim (\gamma/\gamma')^{1/4}$ internal friction will dominate and correspondingly the relaxation times become $q_*$-independent and equal to $\tau^c = \gamma'/B$. The friction coefficient associated with the slow relaxation $\gamma' = \tau^c_{slow}\ B_{static}$, is shown for different temperatures of our measurements in Fig. 6.7(a). The error bars are large due to the like inappropriate exponential fit, the longer, less equilibrated timescale and possible stochastic nature of the source of internal friction. Averaging over temperatures we obtain an internal dissipation $\gamma' \sim 10^5 \text{mPas}\mu\text{m}^4$ and an internal viscosity $\eta' \sim 10^3 \text{mPas}$. Furthermore, using for $\gamma$ the value determined from the fast relaxation we obtain a critical wavevector of $q^c \sim 0.2\mu\text{m}^{-1}$, above which internal friction will dominate.

From this we conclude that on short time scales $< \tau^c \sim 30\text{s}$ the chain is described by an overdamped elastic process. It shows both the expected $q^{-2}$ power law for the fluctuation amplitude and the $q_*^{-4}$ dependence for the relaxation time. This elastic behavior can be captured by a single elastic bending modulus $B_{fast}$, and a drag coefficient $\gamma$. The former is in our case sharply tunable by temperature. However on longer time scales a second more complicated relaxation process occurs. This relaxation still shows a $q^{-2}$ power law allowing us to extract a bending modulus $B_{static}$ that is also temperature tunable. However the non-exponential relaxation and wavelength-independent relaxation time show that this is not a standard overdamped elastic process. In line with previous work, we attribute this slow component to relaxation occurring with a combination of both external and internal friction.

We furthermore show that this slow relaxation is also present between three bonded particle, see appendix 6.5.2. This shows that the origin of the slow relaxation is not a collective effect due to longer ranged coupling between colloids, nor an artefact from the approximations in the mode analysis. Instead, the origin of the internal friction has to lie in the contact mechanics of the bond between two particle patches.

We can speculate about the origin of this internal friction. We envisage a stick-slip like process where the point of contact between the two colloids moves on timescales $\tau^c$. Such process seems likely given the plastic buckling of chains observed in chapter 4. Below this timescale, the point of contact is essentially fixed giving rise to an elastic bending constant $B_{fast}$. Beyond this time, the contact can diffuse, while still being bounded by the finite patch size. This finite patch size gives rise to the second elastic bending constant $B_{slow}$. A potential energy landscape that qualitatively captures such behavior is shown in Fig. 6.7(b). A valley represents a fixed contact point, with a effective spring bending $B_{fast}/d$. Due to thermal energy kicks, hopping between valleys can occur leading to contact slippage, which happens on a timescale $\tau_c$. This landscape has in addition a global curvature giving rise to a long time effective bending constant $B_{fast}/d$. To further show that such a contact point diffusion is in principle possible we note that the average patch size for these particles has been measured directly to be given by a patch arc angle $\theta_p = 0.36\text{rad}$. The explored angle amplitudes are, even on long time scales smaller, $\sim 0.1\text{rad}$, as can be seen from fig. 6.3(h). If this were not smaller, another mechanism apart from contact diffusion would have to be invoked. We speculate that the source of

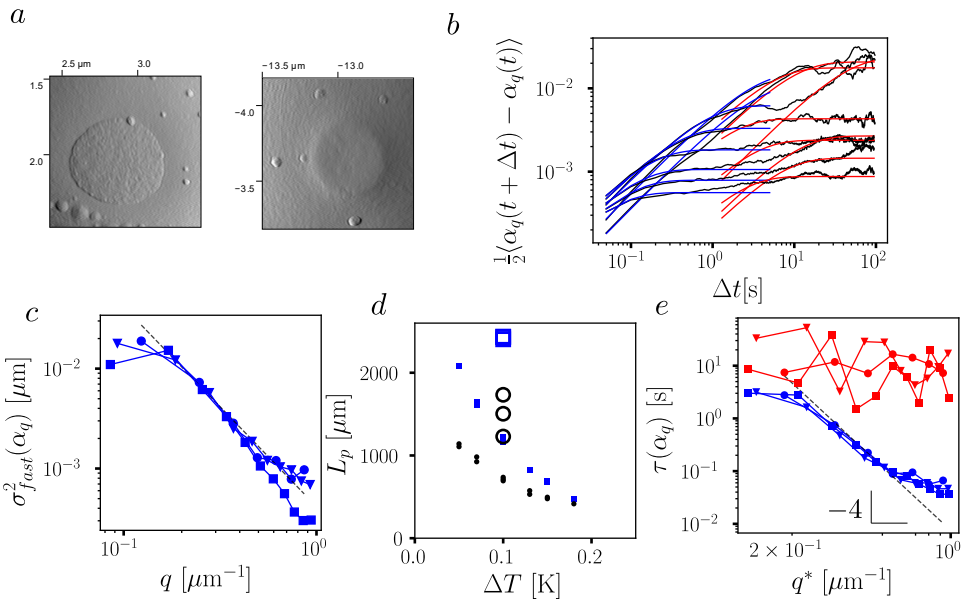


Figure 6.8: (a) atomic force microscope images zommed in on the patch of big dipatch particles (left) and small (right). (b) mean square displacement of the lowest modes of a $N = 13$ chain, with exponential relaxation fits on short (blue) and long (red) timescales. (c) Fitted short time mode variance for an $N = 9$, $N = 12$ and $N = 13$ chain, dotted line is $q^{-2}$ powerlaw fit. (d) $L_p$ on short (blue open squares) and long timescales (black open circles), in addition the big patch values are shown. (e) $\tau_{fast}$ (blue) and $\tau_{slow}$ (red) obtained from the exponential fit, dotted line is a $q_*^{-4}$ fit

these stick-slip dynamics could be heterogeneities on the surface such as roughness or charge, or due to the reptation of intertwined F108 polymer brushes present on the surface.

### 6.3.3 Dependence on patch size

Fig. 6.8(b) shows the mode mean square displacements of particles B with smaller patches. Also indicated are fits to two exponential relaxation processes. The higher acquisition rate of these experiments with respect to particle A experiments allow to probe smaller $\Delta t$'s and show that also on these shorter timescales the fast relaxation decay fits well. The resulting amplitude of the fast relaxation is shown for three different chains in Fig. 6.8(c). In all cases a $q^{-2}$ power law is recovered for wavelengths in an intermediate regime. The extracted persistence lengths $L_p^{slow} = 1500 \pm 250\mu$m, and $L_p^{fast} = 2420 \pm 20\mu$m are compared with the persistence length of the big patch sample, in Fig. 6.8(d). Interestingly, both after short and long relaxation the small-patch particle chains exhibit a factor of two higher rigidity.

Fig. 6.8(e) shows that $\tau_{fast}$ follows a $q^{-4}$ dependence from which we fit a drag coefficient of $\gamma = 73 \pm 7$cP, very close to the drag coefficient for big patch chains. The slow relaxation time $\tau_{slow}$ is within accuracy independent of $q$ with an average of 12s, shorter than for the bigger patches. This is consistent with Eq. 6.10, given the fact that $B_{slow}$ is bigger. From $\tau_{slow}$ we extract an internal friction coefficient $\gamma' = 0.8 \cdot 10^5$ mPas$\mu$m$^4$. This value lies within the error margin of the internal friction of the big patch chains.

These observations highlight the different control parameters in this system. Next to temperature the mechanics of the chains are also tuned by the patch-size, with smaller patches giving more rigid chains. This effects both the overdamped elastic response on short timescales as well as the long time relaxation. The internal friction coefficient however remains unaffected. This indicates that the secondary dissipation mechanism is determined by features set at a length scale smaller than the patch size. These features could be roughness or charge heterogeneities on a length scale smaller than the patch size.

## 6.4 Conclusion

In this chapter we studied the conformation fluctuations due to thermal noise of critical Casimir bonded dipatch chains. Decomposing these fluctuations in bending modes results in a precise analytical tool. Using this, we showed that dipatch chains are well modeled as semiflexible filaments, with a persistence length that is set by patch size and the strength of the critical Casimir bond and can therefore be reversibly varied using temperature. Further dynamical analysis revealed rich viscoelastic behavior, in which chain fluctuations follow a two step relaxation process. We have associated this to a combination of external friction due to drag and an internal friction due to local conformational changes.

Similar internal friction effects have been observed for microtubules [234, 239–242], the presence of them in our colloidal model system suggests that these type of effects are quite general and could be expected in other filaments that consist of segmented units, such as nanoparticles chains [225].

Our results show that the critical Casimir force can not only be used to in situ control the radial interaction strength between particles but by using patchy particles also the shear rigidity between bonded colloids. This further extends to uses of this well controlled model system. For instance, it opens the way to investigate the effect of bending rigidity on larger more dense assemblies of dipatch particles. These form polymer like states, as shown in chapter 5, whose structure and rheology is expected to have a non-trivial dependency on rigidity. Furthermore, by combining dipatch particles with higher valent patchy particles more complex, potentially 3d, colloidal architectures can be made. Such as the patchy gel shown in the previous chapter. Bending rigidity will partly determine structural stability and an in situ control of such rigidity could result in switchable mechanical states and shape changing behavior [70, 243].

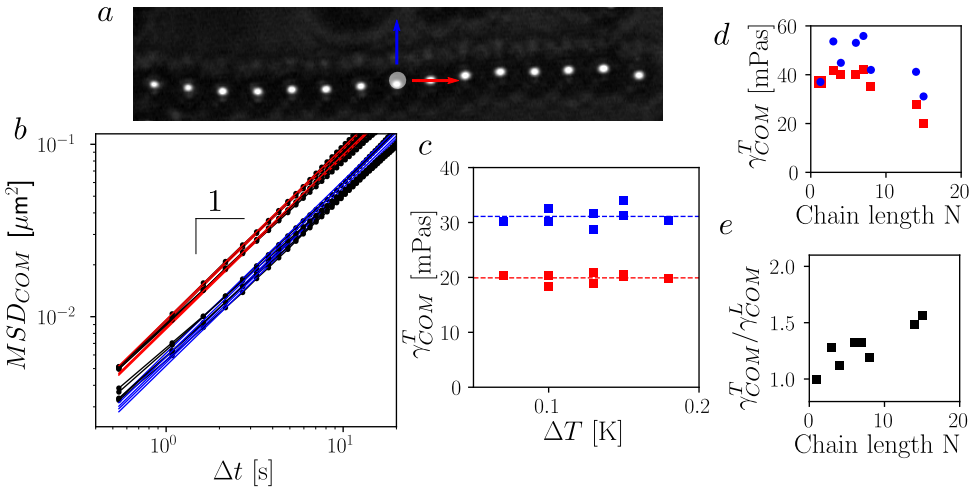


Figure 6.9: Transverse (blue) and longitudinal (red) diffusion and associated drag coefficient of dipatch chains (a) Snapshot of the $N = 15$ big-patch chain with center of mass (white transparent dot) and the two diffusion directions (b) mean square displacement and linear diffusive fits at different temperatures. (c,d) The extracted drag coefficients per unit length as a function of temperature with fixed length $N = 15$ and length with fixed $\Delta T = 0.15$K. (e) Ratio of transverse and longitudinal drag coefficients as a function of chain length

# 6.5 Appendix

## 6.5.1 Transverse and longitudinal chain drag coefficients

The bending relaxation dynamics of a chain is expected to be, at least partly, connected to the diffusion dynamics of the center of mass (COM) of the chain. We can use the exact same data as was used to study the bending dynamics to also determine the COM diffusion. For a semiflexible chain it is convenient to seperate COM diffusion into two components: a transversal and a longitudinal diffusion, see Fig. 6.9(a). To determine the mean square displacement in both directions, first the coordinate system at each frame was rotated by the average tangent angle $\langle\phi\rangle_i$ at that frame. In this way the x-axis coincides with the longitudinal direction and the y-axis with the transversal direction, such that $MSD^T_{COM} = MSD_{COM,x}$ and $MSD^L_{COM} = MSD_{COM,y}$. The resulting mean square displacement of the $N = 15$ chain used for most of the analysis in this chapter is shown in Fig .6.9(b). Good fits are obtained with diffusive relations $MSD^T_{COM} = 2D^T\Delta t$ and $MSD^L_{COM} = 2D^L\Delta t$. A significantly faster diffusion is obtained in the longitudinal direction which is to be expected for a linear object. We extract the associated drag coefficients per unit

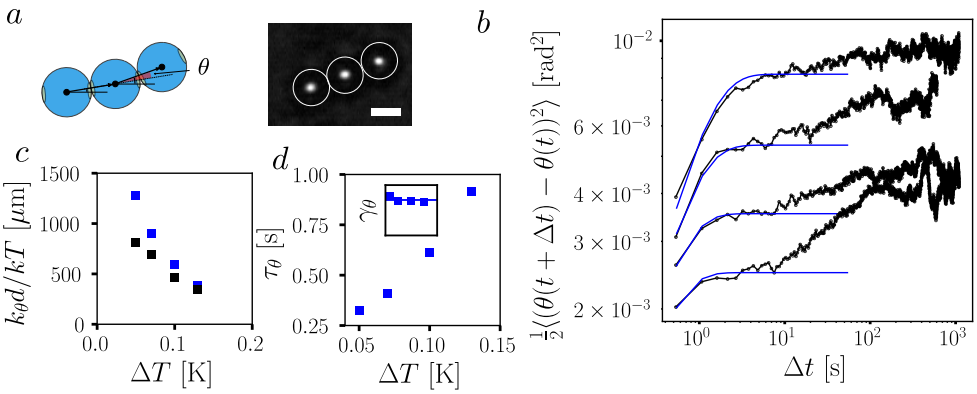


Figure 6.10: (a) Model and experimental snapshot of three dipatch particles forming effectively a single dipolar bond, scalebar 3$\mu$m. (b) Mean square displacement of bond angle $\theta$ for temperature $\Delta T = 1.3, 1, 0.7, 0.5$ from top to bottom. Blue line is best fitted exponential relaxation on short timescales. (c) Temperature tuneability of fitted bending rigidity on short (blue) and long (black) timescales, normalised to correspond to the persistence length of a chain. (d) Fitted short relaxation time and extracted friction coefficient (inset) with mean value as horizontal line.

length $\gamma^T_{COM} = kT/(D_T N d)$ and $\gamma^L_{COM} = kT/(D_L N d)$, where $d$ is the particle dameter, see Fig. 6.9(c). Note that we here normalise by the distance between the two tips $L'_0 = N\ d$ of the chain rather than the distance between the centers of the two end particles $L_0 = N\ d$. No significant dependence on temperature is observed, which also means the bending rigidity range that is explored here does not alter diffusivity, in line with Ref. [233]. We average all temperatures to obtain the best estimates $\gamma^T_{COM} = 31 \pm 3$ mPas and $\gamma^L_{COM} = 20 \pm 1$ mPas. From the absence of a temperature dependence we further can conclude that there is no significant critical Casimir attraction between particles and wall, which, if present, would give rise to an apparent increase in the drag coefficient with increasing temperature.

We have likewise extracted the center of mass drag coeficients for chains of different sizes and noralized by the chain length, see Fig. 6.9(d,e). These normalised drag coefficients appear to be fairly consistent over different chain sizes though appear to decrease for longer chains. In addition, a clear trend towards a larger constast between transversal and longitudinal diffusion is observed, which is to be expected due to the increased assymetry in length.

### 6.5.2 Secondary relaxation is present on single bond level

To get deeper insight into the origin of the slow relaxation we look at three bonded particles only. Three dipatch particles together form effectively a single dipolar bond

parametrized by a single bending angle $\theta$, see Fig. 6.10(a). An overdamped elastic dipolar bond with energy $U(\theta) = k_\theta \theta^2/2$ follows the dynamics

$$\dot{\theta} = -\frac{k_\theta}{\gamma_\theta}\theta + \sqrt{\frac{2kT}{\gamma_\theta}}\xi(t) \tag{6.11}$$

where $\gamma_\theta$ is an effective angular friction coefficient. This equation is completely analogous to a particle in a harmonic well with the lateral displacement replaced by $\theta$. It is thus similarly solved by the MSD [244]

$$\langle \theta^2 \rangle = 2\left(1 - e^{-t/\tau_\theta}\right)\frac{kT}{k_\theta}, \tag{6.12}$$

with $\tau_\theta = \gamma_\theta/k_\theta$. We track the centers of a three-particle chain for different temperatures and follow the evolution of the bending angle.

Fig. 6.10(b) shows the MSD of $\theta$. Interestingly, like the mode dynamics for longer chains, also the dynamics of single bonds shows two relaxation processes. The initial relaxation fits well with Eq. 6.12. The resulting fit parameter $k_\theta$ divided by $kT$ and multiplied by the particle diameter $d$ is shown in Fig. 6.10(c).This ratio $dk_\theta/kT$ is the persistence length a long chain consisting of a series of this single bond would have. We first see that the bond rigidity is tunable with temperature similar to the persistence length of Fig. 6.6. The absolute value is similar, but slightly lower as before. This difference is not surprising given the variability of bond stiffnesses due to particle polydispersity. The fitted relaxation time increases with $\Delta T$, as shown in Fig. 6.10(d). When we extract $\gamma_\theta$ we obtain an almost constant number. The normalised average $\gamma_\theta/d^3 = 16 \pm 1$ mPas is comparable to the drag found for free diffusion and in the mode analysis. From this consistent behaviour we conclude that at short timescales a single bond shows elastic overdamped dynamics.

On longer timescales a second relaxation occurs. This relaxation does not fit well with an exponential relaxation (not shown). If we do attempt a fit we obtain a relaxation time $\tau_{slow} = 15 \pm 5$s, similar to the slow relaxation for chains. Fig. 6.10(c) shows the effective bending rigidity after this second relaxation. Similar to the long chain also this bending rigidity is temperature tuneable and on the order of a factor two smaller than the short time scale rigidity.

From the overall similarity between long chain and single bond behaviour we conclude that in particular the source of the secondary chain relaxation lies at the single bond level. This allows us to exclude possible collective effects as the origin, such as longer ranged interactions or hydrodynamic coupling. Furthermore it shows that analysis artifacts due to approximations during the mode analysis are also not the source. In particular the approximation of cosine modes as normal modes does introduce a small mode mixing, with components of long wavelength, slowly decaying modes, also being present in higher modes. Such an artefact could give rise to an aparent second slow relaxation. However given that the secondary relaxation is also present for the three chain, where no mode analysis is done, convincingly shows that this mode mixing artefact is not dominant.

CHAPTER 7

# Extreme mechanics of dipatch chains under compression: buckling, creep and snapping

*Self-assembling patchy colloidal particles form a promising platform to create designer soft materials. To dress such systems with mechanical functionality, one can take inspiration from the cytoskeleton which consists of semi-flexible filaments, such as microtubules, whose mechanical behavior give a cell it's unique mechanical properties. Here we present mechanical experiments on analogues of biological fibers, "colloidal polymers" made from dipatch colloidal particles. We use optical tweezers to probe their extreme mechanics under increasingly high compressions and reveal a rich non-linear mechanical response involving buckling, viscoelastic creep and stress relaxation, and ultimately fracture. We characterize and model this response using elastic and viscoelastic models involving Euler buckling and stress relaxation. This allows us to relate the critical bending at fracture to the finite patch size of the colloids. These results demonstrate the crucial role of finite patch size in the mechanics of self-assembled colloidal materials, and provide mechanical information essential to design functional colloidal architectures inspired by nature.*

# 7.1 Introduction

Micrometer-size, slender structures are an integral part of many soft and biological materials. They harbor rich mechanical behavior which crucially determines the mechanical response and functionality of these soft architectures. For instance, biological filaments such as microtubules, making up the cell cytoskeleton show non-linear buckling instabilities [245–247], visco-elastic behavior [234, 248, 249], plastic effects [250] and fracture [251]. Likewise, slender colloidal strands, prevalent in colloidal gels [214] and in recent colloidal designer structures [43, 51], are subject to a similarly diverse mechanical response [115, 252]. Such colloidal structures are easier to observe and have more controllable interparticle interactions than their biological counterparts. This makes them excellent model systems and a promising platform for designer materials with controlled internal architecture and tunable physical properties [28]. Self-assembling patchy particles, which have tunable anisotropic interactions, are a particularly promising route to achieve such designer architectures and mimic the functionalities of biological matter [219, 220]. However detailed mechanical information of such patchy structures is still lacking, in particular their non-linear extreme mechanics has so far been little explored.

In order to address such questions, we use dipatch colloidal particles that self-assemble into colloidal chains using temperature-controlled critical Casimir interactions, as described in chapter 5. These chains form semi-flexible filaments that fluctuate due to thermal noise, as was studied in chapter 6. Here, we use optical tweezers to probe their mechanics under extreme deformations, inducing buckling and fracture. We perform a series of different compression tests, similar but extended in scope w.r.t. the ones described in chapter 4 These tests reveal a mechanical response that resembles the richness of biological filaments, involving buckling, viscoelastic effects and ultimately fracture upon a critical bending. We characterize and model the elastic buckling and viscoelastic response and quantitatively relate the fracture point to the patch size. These results provide insight into the mechanics of assembled colloidal structures, essential to design functional colloidal architectures.

# 7.2 Methods

## 7.2.1 Chain formation and micromechanical compression test protocols

Monodispersed dipatch particles, of diameter $d = 3.1(1)$ $\mu$m, are assembled into chains in a double optical tweezer setup using temperature-sensitive critical Casimir interaction. The dipatch particles have small hemi-spherical patches of diameter $d_p = 380$nm, with patch arc-angle $\theta_p = 2\sin^{-1}(d_p/d) = 14°(\pm 2)$. These particles are identical to the small-patch type DP-B particles described in chapter 5 and 6 to which we refer for more details concerning synthesis and characterization. We

use a binary mixture of water and lutidine with lutidine volume fraction $c_L = 0.25$, and 0.375mM Magnesium sulfate, in which the particles sediment to form a quasi two-dimensional layer. This binary mixture was chosen to obtain optimal critical Casimir conditions with a largest temperature window of patch-to-patch attraction, as described in chapter 5. A custom-made objective and condenser lens heater were used, to maintain the sample temperature, while imaging with an oil coupled high-resolution objective with a precision of 0.1 C°. Temperature stability however is observed to be better than this and estimated as $\sim$ 0.05 C°. When heating the sample to $\Delta T = 0.10 \pm 0.05$ K below $T_c = 33.75$ C°, linear chains form.

To study the effect of chain length on the mechanical response, we performed experiments on chains consisting of $N$ particles, where $N$ varied from a smallest chain $N = 6$ to a longest chain of $N = 13$. After chains were formed they were pinned at either ends using optical tweezers. Often times we selected dipatch chains from the sample that had monopatch particles capping the chains at both ends. Such monopatch particles are present in minor fractions in the sample. These capped chains were preferred as they had the advantage that during an experiment there was no chance of another chain fusing with the chain under study. Furthermore, we observed that the monopatch particles due to their slightly smaller size resulted in a more stable trapping.

One (static) tweezer always remained fixed in position. A growing compressive force is exerted by moving the other, mobile tweezer, by an amount $\Delta$ towards the other. To a good approximation, the tweezers form harmonic traps, with spring constants $k_s$ and $k_m$. We can thus measure the force on the chain from the bead displacement out of the static trap center, using $F = k_s(x_s - x_1)$, where $x_s$ and $x_1$ are the x-coordinates of the trap center and of the trapped particle. Here, the coordinate system has been chosen to be in alignment with the chain. The linear compression $u$ is determined by the difference between the equilibrium total (contour)length and the actual end-to-end distance $u = L_0 - L$. Here, the end-to-end distance is defined as $L = x_N - x_1$ and the equilibrium contour length as $L_0 = \sum d_i$, with $d_i$ the distance between two bonded particles when no stress is applied $F = 0$.

By varying the protocol with which we move the mobile trap we can perform different micromechanical tests. We have performed three different tests: (1) A cyclic buckling test, (2) a stress-relaxation test, and (3) a fracture test. Each test is designed to probe different mechanical properties of the chains, respectively: elastic buckling, viscoelastic/plastic deformation and ultimate fracture mechanics. During a cyclic buckling test, the trap is moved with constant speed to a maximum displacement $\Delta_m$ and returned to its initial position in a triangular fashion. During a stress-relaxation test, the mobile trap is moved similarly to a maximum $\Delta_m$ where it is kept fixed for a certain amount of time. During this time, the system can potentially relax the stress, as measured by a reduction of the force exerted on the static particle. During a fracture test, $\Delta$ is increased continuously until a point of failure is reached and the chain breaks. Each of these tests is done at compression speeds around $v_{trap} \approx 0.01\mu$m/s.

During each experiments the chains were imaged using bright field microcopy and

recorded at a frame rate of 20fps with a pixel size of 87.7 nm. The in-plane centers $r_i = (x_i, y_i)$ of each particle were located with a subpixel accuracy of $\epsilon = 10$ nm using particle tracking software [122]. Next, the bond distance $d_i = ||r_{i+1} - r_i||$ and bond tangent angles $\phi_i = \arctan(y_{i+1} - y_i)/(x_{i+1} - x_i)$ are calculated. We note that this 2d representation of the particle chain is validated because their thermal height is very small due to the small gravitational height of the colloids $z_g = 0.35$ $\mu$m. To measure bending we use identical definition as were introduced in chapter 4 and 6. To measure local bending, we define the bending angle $\theta_i = \phi_{i+1} - \phi_i$. To study non-local bending and to compare to theories of continuum elastic structures, such as the Euler elastica, we perform a Fourier transform according to:

$$M_i = \frac{2}{N-1} \sum_{j=1}^{N-2} y_j^{\perp} \sin(\frac{\pi}{N-1} ji) \quad i = 1, ..., N-2 \tag{7.1}$$

Here, $y_i^{\perp}$, is the deflection perpendicular to line connecting the two trapped particles, $i$ runs from 1 to $N-2$ as the end two particles have zero perpendicular deflection by construction. In our setup the perpendicular deflection is close to $y$, such that $y_i^{\perp} \approx y_i$, however to account for a possible global tangent the perpendicular deflection is used.

### 7.2.2 Optical tweezer details and calibration

The force and microscopy measurements were conducted on a setup which has been described earlier [253]. Two laser beams with wavelength 1024 nm at a low intensity of $\sim 5$ mW were focused in narrow spots using the imaging objective. It was important to use such low intensity in order to avoid phase separating the binary mixture and to be able to exert the small forces involved in the mechanics of the chains. The partial absorption of the laser light by the binary solvent causes a local heating which we estimate to be 0.05K. This was measured by increasing the light intensity until phase separation occurs in the laser focus at $\sim 10$ mW. This happens at twice the intensity of the actual tweezing experiment. Since the sample is kept at a fixed temperature $\Delta T = 0.1$K below phase separation, and assuming that the local heating scales linearly with intensity, we estimate a local heating of 0.05K at the trap during the tweezing experiments. This can have a local effect on the bonding strength of particles close to the trap, but is small enough to cause no phase separation of the binary mixture.

The focused laser spots form harmonic traps at the image focal plane [109]. We checked that the trapped particles retained in-plane rotational freedom by using fluorescence microscopy in which only the dyed patches remain visible, Fig. 7.1. Indeed in both traps the position of the patches and the associated particle orientation, $\phi$, rotates over time, Fig. 7.1(b). Interestingly, even though there is free rotation around the z-axis of the trap, there is no free rotation around the x- and y-axis. This is likely due to the difference in refractive index between patch and matrix. This effect does not interfere with our measurement as we focus on in-plane deflection.

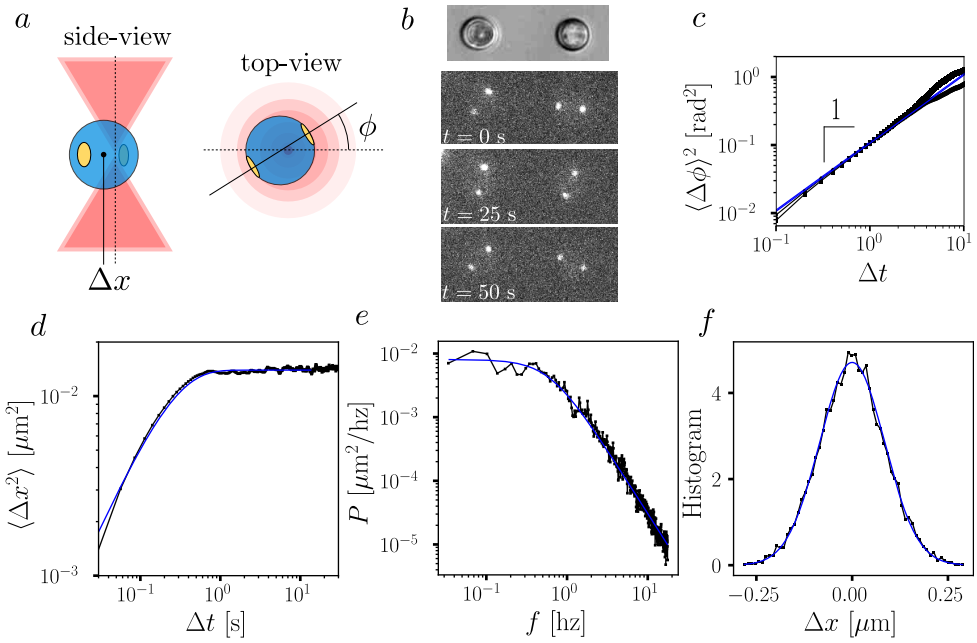


Figure 7.1: Trap calibration of the static optical tweezer (a) Schematic of a dipatch particle in an optical trap (b) one bright field picture that shows particle positions, the three fluorescence images show the dyed patches diffusing over time (c) mean square rotational displacement and diffusive power law fit $\langle \Delta\phi^2 \rangle = 2D_r\Delta t$ (d) mean square displacement of the center of a trapped particle and best fitting exponential relaxation, imaging was done at 35 fps for 5 min (e) power spectral density and best fitting Lorentzian. (f) histogram of the particle positions in x direction and gaussian fit.

Using the fluorescence data of nonbonded trapped dipatch particles we measured the rotational diffusion of the particles. To do so, we located the patch positions using tracking software and calculated the particle orientation $\phi$. We then determined the mean square orientation displacement, $\langle \Delta\phi^2 \rangle$, see Fig. 7.1(c). For both traps the data fits well with a diffusive power-law $\langle \Delta\phi^2 \rangle = 2D_r\Delta t$ with rotational diffusion constant $D_r$. This further proves there is rotational freedom. From the best fit we obtain a $D_r = 0.05(5)$ rad$^2$/s. This is a factor of two higher than the expected Stokes-Einstein diffusion $kT/8\pi r^3\eta = 0.02$, where the viscosity $\eta = 1.9$mPas for the binary mixture [238]. This deviation could be from hydrodynamics effects due to the vicinity of the capillary wall, the assumption of no-slip boundary conditions or the composite nature of the particle [254].

We calibrated the traps by tracking the Brownian movement of a single colloidal dipatch particle in the trap. Such calibrations were performed after each experiment to account for slight differences in laser intensity between measurements. The

overdamped dynamics of a trapped colloidal particle at position $(x, y)$ from the trap center is described by [109]:

$$\dot{x} = -\frac{k}{\gamma}x + \sqrt{\frac{2kT}{\gamma}}\xi(t), \tag{7.2}$$

with $k$ the spring constant of the trap, $\gamma$ the drag coefficient and $\xi(t)$ a normalized Gaussian stochastic process. This equation is solved by the mean square displacement (MSD) $\langle \Delta x^2 \rangle$

$$\langle \Delta x^2 \rangle = 2\left(1 - e^{-\Delta t/\tau}\right)\frac{kT}{k}. \tag{7.3}$$

Showing an exponential relaxation with time constant $\tau = \gamma/k$ where $\Delta t$ is the lag time. Equivalently, Eq.7.2 can be solved in terms of the power spectral density (PSD) $P(f)$ as a Lorentzian [244]

$$P(f) = \frac{kT}{\gamma\pi^2 f^2[1 + (f_c/f)^2]} \tag{7.4}$$

where $f$ is frequency and $f_c = 1/2\pi\tau$ the roll-off frequency. Fig. 7.1(d,e) shows the MSD and PSD of a dipatch colloidal particle in the static optical trap and a fit with Eqs. 7.3 and Eqs. 7.4, respectively. The good quality of the fits proves that the tweezers are well described by harmonic traps. From the best fits of both the PSD and the MSD, we obtain a diffusion coefficient $D = 0.03 \pm 0.001$ $\mu$m$^2$/s and a trap spring constant $k_s = 0.6 \pm 0.01$ pN/$\mu$m. This diffusion constant is consistent with the diffusion constant for freely diffusing particles, $D = 0.035 \pm 0.05$ $\mu$m$^2$/s that was measured in the previous chapter. The spring constant also agrees well with simply fitting a gaussian to the histogram of displacements to obtain $\sigma = 0.08$ $\mu$m, and $k_s = kT/\sigma^2 = 0.58 \pm 0.02$ pN/$\mu$m, see Fig. 7.1(f). Similar calibrations were done after each experiment for the static trap with slight variations in the found trap constants on the order of 0.1 pN/$\mu$m.

## 7.3 Buckling, creep and fracture

An overview of the micromechanical tests together with representative snapshots of the colloidal chain, are shown in Fig. 7.2. These real-space images already highlight the rich non-linear response of the colloidal chain, consisting of buckling, viscoelastic relaxation and fracture present in this simple system. In all cases we observe that above a critical compression $\Delta_c$ the initially straight chain buckles. Upon unloading, the chain reversibly straightens out, as seen in the cyclic compression test Fig. 7.2(b). This reversibility suggests an elastic response. Interestingly, at longer times, viscoelastic effects are present. We observe that when the trap is kept fixed at a certain maximum compression after buckling, the deflection keeps on increasing further, see Fig. 7.2(c). This behavior is reminiscent of a creep response. Typically creep is accompanied by stress relaxation, as can be seen by the trapped particles

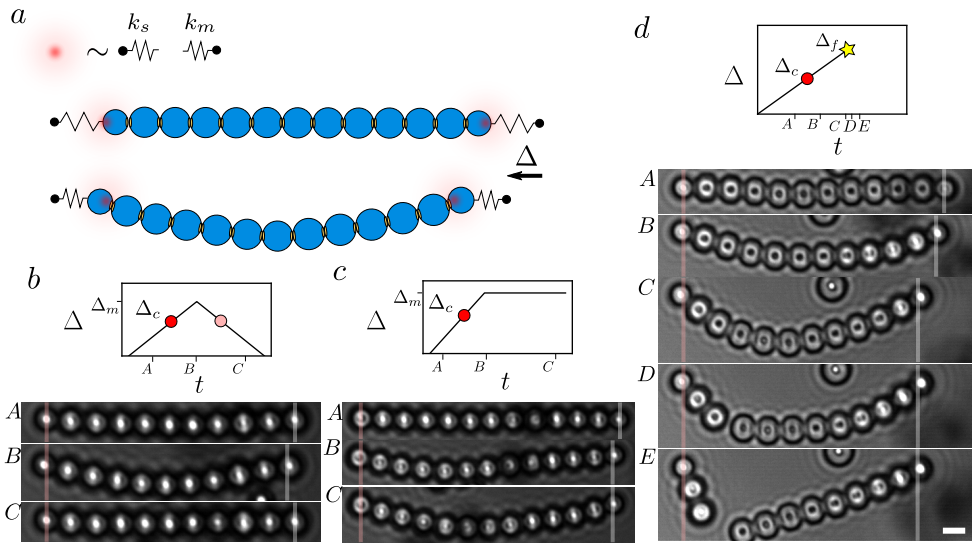


Figure 7.2: Micromechanical tests with optical tweezers: (a) sketch of a dipatch particle chain in two harmonic optical traps (b) Cyclic buckling test protocol and example snapshots at times (A) before buckling, (B) maximum compression and (C) reversible straightening. (c) Relaxation test protocol, snapshots when (B) trap movement is stopped reaching $\Delta_m$, (C) after waiting 100s at $\Delta_m$. (d) Fracture test protocol, snapshots at (C) 1s before fracture (D) 1s after fracture (E) 7s after fracture. Red (white) transparent lines in snapshots correspond to the $x$ position of the fixed (mobile) trap. Scale bar is 3 $\mu$m. (Video: *https://youtu.be/ZkhIux0PzjY*)

moving closer to the trap center. Finally, if we keep increasing the compression far beyond the initial buckling load we observe that at the fracture displacement $\Delta_f$, the chain breaks at a single connection point and two bonded patches separate, as shown by the snapshots in Fig. 7.2(d). This behavior is intimately linked to the limited patch area and strikingly different from the chains assembled for isotropic particle, which do not fracture, but instead show a continued folding through sequential plastic kinking, as shown in chapter 4. After fracture, the two remaining ends quickly release their elastic energy by straightening out, further showing the reversibility of the remaining two chain segments. We note that the short end straightens markedly faster, which makes sense given the faster dynamics of shorter bending modes.

## 7.4 Elastic Euler buckling

In order to better understand the buckling transition we perform various cyclic buckling tests for different lengths of chains from $N = 6$ to $N = 12$. A typical force versus mobile trap displacement is shown in Fig. 7.3(b). Initially, during

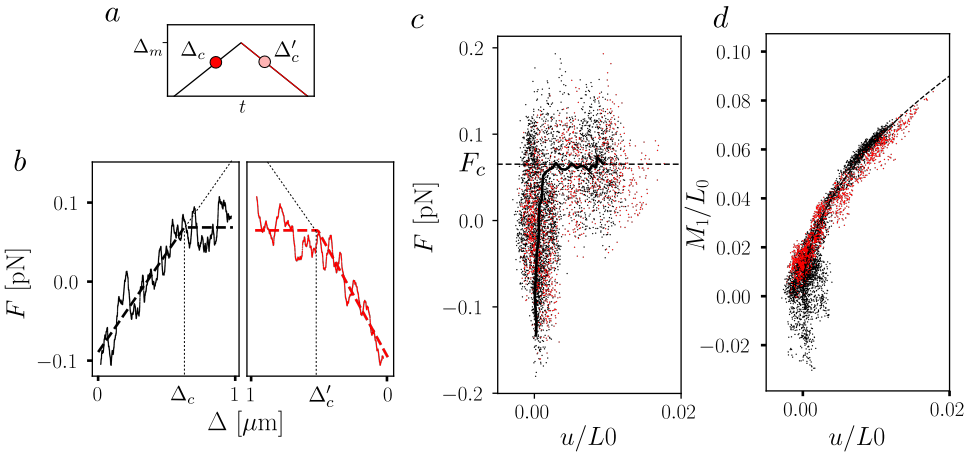


Figure 7.3: Reversible time-invariant elastic Euler buckling of dipatch chains (a) cyclic buckling protocol (b) Force versus trap displacement of loading (black) and unloading (red), data is smoothened by a rolling average over 100 frames. Dashed lines are fits to an initial linear increase followed by a constant plateau. (c) Force versus strain, dot's are individual data points, black line is a binning performed by rotating the dataset by 45°, dashed line is the best fitting $F_c$ for $u/L_0 > 0.005$. (d) Normalized $M_1$ versus strain. Dashed line is perfect first mode deflection $M_1/L_0 = 2/\pi\sqrt{u/L_0}$. All data corresponds to a single typical experiment of a $N = 11$ chain recorded at 20fps with $\Delta_m = 1\mu$m at $v_{trap} = 0.01\mu$m/s.

the loading phase, the force increases linearly with trap displacement, Fig. 7.3(b). The force starts out negative as chains are kept in a stretched state before starting the experiment. The slope of this increase fits to $k_\Delta = 0.25$ pN/$\mu$m. Such a spring constant agrees with the effective spring constant of the two traps, if placed in series. Indeed, the traps were calibrated with $k_s = 0.58$ pN/$\mu$m and $k_m = 0.45$ pN/$\mu$m, such that, if placed in series, they create an effective trap with constant $k_{eff} = 1/\left(1/k_s + 1/k_m\right) = 0.25$. Thus, in the pre-buckling regime, to first order only the trap springs compress and the chain is incompressible within measurement accuracy. However, at a critical trap displacement $\Delta_c$, the force no longer increases, but saturates at a plateau $F_c$. Interestingly, upon unloading a mirrored response occurs. by pinpointing the deflection points by interpolation, we obtain only small difference of $\Delta_c - \Delta_c' = 0.1(\pm 0.1)\mu m \pm (0.1\mu m)$, showing they are very similar. The small difference is explained partly by thermal noise. In addition the finite trap-speed can also delay buckling during loading as the chain becomes temporarily trapped in a non-equilibrium state. Nevertheless the reversible time-invariant behavior indicates an elastic response on these timescales and stress amplitudes. Indeed we can estimate the dissipated energy by integrating the fitted Force curves, using $\oint F d\Delta$, which yields roughly 2kT. This is not significantly above thermal noise.

Plotting the force $F$ versus strain $u/L_0$, instead of the trap displacement $\Delta$, we see

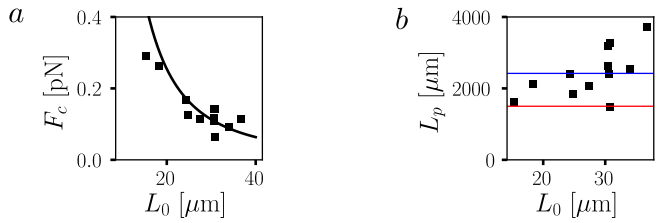


Figure 7.4: Chain buckling is inline with Euler's criterium (a) Buckling force versus chain length of 11 experiments. Solid line is a fit to the Euler's criterium $F_c = \pi^2 B/L_0^2$. (b) Persistence length, calculated by inverting Euler's criterium for each measurement separately. Blue (red) line corresponds to $L_p^{fast} = 2420\mu$m ($L_p^{slow} = ?\mu$m), previously obtained from analyzing thermal vibrations.

that the force transition coincides with a strong increase in strain, see Fig. 7.3(c). The incompressibility of the chain is further confirmed by the steep slope before buckling. The sharp transition at a critical force $F_c$ to a constant force is strongly reminiscent of the elastic response of classical Euler buckling [211–213]. The latter states that a freely hinged elastic rod of bending rigidity $B$ buckles out of its straight configuration into the lowest order mode at a load $F_c^e = \pi^2 B/L_0^2$. Indeed, the dipatch colloidal chain buckles into the first mode, as confirmed by looking at the first mode amplitude $M_1$ versus strain, Fig. 7.3(d). It closely follows the theoretical relation $M_1/L_0 = 2\sqrt{u/L_0}/\pi$, as shown by the dashed curve through the data points. Such agreement with an elastic model further indicates the chain exhibits an elastic response. This behavior closely resembles the buckling response of the chain of isotropic particles described in chapter 4. However, for the dipatch particle chain the agreement with the continuum theory is even more precise. This is likely due to the more perfect straightness of dipatch chains.

We performed similar buckling experiments for approximately 10 chains of different sizes and measured the force displacement curves. To get the most accurate value of $F_c$ for each experiment we average $F$ in the plateau regime by selecting data points with $u/L_0 > 0.005$. Fig. 7.4(a) shows the obtained values of $F_c$ for different chain lengths. A clear trend for larger $F_c$ with smaller chains is visible. The power of this increase is difficult to determine from the noisy data. If we however assume the Euler dependence $L_0^{-2}$, we obtain a best fit with the bending rigidity $B = 10$ pN$\mu$m$^2$, equivalent to a persistence length $L_p = B/kT = 2400$ $\mu$m. It is interesting to compare this with the slow and fast relaxing bending rigidities, $L_p^{fast} = 2420$ and $L_p^{slow} = 1500$ obtained from analysis of thermal vibrations with free boundary conditions. The value obtained from buckling is remarkably close to $L_p^{fast}$. Fig. 7.4(b) shows $L_p$ determined separately for each experiment from the measured critical force, $F_c$, and compares them to $L_p^{fast}$ and $L_p^{slow}$ (blue/red line). Here wee see that in fact there is quite some variation between the chains. The variation is partly explained by the polydispersity in patch area of the dipatch particles constituting the chains. Bigger patches will result in stronger bonds and

longer persistence length. In addition the limited temperature stability and noise in the measurement of $F_c$ can produce variations between different measurement. It is interesting though to see a trend towards lower rigidities for smaller chains. One reason for this could be the larger stress involved with shorter chains, increasing the likeliness of viscoplastic effects that reduce the effective rigidity. Another reason could be a dynamic one: In order for large chains to buckle in the first mode, more time is required due to the slower dynamics of these larger buckling modes, which grows with $L_0^4$, as shown in the previous chapter. As the speed of the trap movement is not reduced for the longer chains, a deviation from a quasi-static situation could occur. Therefore, for longer chains the trap movement is more likely to excite higher-order modes which increases the stress, as similarly occurs for macroscopic elastic slender filaments [255, 256].

We conclude that for moderate strains up to around 1% the chains show elastic Euler buckling, reversible upon unloading and on average in line with the rigidity found during fluctuation analysis on short timescales. However, a trend of growing effective bending rigidity with chain length points to the occurrence of other effects. This trend could be explained by the fact that shorter chains are more susceptible to viscoplastic effects and longer chains to dynamic higher-mode excitations.

## 7.5 Creeping and stress relaxation

We obtain further insight into these viscoelastic effects by analyzing a single representative stress-relaxation experiment in detail. This time, after moving the trap with constant speed until after the buckling point, we stop and keep it at a fixed, strained position. The mobile trap displacement and corresponding force, first-mode amplitude and compression are shown in Fig. 7.5(a). At the trap displacement $\Delta_c$ the chain buckles as described before: $F_c$ plateaus while $M_1$ and $u$ start increasing. Indeed, this regime in the force-compression curve, Fig. 7.5(b), looks almost identical to Fig. 7.3(c). This time, however, the plateau does not hold: Close to the point of maximum trap displacement, indicated by the star, the force starts decreasing. While the trap is held fixed, the force further relaxes to zero. At the same time the strain and deflection continue to increase in a creep-like fashion. The resulting force-compression curve (Fig. 7.5b) shows a pronounced shift to the right. To close the circle, when the chain has fully relaxed, we quickly unload. Again, a delayed response is observed with $u$ and $M_1$ decaying after trap movement has stopped. Fig. 7.5(c) shows the first mode amplitude versus displacement. Interestingly, close to the point where the force started yielding (indicated by star) the first amplitude deviates from a pure first mode deformation (indicated by dotted line). This means that higher bending modes are getting excited, deviating from the pure Euler buckling observed before.

These observations indicate non-elastic effects, as most clearly shown by the force strain curve, Fig. 7.5(b). The curve exhibits a loop with non-zero enclosed area, indicating that energy is dissipated. The enclosed area corresponds to the

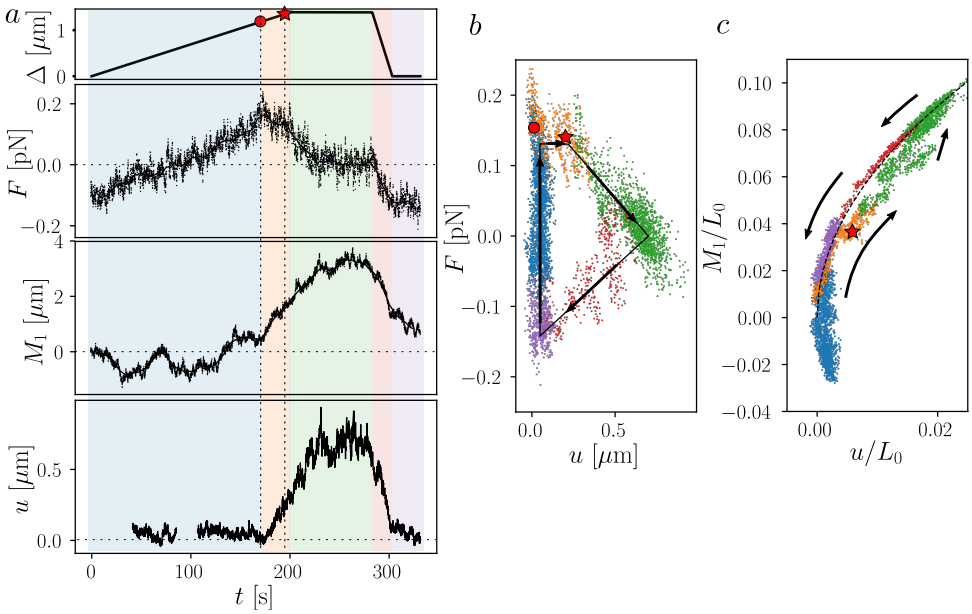


Figure 7.5: Broken time-invariance due to viscoelastic dissipation (a) Time traces of trap displacement, force, first mode amplitude and strain of a $N = 13$ chain undergoing a stress relaxation protocol followed by a quick unloading. Red dot indicates buckling, red star yielding. (b,c) Force, first mode versus strain. The colors and location of the red star are consistent over the panels

amount of dissipated energy. By rough interpolation of the data we can integrate and find $\Delta E_u^\circ = \oint F du = 21\ kT$, significantly higher than thermal energy. We can alternatively integrate the force over the trap displacement $\Delta$ (figure not shown), and find $\Delta E_\Delta^\circ = \oint F d\Delta = 78\ kT$. This is even higher because it includes dissipation of energy that was stored in the trap springs on top of the elastic energy necessary to bend the chain. The values are well above thermal noise, strikingly different than obtained in the elastic experiments below $\Delta_c$.

In order to better understand this dissipative process, we focus on the period after buckling at which the trap movement has stopped and the stress relaxes. Fig. 7.6(b-d) shows zoom-in on this part of the test. The evolution of both the force and the strain are well fitted by exponential relaxations,

$$F = F_i e^{-\Delta t/\tau_F}, \quad u = u_f - u_{creep} e^{-\Delta t/\tau_u}, \tag{7.5}$$

where $\Delta t = t - t_2$, $F_i = 0.13$pN the initial stress, $u_f$ the final displacement and $u_{creep} = 0.46\mu$m the total creep displacement. From these fits we obtain relaxation times of $\tau_F = 13 \pm 1$s, and $\tau_u = 14 \pm 1$s, which agree with each other within error bars. We also fit an exponential relaxation to $M_1$ and find $\tau_{M_1} = 22 \pm 1$s. For a pure first-mode deformation one expects $M_1 \propto \sqrt{u}$, and $\tau_{M_1} = 2\tau_u$. The slightly

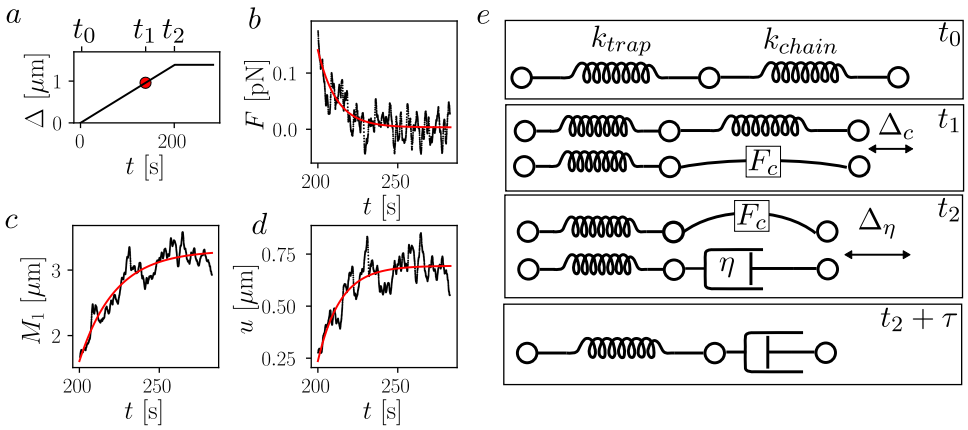


Figure 7.6: (a) Zoom in on the stress relaxation test of the experiment (b,c,d) Stress relaxation, deflection creep and strain creep, time starts at $t_2$. Red lines are exponential relaxation fits. (e) A macroscopic mechanical model for the trap plus chain system. As a function of trap displacement the chain shows a different mechanical response depending if it is straight, buckled or has yielded.

fast $\tau_{M_1}$ we observe is likely caused by additional relaxation of higher modes into the first-mode, speeding up first-mode growth.

We propose a minimal mechanical model to interpret the viscoelastic response, outlined in Fig. 7.6(e). Before buckling, the system can be thought of as two springs in series, one representing both traps, with effective spring constant $k_{trap} = (1/k_s + 1/k_m)^{-1}$, and the other representing the chain in its straight state, with $k_{chain}$. As was shown, while loading only the traps compress since $k_{chain} \gg k_{trap}$. After buckling occurs ($t_1$) the chain becomes compliant but resists with a constant force $F_c$. At an even higher strain (time $t_2$, and $\Delta = \Delta_\eta$), the chain yields and is replaced by a dashpot with effective viscosity $\eta'$. This turns the trap-chain system into a Maxwell material. Here we mean yielding in the sense that a transition occurs from dominated by elastic behavior to dominated by viscous behavior. The mechanical response of the system can be summarized using the following constitutive equations

$$\begin{cases} F = k_{trap}(\Delta - \Delta_0), \quad u = 0 & \text{if } \Delta < \Delta_c, \\ F = F_c, \quad u = \Delta - \Delta_c & \text{if } \Delta_c < \Delta < \Delta_\eta, \\ \dot{\Delta} = \frac{\dot{F}}{k_{trap}} + \frac{F}{\gamma'}, \quad \dot{u} = \frac{F}{\gamma'} & \text{if } \Delta_\eta < \Delta, \end{cases} \tag{7.6}$$

where $\Delta_0$ is the equilibrium trap length, $\gamma'$ is a drag coefficient, associated with an effective viscosity $\gamma' = \eta' A / L_0$ via an area $A$. Fitting the loading and buckling regime, we get a value of $k_{trap} = 0.26$ pN/$\mu$m, and $F_c = 0.14$ pN. If we assume $\Delta_\eta$

coincides with $\Delta_m$, and $\dot{\Delta} = 0$ in the viscous regime it follows that

$$F = F_c e^{-k_{trap}t/\gamma'}, \quad u = -\frac{F_c}{k_{trap}} e^{-k_{trap}t/\gamma'} + u(t = t_2). \tag{7.7}$$

This corresponds directly to the exponential relaxation fit, when $F_c = F_i$ and $k_{trap} = F_i/u_{creep} = 0.3$ pN/$\mu$m and $\gamma' = 4$ Pas$\mu$m. The spring constant and $F_c$ agree well with the values obtained for the loading and buckling regime. Moreover the small overestimation of $k_{trap}$ with respect to the expected value $(1/k_s + 1/k_m)^{-1} = 0.26$ pN/$\mu$m, is likely due to the assumption that $\Delta_\eta = \Delta_m$. Yielding probably occurred slightly earlier at the point where higher modes got excited. For such a minimal model, the agreement is striking.

Though this effective model correctly describes the observed response it does not give insight into the source of the drag coefficient $\gamma'$. This must be a consequence of the bending as the viscous effect is only observed after buckling. Could the origin of this effective drag coefficient be simply the viscosity of the fluid? From thermal fluctuation measurements we extracted a drag coefficient for $M_1$, $\gamma_{M_1} = 50$ mPas$\mu$m (data, not shown). For a pure first-mode deformation close to a non-zero strain $u^0$ and mode amplitude $M_1^0$, $\dot{M}_1 = \frac{M_1^0}{u^0}\dot{u}$. Therefore, $\gamma = \frac{M_1^0}{u^0}\gamma_{M_1}$. In our experimental case $\frac{u^0}{M_1^0} \sim 1$, and $\gamma \sim 60$ mPas$\mu$m. This is almost two orders of magnitude lower than $\gamma'$. We conclude that the source of the drag cannot be the outside fluid and therefore has to come from internal friction.

We found in chapter 6 (free fluctuation chain) that on timescale on the order of 10s, dissipative effects take place. This was then also associated with internal friction with an effective viscosity of 1Pas. Associating the $\gamma'$ in the mechanical model with a viscosity via the area $A = d^2$, this yields $\eta' = \gamma' L_0/A = 14$Pas. The similarity of timescales and effective viscosity values indicates that both effects have the same origin. We speculated before that the origin of this dissipation is slow conformational changes, specifically contact slippage. Using the buckling experiments we can get some more insight in the microscopic origin of this friction. It is striking that at the yielding point a strong deviation from a perfect first mode occurs. This suggests indeed that conformational changes occur that excite higher modes. The real-space snapshots suggest that the higher-order modes localize bending on a single bond, indicating bond shear slip. For a while, this slip is localized on this particular bond and grows in time. With increased strain this localization diminishes and now other bonds also get more bend, until finally a pure first mode buckling is recovered. One can understand this if slipping stops when a deeper local minimum is reached. This would lead to a local strain hardening at this contact and instead lead to other bonds bending further, effectively restoring the pure first-mode deflection.

## 7.6 From bending to snapping

At even larger strains, the dipatch particle chains show a transition from bending to snapping, dramatically different from the behavior of the isotropic colloidal chains.

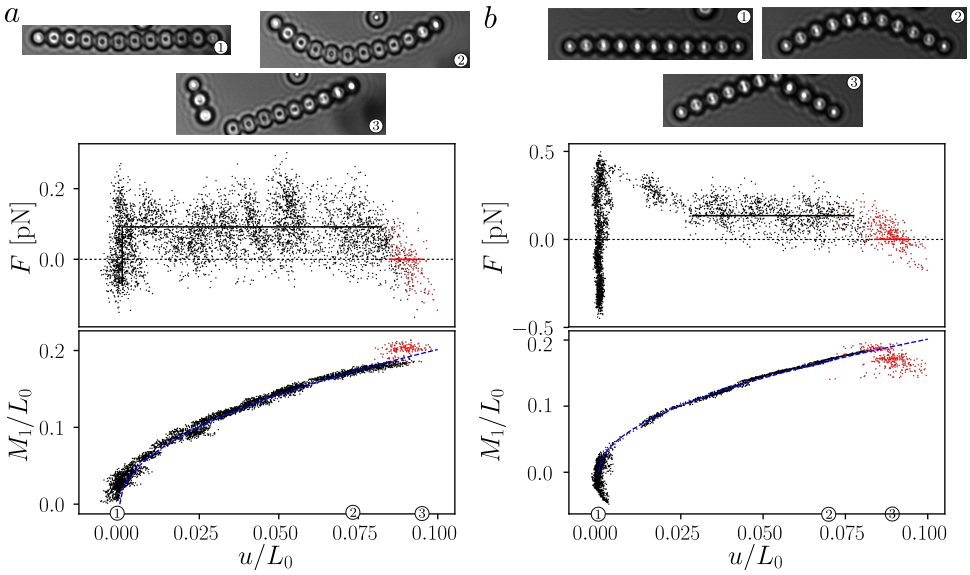


Figure 7.7: Force and first-mode deflection of two representative fracture tests (a) $N = 12$ chain, trap speed $0.015\mu$m/s(b) $N = 11$ chain, trap speed $0.02\mu$m/s Red dots are post-fracture data points. Numbers mark corresponding microscopy images of the chains before and after breaking. (Video: *https://youtu.be/2_anFaXxZzE*)

To get more insight into this transition, we performed fracture tests on different chains. The extracted force-strain curves and first-mode deflection curves of two typical test are shown together with microscope images of the snapping chain in Fig.7.7(a,b). The large applied strain, reaching about $u/L_0 \sim 10\%$, causes a strong chain bending. At a fracture strain $u_f/L_0$, the chain breaks at a single bond, after which the average force reduces to zero (red data points). This quick stress release together with the visible straightening of the chains, again indicates that there was stored elastic bending energy in the chain. As is seen in these two examples a chain does not always break in the middle where the highest curvature is expected to be localized. This can be explained first of all as a consequence of thermal noise which also excites higher mode bending which have a maximum curvature not in the middle. A second explanation comes from the polydispersity in patch-size of the particles, particles with smaller patch-size likely form weak spots that will break at a lower bending angle.

Given the fact that we observe viscoelastic effects already for lower strain, it is slightly surprising that, before breaking, the force and deflection curves on first inspection are very reminiscent of the elastic buckling behavior: The force curve shows the characteristic buckling transition from incompressible increase to a plateau bending regime, and the mode deflection overlaps almost perfectly with the theoretical one, as seen Fig. 7.7(a). Though we note that the chain of Fig. 7.7(b), shows an

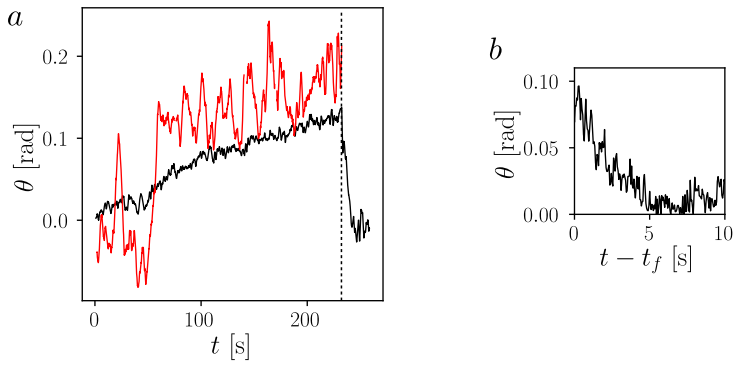


Figure 7.8: Bending angles of bonded particles versus time showing rapid straightening after the chains breaks (a) black line is the average of all bending angles $\langle\theta\rangle$, red line is the mean of the two bending angle next to the broken bond. Vertical dashed line marks the time at which the chains breaks (b) zoom in on 10s after fracture. Data comes from the same experiment as shown in Fig. 7.7(a)

especially large overshoot at the buckling compression. We attribute this to a dynamic buckling overshoot where the chain gets stuck in the straight state, causing a force overshoot because the buckling of the elastic chain is delayed. This apparent elastic response is surprising, given that at these large strains one expects to overcome the viscoelastic yield strain. However, at the current loading speed, the chain does not have time plastic relaxation. To estimate the plastic relaxation time scale, we use Eq. 7.6 to determine the post-yielding creep rate as $\dot{u} = \frac{F}{\gamma'} \sim 2.5\mu$m/s, where we have used the previously obtained value for the internal drag coefficient $\gamma' = 4Pas\mu$m and the force $F \sim 0.1$pN. This speed is in the same order of magnitude as the current loading speed of the trap such that the chain does not have time to fully relax. Furthermore, we attribute the source of viscous effects to bond slippage towards a new contact point with a new energy minimum. This could lead to strain hardening when arresting in a deeper energy well and to stick-slip behavior upon continued compression. Indeed, upon second inspection, the plateau region of the force curve of particularly the chain shown in Fig.7.7(a), does show some signatures of that. Instead of a constant force, a sequence of stress build ups and decays seem to occur. This could be a sign of sequential stress relaxation due to internal friction followed by strain hardening. However the noisy data due to thermal fluctuations makes it difficult to be more quantitative about this point.

When the chain breaks, stress is released as is evident from the force dropping to zero, further proving that there was bend energy stored in the chain. Fig.7.8(a) shows the average bending angle (black) and the bending angle associated with the bond that breaks (red). The average bending angle increases until the fracture point, reaching a maximum $\langle\theta\rangle_f$. The bond that breaks has a higher than average bend angle at the moment of breaking. Right after breaking, the average bend angle of the two broken chain parts straightens out quickly and relaxes to zero. The timescale

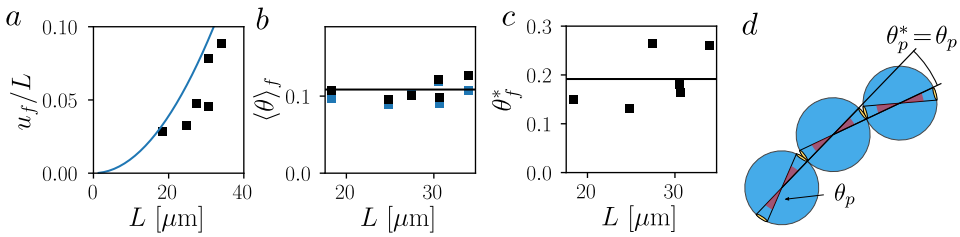


Figure 7.9: Fracture occurs at a critical bending angle (a) the maximum strain reached right before fracture, blue line is a prediction based on a maximum bending criterium, see text (b) the mean bending angle right before fracture versus chain length, black line is the average (c) the maximum bending angle of the bond that snaps, black line is the average (d) Geometric argument that the expected maximum bond bending angle $\theta_p^*$ equals the patch arc angle $\theta_p$

of straightening is limited by solvent friction (rather than internal friction) and is of the order of a few seconds, see zoom-in in Fig.7.8(b).

We performed many more fracture experiments, and plot their fracture strains as a function of chain length in Fig. 7.9(a). A clear systematic increase is observed. This is to be expected as longer chains show less local bending for the same strains. Interestingly, the average bending angle right before fracture $\langle\theta\rangle_f$ appears almost insensitive with an average $\langle\bar{\theta}\rangle_f = 0.11(1)$rad to chain length, see Fig. 7.9(b). This suggests that $\langle\theta\rangle_f$ is a critical bending angle that we can use as predictive criterium for fracture. We also plotted an alternative bending angle, $\langle\theta_{M_1}\rangle_f$, corresponding to the average bending angle in case of a pure first mode deformation, defined by, $\langle\theta_{M_1}\rangle_f = 2\pi d M_{1,f}/L_0^2$ (blue data points). These two quantities almost overlap, further showing that deformation is close to a pure first mode and that $\langle\theta_{M_1}\rangle_f$ forms an equivalent critical bending criterium. We can use this criterium together with the relation $M_1/L_0 = 2\sqrt{u/L_0}/\pi$ to obtain a prediction for the fracture strain $u_f/L_0 = (L_0/d)^2\langle\theta_{M_1}\rangle_f^2/16$, which is shown Fig. 7.9(a, blue line). Given that there are no fitting parameters in this prediction for the fracture strain the agreement with experiment is striking.

These robust bending criteria can be evaluated with respect to the patch size. The patch has a diameter of approximately $d_p = 0.38(5)$ $\mu$m, which translates to an arc angle $2\sin^{-1}(d_p/d) = 0.14(2)^\circ = 0.24(3)$rad (see chapter 2). Here the uncertainty is an estimation of the particle patch area polydispersity. We expect that the chain will break when one bond angle reaches the patch arc angle, as is graphically explained in Fig. 7.9(d). The critical bending criterium is in terms of the average bending angle, but for a pure first mode deformation this can be translated to a maximum bending angle $max(\theta_{M_1})_f = \pi\langle\theta_{M_1}\rangle_f/2 = 0.17(1)$. This is indeed close to the patch arc angle, yet is slightly smaller, which means chains break slightly earlier than this limit. The difference can be explained by patch size polydispersity, but using the estimation of polydispersity this would still be lower than expected. More important is probably the thermal noise which can temporarily increase local bending, as can

be seen in the red curve of Fig.7.8(a). Based on the fluctuation results in chapter 6 such fluctuations are indeed significant and on the order of $\sim$ 0.05rad. That there is a higher local bending is also confirmed by the fact that actual measured bending angle of the bond that snaps $\theta_f^*$, is typically higher than 0.17, as shown in Fig. 7.9(c). Averaging over all the measurements yields $\bar{\theta_f^*} = 0.20(5)$rad, consistent within accuracy with the patch arc angle. From this correspondence we conclude that the fracture transition arises from the limited patch size, which explains the striking difference with the response of isotropic particle chains.

## 7.7 Conclusion

We have shown that chains of dipatch colloidal particles buckle elastically, showing an ideal elastic Euler buckling behavior when strain is kept below the yield strain. For larger strains, viscoelastic effects lead to stress-relaxation. Ultimately, if strain is increased even further, the chains break. The elastic buckling agrees well with macroscopic Euler buckling and we recover the $F_c \propto L^{-2}$ scaling of buckling load with filament length. From the buckling load we, extracted a persistence length that compared favorably with the independent fluctuation experiments reported in the previous chapter. Viscoelastic effects occurring beyond the yield strain are attributed to internal friction due to bond slippage. We used a simple linear viscoelastic model that provided a good fit to the experimental stress-relaxation data. Finally, we showed that chain fracture occurs at a critical maximum bending angle, the value of which we could rationalize based on the size of the patch and thermal noise.

These results highlight the rich non-linear, viscoelastic and fracture mechanics present in self-assembled patchy particle chains. They also show that we can model and predict essential features of this mechanical behavior accurately. The elastic loading, viscoelastic relaxation with apparent stick-slip dynamics, and final failure of these chains strongly remind of the mechanical properties of bulk materials. The finite patch size has been proven essential not only in determining the structures formed through self-assembly, but also in determining the resulting mechanics of these structures. In particular, they impart these structure with a breaking mechanism that is fully absent in non-patchy assemblies. These results show patchy particle self-assembly are a promising route to achieve colloidal architectures with designer mechanical properties, further extending the uses of dipatch chains as model filaments.

# References


[1] S. Tibbits, *https://selfassemblylab.mit.edu*, Accessed: 26-08-2019.

[2] C. R. Shalizi, "Causal architecture, complexity and self-organization in the time series and cellular automata", PhD thesis (University of Wisconsin–Madison, 2001).

[3] L. L. A. Simon J. DePasquale., *https://apod.nasa.gov/apod/ap180903.html*, Aurora around Saturn's North Pole. Astronomy picture of the day 03-09-2018. Accessed: 28-08-2019.

[4] A. Goldsworthy, *Andy goldsworthy: a collaboration with nature* (New York: Harry N. Abrams, 1990).

[5] C. R. Reid, M. J. Lutz, S. Powell, A. B. Kao, I. D. Couzin, and S. Garnier, "Army ants dynamically adjust living bridges in response to a cost–benefit trade-off", Proc. Natl. Acad. Sci. U.S.A. **112**, 15113–15118 (2015).

[6] S. Köhler, F. Schmid, and G. Settanni, "The internal dynamics of fibrinogen and its implications for coagulation and adsorption", PLOS Computational Biology **11**, 1–19 (2015).

[7] G. M. Whitesides and B. Grzybowski, "Self-assembly at all scales", Science **295**, 2418–2421 (2002).

[8] J. Butterfield, "Emergence, reduction and supervenience: a varied landscape", Foundations of Physics **41**, 920–959 (2011).

[9] P. W. Anderson, "More is different", Science **177**, 393–396 (1972).

[10] R. B. Laughlin, *A different universe: reinventing physics from the bottom down* (Basic Books, 2008).

[11] S. J. Blundell, "Emergence, causation and storytelling: condensed matter physics and the limitations of the human mind", Philosophica **92**, 139 (2017).

[12] S. Sacanna, *https://www.sacannalab.com/*, For more examples of beautiful colloidal particles and some recipes how to make them. Accessed: 28-08-2019.

[13] S. Sacanna, W. T. M. Irvine, P. M. Chaikin, and D. J. Pine, "Lock and key colloids", Nature **464**, 575 (2010).

[14] Y. Wang, Y. Wang, D. R. Breed, V. N. Manoharan, L. Feng, A. D. Hollingsworth, M. Weck, and D. J. Pine, "Colloids with valence and specific directional bonding", Nature **491**, 51 (2012).

[15]A. A. Shah, B. Schultz, W. Zhang, S. C. Glotzer, and M. J. Solomon, "Actuation of shape-memory colloidal fibres of janus ellipsoids", Nature Materials **14**, 117 (2014).

[16]Q. Chen, S. C. Bae, and S. Granick, "Directed self-assembly of a colloidal kagome lattice", Nature **469**, 381 (2011).

[17]F. Sciortino and E. Zaccarelli, "Reversible gels of patchy particles", Curr. Opin. Solid State Mater. Sci. **15**, 246 –253 (2011).

[18]M. Rubenstein, A. Cornejo, and R. Nagpal, "Programmable self-assembly in a thousand-robot swarm", Science **345**, 795–799 (2014).

[19]S. Felton, M. Tolley, E. Demaine, D. Rus, and R. Wood, "A method for building self-folding machines", Science **345**, 644–646 (2014).

[20]J.-M. Lehn, "Toward self-organization and complex matter", Science **295**, 2400–2403 (2002).

[21]J. N. Israelachvili, *Intermolecular and surface forces* (Academic press, 2015).

[22]F. Herbst, D. Döhler, P. Michael, and W. H. Binder, "Self-healing polymers via supramolecular forces", Macromolecular Rapid Communications **34**, 203–220 (2013).

[23]M. L. Hammock, A. Chortos, B. C.-K. Tee, J. B.-H. Tok, and Z. Bao, "25th anniversary article: the evolution of electronic skin (e-skin): a brief history, design considerations, and recent progress", Advanced Materials **25**, 5997–6038 (2013).

[24]M. R. Jones, N. C. Seeman, and C. A. Mirkin, "Programmable materials and the nature of the dna bond", Science **347** (2015) *10.1126/science.1260901*.

[25]C. R. Kagan and C. B. Murray, "Charge transport in strongly coupled quantum dot solids", Nature Nanotechnology **10**, 1013 (2015).

[26]W. B. Russel, D. A. Saville, and W. R. Schowalter, *Colloidal dispersions* (Cambridge University Press, Cambridge, 1989).

[27]D. F. Evans and H. Wennerstrom, *Colloidal domain* (Wiley-Vch, 1999).

[28]V. N. Manoharan, "Colloidal matter: packing, geometry, and entropy", Science **349**, 1253751 (2015).

[29]B. Li, D. Zhou, and Y. Han, "Assembly and phase transitions of colloidal crystals", Nature Reviews Materials **1**, 15011 (2016).

[30]P. N. Pusey and W. van Megen, "Phase behaviour of concentrated suspensions of nearly hard colloidal spheres", Nature **320**, 340–342 (1986).

[31]M. E. Leunissen, C. G. Christova, A.-P. Hynninen, C. P. Royall, A. I. Campbell, A. Imhof, M. Dijkstra, R. van Roij, and A. van Blaaderen, "Ionic colloidal crystals of oppositely charged particles", Nature **437**, 235–240 (2005).

[32]M. Y. Lin, H. M. Lindsay, D. A. Weitz, R. C. Ball, R. Klein, and P. Meakin, "Universality in colloid aggregation", Nature **339**, 360–362 (1989).

[33]P. N. Pusey and W. van Megen, "Observation of a glass transition in suspensions of spherical colloidal particles", Phys. Rev. Lett. **59**, 2083–2086 (1987).

[34]U. Gasser, E. R. Weeks, A. Schofield, P. N. Pusey, and D. A. Weitz, "Real-space imaging of nucleation and growth in colloidal crystallization", Science **292**, 258–262 (2001).

[35]A. Pertsinidis and X. S. Ling, "Diffusion of point defects in two-dimensional colloidal crystals", Nature **413**, 147–150 (2001).

[36]P. Schall, D. A. Weitz, and F. Spaepen, "Structural rearrangements that govern flow in colloidal glasses", Science **318**, 1895–1899 (2007).

[37]S. Sacanna, M. Korpics, K. Rodriguez, L. Colón-Meléndez, S.-H. Kim, D. J. Pine, and G.-R. Yi, "Shaping colloids for self-assembly", Nature Communications **4**, 1688 (2013).

[38]Z. Gong, T. Hueckel, G. R. Yi, and S. Sacanna, "Patchy particles made by colloidal fusion", Nature **550**, 234–238 (2017).

[39]L. Rossi, S. Sacanna, W. T. M. Irvine, P. M. Chaikin, D. J. Pine, and A. P. Philipse, "Cubic crystals from cubic colloids", Soft Matter **7**, 4139–4142 (2011).

[40]M. Youssef, T. Hueckel, G.-R. Yi, and S. Sacanna, "Shape-shifting colloids via stimulated dewetting", Nature Communications **7**, 12216 (2016).

[41]W. B. Rogers, W. M. Shih, and V. N. Manoharan, "Using dna to program the self-assembly of colloidal nanoparticles and microparticles", Nat. Rev. Mater. **1**, 16008 (2016).

[42]M. Y. Ben Zion, X. He, C. C. Maass, R. Sha, N. C. Seeman, and P. M. Chaikin, "Self-assembled three-dimensional chiral colloidal architecture", Science **358**, 633–636 (2017).

[43]A. McMullen, M. Holmes-Cerfon, F. Sciortino, A. Y. Grosberg, and J. Brujic, "Freely jointed polymers made of droplets", Phys. Rev. Lett. **121**, 138002 (2018).

[44]V. D. Nguyen, M. T. Dang, T. A. Nguyen, and P Schall, "Critical casimir forces for colloidal assembly", J. Phys.: Condens. Matter **28**, 043001 (2016).

[45]J. Van Doorn, J. Sprakel, and T. Kodger, "Temperature-triggered colloidal gelation through well-defined grafted polymeric surfaces", Gels, 21 (2017).

[46]A. van Blaaderen, "Colloids under external control", MRS Bulletin **29**, 85–90 (2004).

[47]C. Bechinger, R. Di Leonardo, H. Löwen, C. Reichhardt, G. Volpe, and G. Volpe, "Active particles in complex and crowded environments", Rev. Mod. Phys. **88**, 045006 (2016).

[48]D. Needleman and Z. Dogic, "Active matter at the interface between materials science and cell biology", Nature Reviews Materials **2**, 17048 (2017).

[49]D. J. Kraft, R. Ni, F. Smallenburg, M. Hermes, K. Yoon, D. A. Weitz, A. van Blaaderen, J. Groenewold, M. Dijkstra, and W. K. Kegel, "Surface roughness directed self-assembly of patchy particles into colloidal micelles", Proc. Natl. Acad. Sci. U.S.A. **109**, 10787–10792 (2012).

[50]J. R. Wolters, G. Avvisati, F. Hagemans, T. Vissers, D. J. Kraft, M. Dijkstra, and W. K. Kegel, "Self-assembly of "mickey mouse" shaped colloids into tube-like structures: experiments and simulations", Soft Matter **11**, 1067–1077 (2015).

[51]Q. Chen, J. K. Whitmer, S. Jiang, S. C. Bae, E. Luijten, and S. Granick, "Supracolloidal reaction kinetics of janus spheres", Science **331**, 199–202 (2011).

[52]P. Song, Y. Wang, Y. Wang, A. D. Hollingsworth, M. Weck, D. J. Pine, and M. D. Ward, "Patchy particle packing under electric fields", J. Am. Chem. Soc. **137**, 3069–3075 (2015).

[53]C. H. J. Evers, J. A. Luiken, P. G. Bolhuis, and W. K. Kegel, "Self-assembly of microcapsules via colloidal bond hybridization and anisotropy", Nature **534**, 364 (2016).

[54]P. G. Moerman, "Dynamics of active droplets and freely-jointed colloidal trimers", PhD thesis (Utrecht University, 2019).

[55]J. Yan, M. Han, J. Zhang, C. Xu, E. Luijten, and S. Granick, "Reconfiguring active particles by electrostatic imbalance", Nat. Mater. **15**, 1095–1100 (2016).

[56]A. Aubret, M. Youssef, S. Sacanna, and J. Palacci, "Targeted assembly and synchronization of self-spinning microgears", Nature Physics **14**, 1114–1118 (2018).

[57] Ducrot, M. He, G.-R. Yi, and D. J. Pine, "Colloidal alloys with preassembled clusters and spheres", Nature Materials **16**, 652 (2017).

[58]S. Whitelam and R. L. Jack, "The statistical mechanics of dynamic pathways to self-assembly", Annual Review of Physical Chemistry **66**, PMID: 25493714, 143–163 (2015).

[59]F. Smallenburg and F. Sciortino, "Liquids more stable than crystals in particles with limited valence and flexible bonds", Nature Physics **9**, 554 (2013).

[60]X. Mao, Q. Chen, and S. Granick, "Entropy favours open colloidal lattices", Nature Materials **12**, 217 (2013).

[61]P. F. Damasceno, M. Engel, and S. C. Glotzer, "Predictive self-assembly of polyhedra into complex structures", Science **337**, 453–457 (2012).

[62]G. van Anders, D. Klotsa, N. K. Ahmed, M. Engel, and S. C. Glotzer, "Understanding shape entropy through local dense packing", Proc. Natl. Acad. Sci. U.S.A. **111**, E4812–E4821 (2014).

[63]A. V. Tkachenko, "Theory of programmable hierarchic self-assembly", Phys. Rev. Lett. **106**, 255501 (2011).

[64]Z. Zeravcic, V. N. Manoharan, and M. P. Brenner, "Colloquium: toward living matter with colloidal particles", Rev. Mod. Phys. **89**, 031001 (2017).

[65]Z. Zeravcic and M. P. Brenner, "Self-replicating colloidal clusters", Proc. Natl. Acad. Sci. U.S.A. **111**, 1748–1753 (2014).

[66]Z. Zeravcic and M. P. Brenner, "Spontaneous emergence of catalytic cycles with colloidal spheres", Proc. Natl. Acad. Sci. U.S.A. **114**, 4342–4347 (2017).

[67]J. Mewis and N. J. Wagner, *Colloidal suspension rheology* (Cambridge University Press, 2012).

[68]C. P. Broedersz and F. C. MacKintosh, "Modeling semiflexible polymer networks", Rev. Mod. Phys. **86**, 995–1036 (2014).

[69]S. L. Biswal and A. P. Gast, "Mechanics of semiflexible chains formed by poly-(ethylene glycol)-linked paramagnetic particles", Phys. Rev. E **68**, 021402 (2003).

[70]K. Bertoldi, V. Vitelli, J. Christensen, and M. van Hecke, "Flexible mechanical metamaterials", Nat. Rev. Mater. **2**, 17066 (2017).

[71]P. Hänggi and F. Marchesoni, "Artificial brownian motors: controlling transport on the nanoscale", Rev. Mod. Phys. **81**, 387–442 (2009).

[72]T. E. Kodger, R. E. Guerra, and J. Sprakel, "Precise colloids with tunable interactions for confocal microscopy", Sci. Rep. **5**, 14635 (2015).

[73]R. Arshady, "Suspension, emulsion, and dispersion polymerization: a methodological survey", Colloid and Polymer Science **270**, 717–732 (1992).

[74]J. Lee, J. U. Ha, S. Choe, C.-S. Lee, and S. E. Shim, "Synthesis of highly monodisperse polystyrene microspheres via dispersion polymerization using an amphoteric initiator", J. Colloid Interface Sci. **298**, 663 –671 (2006).

[75]Z. Gong, "T.b.d.", PhD thesis (New York University, 2019).

[76]H. E. Stanley, *Phase transitions and critical phenomena* (Clarendon Press, Oxford, 1971).

[77]N. Goldenfeld, *Lectures on phase transitions and the renormalization group* (CRC Press, 2018).

[78]M. Kardar and R. Golestanian, "The "friction" of vacuum, and other fluctuation-induced forces", Rev. Mod. Phys. **71**, 1233–1245 (1999).

[79]H. B. G. Casimir, "On the Attraction Between Two Perfectly Conducting Plates", Indag. Math. **10**, [Kon. Ned. Akad. Wetensch. Proc.100N3-4,61(1997)], 261–263 (1948).

[80]M. E. Fisher and P. G. de Gennes, "Phenomena at the walls in a critical binary mixture", C. R. Acad. Paris Ser. B **287**, 207–209 (1978).

[81]M. Krech, *The casimir effect in critical systems* (World Scientific, 1994).

[82]A. Maciołek and S. Dietrich, "Collective behavior of colloids due to critical casimir interactions", Rev. Mod. Phys. **90**, 045001 (2018).

[83]J. L. Sengers, *How fluids unmix: discoveries by the school of van der waals and kamerlingh onnes* (2002).

[84]S. R. Kline and E. W. Kaler, "Colloidal interactions in water/2-butoxyethanol solvents", Langmuir **10**, 412–417 (1994).

[85]R. D. Koehler and E. W. Kaler, "Colloidal phase transitions in aqueous nonionic surfactant solutions", Langmuir **13**, 2463–2470 (1997).

[86]S. Buzzaccaro, J. Colombo, A. Parola, and R. Piazza, "Critical depletion", Phys. Rev. Lett. **105**, 198301 (2010).

[87]U. Capasso Palmiero, A. Agostini, E. Lattuada, S. Gatti, J. Singh, C. T. Canova, S. Buzzaccaro, and D. Moscatelli, "Use of raft macro-surfmers for the synthesis of transparent aqueous colloids with tunable interactions", Soft Matter **13**, 6439–6449 (2017).

[88]M. N. Barber, "Finite size-scaling", in *Phase transitions and critical phenomena*, Vol. 8, edited by C. Domb and J. L. Lebowitz (Academic Press, 1983), p. 145.

[89]A. Gambassi, A. Maciołek, C. Hertlein, U. Nellen, L. Helden, C. Bechinger, and S. Dietrich, "Critical casimir effect in classical binary liquid mixtures", Phys. Rev. E **80**, 061143 (2009).

[90]J. S. van Duijneveldt and D. Beysens, "Adsorption on colloids and flocculation: the influence of salt", The Journal of Chemical Physics **94**, 5222–5225 (1991).

[91]U. Nellen, J. Dietrich, L. Helden, S. Chodankar, K. Nygård, J. Friso van der Veen, and C. Bechinger, "Salt-induced changes of colloidal interactions in critical mixtures", Soft Matter **7**, 5360–5364 (2011).

[92]H. Guo, T. Narayanan, M. Sztuchi, P. Schall, and G. H. Wegdam, "Reversible phase transition of colloids in a binary liquid solvent", Phys. Rev. Lett. **100**, 188303 (2008).

[93]V. D. Nguyen, S. Faber, Z. Hu, G. H. Wegdam, and P. Schall, "Controlling colloidal phase transitions with critical casimir forces", Nat. Commun. **4**, 1584 (2013).

[94]S. Z. Mirzaev, R. Behrends, T. Heimburg, J. Haller, and U. Kaatze, "Critical behavior of 2,6-dimethylpyridine-water: measurements of specific heat, dynamic light scattering, and shear viscosity", J. Chem. Phys. **124**, 144517 (2006).

[95]F. Pousaneh, A. Ciach, and A. Maciołek, "How ions in solution can change the sign of the critical casimir potential", Soft Matter **10**, 470–483 (2014).

[96]T. F. Mohry, S. Kondrat, A. Maciołek, and S. Dietrich, "Critical casimir interactions around the consolute point of a binary solvent", Soft Matter **10**, 5510–5522 (2014).

[97]T. Zemb and P. Lindner, *Neutrons, x-rays and light: scattering methods applied to soft condensed matter* (North-Holland, 2002).

[98]M. S. Elliot and W. C. Poon, "Conventional optical microscopy of colloidal suspensions", Advances in Colloid and Interface Science **92**, 133 –194 (2001).

[99]V Prasad, D Semwogerere, and E. R. Weeks, "Confocal microscopy of colloids", Journal of Physics: Condensed Matter **19**, 113102 (2007).

[100]J. C. Crocker and D. G. Grier, "Methods of digital video microscopy for colloidal studies", J. Colloid Interface Sci. **179**, 298 –310 (1996).

[101]M. Jenkins and S. Egelhaaf, "Confocal microscopy of colloidal particles: towards reliable, optimum coordinates", Advances in Colloid and Interface Science **136**, 65 –92 (2008).

[102]J. Palacci, S. Sacanna, A. P. Steinberg, D. J. Pine, and P. M. Chaikin, "Living crystals of light-activated colloidal surfers", Science **339**, 936–940 (2013).

[103]G. Sluder and D. E. Wolf, *Digital microscopy*, Vol. 114 (Academic Press, 2013).

[104]D. G. Grier, "A revolution in optical manipulation", Nature **424**, 810–816 (2003).

[105]S. Chu, "Nobel lecture: the manipulation of neutral particles", Rev. Mod. Phys. **70**, 685–706 (1998).

[106]F. M. Fazal and S. M. Block, "Optical tweezers study life under tension", Nature Photonics **5**, 318 (2011).

[107]A. Ashkin, "Acceleration and trapping of particles by radiation pressure", Phys. Rev. Lett. **24**, 156–159 (1970).

[108]A. Ashkin, J. M. Dziedzic, J. E. Bjorkholm, and S. Chu, "Observation of a single-beam gradient force optical trap for dielectric particles", Opt. Lett. **11**, 288–290 (1986).

[109]K. C. Neuman and S. M. Block, "Optical trapping", Rev. Sci. Instrum. **75**, 2787–2809 (2004).

[110]D. G. Grier, "Optical tweezers in colloid and interface science", Current Opinion in Colloid & Interface Science **2**, 264 –270 (1997).

[111]S. Paladugu, A. Callegari, Y. Tuna, L. Barth, S. Dietrich, A. Gambassi, and G. Volpe, "Nonadditivity of critical casimir forces", Nature Communications **7**, 11403 (2016).

[112]F. Schmidt, A. Magazzù, A. Callegari, L. Biancofiore, F. Cichos, and G. Volpe, "Microscopic engine powered by critical demixing", Phys. Rev. Lett. **120**, 068004 (2018).

[113]D. L. J. Vossen, A. van der Horst, M. Dogterom, and A. van Blaaderen, "Optical tweezers and confocal microscopy for simultaneous three-dimensional manipulation and imaging in concentrated colloidal dispersions", Review of Scientific Instruments **75**, 2960–2970 (2004).

[114]J. M. van Doorn, R. Higler, R. Wegh, R. Fokkink, A. Zaccone, J. Sprakel, and J. van der Gucht, "Infrasonic wave propagation in ultrasoft solids at low reynolds numbers", arXiv preprint arXiv:1907.10736 (2019).

[115]E. M. Furst and A. P. Gast, "Micromechanics of dipolar chains using optical tweezers", Phys. Rev. Lett. **82**, 4130–4133 (1999).

[116]J. P. Pantina and E. M. Furst, "Elasticity and critical bending moment of model colloidal aggregates", Phys. Rev. Lett. **94**, 138301 (2005).

[117]K. I. Mortensen, L. S. Churchman, J. A. Spudich, and H. Flyvbjerg, "Optimized localization analysis for single-molecule tracking and super-resolution microscopy", Nature Methods **7**, 377 (2010).

[118]T. Savin and P. S. Doyle, "Static and dynamic errors in particle tracking microrheology", Biophysical Journal **88**, 623 –638 (2005).

[119]M. K. Cheezum, W. F. Walker, and W. H. Guilford, "Quantitative comparison of algorithms for tracking single fluorescent particles", Biophysical Journal **81**, 2378 –2388 (2001).

[120]S.-H. Lee, Y. Roichman, G.-R. Yi, S.-H. Kim, S.-M. Yang, A. van Blaaderen, P. van Oostrum, and D. G. Grier, "Characterizing and tracking single colloidal particles with video holographic microscopy", Opt. Express **15**, 18275–18282 (2007).

[121]C. van der Wel and D. J. Kraft, "Automated tracking of colloidal clusters with subpixel accuracy and precision", Journal of Physics: Condensed Matter **29**, 044001 (2016).

[122]D. Allan, T. Caswell, N. Keim, and C. van der Wel, "Trackpy v0.3.1", Zenodo **55143** (2016).

[123]C. Hertlein, L. Helden, A. Gambassi, S. Dietrich, and C. Bechinger, "Direct measurement of critical casimir forces", Nature **451**, 172 (2008).

[124]U. Nellen, L. Helden, and C. Bechinger, "Tunability of critical casimir interactions by boundary conditions", EPL (Europhysics Letters) **88**, 26001 (2009).

[125]M. T. Dang, A. V. Verde, V. D. Nguyen, P. G. Bolhuis, and P. Schall, "Temperature-sensitive colloidal phase behavior induced by critical casimir forces", J. Chem. Phys. **139**, 094903 (2013).

[126]P. B. Shelke, V. D. Nguyen, A. V. Limaye, and P. Schall, "Controlling colloidal morphologies by critical casimir forces", Adv. Mater. **25**, 1499–1503 (2013).

[127]D. Beysens and D. Estève, "Adsorption phenomena at the surface of silica spheres in a binary liquid mixture", Phys. Rev. Lett. **54**, 2123–2126 (1985).

[128]P. D. Gallagher and J. V. Maher, "Partitioning of polystyrene latex spheres in immiscible critical liquid mixtures", Phys. Rev. A **46**, 2012–2021 (1992).

[129]P. D. Gallagher, M. L. Kurnaz, and J. V. Maher, "Aggregation in polystyrene-sphere suspensions in near-critical binary liquid mixtures", Phys. Rev. A **46**, 7750–7755 (1992).

[130]T. F. Mohry, A. Maciołek, and S. Dietrich, "Crossover of critical casimir forces between different surface universality classes", Phys. Rev. E **81**, 061117 (2010).

[131]C. M. Sorensen and G. A. Larsen, "Light scattering and viscosity studies of a ternary mixture with a double critical point", J. Chem. Phys. **83**, 1835–1842 (1985).

[132]V. Privman, *Finite size scaling and numerical simulation of statistical systems* (World Scientific Singapore, 1990).

[133]H. W. Diehl, "Field-theoretic approach to critical behaviour at surfaces", in *Phase transitions and critical phenomena*, Vol. 10, edited by C. Domb and J. L. Lebowitz (Academic Press, 1986), p. 76.

[134]M Krech, "Fluctuation-induced forces in critical fluids", J. Phys.: Condens. Matter **11**, R391–R412 (1999).

[135]J. G. Brankov, D. M. Danchev, and N. S. Tonchev, *The theory of critical phenomena in finite-size systems - scaling and quantum effects* (World Scientific, Singapore, 2000).

[136]A. Gambassi, "The casimir effect: from quantum to critical fluctuations", J. Phys. Conf. Ser. **161**, 012037 (2009).

[137]A. Pelissetto and E. Vicari, "Critical phenomena and renormalization-group theory", Phys. Rep. **368**, 549 –727 (2002).

[138]F. Schlesener, A. Hanke, and S. Dietrich, "Critical casimir forces in colloidal suspensions", J. Stat. Phys. **110**, 981–1013 (2003).

[139]B. Derjaguin, "Untersuchungen über die reibung und adhäsion, iv", Kolloid-Zeit. **69**, 155–164 (1934).

[140]M. Krech, "Casimir forces in binary liquid mixtures", Phys. Rev. E **56**, 1642–1659 (1997).

[141]A. Hucht, "Thermodynamic casimir effect in 4He films near $T_\lambda$: monte carlo results", Phys. Rev. Lett. **99**, 185301 (2007).

[142]O. Vasilyev, A. Gambassi, A. Maciołek, and S. Dietrich, "Monte carlo simulation results for critical casimir forces", Europhysics Letters (EPL) **80**, 60009 (2007).

[143]O. Vasilyev, A. Gambassi, A. Maciołek, and S. Dietrich, "Universal scaling functions of critical casimir forces obtained by monte carlo simulations", Phys. Rev. E **79**, 041142 (2009).

[144]M. Hasenbusch, "Thermodynamic casimir effect: universality and corrections to scaling", Phys. Rev. B **85**, 174421 (2012).

[145]O. A. Vasilyev and S. Dietrich, "Critical casimir forces for films with bulk ordering fields", EPL (Europhysics Letters) **104**, 60002 (2013).

[146]O. A. Vasilyev, "Critical casimir interactions between spherical particles in the presence of bulk ordering fields", Phys. Rev. E **90**, 012138 (2014).

[147]Z. Borjan and P. J. Upton, "Off-critical casimir effect in ising slabs with symmetric boundary conditions in $d = 3$", Phys. Rev. Lett. **101**, 125702 (2008).

[148]R. Okamoto and A. Onuki, "Casimir amplitudes and capillary condensation of near-critical fluids between parallel plates: renormalized local functional theory", J. Chem. Phys. **136**, 114704 (2012).

[149]M. Tröndle, S. Kondrat, A. Gambassi, L. Harnau, and S. Dietrich, "Normal and lateral critical casimir forces between colloids and patterned substrates", EPL (Europhysics Letters) **88**, 40004 (2009).

[150]M. Tröndle, S. Kondrat, A. Gambassi, L. Harnau, and S. Dietrich, "Critical casimir effect for colloids close to chemically patterned substrates", J. Chem. Phys. **133**, 074702 (2010).

[151]A. Hanke, F. Schlesener, E. Eisenriegler, and S. Dietrich, "Critical casimir forces between spherical particles in fluids", Phys. Rev. Lett. **81**, 1885–1888 (1998).

[152]T. F. Mohry, A. Maciołek, and S. Dietrich, "Phase behavior of colloidal suspensions with critical solvents in terms of effective interactions", J. Chem. Phys. **136**, 224902 (2012).

[153]T. F. Mohry, A. Maciołek, and S. Dietrich, "Structure and aggregation of colloids immersed in critical solvents", J. Chem. Phys. **136**, 224903 (2012).

[154]E. Eisenriegler and M. Stapper, "Critical behavior near a symmetry-breaking surface and the stress tensor", Phys. Rev. B **50**, 10009–10026 (1994).

[155]D. B. Abraham and A. Maciołek, "Casimir interactions in ising strips with boundary fields: exact results", Phys. Rev. Lett. **105**, 055701 (2010).

[156]O. Vasilyev, A. Maciołek, and S. Dietrich, "Critical casimir forces for ising films with variable boundary fields", Phys. Rev. E **84**, 041605 (2011).

[157]M. Hasenbusch, "Thermodynamic casimir force: a monte carlo study of the crossover between the ordinary and the normal surface universality class", Phys. Rev. B **83**, 134425 (2011).

[158]D. Bonn, J. Otwinowski, S. Sacanna, H. Guo, G. Wegdam, and P. Schall, "Direct observation of colloidal aggregation by critical casimir forces", Phys. Rev. Lett. **103**, 156101 (2009).

[159]J.-P. Hansen and H. Löwen, "Effective interactions between electric double layers", Annu. Rev. Phys. Chem. **51**, 209–242 (2000).

[160]J.-L. Barrat and J.-P. Hansen, *Basic concepts for simple and complex liquids* (Cambridge University Press, 2003).

[161]V. A. Parsegian, *Van der waals forces: a handbook for biologists, chemists, engineers, and physicists* (Cambridge University Press, 2005).

[162]Y. Levin, "Electrostatic correlations: from plasma to biology", Rep. Prog. Phys. **65**, 1577–1632 (2002).

[163]J.-P. Hansen and I. R. McDonald, *Theory of simple liquids* (Elsevier, 1990).

[164]G. A. Vliegenthart and H. N. W. Lekkerkerker, "Predicting the gas–liquid critical point from the second virial coefficient", J. Chem. Phys. **112**, 5364–5369 (2000).

[165]M. G. Noro and D. Frenkel, "Extended corresponding-states behavior for particles with variable range attractions", J. Chem. Phys. **113**, 2941–2944 (2000).

[166]J. D. Weeks, D. Chandler, and H. C. Andersen, "Role of repulsive forces in determining the equilibrium structure of simple liquids", J. Chem. Phys. **54**, 5237–5247 (1971).

[167]R. J. Baxter, "Percus–yevick equation for hard spheres with surface adhesion", J. Chem. Phys. **49**, 2770–2774 (1968).

[168]M. A. Miller and D. Frenkel, "Competition of percolation and phase separation in a fluid of adhesive hard spheres", Phys. Rev. Lett. **90**, 135702 (2003).

[169]M. A. Miller and D. Frenkel, "Phase diagram of the adhesive hard sphere fluid", J. Chem. Phys. **121**, 535–545 (2004).

[170]J. D. Cox, "897. phase relationships in the pyridine series. part ii. the miscibility of some pyridine homologues with deuterium oxide", Journal of the Chemical Society (Resumed), 4606–4608 (1952).

[171]M. Bier, A. Gambassi, M. Oettel, and S. Dietrich, "Electrostatic interactions in critical solvents", EPL (Europhysics Letters) **95**, 60001 (2011).

[172]F. Pousaneh and A. Ciach, "The origin of the attraction between like charged hydrophobic and hydrophilic walls confining a near-critical binary aqueous mixture with ions", J. Phys.: Condens. Matter **23**, 412101 (2011).

[173]F. Pousaneh, A. Ciach, and A. Maciołek, "Effect of ions on confined near-critical binary aqueous mixture", Soft Matter **8**, 7567–7581 (2012).

[174]A. F. Kostko, M. A. Anisimov, and J. V. Sengers, "Criticality in aqueous solutions of 3-methylpyridine and sodium bromide", Phys. Rev. E **70**, 026118 (2004).

[175]J. Leys, D. Subramanian, E. Rodezno, B. Hammouda, and M. A. Anisimov, "Mesoscale phenomena in solutions of 3-methylpyridine, heavy water, and an antagonistic salt", Soft Matter **9**, 9326–9334 (2013).

[176]J. K. Bhattacharjee, R. A. Ferrell, R. S. Basu, and J. V. Sengers, "Crossover function for the critical viscosity of a classical fluid", Phys. Rev. A **24**, 1469–1475 (1981).

[177]H. C. Burstyn and J. V. Sengers, "Decay rate of critical concentration fluctuations in a binary liquid", Phys. Rev. A **25**, 448–465 (1982).

[178]H. C. Burstyn, J. V. Sengers, J. K. Bhattacharjee, and R. A. Ferrell, "Dynamic scaling function for critical fluctuations in classical fluids", Phys. Rev. A **28**, 1567–1578 (1983).

[179]S. K. Das, J. V. Sengers, and M. E. Fisher, "Simulating critical dynamics in liquid mixtures: short-range and long-range contributions", J. Chem. Phys. **127**, 144506 (2007).

[180]K. Kawasaki, "Mode coupling and critical dynamics", in *Phase transitions and critical phenomena*, Vol. 5a, edited by C. Domb and M. S. Green (Academic Press, 1976), p. 165.

[181]A. Oleinikova, L. Bulavin, and V. Pipich, "The viscosity anomaly near the lower critical consolute point", Int. J. Thermophys. **20**, 889–898 (1999).

[182]A. L. Loeb, J. T. G. Overbeek, and P. H. Wiersema, *The electrical double layer around a spherical colloid particle* (MIT Press, Cambridge, 1961).

[183]T. Narayanan, A. Kumar, E. S. R. Gopal, D. Beysens, P. Guenoun, and G. Zalczer, "Reversible flocculation of silica colloids in liquid mixtures", Phys. Rev. E **48**, 1989–1994 (1993).

[184]P. S. Mohanty, D. Paloli, J. J. Crassous, E. Zaccarelli, and P. Schurtenberger, "Effective interactions between soft-repulsive colloids: experiments, theory, and simulations", J. Chem. Phys. **140**, 094901 (2014).

[185]A. Oleinikova, L. Bulavin, and V. Pipich, Chem. Phys. Lett. **278**, 121 (1997).

[186]M. Wagner, O. Stanga, and W. Schröer, "Corresponding states analysis of the critical points in binary solutions of room temperature ionic liquids", Phys. Chem. Chem. Phys. **5**, 3943–3950 (2003).

[187]H. Guo, "The phase behavior of a weakly attractive colloidal systems", PhD thesis (University of Amsterdam, 2008).

[188]M. L. Kurnaz and J. V. Maher, "Interaction of dilute colloidal particles in a mixed solvent", Phys. Rev. E **51**, 5916–5921 (1995).

[189]M. L. Kurnaz and J. V. Maher, "Measurement of the second virial coefficient for the interaction of dilute colloidal particles in a mixed solvent", Phys. Rev. E **55**, 572–576 (1997).

[190]I. S. Gradshteyn and I. M. Ryzhik, *Table of integrals, series, and products*, 6th ed. (Academic Press, London, 2000).

[191]D. Morphew and D. Chakrabarti, "Clusters of anisotropic colloidal particles: from colloidal molecules to supracolloidal structures", Curr. Opin. Colloid Interface Sci. **30**, 70–80 (2017).

[192]J. F. Galisteo-López, M. Ibisate, R. Sapienza, L. S. Froufe-Pérez, Blanco, and C. López, "Self-assembled photonic structures", Adv. Mater. **23**, 30–69 (2011).

[193]Y. Suzuki, G. Cardone, D. Restrepo, P. D. Zavattieri, T. S. Baker, and F. A. Tezcan, "Self-assembly of coherently dynamic, auxetic, two-dimensional protein crystals", Nature **533**, 369 (2016).

[194]E. Zaccarelli, "Colloidal gels: equilibrium and non-equilibrium routes", J. Phys.: Condens. Matter **19**, 323101 (2007).

[195]J. M. van Doorn, J. E. Verweij, J. Sprakel, and J. van der Gucht, "Strand plasticity governs fatigue in colloidal gels", Phys. Rev. Lett. **120**, 208005 (2018).

[196]C. van der Wel, A. Vahid, A. Šarić, T. Idema, D. Heinrich, and D. J. Kraft, "Lipid membrane-mediated attraction between curvature inducing objects", Sci. Rep. **6**, 32825 (2016).

[197]D. Li, S. Banon, and S. L. Biswal, "Bending dynamics of dna-linked colloidal particle chains", Soft Matter **6**, 4197–4204 (2010).

[198]H. R. Vutukuri, A. F. Demirörs, B. Peng, P. D. J. van Oostrum, A. Imhof, and A. van Blaaderen, "Colloidal analogues of charged and uncharged polymer chains with tunable stiffness", Angew. Chem. Int. Ed. **51**, 11249–11253 (2012).

[199]G. Meng, N. Arkus, M. P. Brenner, and V. N. Manoharan, "The free-energy landscape of clusters of attractive hard spheres", Science **327**, 560–563 (2010).

[200]P. Cicuta and D. Vella, "Granular character of particle rafts", Phys. Rev. Lett. **102**, 138302 (2009).

[201]B. D. Leahy, L. Pocivavsek, M. Meron, K. L. Lam, D. Salas, P. J. Viccaro, K. Y. C. Lee, and B. Lin, "Geometric stability and elastic response of a supported nanoparticle film", Phys. Rev. Lett. **105**, 058301 (2010).

[202]D. Vella, E. du Pontavice, C. L. Hall, and A. Goriely, "The magneto-elastica: from self-buckling to self-assembly", Proc. Royal Soc. Lond. **470**, 20130609 (2014).

[203]M. Dogterom and B. Yurke, "Measurement of the force-velocity relation for growing microtubules", Science **278**, 856–860 (1997).

[204]O. Chaudhuri, S. H. Parekh, and D. A. Fletcher, "Reversible stress softening of actin networks", Nature **445**, 295 (2007).

[205]J. Paulose, G. A. Vliegenthart, G. Gompper, and D. R. Nelson, "Fluctuating shells under pressure", Proc. Natl. Acad. Sci. U.S.A. **109**, 19551–19556 (2012).

[206]X. Mao, A. Souslov, C. I. Mendoza, and T. C. Lubensky, "Mechanical instability at finite temperature", Nat. Commun. **6**, 5968 (2015).

[207]K. Baczynski, R. Lipowsky, and J. Kierfeld, "Stretching of buckled filaments by thermal fluctuations", Phys. Rev. E **76**, 061914 (2007).

[208]J. Kierfeld, K. Baczynski, P. Gutjahr, T. Kühne, and R. Lipowsky, "Modelling semiflexible polymers: shape analysis, buckling instabilities, and force generation", Soft Matter **6**, 5764 (2010).

[209]E. Pilyugina, B. Krajina, A. J. Spakowitz, and J. D. Schieber, "Buckling a semiflexible polymer chain under compression", Polymers **9**, 99 (2017).

[210]D. S. Bedi and X. Mao, "Finite-temperature buckling of an extensible rod", Phys. Rev. E **92**, 062141 (2015).

[211]J. W. Hutchinson and W. T. Koiter, "Postbuckling theory", Appl. Mech. Rev. **23**, 1353–1366 (1970).

[212]Z. P. Bazant and L. Cedlin, *Stability of structures, Elastic, inelastic, fracture and damage theories* (World Scientific, 2009).

[213]C. Coulais, J. T. B. Overvelde, L. A. Lubbers, K. Bertoldi, and M. van Hecke, "Discontinuous buckling of wide beams and metabeams", Phys. Rev. Lett. **115**, 044301 (2015).

[214]A. D. Dinsmore, V. Prasad, I. Y. Wong, and D. A. Weitz, "Microscopic structure and elasticity of weakly aggregated colloidal gels", Phys. Rev. Lett. **96**, 185502 (2006).

[215]D. L. Ermak and J. A. McCammon, "Brownian dynamics with hydrodynamic interactions", J. Chem. Phys. **69**, 1352–1360 (1978).

[216]A. Magnusson, M. Ristinmaa, and C. Ljung, "Behaviour of the extensible elastica solution", Int. J. Solids Struct. **38**, 8441 –8457 (2001).

[217]F. Gittes, B. Mickey, J. Nettleton, and J. Howard, "Flexural rigidity of microtubules and actin filaments measured from thermal fluctuations in shape.", J. Cell Biol. **120**, 923 (1993).

[218]Z. Zeravcic, V. N. Manoharan, and M. P. Brenner, "Size limits of self-assembled colloidal structures made using specific interactions", Proc. Natl. Acad. Sci. U.S.A. **111**, 15918–15923 (2014).

[219]Z. Zhang and S. C. Glotzer, "Self-assembly of patchy particles", Nano Lett. **4**, 1407–1413 (2004).

[220]Étienne Duguet, C. Hubert, C. Chomette, A. Perro, and S. Ravaine, "Patchy colloidal particles for programmed self-assembly", C. R. Chim. **19**, Emerging Chemistry in France, 173 –182 (2016).

[221]E. Bianchi, J. Largo, P. Tartaglia, E. Zaccarelli, and F. Sciortino, "Phase diagram of patchy colloids: towards empty liquids", Phys. Rev. Lett. **97**, 168301 (2006).

[222]F. Romano and F. Sciortino, "Patterning symmetry in the rational design of colloidal crystals", Nature Communications **3**, 975 (2012).

[223]T. A. Nguyen, A. Newton, S. J. Veen, D. J. Kraft, P. G. Bolhuis, and P. Schall, "Switching colloidal superstructures by critical casimir forces", Adv. Mater. **29**, 1–6 (2017).

[224]F. Soyka, O. Zvyagolskaya, C. Hertlein, L. Helden, and C. Bechinger, "Critical casimir forces in colloidal suspensions on chemically patterned surfaces", Phys. Rev. Lett. **101**, 208301 (2008).

[225]K. Liu, Z. Nie, N. Zhao, W. Li, M. Rubinstein, and E. Kumacheva, "Step-growth polymerization of inorganic nanoparticles", Science **329**, 197–200 (2010).

[226]G. Odian et al., *Principles of polymerization* (John Wiley & Sons, 2004).

[227]L. Rovigatti, F. Smallenburg, F. Romano, and F. Sciortino, "Gels of dna nanostars never crystallize", ACS Nano **8**, 3567–3574 (2014).

[228]F. Sciortino, E. Bianchi, J. F. Douglas, and P. Tartaglia, "Self-assembly of patchy particles into polymer chains: a parameter-free comparison between wertheim theory and monte carlo simulation", J. Chem. Phys. **126**, 194903 (2007).

[229]B. Ruzicka, E. Zaccarelli, L. Zulian, R. Angelini, M. Sztucki, A. Moussaïd, T. Narayanan, and F. Sciortino, "Observation of empty liquids and equilibrium gels in a colloidal clay", Nature Materials **10**, 56 (2010).

[230]F. Bomboi, F. Romano, M. Leo, J. Fernandez-Castanon, R. Cerbino, T. Bellini, F. Bordi, P. Filetici, and F. Sciortino, "Re-entrant dna gels", Nature Communications **7**, 13191 (2016).

[231]N. Conrad, T. Kennedy, D. K. Fygenson, and O. A. Saleh, "Increasing valence pushes dna nanostar networks to the isostatic point", Proc. Natl. Acad. Sci. U.S.A. **116**, 7238–7243 (2019).

[232]L. Feng, L.-L. Pontani, R. Dreyfus, P. Chaikin, and J. Brujic, "Specificity, flexibility and valence of dna bonds guide emulsion architecture", Soft Matter **9**, 9816–9823 (2013).

[233]B. Biswas, R. K. Manna, A. Laskar, P. B. S. Kumar, R. Adhikari, and G. Kumaraswamy, "Linking catalyst-coated isotropic colloids into "active" flexible chains enhances their diffusivity", ACS Nano **11**, 10025–10031 (2017).

[234]C. P. Brangwynne, G. H. Koenderink, E. Barry, Z. Dogic, F. C. MacKintosh, and D. A. Weitz, "Bending dynamics of fluctuating biopolymers probed by automated high-resolution filament tracking", Biophys. J. **93**, 346–359 (2007).

[235]G. A. Buxton and N. Clarke, ""'bending to stretching" transition in disordered networks", Phys. Rev. Lett. **98**, 238103 (2007).

[236]X. Mao, N. Xu, and T. C. Lubensky, "Soft modes and elasticity of nearly isostatic lattices: randomness and dissipation", Phys. Rev. Lett. **104**, 085504 (2010).

[237]M. D. Carbajal-Tinoco, R. Lopez-Fernandez, and J. L. Arauz-Lara, "Asymmetry in colloidal diffusion near a rigid wall", Phys. Rev. Lett. **99**, 138303 (2007).

[238]A. Stein, S. J. Davidson, J. C. Allegra, and G. F. Allen, "Tracer diffusion and shear viscosity for the system 2,6-lutidine-water near the lower critical point", J. Chem. Phys. **56**, 6164–6168 (1972).

[239]M. G. Poirier and J. F. Marko, "Effect of internal friction on biofilament dynamics", Phys. Rev. Lett. **88**, 228103 (2002).

[240]A. Maghsoodi and N. Perkins, "Shear deformation dissipates energy in biofilaments", Sci. Rep. **8**, 11684 (2018).

[241]K. M. Taute, F. Pampaloni, E. Frey, and E.-L. Florin, "Microtubule dynamics depart from the wormlike chain model", Phys. Rev. Lett. **100**, 028102 (2008).

[242]T. Hiraiwa and T. Ohta, "Linear viscoelasticity of a single semiflexible polymer with internal friction", J. Chem. Phys. **133**, 044907 (2010).

[243]M. Z. Miskin, K. J. Dorsey, B. Bircan, Y. Han, D. A. Muller, P. L. McEuen, and I. Cohen, "Graphene-based bimorphs for micron-sized, autonomous origami machines", Proc. Natl. Acad. Sci. U.S.A. **115**, 466–470 (2018).

[244]B. Lukić, S. Jeney, Sviben, A. J. Kulik, E.-L. Florin, and L. Forró, "Motion of a colloidal particle in an optical trap", Phys. Rev. E **76**, 011112 (2007).

[245]K. D. Costa, W. J. Hucker, and F. C.-P. Yin, "Buckling of actin stress fibers: a new wrinkle in the cytoskeletal tapestry", Cell Motil. Cytoskeleton **52**, 266–274 (2002).

[246]M. Kikumoto, M. Kurachi, V. Tosa, and H. Tashiro, "Flexural rigidity of individual microtubules measured by a buckling force with optical traps", Biophys. J. **90**, 1687 –1696 (2006).

[247]V. Kantsler and R. E. Goldstein, "Fluctuations, dynamics, and the stretch-coil transition of single actin filaments in extensional flows", Phys. Rev. Lett. **108**, 038103 (2012).

[248]S. Kumar, I. Z. Maxwell, A. Heisterkamp, T. R. Polte, T. P. Lele, M. Salanga, E. Mazur, and D. E. Ingber, "Viscoelastic retraction of single living stress fibers and its impact on cell shape, cytoskeletal organization, and extracellular matrix mechanics", Biophys. J. **90**, 3762 –3773 (2006).

[249]J. Block, H. Witt, A. Candelli, J. C. Danes, E. J. G. Peterman, G. J. L. Wuite, A. Janshoff, and S. Köster, "Viscoelastic properties of vimentin originate from nonequilibrium conformational changes", Sci. Adv. **4** (2018) *10.1126/sciadv.aat1161*.

[250]F. Rückerl, M. Lenz, T. Betz, J. Manzi, J.-L. Martiel, M. Safouane, R. Paterski-Boujemaa, L. Blanchoin, and C. Sykes, "Adaptive response of actin bundles under mechanical stress", Biophys. J. **113**, 1072–1079 (2017).

[251]T. Sanchez, D. T. N. Chen, S. J. DeCamp, M. Heymann, and Z. Dogic, "Spontaneous motion in hierarchically assembled active matter", Nature **491**, 431 (2012).

[252]E. M. Furst and J. P. Pantina, "Yielding in colloidal gels due to nonlinear microstructure bending mechanics", Phys. Rev. E **75**, 050402 (2007).

[253]I. Heller, G. Sitters, O. D. Broekmans, G. Farge, C. Menges, W. Wende, S. W. Hell, E. J. G. Peterman, and G. J. L. Wuite, "Sted nanoscopy combined with optical tweezers reveals protein dynamics on densely covered dna", Nat. Methods **10**, 910 (2013).

[254]G. H. Koenderink, H. Zhang, D. G.A. L. Aarts, M. P. Lettinga, A. P. Philipse, and G. Nägele, "On the validity of stokes–einstein–debye relations for rotational diffusion in colloidal suspensions", Faraday Discuss. **123**, 335–354 (2003).

[255]J. R. Gladden, N. Z. Handzy, A. Belmonte, and E. Villermaux, "Dynamic buckling and fragmentation in brittle rods", Phys. Rev. Lett. **94**, 035503 (2005).

[256]J. Chopin, M. Dasgupta, and A. Kudrolli, "Dynamic wrinkling and strengthening of an elastic filament in a viscous fluid", Phys. Rev. Lett. **119**, 088001 (2017).

# List of publications

**This thesis is based on the following publications:**

S. G. Stuij, M. Labbé-Laurent, T. Kodger, A. Maciołek, and P. Schall, "Critical casimir interactions between colloids around the critical point of binary solvents", Soft Matter **13**, 5233-5249 (2017), Chapter 3.

S. G. Stuij, J. M. van Doorn, T. Kodger, J. Sprakel, C. Coulais, and P. Schall, "Stochastic buckling of self-assembled colloidal structures", Phys. Rev. Research **1**, 023033 (2019), Chapter 4.

S. G. Stuij, Z. Gong, S. Sacanna, and P. Schall, "Self-assembly of colloidal molecules, polymers and networks using patchy critical casimir forces", *In preparation.* Chapter 5.

S. G. Stuij, Z. Gong, S. Sacanna, and P. Schall, "Dipatch colloidal chains with temperature tuneable rigidity", *In preparation.* Chapter 6.

S. G. Stuij, Z. Gong, A. S. Biebricher, S. Sacanna, E. J. G. Peterman, I. Heller, and P. Schall, "Extreme mechanics of dipatch colloidal chains", *In preparation.* Chapter 7.

# Summary

Colloids currently form one of the most exciting platforms for developing self-assembling designer materials. Such materials mimic biological matter in their bottom-up hierarchical organization, and in the way they derive function from dynamic mechanical properties. Recent breakthroughs in synthesis have yielded colloidal building blocks with precise control over shape and surface properties. However, their assembly in functional architectures remains challenging, requiring interaction control, fundamental understanding of in and out-of-equilibrium self-assembly pathways, and a deeper knowledge of micromechanical behavior.

This thesis presents a colloidal system for directed and controlled self-assembly, using temperature tunable critical Casimir forces and patchy particles, which have a heterogenous surface with patches of tunable size. We show that these particles self-assemble in different architectures ranging from various small scale well-defined structures to sample-spanning networks. In addition, these architectures are put to the test by a series of micromechanical studies on simple basic structures: Straight colloidal chains. Using optical tweezers and thermally induced bending fluctuations, a rich semiflexible mechanics is revealed, which involves stochastic buckling instabilities, viscoplastic effects and fracture.

Chapter 2 starts with a description of the synthesis of dipatch and tetrapatch particles. This synthesis was conducted according to a recently published technique called colloidal fusion. After synthesis, the particle patch size and shape are precisely characterized using AFM microscopy. This is followed by an introduction to the critical Casimir interaction as a tool for self-assembly. Critical Casimir interactions arise in near critical binary mixtures. This chapter shows how to obtain a boundary condition contrast between the patch and bulk of a particle, essential to achieve pure patch-to-patch attraction. One crucial element, it is found, is to use binary mixture at slightly off-critical concentrations.

The critical Casimir interaction can be calculated using a combination of field-theoretical techniques and Monte Carlo simulations. Specifically at the off-critical conditions optimal for patchy assembly, these theoretical predictions had so far not been compared to experiments. In Chapter 3, the critical Casimir interaction is directly measured between two isotropic particles and found to agree with theoretical models at these experimentally relevant conditions. Precise knowledge of the interaction potential is essential to rationally design self-assembly pathways and to interpret the behavior of assembled structures.

In Chapter 4, the focus is shifted to the mechanics of colloidal structures. In this

chapter we do not yet use patchy particles and instead assemble a chain of isotropic particles using critical Casimir forces. We investigate, by experiments, simulations and theory, the mechanical instabilities of this slender, colloidal structure. Upon compression the chain undergoes a novel form of stochastic buckling instability, for which fluctuations become amplified and diverge in the vicinity of the critical buckling transition. We fully characterize how the persistence length and plasticity controls the stochastic buckling transition, leading to intriguing higher-order buckling modes.

Chapter 5 is a pivotal chapter. The patchy particles are shown to undergo single bond-per-patch interactions that are reversible and tunable using temperature dependent Critical Casimir forces. We assemble different types of 'colloidal molecules' using dipatch and tetrapatch particles and mixtures thereof: Pure dipatch particles form short chains, tetrapatch particles introduce tetrahedral bond angles that result, among others, in zigzag chains and cyclic structures. Larger numbers of dipatch particles form analogues of polymers that can crosslink with the addition of tetrapatch particles and we study their growth kinetics. Finally, by decreasing particle size to speed up formation kinetics, dipatch and tetrapatch mixtures form a percolated gel. These results demonstrate the assembly control that patchy particles in combination with the in-situ controllable critical Casimir interaction offer.

With the realization of a well controlled and patchy aggregating system, the stage is set to ask detailed questions about the physics of such assemblies. In Chapter 6, we study the dynamics of thermally induced bending fluctuations in dipatch chains to characterize their mechanics. We show that they are well modeled as semiflexible filaments, with a persistence length that is set by patch size and the strength of the critical Casimir bond. We furthermore reveal viscoelastic effects on longer timescales that we attribute to internal friction. Our results show that the critical Casimir force can not only be used to in-situ rationally control the radial interaction strength between particles but, by using patchy particles, can also control the shear rigidity between bonded colloids. This paves the way for using patchy particle assemblies as building blocks of colloidal architectures with bending rigidity as a rational control parameter.

The final Chapter 7 uses optical tweezers to probe the mechanics of dipatch chains under extreme deformations, inducing buckling and fracture. Optical tweezers probe their extreme mechanics under increasingly high compressions. This reveals a rich non-linear mechanical response involving buckling, viscoelastic creep and stress relaxation, and ultimately fracture. We characterize and model this response using elastic and viscoelastic models involving Euler buckling and stress relaxation. This allows us to relate the critical bending at fracture to the finite patch size of the colloids. These results demonstrate the crucial role of finite patch size in the mechanics of self-assembled colloidal materials.

With the fracture of these colloidal structures, this thesis has come to a symbolic end. However, as all proper self-assembling systems do, when stress is released, these chains patch up, and self-heal. The future looks bright for such versatile life-like materials. It is my hope that, in the long run, colloids and other self-assembling

systems blur the boundary between what is man-made and what is natural. Maybe the engineer of the future will look more like a gardener, carefully nurturing his creations, until they grow, by themselves, to the machines he envisioned.

# Populaire Samenvatting

Van staal tot boter, en van diesel tot verf, alles in deze wereld is opgebouwd uit kleinere bouwstenen. Deze bouwstenen, zoals atomen of colloïden, zijn op zichzelf vrij eenvoudig, als de bakstenen van een huis. Het is de collectieve samenwerking, meer dan de aard van individuele bouwstenen, die de eigenschappen van materialen bepaalt. Dit eeuwenoude atomistische gegeven kan nog steeds verbazen. In het bijzonder als je de adembenemende complexiteit van levende structuren beschouwt. De diversiteit en functionaliteit van jouw lichamelijk weefsel komt uiteindelijk voort uit een ontzettend geavanceerde aaneenschakeling van vrij eenvoudige atomen en moleculen. Hoe kan zoiets complex en moois voortkomen uit zulke simpele bouwstenen? En hoe vinden al deze bouwstenen de juiste locatie, zonder dat er iets is dat ze één voor één op hun plek zet?

Een belangrijk mechanisme van de natuur is het gebruik van 'self-assembly', dat vertaald kan worden als 'spontane samenstelling' of 'zelf-bouwing'. Self-assembly is enigszins tegenintuïtief voor ons. Immers, we zien zelden een ontbonden object, zoals een gebroken auto, zich spontaan met een beetje schudden weer in elkaar klikken. Toch zijn er voorbeelden die je met het blote oog kunt zien (zie figuur 1 van de introductie, blz. 3): In de herfst kunnen drijvende blaadjes soms in opvallend geordende structuren samenkomen. Meer geavanceerd zijn de zogenaamde vuurmieren, nomadische mieren die in tropische regenwouden leven. Door elkaar vast te grijpen bouwen de mieren bruggen, en zelfs hele mobiele burchten van hun eigen lichamen. In de onzichtbare, microscopische natuur is self-assembly wijdverspreid. Het stollen van bloed bijvoorbeeld maakt gebruik van de self-assembly van fibrine netwerken. Ook het vouwen van eiwitten, een proces dat aan de basis staat van het functioneren van iedere cel, is niets anders dan een zeer precieze vorm van self-assembly.

*Colloidal Design.* In dit proefschrift heb ik de zelf-bouwende eigenschappen van de natuur proberen na te bootsen met behulp van colloïden. Een colloïd is een technische naam voor stoffen die bestaan uit kleine deeltjes van ongeveer 1 micrometer verspreid in een vloeibaar medium. Alledaagse voorbeelden van colloïden zijn melk, verf en tandpasta. Sinds kort bestaan er ook synthetische colloïden waarvan de deeltjes met hoge precisie ontworpen kunnen worden. Dit soort 'designer' colloïden vormen een veelbelovend platform voor de ontwikkeling van zelf-bouwende, slimme materialen.

*Bouwen.* De designer colloïden in dit proefschrift zijn zogenaamde 'patchy' deeltjes. Deze deeltjes hebben op hun oppervlak een aantal stippen. Deze stippen fungeren als een soort microscopische handen. Alleen als deeltjes met de stippen naar

elkaar toewijzen voelen ze een aantrekkingskracht, dan grijpen de handen elkaar beet. Wanneer er deeltjes met elk twee stippen samengevoegd worden, dan ontstaan er kettingen. Net zoals een groep mensen een ketting vormt als de handen ineen worden geslagen. Als er deeltjes met meer dan twee stippen worden toegevoegd, dan kunnen die als vertakkingspunten fungeren waar meerdere kettingen samenkomen. Met genoeg van dit soort vertakkingspunten ontstaat er een netwerk. Zo'n colloïdaal netwerk is artistiek weergegeven op de omslag van het proefschrift. In de hoofdstukken 2,3 en 5, wordt beschreven hoe deze patchy deeltjes gemaakt worden, hoe we de aantrekkingskracht tussen de deeltjes kunnen instellen met behulp van de temperatuur, en hoe in dit systeem spontaan kettingen en netwerken ontstaan.

*Buigen en Breken.* Na het bouwen van deze structuren, wordt in de hoofdstukken 4, 6 en 7, hun mechanische eigenschappen onderzocht. Met behulp van laser pincetten is het mogelijk om één deeltje vast te pakken, en naar gelieve te verplaatsen. Een colloïdale ketting kan met behulp van twee van zulke pincetten bij de uiteinden vast worden gepakt. Vervolgens oefenen we krachten op de ketting uit door de uiteinden naar elkaar toe te duwen. Verassend genoeg blijken de kettingen zich niet als flexibele kralenkettingen te gedragen maar meer als microscopische buigbare latten. Dit resulteert in bijzonder mechanisch gedrag: Als een liniaal die knikt tussen je handen, zo buigen de colloïdale kettingen onder voldoende compressie. Door de compressie nog verder op te voeren wordt de buiging zo extreem dat de ketting zelfs breekt.

Met het breken van deze colloïdale structuren bereikt het proefschrift een symbolisch einde. Maar niet getreurd, zoals het elk zelf-bouwend systeem betaamt, kan de breuk zichzelf helen als de spanning eraf is. Zulke materialen, geïnspireerd op de levende natuur, lijken een veelbelovende toekomst te hebben. Ik hoop dat op de lange termijn, colloïden en andere zelf-bouwende systemen het verschil vervagen tussen wat natuurlijk en synthetisch is. In zo'n wereld lijkt een ingenieur misschien wel meer op een tuinman, die zijn creaties zorgzaam voedt, zodat ze uit zichzelf groeien tot machines naar zijn ontwerp.

# Acknowledgements

There were two reasons why I decided to do a PhD. The first was believing a merry visiting professor during an after work group dinner. He said that in academia you have no colleagues or competitors, you just have an international network of friends with shared interests. The second was a quite sudden realization that I was really very fascinated by the concept of emergence, and would love to have some time to think about that. However, during studies I learned that too much thinking is unhealthy. So, as a form of self-protection, I decided to apply for an experimental PhD, with enough manual labor to keep me grounded, while having a topic that would allow for the occasional philosophical stroll in the land of complexity and emergence. Though there were struggles (stubborn particles), and a fair amount of experimental frustration (I suggest a new confocal Peter), the PhD has been a very happy choice, and I'm grateful to everyone who made this possible. I look back on an amazing period, for many more reasons than just these two above, though I definitely like to think I've gained a lot of friends.

First of all, I want to thank my promotor Peter Schall and copromotor Tom Kodger. *Peter*, I still remember the first time I visited the lab and I walked away from the job-interview feeling like: Yes, this is a man who is very kind and who is honestly passionate about the science he is doing. You have given me a lot of freedom and trust from the start, which I tremendously appreciate. In due time I learned that you are not only passionate, but also ambitious. Sometimes I felt some worries from your side: Is this free-floating guy really focused enough to get to some tangible results? I admit that I shared these worries. I think we managed to find a reasonable balance where we checked once every so often whether I was still heading anywhere. For a busy group leader, I'm amazed how your door is always open and how generous you are with help. Particularly with paper and thesis writing this help was crucial, and taught me a lot about scientific writing. *Tom*, I also remember meeting you the first time I visited the lab, and quite frankly you were an important reason why I decided to accept the position. If this guy will supervise me all will be fine, I reasoned. Your broad knowledge, technical skills, and your extreme helpfulness were obvious from the start. You taught me how to hold a pipette, how to operate a microscope, and by example how to be a good and honest scientist. You opened my eyes to look beyond my theoretical background, and introduced me to the rich worlds of chemistry and biology. Next to that you also are a very social presence, coffee breaks were always interesting conversations and after you moved to Wageningen it was so nice to see you again during visits and catch up.

Throughout my PhD I was lucky to collaborate with a number of great scientists around Netherlands and the globe. Chapter 3 is the result of a stimulating collaboration with MPI Stuttgart theorists Ania Maciołek and Marcel Labbé-Laurent. *Ania*, your deep knowledge of the critical Casimir force was crucial for my first thesis publication. *Marcel*, whenever I had a question about the CCF I would turn to you, writing terribly long emails. You are such a friendly person. It was lovely to visit Stuttgart, in that snowy week right after new year, it helped and motivated me a lot. Chapter 4 came to be through a close collaboration with Joris Sprakel and Jan Maarten van Doorn, from the WUR, and Corentin Coulais, here at UvA. *Joris*, you lead a strong research team, thank you for opening up your lab and allowing me to use the tweezer setup. *Jan Maarten*, thank you for introducing me to optical tweezing. *Corentin*, with your insight and enthusiasm you really pushed the work of chapter 5 further. Your metamechanical perspective was new and exciting to me and your just-do-it mentality towards simulations gave me confidence. You inspire people, I'm so curious where all your ambitious research ideas will lead to. Chapters 5, 6, and 7, all relied on the amazing colloidal synthesis work taking place in Stefano Sacanna's lab at NYU, specifically the patchy particles made by Zhe Gong. *Stefano*, thank you for welcoming me in your lab, it turned my PhD around. *Zhe*, I'm so indebted to you and to the packages you sent across the Atlantic containing your precious samples. It was great to really meet in New York and work together during my short but intense stay. The experiments of chapter 7 were performed at the VU in the biophysics labs of Erwin Peterman and Iddo Heller with crucial technical support from Andreas Bechinger. *Erwin* and *Iddo*, thank you for allowing me to use your beautiful tweezer setups on such a short notice and being supportive throughout. *Andreas*, thank you for all the help, it was really enjoyable and efficient to setup the experiments with you. The understanding of patchy self-assembly has further benefited a lot from the ongoing numerical work in the group of Peter Bolhuis, currently pursued by Hannah Jonas. *Peter*, your sharp observations during colloid meetings were always enlightening. *Hannah*, it was so nice to dive into all kind of details of the patchy system with you, part of me wished you started your PhD earlier so we would've had more time to work together, but I think you came at the right time to hopefully reap some nice results, good luck!

In addition, I would like to thank *Sander Woutersen* for his enthusiasm and the chemical perspective on colloidal molecules, *Casper van der Wel* for developing and introducing me to the wonderful python package 'trackpy', *Julien Chopin* for insightful discussions on dynamic buckling, *Michele Zanini* for help with obtaining AFM data, *Naomi Boye* for her language corrections of the thesis introduction and summary, and *Leon Friederichs* for his beautiful cover painting and typesetting. I was further helped by a group of talented and all very cool students. *Marc, Bastiaan, Nathaniel, Nicola, Rosa* and *Thekla*, it was a pleasure to supervise your projects. *Nicola*, you dared to do your masters project with me, your energy made it very exciting to work with you, all the best in your future endeavors. I further like to warmly thank the *IOP secretariat* for their unwavering support with all practical manners, and everyone at the *Technical Workshop* for their beautiful work and

technical assistance.

The Amsterdam soft matter lab is a colorful and human place, especially for someone coming from the stern, and somewhat depressing fortress that is the ITF in Utrecht. It is also extremely dynamic. People come and go all the time, making the group almost unrecognizable from the time I started. So let's do this somewhat chronologically. *Mohsin*, I've been looking forward to writing this paragraph. You started your PhD one week before me, and easily kept this advantage until the end. This meant that you had to do all administration matters just before me, and I could always bother you to enquire about this and that form. Was it still in that same first week that I tasted your curry for the first time? The friendship that developed from there on has been one of the big joys of my PhD. Your hospitality and generosity are beyond this world. I have shamelessly taken advantage of them, and they are a constant source of inspiration. I think we both developed in many ways during these years, and it was wonderful to see you find your footing in this strange land. Wherever you end up, remember me as a brother, this has been a very good story.

*Sanne*, we begonnen ongeveer tegelijkertijd onze promotie bij Peter, zaten tegenover elkaar, en hadden vrijwel hetzelfde onderwerp. Toen kregen we ook nog eens de prachtige woning van Ahn en Triet aangeboden, en werden we huisgenoten. Onze levens begonnen wel heel veel gelijkenissen te vertonen. Het waren soms roerige tijden. Ik heb heel veel respect voor je, hoe je je eigen weg hebt bewandeld. Bedankt ook voor de basis van hoofdstuk 5, je hebt me ontzettend geholpen. *Joep*, het duurde niet lang of je sloot je ook aan als promovendus bij Peter. Ik vond ons best een bont stel, Sanne, jij en ik. Drie Nederlandse colloïd musketiers die soms ook wel wat andere zaken aan ons hoofd hadden dan die PhD. Bedankt voor het introduceren van Amsterdam, zijn geschiedenis, de feesten, de krakers. Mede dankzij jou voelde ik me hier snel thuis. Ik wens je alle goeds samen met Nus, die fantastisch is, en alle gezondheid en geluk met de verwachte grote kleine.

*Ahn*, thank you for starting the patchy particle project, it was not always easy to reproduce your results, and I never mastered you delicate sample preparation techniques, in the end however, things worked out. *Triet*, with Ahn you helped me get started, it was inspiring to see your proactive approach and your collaboration with the workshop. And to both of you, thanks for the apartment! *Emanuele*, your passionate ambition was sometimes contagious, sometimes intimidating. Might there even have been some subconscious competition between us? Just teasing, it was great being around your liveliness in the lab, during coffee breaks and dinner parties. *Laura*, queen of colloids, you brought a lot of expertise to the group, very good master students and some (in my case direly needed) order and lab etiquette. Your network turned out very important for my PhD. *Luci*, you are so talented, it was inspiring to share the lab for a while. Loved all our discussions, your acting skills and cookie baking. *Antoine*, with your big heart you have become the social glue that keeps the lab together, and you know I love your work, keep me in the loop for future postdoc positions. *Chia-ching*, you truly are a bass: grounded and radiating a deep happiness, no matter what people through at you. It was great having opposite desks these years and watching your beautiful family grow. *Paul*, sorry for my mess,

you really have done a great job with the lab. *Piet*, I'm happy to know the patchy particles are in good hands. And my god that NASA project was stressful. I'm amazed how you managed it all. It was always good to discuss with you, looking forward to read your thesis. There were many more that made the lab what it is, thank you *Bart, Bruce, Bijoy, Ines, Stefan, Thijs, Rick, Maureen, Stefania, Andreas, Martin, Etienne, Guillaume, Rinse, Heleen, Ellen, Marius, Janne-Mieke, Riande, David*, and all the others that were there.

Binnen alles wat krioelt in stad en natuur is het niet zo moeilijk om afleiding te vinden van weerbarstige colloïdale deeltjes. Bovenal zijn daar mijn dierbare vrienden, zonder jullie ben ik niks. *Pim*, je bent zo'n betrouwbare gast, jouw vriendelijkheid, gastvrijheid en positiviteit maken het fijn om samen met je te zijn en dingen te doen. Wat een mooi avontuur was dat in India, en vast niet het laatste. Oneindige dank ook voor je bereidheid paranimf te zijn, help me alsjeblieft bij het strikje. *Joram*, mijn coach, zonder jou was ik ongetwijfeld nog steeds met m'n masterscriptie bezig geweest, volledig berooid (door jou!). Ons volgende doel: jij in't Concertgebouw en ik in de Paradiso. *Youssef*, it seems for you the world works according to different laws, it is exhilarating to be around you and see what unexpectedness unfolds, but the most amazing are your big heart and warmth. *Ido* en *Gerben*, onze kortstondige muzikale affaire zorgde dat ik me snel thuisvoelde in Amsterdam en verdient een vervolg. *Sam*, wat een mazzel dat ik tijdens de lunch toen naast je ging zitten, ons samenwonen was gelukzalig, ik mis je. Don't worry *Greg*, I won't forget you, you are a very gentle bear, the sweetest roommate I ever had. Er zijn er nog velen onbenoemd, goede oude studievrienden, de Descartes-groep, de Rijpenhof-groep, schandalig verwaarloosde vrienden uit Limburg, vriendelijke vreemden, mijn dank is groot.

In the reflection of city voices, tram noises and pigeons being scared away, an odd musical creature emerged: *Echofly*. Thank you so much *Ida, Selina, Daryo* and *Tobi*, for all the street performances, gigs, recording adventures and above all the joy of making music.

Ik wil ook iedereen die betrokken is bij inloophuis *De Kloof* bedanken, waar ik een paar keer per maand mijn kookskills heb mogen verfijnen. Bedankt lieve vrijwilligers en soms lieve, soms boze, maar altijd oprechte bezoekers, ik hoop dat dit boekje in de boekenkast zal prijken (en *Bernard*, het is eindelijk af!).

Als ik aan mijn familie denk dan voel ik mij onwaarschijnlijk gezegend. *Oma*, jouw liefde voor alle mensen en het leven is een eeuwige bron van inspiratie. Alle *ooms, tantes, neven* en *nichten*, te talrijk om op te noemen, binnen jullie rijke schakering is altijd iets te beleven. Je vindt er reisgenoten, festivalgangers en schaatsfanaten, maar ook hulp bij autoproblemen en boekadviezen. *Papa* en *mama*, wat hebben we het toch goed, en als er eens iets is dan kan ik altijd bij jullie terecht. Jullie energie, sportiviteit en liefde hebben ervoor gezorgd dat ik überhaubt aan dit werk kon beginnen en het nog heb weten af te ronden ook. En dan mijn drie knappe, intelligente en lieve zusjes. *Ida*, de afgelopen jaren hebben we veel mooie dingen samen beleefd, als wilde goden op de toppen van de ring of Steall of losgaan op het podium. Onze verschillen maken dat ik altijd van je leer, dankjewel voor

alle steun. *Tamara*, mijn mede linkshandige zuster, nu wordt jij de wetenschappelijk vaandeldrager van het gezin, natuurlijk met een veel cooler onderwerp, blub. Lieve *Judith*, je zult altijd de jongste blijven, en ik helaas altijd de oudste, maar je bent al zo sterk, ik bewonder hoe jij je mooie werk doet en het avontuur aangaat.

Tot slotte is er nog iemand die ik aan het begin van mijn promotie in het geheel niet kende, maar die mijn leven helemaal op zijn kop heeft gezet. *Selina*, onze liefde is voor mij het mooiste bouwwerk van mijn promotietijd. Soms buigt en breekt er iets, maar onze reis is nog lang niet voorbij, de Bumblebee staat klaar om samen de toekomst tegemoet te rijden.